Imperial College London
Department of Physcis

Towards Interfacing Single Photons Emitted from Dibenzoterrylene with Rubidium Ensemble Quantum Memories

Paul Burdekin

Supervised by
Alex Clark and Mike Tarbutt

Submitted for the degree of Doctor of Philosophy in Physics

March 2023

Acknowledgements

I feel incredibly fortunate to have been part of DBTeam. First and foremost, I would like to thank my supervisor Alex Clark for your incredible support and insight. Thanks to Kyle and Rowan for the huge amount you have taught me and for keeping the lab running. Thanks to Ross for the many discussions (rants) about science and other things. Thanks to Dominka, Salahudin and Seb for all of your efforts in fabricating the samples. For all their help behind the scenes, an enormous thank you to Sanja Maricic, Judith Baylis and Marcia Salviato. Thank you to Jon Dyne and the rest of the workshop for their technical expertise. And to the Centre for Cold Matter as a whole, thank you for making my PhD such an enjoyable and supportive experience.

Outside of work, there are no shortage of people to thank. While work could be tiring, I always had amazing housemates to go home to. To Dolly, Nina and Ross, for all of the great times at Lauderdale road. To Carys, who has put up with me for over a decade, thanks for the endless debates and wine. To Harry and Angel, thanks for being amazing friends and all of your years of service.

Thank you to Nishal, Filip and Amalia, for all help in Bristol and everything since. To Ryan and Webbo, thank you for bearing with me during the never-ending “about to finish my thesis” phase.

To all of Eggs, I could not have asked for a better group of friends.

To Mum and Dad, thank you for everything you’ve done, I couldn’t have done it without you. And to the rest of my family, who have been there throughout the years, thank you for all the support.

Last but definitely not least, Rosie. Thank you for always being there for me. It means the world.

Declaration

Unless otherwise noted and referenced, all work contained within this thesis is my own.

Author Publications

Articles

'Uniaxial Strain Tuning of Organic Molecule Single Photon Sources', Fasoulakis A., Major K. D., Hoggarth R. A., Burdekin P. M., Bogusz D. P., Schofield R. C. and Clark A. S., *Nanoscale*, **15**, 177-184 (2023) doi:10.1039/D2NR02439J

'Narrow and Stable Single Photon Emission from Dibenzoterrylene in para-Terphenyl Nanocrystals' Schofield R. C., Burdekin P. M., Fasoulakis A., Devanz L., Bogusz D. P., Hoggarth R. A., Major K. D. and Clark A. S. *ChemPhysChem*, **23**, 4 (2021) doi: 10.1002/cphc.202100809

'Single-Photon-Level Sub-Doppler Pump-Probe Spectroscopy of Rubidium', Burdekin P. M., Grandi S., Newbold R., Hoggarth R. A., Major K. D., and Clark A. S., *Phys. Rev. Applied*, 14, 044046. (2020) doi: 10.1103/PhysRevApplied.14.044046.

Conferences and Presentations

'Optimisation of Storage and Telecom Conversion of Single Photons in Rubidium' [POSTER] Burdekin P. M., Hoggarth R. A., Scholfield R. C., Bogusz D. P., Major K. D., Clark A. S., *BQIT* (2022)

'Waveguide-QED and Atom-light Interfaces' [TALK] Burdekin P. M., *CLEO Europe* (2021)

'An atomic quantum memory for light' [TALK] Burdekin P. M., *Imperial Optics Society* (2021)

'Sub-Doppler Single Photon Spectroscopy' [POSTER] Burdekin P. M., Grandi S., Newbold R., Hoggarth R. A., Scholfield R. C., Bogusz D. P., Major K. D., Clark A. S., *BQIT* (2020)

'Sub-Doppler Single Photon Spectroscopy' [POSTER] Burdekin P. M., Grandi S., Newbold R., Hoggarth R. A., Scholfield R. C., Bogusz D. P., Major K. D., Clark A. S., *PGR Symposium* (2019)

'Sub-Doppler Single Photon Spectroscopy' [POSTER] Burdekin P. M., Grandi S., Newbold R.,

Hoggarth R. A., Scholfield R. C., Bogusz D. P., Major K. D., Clark A. S., *Erice Summer School* (2019)

'Single Photon Sub-Doppler Spectrscopy of Rubidium' [POSTER] Burdekin P. M., Boissier S., Grandi S., Newbold R., Major K. D., Hinds E. A., Clark A. S. *QSUM* (2019)

Abstract

Photonic quantum information processing is a pivotal aspect of the emerging quantum technology landscape, with a wide range of applications in quantum computing, communication, simulation and sensing. The use of single photons for these applications is of immense interest, but requires both the generation of single photons and the ability to interact them separately, often relying on probabilistic processes.

The first part of this thesis showcases work on the generation of single photons, utilizing an organic molecule, Dibenzoterrylene (DBT), doped into an anthracene (Ac) crystal. We will introduce a comprehensive theoretical framework for characterizing these molecules, and present experimental results where the wavlength of emission from DBT is tuned through three different tuning mechanisms. Additionally, we will explore techniques for enhancing the emission properties of DBT, before finally demonstrating single photon emission from DBT in a novel host matrix: *para*-Terphenyl.

In the second part of this thesis, we shift our focus to quantum memories - critical devices capable of storing and on-demand recall of quantum states of light, required to overcome the limitations of probabilistic photon-photon interactions. We will derive equations of motion governing the memory interaction with single photons and an ensemble of atoms. Next, we will explore methods for optimizing the memory interaction, while increasing the complexity of our model to more accurately resemble an interface between photons emitted from DBT/Ac and a rubidium (Rb) vapour, near resonant with the DBT/Ac. Finally, we will present the major challenges facing these systems and potential avenues for overcoming them.

The results presented in this thesis pave the way for interfacing photons emitted from DBT with quantum memories based on a Rb ensemble.

Contents

Chapter 1

Introduction

1.1 Quantum Technologies

The goal of quantum technologies is to harness quantum mechanics to build devices that can outperform their classical counterparts. Non-intuitive notions such as superposition, where a quantum object can exist in more than one state at once, and entanglement, where two quantum objects can have non-local correlations, theoretically allow improvements in computational time [1,2,3], information security [4,5,6] and measurement sensitivity [7] when compared with today's classical state of the art. The field of quantum technology has exploded over the past few decades, but more recently we have seen many startup companies being founded, with ever growing commercial investment[1]. This suggests that these technologies will soon have an impact in the real world.

1.1.1 Computation

The holy grail of the field is to build a universal quantum computer; universal meaning that the computer could run any quantum algorithm (and coincidentally any classical algorithm).

---

[1] In 2017 and 2018, the amount of investment raised by quantum startups worldwide increased by 4 times compared with the previous two years, though since information on private funding deals in China is lacking, global investment is believed to be much higher [8]

A quantum algorithm performs the same tasks as a classical algorithm, but leverages quantum physics in order to potentially complete the task more efficiently [2, 9, 10, 11]. The quantum computing framework most analogous to classical computation is the quantum circuit model, where in much the same way as an everyday classical computer uses bits (ones and zeros) on which it successively applies logical gates (OR, XOR, AND etc.), a circuit model quantum computer uses qubits and quantum logic gates. Qubits are similar to bits in that they can be zero or one, yet due to their quantum nature, may be in a superposition of both states, as well as be entangled to one another, allowing the measurement of one qubit to influence the states of the others. An array of qubits defines an exponentially larger space than the same number of classical bits. Just as any classical computation can be performed provided we can apply single bit gates and NAND gates to pairs of bits, universal quantum computation also only requires single qubit gates, allowing a qubit to be placed into an arbitrary superposition, and two-qubit gates, to facilitate entanglement [12, 13].

In the quantum circuit model, to realise a particular algorithm, we initialise our qubits into some known state, apply a sequence of logic gates, and then measure the final output, thus collapsing any superposition into a ‘classical’ answer. This procedure is not guaranteed to yield the correct answer, due to the probabilistic nature of measurement and therefore might require multiple tries of the algorithm, however for certain problems where the solution is hard to compute but easy to check, a quantum computer has been proven to provide an exponential speed up. One such example is Shor’s algorithm, which computes the prime factors of an integer in polynomial time (the time scales as N^k where N is the input integer and k is a positive constant) [2]. The best known classical factoring algorithm, the general number field sieve, works in sub-exponential time (grows faster than polynomial but slower than exponential). The classical ‘hardness’ of the factorisation problem led to much of the internet security being based upon it, such as the RSA cryptosystem [14]. Some other algorithms shown to have a quantum advantage are Grover’s algorithm [9], for search of an unordered database, or algorithms for data fitting [15] and linear solvers [16].

Equivalently to the quantum circuit model we have just described, quantum computing may also be performed using measurement based protocols. Here the array of qubits is first initialised into a large cluster state (a network of highly entangled qubits), on which single qubit measurements and operations are then performed, with the outcomes used in a feedforward manner to inform subsequent measurements and operations [17, 18, 19, 20]. This alternative approach swaps out the difficult task of performing many high fidelity multi-qubit gates, as is the case in the circuit model, for the difficult task of preparing a large cluster state. While preparing a cluster state also requires performing many entangling gates, we can post select on the successful generation of the cluster state.

1.1.2 Simulation

One of the most promising short-term applications of a quantum computer would be to efficiently simulate quantum systems [21]. Currently, around one third of all supercomputing time is spent solving problems in quantum chemistry and material science [22]. For this use case, a quantum simulator would not necessarily need to be a universal quantum computer. For interesting quantum systems that are difficult to study directly, instead we can construct an analogous and experimentally more achievable quantum system; its dynamics can then be studied and used to infer the dynamics of the target system [23]. One such example is Boson sampling being used to generate molecular vibrational spectra [24].

Alternatively, some NP hard problems can be reduced to finding the ground state of a certain Hamiltonian [25, 26]. This is known as quantum annealing and begins by preparing a quantum system with a known Hamiltonian in the ground state, before adiabatically evolving the system Hamiltonian into the desired one. Provided the evolution continues to be adiabatic, the system will remain in the ground state, allowing the final Hamiltonian ground state to be determined [27]. Examples of such problems include a variety of optimisation problems, such as training deep neural networks [28] and simulating complex molecules [29, 29]. In fact, quantum annealing has been shown to be capable of universal quantum computation [30]. Another simulation approach is Trotterisation, where the desired Hamiltonian is approximated by a sequence of small operations [31, 32]

1.1.3 Communication

Quantum communication deals with the distribution of quantum information to remote places. One use would be to link multiple quantum computers or simulators with a quantum channel, creating a quantum network or internet [33, 34, 35]. Another hugely pursued area is quantum key distribution (QKD). This is a technique for allowing the distribution of a private key[2] over a quantum channel between two parties, commonly named Alice and Bob. Using the fact that measurement of a quantum system irrevocably alters it, a key can be distributed between Alice and Bob in such a way that it is impossible for a third party, Eve, to learn information about the shared key without Alice and Bob knowing. Once the key has been shared and provided the key was generated at random, it can be used to encrypt and send a message over a public classical channel. Eve could then intercept the message, but without access to the private key, Eve cannot hope to decrypt the message. After the key has been used, it is discarded so that no one message can yield information about any other. This protocol is known as the one time pad. In this way, QKD allows for perfectly secure messages to be distributed [4, 6, 36].

So far, QKD has been demonstrated over a distance of 1203km using satellites [37], while 421km has been reached in optical fiber [38].

1.1.4 Metrology

In classical estimation theory, the error in estimating a parameter scales as $n^{-1/2}$, where n is the number of measurements made using a classical probe. Using a quantum system as a probe, it is possible to improve upon this bound and reach the Heisenberg limit of n^{-1} [7], or further still, if there are interactions between successive quantum probes, the so called super-Heisenberg scaling can be achieved: theoretically a k-particle interaction could achieve a scaling of n^{-k} [39, 40].

Some key applications of quantum metrology are phase and amplitude estimation. Phase estimation is useful for a wide variety of tasks, such as magnetometry [41, 42] or spectroscopy [43].

---

[2] By key we mean a string of bits which can be used to encrypt and decrypt a message.

A relative phase between two paths carrying quantum states can be introduced by way of a Mach-Zehnder interferometer in which the detection probabilities at the outputs are dependent on the relative phases. Alterations to one or both of the two paths, such as from a changing magnetic field [44] or gravity [45], results in a measurable change at the output of the interferometer, with a greater precision than could be achieved using purely classical probe states [46]. One use case of amplitude estimation is thermometry, where a quantum probe, such as an atomic two level system, is brought into thermal contact with the target system and allowed to thermalise. The temperature can then be read out from the steady state of the probe [47].

1.2 Platforms for quantum technologies

There are a whole host of physical systems to choose from when trying to build the technologies we have just described, each with their advantages and disadvantages. When trying to construct a system for quantum information processing (QIP), such as for a quantum computer or simulator, we need to be able to perform one and two qubit gates with a high fidelity, and we would like to be able to perform many of these gates before our system decoheres[3]. We should be able to initialise and read out the state of each qubit, and the physical system should be scalable [48]. Together, these requirements are known as the DiVincenzo criteria.

Systems based on neutral atoms and ions can have very high gate fidelities of over 99% [49,50,51] but face challenges in scaling up the qubit array size (2D arrays of berylium ions have reached numbers of around 345 [52] and 256 rubidium atoms have been successfully trapped in a 2D lattice [53]). Gates can take of order a microsecond to perform [51], with decoherence rates ranging from Hz for trapped ions, limited by stray magnetic fields [54], to ∼mHz for neutral atoms trapped in an optical lattice [55]. IonQ [56] and Quantinuum [57] are both pursuing trapped ions as an architecture for quantum computing, with the number of qubits available for complex algorithms currently around 30 [56]. QuEra recently revealed a 256 neutral atom quantum simulator [53].

---

[3] Decoherence is the loss of a definite phase relationship between the quantum states of interest.

Trapped atoms are also promising as magnetomoeters, where the Zeeman effect results in a precession of the atomic spin [58], as well as gravimeters, using interference of matter waves to measure acceleration [59].

Solid state platforms such as superconducting qubits [60,61] and spin defects [62,63,64,65,66] can leverage the already established semiconductor industry and so are more scalable in principle. However, for defects located in macroscopic lattices, such as phosphorus implanted in silicon, the semiconductor lattices have to have a high isotropic purity to reduce the decoherence due to the spin background of the surrounding lattice [67,68]. Even with highly pure and well engineered substrates, superconducting [69, 70] and spin qubits [67, 68] require cryogenic temperatures to operate, which can create further scaling issues. Superconducting qubits can achieve above 99% single and two qubit gate fidelities [69] on timescales of hundreds of nanoseconds, though coherence times are on the order of a hundred microseconds [70]. Phosphorus donor electron spin qubits in silicon have shown $> 99.9\%$ fidelity single qubit control [66] and two-qubit gates of 94% on time-scales of ~ 1ns at $50\,\mathrm{mK}$ [65].

Both IBM [71] and Google [72] have shown quantum processors of 20 and 53 qubits respectively, with Google recently claiming quantum supremacy [72].

Solid state platforms are another potential avenue for quantum sensing, as the sensitivity of spins housed within lattices can be used to monitor the surrounding environment. One example is nitrogen-vacancy centers combining strong electronic and magnetic moments and achieving high defect densities, where their quantum state can be optically read out [73, 74]. These defects can also be made very stable at room temperature, allowing their use in a larger range of environments. However, high density ensembles suffer from low detection efficiency and short coherence times [75].

Superconducting quantum interference devices (SQUIDs) are some of the longest researched magnetic sensors [76], and some of the most sensitive [77]. Quantum superpositions of superconducting qubits are associated with large electric and magnetic moments and have also demonstrated a variety of quantum sensing protocols [78].

Then we have photonics. Photonics is a natural candidate for quantum communication due to the photons inherent speed and information capacity as a result of their large bandwidth [79] and many degrees of freedom [80, 81, 82, 83, 84].

Unlike the other systems mentioned, photons are somewhat resistant to decoherence because of their weak interactions. However, their greatest strength is also a major weakness when trying to realise two-qubit gates: photons aren't just weakly interacting with their environment but also weakly interacting with each other.

The Knill, Laflamme and Milburn (KLM) scheme [85] showed how linear optical elements, single photon detectors and ancillary photons are sufficient to realise two-qubit gates, albeit probabilistically. With this scheme, it is possible to do all of the photon processing we require at room temperature, which significantly reduces the technical overhead required compared with other systems. Yet, due to the probabilistic nature of the two qubit gates, in order to scale up this technology, some form of multiplexing is required probabilistically [86]. Spatial multiplexing attempts many two-qubit gates in parallel, then uses fast detection and switching to send the successful outputs into the next stage of the processor. This requires a huge amount of resources and necessitates the detectors to be cryogenic to improve their efficiency, as well as be located close to the switching electronics, to reduce the feed-forward time. The result is that the photonic chips now need to be cryogenically cooled and the chip tolerances become very strict. Alternatively, temporal multiplexing repeatedly attempts the same two-qubit gate until successful and then stores the success in some form of quantum memory. Once enough two-qubit gates have been completed, the successes can be recalled from their respective memories and move along to the next processing stage. This solution requires the memory to be very efficient in storage and retrieval over the timescale of interest.

Rather than using linear optics to realise two qubit gates, a second approach is to use high single-photon non-linearities, such as non-linear crystals, to perform deterministic two-qubit gates [87]. Alternatively, the photon coherence can be mapped onto a highly interactive medium, such as neutral atoms [88] or another one of the previously discussed architectures [89, 90]. Once the entanglement has been completed, the coherence can be mapped back to an optical photon.

This leads us naturally to the idea of a hybrid platform: one which combines the advantages of multiple systems connected together with a quantum network or quantum internet [91]. Photons are naturally suited to the role of connecting different static systems together via photonic links [92,93].

Photons are also a useful resource for sensing. Quantum correlations between photons have allowed superesolution imaging beyond the diffraction limit of telescopes [94], microscopes [95] and lithography [96]. Macroscopic squeezed states of light have famously been employed to measure gravitational waves at LIGO [97], along with spatial correlations of light fields being used to image an object using light that never physically interacted with the object, known as ghost imaging [98].

For a hybrid platform, it is likely that the static quantum system will generate photonic flying qubits needed to link many nodes. However, when using photons for quantum computing, long distance quantum communication and quantum metrology, an on-demand source of single photons will be a useful technology[4]. The next section will discuss the ideal characteristics for a single photon source and review some of the sources found in the literature.

1.3 Photon Sources

Given that we wish to use photons as qubits, or as flying-qubits linking stationary quantum nodes, we need an on demand source of photons. Photon sources can in general be split into two camps: probabilistic and deterministic. A probabilistic source is one that uses a non-linear interaction with a medium (such as parametric down conversion or four wave mixing) to produce a pair of photons [102]. The detection of one of the photons heralds the existence of the other. For current photon-pair sources, the probability of producing a photon for a

---

[4] It's worth noting that the technologies mentioned can also employ macroscopic states of light, such as continuous variables (CVs) [99]. CV schemes rely on squeezing and can be deterministic but often have lower gate fidelities than single-photon technology [100]. Hybrid approaches between CV and single photons have been proposed [101].

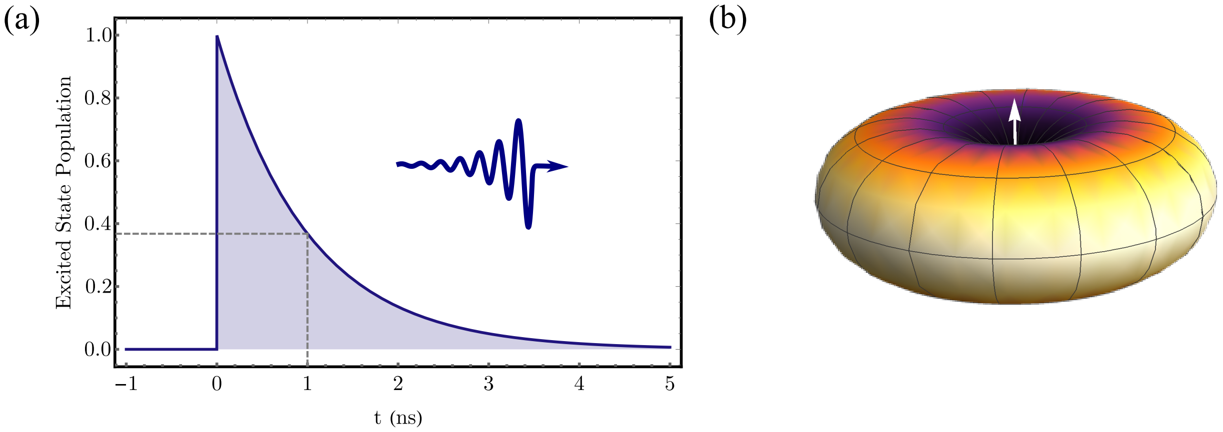

Figure 1.1: (a) Excited state population as a function of time for an emitter with lifetime $\tau = 1$ns, after being excited at $t = 0$ns. (b) Far-field dipole emission pattern of a dipole. Lighter colour indicates higher probability of emission in this direction.

given input pulse must be kept low to minimise the chance of producing multiple photons. We can overcome this nonideality through multiplexing [103,104,105,106] as mentioned previously when discussing solutions to probabilistic multi-qubit gates. Given enough multiplexing, a heralded probabilistic source can approach an on demand source of photons.

Alternatively, deterministic sources can be constructed from the fluorescent decay of a two-level system (TLS), illustrated in Fig. 1.1a. Here we send a fast trigger (fast relative to the decay time of the emitter) at $\tau = 0$ ns to excite the TLS and expect to collect a photon at some specified time later. With such systems, it is possible to have a high probability of single photon generation with negligible chance of multiphoton emission. We define the efficiency of our source as the probability of collecting a photon, given that we have triggered the source. Most of the quantum applications described have a minimum efficiency requirement in order to be feasible. For example, quantum computing error correction schemes require efficiencies of above 93% [106]. We can further separate efficiency η into four parts: excitation efficiency η_e, quantum yield Q, branching ratio α and collection efficiency η_c,

$$\eta = \eta_e Q\, \alpha\, \eta_c\,. \tag{1.1}$$

Excitation efficiency refers to the probability that the excitation method successfully drives the emitter into the excited state. This will be discussed in more detail in the Chapter 2 but in general, with a suitable choice of excitation scheme, this can approach unity [107]. Quantum yield quantifies the probability that the emitter decays via fluorescence to the ground state, rather than a non-radiative process. Here again, we want to choose a system where this is near unity. Aside from quantum yield, photoemitters will typically have multiple fluorescent decay pathways. The ratio of fluorescence on the desired transition to all other transitions is termed the branching ratio, and is another important parameter to consider. Collection efficiency measures the probability that the emitted photon is collected into a given spatial mode, which is where two level emitters tend to fall short of their probabilistic cousins. The radiation pattern of TLSs is naturally spread over a wide angular range (see Fig. 1.1b) which can lead to low collection efficiencies on the order of 1% [108, 109, 110], resulting in deterministic sources also becoming probabilistic. The collection efficiency can be improved through placing the emitter in a photonic structure to selectively enhance emission into a particular spatial mode [109, 111, 112]. These structures can also enhance or suppress decay on particular frequency modes, referred to as Purcell enhancement, leading to improved quantum yield and branching ratio of the emitter. The Purcell factor is the ratio of modified spontaneous emission rate, to the emission rate in the absence of a photonic structure. Section 3.1.3 will examine some of these structures in more detail.

There are many candidates for deterministic photon sources based on a TLS [113, 114] and the following section will discuss the optical properties of the ideal photon source derived from such a scheme.

1.3.1 Ideal Photon Source

Firstly the wavelength of the photons, determined by the energy difference between two energy levels used in photoemission. Shorter wavelength photons are typically easier to detect with high efficiencies, owing to their larger energies [115]. On the other hand, longer wavelength photons, particularly in the telecommunications band, benefit from low-loss transmission through optical fibers [116, 117] and silicon chips [118]. Aside from detection efficiency, if we want the emitted photons to interact with another system, such as a quantum memory, we need the photons to

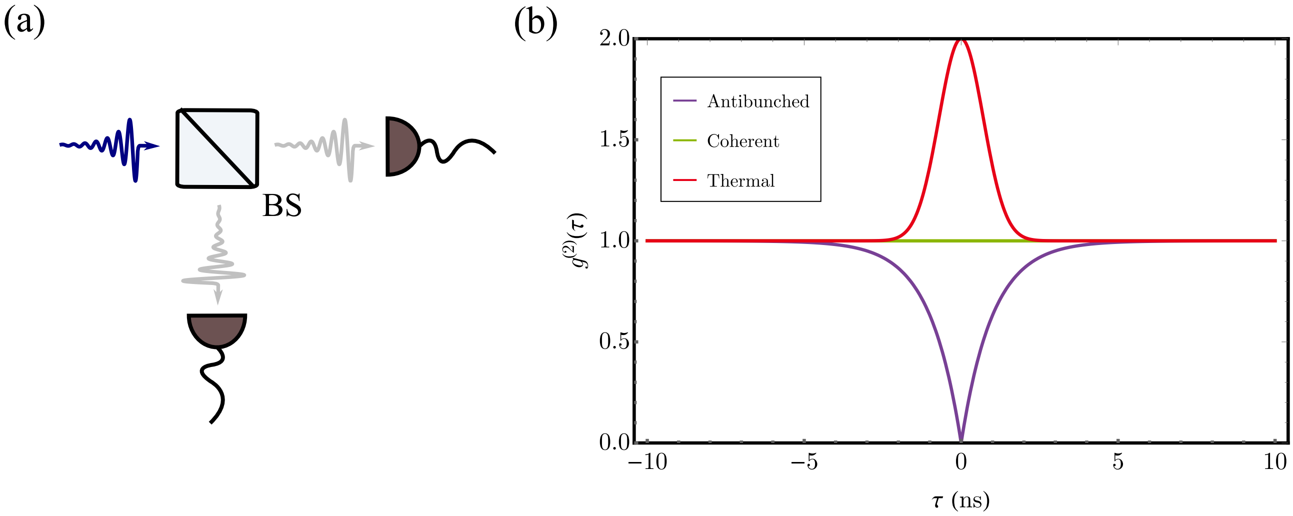

Figure 1.2: (a) Schematic of a Hanbury-Brown-Twiss interferometer. A photon is split by the beamsplitter (BS) but can only be detected at one of the detectors. After measuring a photon at one of the detectors, the probability of simultaneously measuring a photon at the other detector is zero for a true single photon source. (b) A plot of normalised second-order correlation functions (Eq. 1.2) for a thermal (red), coherent (green) and antibunched (purple) photon source, after detecting a photon at $\tau = 0$. The photon source used in this simulation had a lifetime of 1ns and was excited using a continuous wave laser.

be compatible with the available transitions in the partner system [119, 120, 121].

In terms of scalability, a solid state source is advantageous. Trapped atoms or ions offer the necessary TLSs to realise on demand photon generation but suffer from experimental complexity of trapping and cooling. In addition, these sources are often inefficient, owing to the difficulty in collecting the emitted photons [115]. Solid state sources allow photonic structures to be patterned around the emitter to improve its optical properties [109, 111, 112], whereas clouds of laser-cooled atoms require being dropped through an optical cavity [122, 123, 124]. It is also technically easier to place a lens or fiber optic close to the solid state emitter to improve collection, along with having emitters directly on chip, where the photon can be immediately coupled to waveguides and connected to later processing elements.

The photon purity of the source refers to the likelihood that only one photon is emitted at once. This is a key requirement for secure quantum communication and error free quantum computation [92]. Experimentally this is measured through a Hanbury Brown and Twiss interferometer [94], depicted in Fig. 1.2a. Emitted photons are collected and directed at a beam splitter, with two single photon detectors at the output. The correlation between detecting a

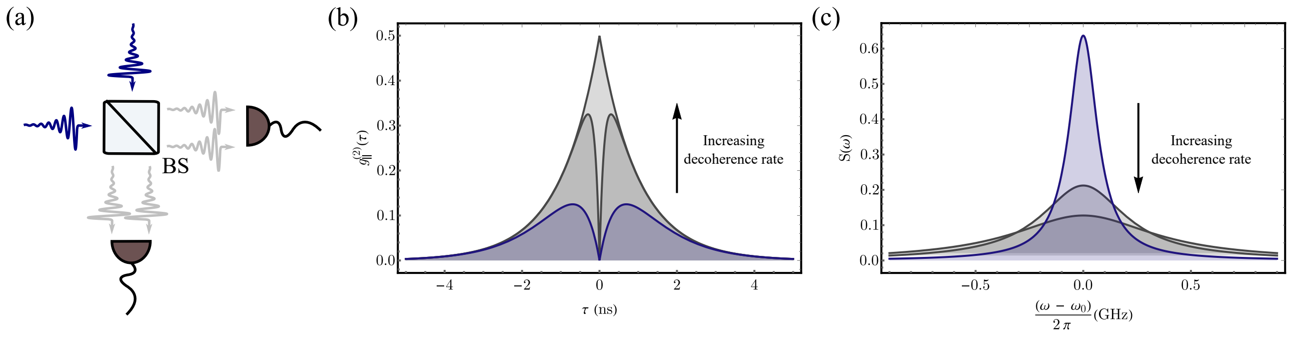

Figure 1.3: (a) Schematic of Hong-Ou-Mandel (HOM) interference. When two identical photons arrive at the two input ports, bunching occurs at the output, resulting in a zero probability of simultaneously detecting photons at both detectors at the same time. (b) Coincidence probability around zero time delay for a HOM measurement, where the emitter is excited by a pulsed laser. As Γ_2^* is increased, successive photons show a shorter time in which they are indistinguishable (where the coincidence probability drops to zero) (c) .Frequency spectrum of a photon emitted through fluorescent decay as dephasing (Γ_2^*) is increased, causing the linewidth to broaden.

photon at one detector at time t, followed by detecting another photon at time $t + \tau$, is given by the second-order correlation function,

$$g^{(2)}(\tau) = \frac{\langle I(t)I(t+\tau)\rangle}{\langle I(t)\rangle^2}\,, \tag{1.2}$$

where $I(t)$ is the intensity of the light field at time t. The angle brackets denote the cycle-average of the contained quantities. Setting $\tau = 0$ gives the probability of detecting a photon at both detectors simultaneously. A true single photon emitter will emit antibunched light and have a $g^{(2)}(0) = 0$, illustrated in Fig. 1.2, provided all other nearby emitters and background can be rejected. For $\tau > 0$, antibunched light will show an increasing probability of a coincident count which follows the decay envelope of the emitter. Coherent states, such as those emitted from a laser, show no correlations between successive photons, displaying $g^{(2)}(\tau) = 1$ for all delay times. Individual modes of thermal light sources, including incandescent light bulbs, display bunching and are more likely to emit multiple photons at once. These display $g^{(2)}(0) > 1$.

For quantum information applications, we require that each emitted photon is indistinguishable [125, 126]. The indistigiushability of two photons can be verified through a two-photon interference effect, first demonstrated by Hong, Ou and Mandel [127]. The general principle is illustrated in Fig. 1.3a. Two photons are made to be incident on the two input ports of a 50 : 50 beam splitter. If the two photons are perfectly indistinguishable, their probability amplitudes on the two output ports of the beam splitter interfere to cause both photons to exit from the same port (the photons are actually in a superposition of both exiting from the top port and both exiting from the bottom port) [128]. That is, if a single photon detector where placed at each of the outputs, the probability of recording a coincidence count would be zero for zero time delay - similarly to the antibunched photon source when measuring the photon purity [112, 129]. An illustration of such a measurement is shown in Fig. 1.3b in dark blue, for a photon source with a decay rate of 4 ns excited by a pulsed laser.

Two photons emitted by the same type of source, may be rendered distinguishable for many reasons, such as due to variations in the local environment from nearby charges or spins, causing the central frequency of the photon to fluctuate, known as spectral diffusion. In addition, interactions with phonons in the local environment can bring about an increase in the decoherence rate of the emitter, also resulting distinguishable photons. In this case, the central dip seen in the dark blue plot of Fig. 1.3b will become increasingly sharper until it is impossible to resolve the dip, indicated by the grey and lighter grey plots. A larger decoherence rate will also broaden the spectral linewidth of the photons, as shown in Fig. 1.3c. Cryogenic temperatures can freeze out many of the phononic modes in a solid state system, reducing the dephasing rate to an acceptable level, allowing the Fourier-limited bandwidth to be reached - the smallest bandwidth possible for a photon of a particular temporal duration and shape [130, 131]. An ideal source should have long-term stability in emission frequency and minimal dephasing, such that emitted photons are Fourier-limited.

The repetition rate of our source is another important consideration. Fluorescence from a TLS follows an exponential decay, as shown in Fig. 1.1a, with a lifetime $\tau = 1/\Gamma$ where Γ is the decay rate of the excited state. This decay limits the repetition rate of our source, as the excitation rate must be slow when compared with Γ. Therefore a higher bandwidth source may be excited at a higher repetition rate, allowing for more information per unit time to be transmitted.

The choice of solid state system will impact the bandwidth of the photons, as we shall see in Section 1.3.2, but additionally to this, Purcell enhancement may be used to increase the decay rate of the emitter, and thus increase the bandwidth. This has the added benefit of reducing the opportunity for dephasing from the environment to occur during the spontaneous emission process.

It is important when choosing a solid state system, that the bulk material containing the dopant emitters, protects the emitters from unwanted chemical reactions or nearby impurities, which otherwise could lead to degradation of the emitter optical properties. However, even for a perfect combination of host and dopant, the differing environments around each emitter will give rise to an inhomogeneous distribution of emission wavelengths and excited state lifetimes. In order to interfere photons from separate emitters, or to bring an emitter onto resonance with another system, an ability to tune the photoemission frequency is desirable. This can be achieved for example through Stark tuning, where an electric field alters the energy difference between the two levels of an emitter [132, 133], or strain tuning, where a strain field modifies the bulk material [134, 135]. There will be more on this in Section 3.1.2.

The next section will review the current state of the art in solid state TLS single photon sources.

1.3.2 State of the art

Quantum Dots

A quantum dot (QD) is an artificial atom, where three dimensional confinement of electron wavefunctions gives rise to a discrete energy level structure. The spatial confinement is constructed by having a nano-island of lower band-gap semiconductor surrounded by a larger band-gap semiconductor material, forming a potential trap for electrons and holes[5] [115]. A photon is generated through excitation of the QD to a higher energy level, where an electron is promoted from the valence band to the conduction band, leaving behind a hole within the valence band. This can be done using either an optical [136,137] or electronic pulse [138], with high excitation probability. Following this, the recombination of the electron-hole pair leads to photoemission, with potentially high quantum yields and low $g^{(2)}(0)$ values [139,140]. QDs have

---

[5] A positive quasi-particle, representing the absence of an electron.

also shown deterministic generation of entangled photon-pairs [141] and GHZ states[6] [143].

Fabrication of QDs is typically done through epitaxial growth on a semiconductor substrate, or synthesized in solution to produce colloidal QDs. Both epitaxial [129,136,144,145,146,147,148] and colloidal QDs [149,150,151] have been used as bright single photon emitters. Epitaxial QDs are more frequently used due to the relative ease through which they can be integrated into other solid state devices, such as micro pillar cavities [139] and photonic crystal waveguides [152]. Photonic structures have been very successful at improving the collection efficiency, particularly when the structures have been deterministically placed around pre-fabricated QDs [153, 154]. On the other hand, colloidal QDs have also shown potential as single photon sources, with photon purities of $g^{(2)} < 0.05$ shown at room temperature [155], but have not yet shown fourier-limited emission, even at cryogenic temperatures [156].

A variety of emission wavelengths can be tailored, from 350nm to 1550 nm [114, 149, 157, 158, 159, 160], depending on the materials used and size of the QDs. QDs fabricated from III-V semiconductors[7] seem to perform best, owing to their strong optical dipoles, allowing large coupling to optical modes [114,161]. These typically sit around 900 nm, with radiative lifetimes of order 1 ns [162,163,164]. An ensemble of QDs present an inhomogeneous distribution of tens of nanometers due to their differing sizes and environments, which presents a problem when trying to tune separate QDs onto resonance using Stark fields [147] . Strain fields have been used to tune InAs QDs over the full inhomogeneous range [129]. Improved synthesis can reduced the size of the inhomogeneous broadening down to a much more manageable span of a few nanometers [165].

Ideally, for pulsed laser excitation, a non resonant laser would be used to excite the QDs, as this could be spectrally filtered out, leaving just the emitted photons. Non-resonant excitation has demonstrated collection efficiencies of 80% and photon purities of $g^{(2)}(0) = 0.009$. Unfortunately, this excitation scheme limits the indistinguishability of successively emitted photons to

---

[6] A GHZ state, named after Greenberger, Horne and Zeilinger [142], is a three-qubit entangled state $|GHZ\rangle = (|000\rangle + |111\rangle)/\sqrt{2}$, from which arbitrary large cluster states for universal quantum computation can be created [126].

[7] A III-V semiconductor is a compound made from a semiconductor with three valence electrons, and one with five valence electrons, respectively. Examples include InP, InAs, GaAs, GaN, and InSb.

75% [153]. When integrated into a photonic cavity, the increased radiative decay rate (caused by Purcell enhancements between $5 - 20$) can begin to approach the non-radiative decay rate used in non-resonant excitation. This results in a timing jitter of the emitted photons comparable to their temporal duration, limiting the achievable indistinguishability [114, 166]. An additional limitation can come from excess charge carriers produced in the surrounding bulk and wetting layers. Through carrier collisions, interaction with phonons and strong Coulomb interactions, the generated photons undergo fast dephasing [114].

Resonant excitation is more challenging to filter out, but can be accomplished through spatially decoupling the excitation and emission optical modes, and through a crossed polarization scheme [136]. Using resonant cross polarized excitation, collection efficiencies of 66% have been reached, along with photon purities of $g^2(0) = 0.009$ and HOM dips with visibility of $96.4 \pm 2\%$ [167]. Coalescence probability measured using photons from two different QDs, tuned onto resonance with each other through the quantum-confined Stark effect, yielded a visibility of 93% [168].

Alternatively, electric pulses have been shown to drive QDs to emit photons through electroluminescence [146,147]. For electrically driven systems, a $g^2(0) = 0.03 \pm 0.01$ has been measured [147]. Indistinguishabilities are on the low side, at around 60% [169, 170]. Overall efficiencies are comparable to optically excited QDs [138].

1.3.3 Colour centres

Color centres are impurities or crystallographic point defects within a generally wide bandgap semiconductor, resulting in energy levels residing within the bandgap. A commonly used host semiconductor is diamond [113,115,171,172], containing defects such as nitrogen-vacancy (NV) [173,174], silicon-vacancy (SiV) [175],germanium-vacancy (GeV) [176] and tin-vacancy centres [177]. These are generally produced through ion implantation and annealing [113,171,176,178, 179], and show narrow emission at cryogenic temperatures [113, 171, 180], with wavelengths typically ranging from $600 - 750\,\text{nm}$ [174,175,176]. SiV and GeV centres show superior optical properties when compared the NV centres. SiV and GeV complexes exhibit inversion symmetry which makes them more robust to spetral diffusion caused by electric fields and local strain variation [181]. They also show a more favourable branching ratio (around 90% [182] and 70% [176] for SiV and GeV respectively) when compared to NV centres ($\sim 3.2\%$ [183]).

Due to low quantum efficiency attributed to a large non-radiative decay rate and the high refractive index of diamond, these single-photon sources typically present low intrinsic efficiencies. This can be mitigated through using sub-wavelength nanocrystals and engineering photonic structures near or around the defects, leading to an increased collection efficiency [115]. Nanodiamonds grown on iridium containing negatively charged SiV centres showed count rates of up to 6.2 Mcounts/s, due to reducing the non-radiative decay rate and less total internal reflection [175]. Single photon purities of $g^2(0) < 0.1$ [184] and HOM dip visibilities of $72 \pm 5\%$ [185] have been shown. It is possible to electrically drive diamond, though due to a high defect concentration and lack of control of the charged state, this typically leads to a higher background level [113].

An alternative bulk material is silicon carbide (SiC), with emission ranging from $520-1388$ nm, lifetimes from $1-170$ ns and quantum efficiencies up to 70% [171,186,187,188]. Nanofabrication techniques of SiC are well established and it can be doped with donors and acceptors in order to allow efficient electrical driving of the vacancies to the excited state. Another advantage is that SiC is an indirect bandgap semiconductor and so has low background luminescence when driven electrically. SiV centres in SiC have shown HOM dip visibilities of 90% at 5 K [189].

Rather than point defects in bulk materials, it is also possible to engineer colour centers in 2d materials. Emitters in hexagonal boron nitride (hBN) show emission from $302-825$ nm [190,191,192] with brightness ~ 4 Mcounts/s without any additional immersion lenses or Purcell enhancement [191]. However, the atomic structure of these emitters is not yet well understood. Samples of hBN typically display a large inhomogeneous broadening, with lifetimes spaning 1 to 10 ns [192]. Some emitters are observed to be to be photostable, and as the mechanisms governing these defects are better understood, it is expected that their optical properties will improve. The atomically thin films allow easy incorporation into cavties, with Purcell enhancements of 2.3 being reported [193]. Defects in carbon nanotubes have been placed within plasmonic nanocavities, with quantum yields equal to 74% and single photon purities of near unity at 1320 nm.

1.3.4 Organic Molecules

Organic crystal matrices doped with single polycyclic aromatic hydrocarbons (PAHs) are another potential source of on demand photons. Larger PAHs lead to longer wavelength fluorescence [194], ranging from $200-800$nm [195], as well as increasing quantum yield of fluorescence. Near unity excitation efficiencies have been demonstrated, and quantum yields above 95% have been reported [196, 197], along with branching ratios of up to 50% [121, 198].

PAH molecules that have shown single photon emission include pentacene, terrylene (Tr), perylene, dibenzanthanthrene (DBATT) and dibenzoterrylene (DBT) [195]. Both resonant and non-resonant excitation can be used, with excited state lifetimes on the order of a few nanoseconds. A single photon purity of $g^2(0) = 0^{+0.03}_{-0.00}$ has been recorded for DBATT [199]. PAHs embedded within an organic matrix show indefinitely photo-stable emission, over a inhomogeneous broadening of several GHz [200], capable of being excited over a trillion times without photo-bleaching. Molecules are somewhat protected from lattice phonons owing to the organic molecules being held within the host by van der Waal forces, in contrast to QDs and colour centers which are strongly coupled to the surrounding crystal [201]. Even so, molecular systems require liquid helium temperatures ($\sim 4\,\mathrm{K}$) to produce Fourier-limited photons [202]. Photons emitted from DBATT have reached indistinguishabilities of 97% [199].

Integration with solid state devices is more challenging for molecules, compared with QDs and colour centers. Organic molecules can be degraded by conventional fabrication techniques and post processing of structures is limited due to high sublimation rates and low-melting points of the organic host matrices. Nevertheless some progress has been made in this area [203, 204]. Wang et al. [205] realised a DBT doped Anthracene crystal in an open micro-cavity. Through tuning the cavity frequency mode to the transition of interest, they were able to increase the branching ratio from $\alpha \approx 33\%$ to 95%, resulting in a photon generation efficiency of 95% - though the collection efficiency from the cavity was poor. Coupling molecules to waveguides has been shown at room temperature with collection efficiencies of 42% [206], as well as cryogenic temperatures with collection efficiencies of 7% for evanescent coupling [201], or up to 9% when the emitter was placed within a nanogap between two waveguides [207]. DBT has also been coupled to titanium-dioxide ring-resonators, showing Purcell factors of 11 and coupling into the waveguide of 3.5% [208]. Collection efficiencies of close to 100% have been shown using a planar antenna with high-numerical-aperture optics at room-temperature [209].

Both Stark [132] and strain tuning [135] have been demonstrated, with the former demonstrating tuning over $> 200\,\mathrm{GHz}$. A third tuning method has also been reported, where intense laser light can cause a permanent red tuning of the molecule optical wavelength, without the need for any nanofabrication steps [210].

In Chapter 3 will discuss DBT doped into two different host matrices: Ac and para-terphenyl.

1.4 Quantum Memories

We have previously discussed how photons are an excellent candidate for quantum technologies, but how they can suffer from probabilistic processes and weak interactions. We have also alluded to the idea of a quantum memory (a device that can store and retrieve a quantum state) being used to temporally multiplex probabilistic multi-photon gates. The storage is required to be coherent and involve no measurement of the input state, otherwise the retrieved state would be altered. In this section we will discuss how a quantum memory can circumvent many of the challenges faced by a photonic platform and what metrics are important for judging a quantum memory, before finally reviewing the current state of the art.

1.4.1 Applications

Temporal multiplexing and filtering

Photon generation and multi-qubit photonic gates both suffer from being probabilistic. Probabilistic photon generation can be turned into on-demand generation if the heralded photon is

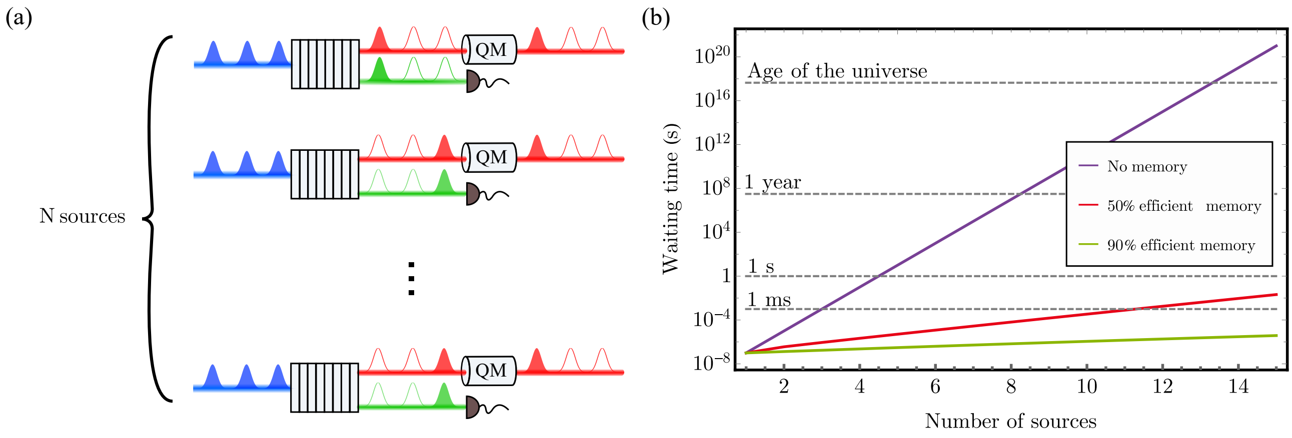

Figure 1.4: (a) Schematic of N parametric down conversion sources, pulsed by a laser from the left. At each pulse there is some small probability of a photon pair being generated. Quantum memories (QM) can be used to synchronise the N probabilistic sources. (b) The average waiting time to produce a N-photon state from N photon sources with photon generation probability of 1% (purple), operating at a rep rate of 1GHz. When combined with quantum memories to temporally multiplex the sources, the waiting time becomes more feasible. Here we simulated a memory with a memory lifetime 1000 times longer than the photon lifetime and a total efficiency of 50% (red) and 90% (green) [214].

saved until needed [211, 212, 213]. For example, a photonic quantum computer with millions of qubits requires millions of photons generated all at once. The likelihood of this many photons being probabilistically generated is vanishingly small. However, if we were to store photons after they have been heralded and wait until all of the photons have been generated successfully, then we no longer need all of the photon sources to be successful at the same instant. Provided the storage lifetime is much longer than the repetition period of the source, it is possible to store all successes in a particular time window, and then retrieve all of the photons at the end of the window, represented in Fig. 1.4a. The combined affect is something akin to a deterministic photon source, with an efficiency equal to the probability of a photon being generated within the time window, multiplied by the efficiency of the memory over that time window[8] [214]. In Fig.1.4b, we show the average waiting time to generate an N-photon state on a log-scale. While deterministic photon sources will most likely produce a higher rate of photons, combining an optical memory with a probabilistic photon source can drastically increase the probability of generating multiple photons at the same time [214].

The same argument of saving successful outcomes can be applied to entangling gate operations

---

[8] We will quantify efficiency in Section 1.4.2.

using linear optical elements, as in the KLM scheme [85] described in Section 1.2. Performing the gate multiple times on an auxiliary system while the target qubits are stored in memory, we can then use quantum teleportation [215] to teleport the gate operation onto the two target qubits.

For deterministic sources, quantum memories could function as a filter. Many processes could result in successively emitted photons being distinguishable. By carefully tuning the parameters of our memory, we could allow the storage of only certain modes; the rest would pass straight through the memory and be lost. The overall efficiency of the memory would take a hit, but the retrieved photons would then show a higher degree of indistinguishability, improving the probability of multi-photon gates [216].

Quantum state manipulation

Quantum memories are time non-stationary due to an auxilary control field mediating the interaction, as opposed to passive linear optical elements as are used in schemes such as KLM, and as such can be viewed as a beam-splitter between travelling light modes and stationary spin wave modes, allowing manipulation of time-bins [217,218], in contrast to a usual beam-splitter which acts on spatial modes. A quantum memory scheme has been used to perform a two mode squeezing operation, which was shown to be sufficient for generating and manipulating continuous-variable cluster states, and therefore sufficient for universal quantum computation [219].

Quantum memories may also utilise atomic Rydberg states, which are highly excited energy levels - the excited electron has a very high principle quantum number n. This results in the electron occupying a comparatively large average distance from the nucleus. Because of this, other atoms nearby the Rydberg atom experience a dipole interaction which shifts their energy levels, preventing them interacting with previously near-resonant optical fields. This is known as the Rydberg blockade. As a result, Rydberg atoms demonstrate a strong non-linearity [220,221] which has been used to demonstrate cross-phase modulation of single photon level pulses [222], and single photon collisions [223].

Quantum Repeaters

In Section 1.1.3, we mentioned how distributing quantum information between remote parties can allow for quantum networks and secure communication. However physical channels are lossy. Photons travelling through commercial optical fibers are limited to transmission over tens of kilometers due to attenuation [224]. In classical communication channels, a repeater measures and amplifies the signal, allowing for transmission over global distances. However for quantum signals, measurement of the signal will irrevocably alter it and it is impossible to deterministically copy an arbitrary unknown quantum state[9].

Rather than transmit our quantum information directly over the network, one alternative is to share part of an entangled resource [215]. Distributed entanglement can be used for quantum teleportation, allowing quantum states to be delivered to a remote place without sending them through a lossy channel. Distributed entanglement can also be consumed as a resource for QKD, allowing secure communication over arbitrary distances.

However, this just replaces the problem of transmitting quantum information directly over the network to the problem of distributing entangled resources, which still suffer from the same attenuation losses. Yet, while it is impossible to copy an arbitrary quantum state, it is possible to swap entanglement from one quantum particle to another. This is the basis for a quantum repeater [225]. By subdividing the transmission link into multiple short segments where we can faithfully distribute entanglement with acceptable loss, we can then swap the entanglement between adjacent nodes [226]. This is illustrated in Fig. 1.5, where we wish to share an entangled resource between QM1 and QM4.

Photons can be entangled in many degrees of freedom. Here we will discuss implementation of a quantum repeater while using photon number to encode information. Suppose we have a photon source which emits a photon into either the left or right path, shown in light blue in Fig. 1.5. The state can be written as the Bell state,

$$|\psi\rangle = \frac{1}{\sqrt{2}}(|0\rangle_L |1\rangle_R + |1\rangle_L |0\rangle_R) \,, \tag{1.3}$$

---

[9] No-cloning theorem.

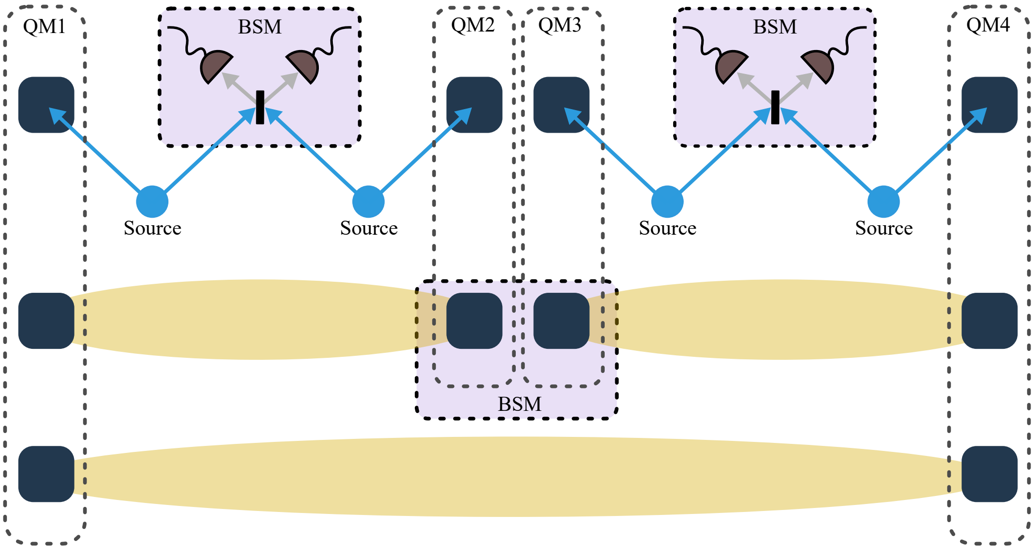

Figure 1.5: Schematic of simple quantum repeater protocol. A single photon source emits a photon either to the left or right. One path is connected to a quantum memory (QM), while the other is sent to a Bell-state measurement (BSM) device. Detection of one photon at the output of the beamsplitter means the BSM was successful and the two neighbouring QMs become entangled. The process is repeated for QM2 and QM3, which if successful, results in QM1 and QM4 being entangled.

where $|0\rangle_i$ and $|1\rangle_i$ indicate the absence and presence of a photon in the i'th channel respectively. The state described by Eq. 1.3 is an entangled photon number state. Before detection, the photon is in an equal superposition of travelling in either the left or right path. Detection of the photon in one of the paths immediately signifies the absence of a photon in the alternative path.

Now say we have two of these sources, both producing the entangled state described by Eq. 1.3. To perform a Bell-state measurement (BSM) and thus swap the entanglement to the two outer paths, we direct one of the paths from each source to a $50:50$ beamsplitter with the two output modes sent to a pair of single-photon number-resolving detectors. By number-resolving we mean that two photons incident of the detector would yield a different signal than if there was only one photon. Such a detector could be built using multiple non-number-resolving detectors, where the measurement channel is split through multiple beam-splitters, such that the probability of two photons following the same path becomes vanishingly small, and the now many channels are each sent to a non-number-resolving detector. The beam-splitter shown in Fig. 1.5 (not involved in the number-resolving detection) acts to remove information from our system. If we detect one photon at either of our detectors, but not the other one, we cannot know from which source it originated. This projects the quantum state of the two arms not involved in the BSM to exactly that of Eq. 1.3. Detection of no photons, or of two at the same detector, does not result in entanglement swapping. For this particular scheme the success probability is 50%.

After a successful BSM, the two arms originating from the adjacent sources which were not sent to the BSM, are now entangled. These are each saved in a pair of remote quantum memories (QM1-QM2 and QM3-QM4), thereby entangling the quantum memories: one of the memories contains a photon, and one does not. Photons contained within the two central nodes (QM2 and QM3) are then recalled and a BSM is performed on them, which if successful, results in QM1 and QM4 being entangled. In this demonstration, each photon has only travelled an eighth of the total distance, yet we have distributed entanglement across the full network.

As BSMs are probabilistic, the probability of each node successively swapping entanglement becomes exceedingly small as the number of nodes is increased. In much the same way as quantum memories can save successful gate operations, as discussed in Section 1.4.1, here too we can save successful entanglement swapping operations until the adjacent nodes have also been successful. We then obtain a similar speedup as shown in Fig. 1.4b. Attempting multiple entanglement swapping operations in parallel is also useful to increase the success probability. We will discuss this more in Section 1.4.2.

Alternatively to using separate photon sources and memories, we can instead integrate the photon source and memory. The Duan, Lukin, Cirac, Zoller (DLCZ) protocol [5] spontaneously generates a heralded spin wave matter excitation, depicted in Fig. 1.6a. Firstly, an intense control laser generates entanglement between a photon and an atomic excitation in an ensemble of atoms, through Raman scattering. Photons from two DLCZ memories are then directed to a BSM node. The probability of a photon being generated at any one time, in the required spatial mode to be sent to the BSM, is small, but a photon detection heralds that one of the DLCZ memories is primed with an excitation, without any information as to which one, illustrated in Fig. 1.6c. We have now established the entangled state described by Eq. 1.3, with $|0\rangle$ and $|1\rangle$

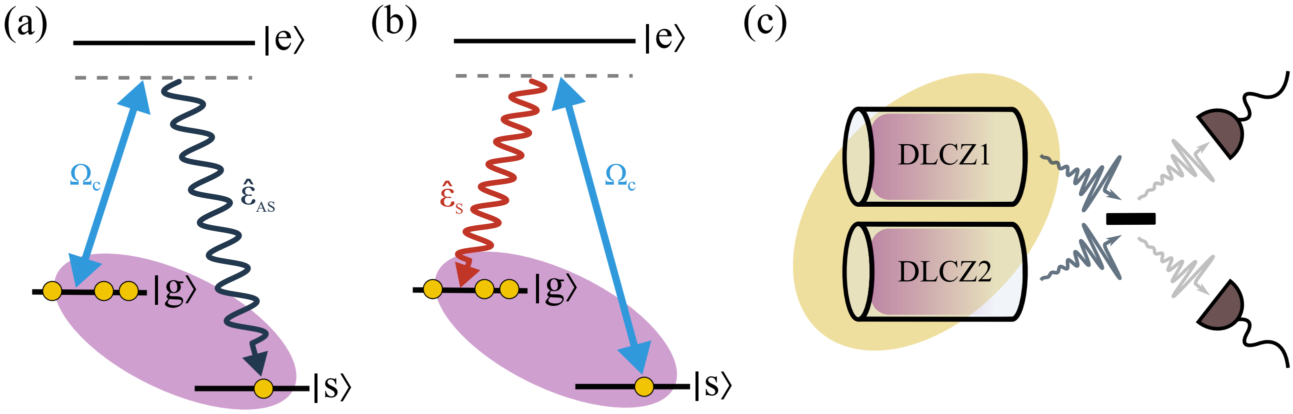

Figure 1.6: (a) Write stage of the Duan, Lukin, Cirac, Zoller (DLCZ) protocol [5]. A control laser Ω_c, incident on an atomic ensemble, spontaneously scatters an anti-stokes photon $\hat{\mathcal{E}}_{AS}$. Each atom within the ensemble is now in a collective entangled state of having scattered the control field and thus now populating $|s\rangle$. The coherence of this entanglement is represented by the purple highlight. (b) The read stage of the DLCZ protocol. Another control field reads out the stored excitation from the ensemble into a well defined spatial mode, producing a stokes photon $\hat{\mathcal{E}}_S$ and returning all of the atoms to state $|g\rangle$. (c) Illustration of a Bell-state measurement (BSM) between two DLCZ quantum memories. The detection of one photon at the output of the beamsplitter results in the two quantum memories being entangled.

representing the absence or presence of a memory stored excitation respectively, which can be stored until the neighbouring nodes have also established entanglement. We then proceed by recalling the stored excitation as a photon (Fig. 1.6b) and performing further BSMs.

The distribution of entanglement over large distances is also a valuable tool for testing existing theories of non-locality over large distances [227].

Metrology

Quantum memories have primarily been explored as means to improve the scaling of probabilistic operations. Another avenue of research is in using the transfer of optical coherence to matter coherence as a means to improve or facilitate quantum sensing. Through applying a spatially varying field to an atomic ensemble, we can not only store and retrieve light, but map different frequency components within the photon to different spatial components within the spin wave. This allows a physical analogue of the Fourier transform to be performed, which can be exploited to improve the frequency resolution of detectors [228].

Instead of mapping frequency to space, researchers have also used a protocol known as an atomic frequency comb (AFC - see Section 1.5) which causes different frequency components to be retrieved at different times [229]. This, when used in combination with ultrasound imaging, improved the ultrasound detection sensitivity.

Quantum memories have also been combined with a ghost imaging protocol [230] to store idler photons and release them upon detection of a signal photon, allowing real-time generation of the image. Here the authors used the DLCZ protocol discussed previously to generate time delayed Bell states, made up of a signal and idler photon, which were correlated in position but anti-correlated in momenta. The signal photon is detected via a ‘bucket’ detector (multimode fibre coupled to a single photon detector) which then gates the detection of the remaining idler photon via a spatially-resolving camera. In this way, the resulting image acquired of the idler photons by the camera can be used to infer a corresponding image for the signal photons, which were detected by a non spatially resolving detector. The signal photon can be made to interact with an object while an image is constructed by measuring the spatial distribution of the idler photons, which have not interacted with the object. The memory in this instance allows the idler to be stored until an electrical trigger has been received from detection of a signal photon, which simplifies the experimental setup.

1.4.2 Figures of Merit

The requirements for a quantum memory will vary depending on which of the above applications it is being used for [231]. Just as with single photon sources, in order for the quantum memory to be compatible with other components, the wavelength of operation should be considered. Here we identify some key metrics and discuss the importance of each metric with regards to the applications previously mentioned.

Efficiency

One of the most frequently cited metrics is efficiency. Efficiency quantifies the ratio of energy in the retrieved pulse to the energy in the input pulse. Specifically for photons, efficiency refers to the probability of storing a photon and then retrieving a photon after the required time [232, 233]. Efficiency (or total efficiency η) can be split into several parts,

$$\eta = \eta_s \eta_r \eta_{\text{setup}} \tag{1.4}$$

quantifying the efficiency of storage η_s, retrieval η_r and the overall efficiency of the η_{setup}, which includes losses introduced by optical components.

If η_{setup} is known, we can determine η_s by measuring the probability of a photon traversing through the memory after we have attempted storage. With the total efficiency, η_{setup} and η_s, we can then determine η_r, which will in general be time dependant.

For quantum computation and quantum communication, a higher total efficiency means a lower waiting time for the required operations to be complete, see Fig. 1.4b. Typically an efficiency of 90% is quoted as the required benchmark [234]. For other applications such as sensing, there may be a less stringent threshold for a memory to still be useful.

Chapters 5 and 6 will be mainly concerned with optimising η_{storage} and $\eta_{\text{retrieval}}$ for two distinct schemes of quantum memory. We will also discuss how the different configurations investigated might impact η_{setup}.

Fidelity

The fidelity of the memory measures how closely the output state resembles the input state, or equivalently, the overlap of the photonic wave functions for the input and output photon [212, 233]. Mathematically we can define the fidelity between the input state ρ_{in} and output state ρ_{out} as,

$$F(\rho_{\text{in}}, \rho_{\text{out}}) = \text{Tr}\left[\sqrt{\sqrt{\rho_{\text{in}}}\rho_{\text{out}}\sqrt{\rho_{\text{in}}}}\right], \tag{1.5}$$

where Tr denotes the trace. This definition gives a monotonic metric between 0 and 1 of how similar the two states are. However, fidelity can often miss an important concept: that is if the retrieved state is related to the stored state by some unitary, while the states may be completely orthogonal (resulting in $F = 0$), this discrepancy can be easily adjusted for provided it is known and consistent. Rather than measuring the fidelity, an often performed simpler measurement is the purity of the output quantum state, which doesn't require the full tomography of the output state [233].

Noise level

Directly impacting the purity of the output state and memory fidelity is the level of noise photons produced in the memory interaction. Storage of coherent states involving a large photon number are less susceptible to these noise processes, but for the case of a single photon, any noise photons will contaminate the signal [235, 236] and may be impractical or impossible to filter out (as is the case in four-wave mixing noise [44, 237], see Chapter 5). We can quantify the amount of noise in a qunatum memory μ, by the signal to noise ratio at the output of the memory [238],

$$\mu = \frac{\langle N_{\text{noise}} \rangle}{\eta} \approx \frac{1}{\text{SNR}}\,, \tag{1.6}$$

where $\langle N_{\text{noise}} \rangle$ is the average number of noise photons produced. For an input signal of average photon number equal to one, $\mu = \frac{1}{\text{SNR}}$.

However, even a small amount of noise can drastically harm the memory fidelity if the variance is large. The SNR is only a first order measure and doesn't offer any information on the retrieved photon correlations. Here the single photon purity at zero time delay $g^2(0)$ is a good measure, as described in Section 1.3.1. Given that we have stored a single photon, we ideally find that the retrieved photon state continues to have a $g^2(0) = 0$.

While there is some fault tolerance in fidelity when these systems are combined with error correction [212], any noise introduced by the memory must be compensated at some point to outperform direct transmission. How much tolerance will again depend on the specific situation. For example, error correction using surface code is tolerant up to a 1% error rate [239]. If the goal is to simply preserve nonlocal correlations of a maximally entangled pair of photons such as in the Bell-states defined in Eq. 1.3, fidelities of over 85% are compatible with long distance Bell tests or QKD [240].

Lifetime

We can define the memory lifetime, τ_{mem} as the time it takes for the retrieval efficiency to decrease by some factor, most commonly $1/e$ or 50%. Once the input photon has been mapped to an atomic coherence, various dephasing processes will cause the retrieval efficiency to decrease. These will be discussed in Chapter 5 and 6 in more detail.

For applications such as quantum repeaters we would need high efficiencies on time scales of milliseconds to seconds [234]. For the case of local synchronisation, these long lifetime requirements may be somewhat relaxed to microseconds [214].

Spectral Bandwidth

In general, as we increase the spectral bandwidth, B, of the input photon, the memory efficiency will decrease [241]. Given that we would like our memory efficiency above some threshold value, this puts a limit on the maximum achievable bandwidth for a given system and therefore limits the rate of information processing possible by the memory.

Time-bandwidth product

If the memory application is synchronisation, often a more useful metric than lifetime and bandwidth is the time-bandwidth product, $\beta = \tau_{\text{mem}} B$. This metric quantifies how many storage attempts can be made within the lifetime of the memory and so how many successive photons the memory can synchronise [242]. A $\beta > 1000$ offers a sizeable advantage when used for temporal multiplexing of photon sources or multi-photon gates, as plotted in Fig. 1.4b [214].

Modal Capacity

Modal capacity quantifies how many optical modes can be stored in parallel, such as spatial [243, 244, 245], temporal [246, 247, 248] or spectral modes [249, 250]. This is of particular use in a quantum repeater, where if a memory can store N modes, this allows for a factor N increase in entanglement swapping probability, thereby reducing the overall number of memories needed [246]. Conversely, a single mode memory can be used as a filter, only storing a particular mode from the input signal and so enhancing the purity or indistinguishability of single photons [216].

Scalability

Even with a large multimode capacity, for a given application, many quantum memories will be required and so our choice of memory architecture should be feasible to produce on mass. Therefore, it's advantageous for memories to operate at conventional wavelengths, such as near-infrared or in a telecommunications band, and for any preparation of the memory preceding storage to be technically simple. While some degree of cooling will likely be required for memory lifetimes above a microsecond, memories with minimal preparation and simple storage mechanisms will be preferable.

1.5 Memory schemes

Now that we have established the usefulness and the means by which to judge a quantum memory, we will now review some of the proposed schemes seen in the literature.

The simplest implementation is a delay line, such as a loop of optical fiber [251] or cavity [252]. Delay lines can be low loss, have a broad wavelength of operation and do not contribute additional noise. However, the delay is predetermined and so does not allow on-demand retrieval of the photon - though for some applications this may be sufficient. Combining shorter delay lines with fast switches can allow for a finer choice of storage times, provided the switch is low-loss to enable long storage times and fast enough to permit high clock rates of photons. Such a scheme has been demonstrated with Pockels cells [253], though scaling this device up would be challenging.

Alternatively, light can be stored as a stationary matter excitation, which has potential for on-demand readout. Naturally we might imagine using a single TLS to store the optical coherence. A photon, near resonant and incident with a stationary TLS, can couple through an electric dipole transition and be absorbed, exciting the TLS from its ground state to an excited state. However, there are a few major drawbacks with this approach.

Firstly, just as a photon can interact with a TLS, the TLS is constantly interacting with the surrounding reservoir of electromagnetic field modes, depicted in Fig. 1.7a. The effect of these surrounding modes is to cause the excitation to decohere and decay in the form of a spontaneously emitted photon. The stronger the coupling of the TLS dipole to our input

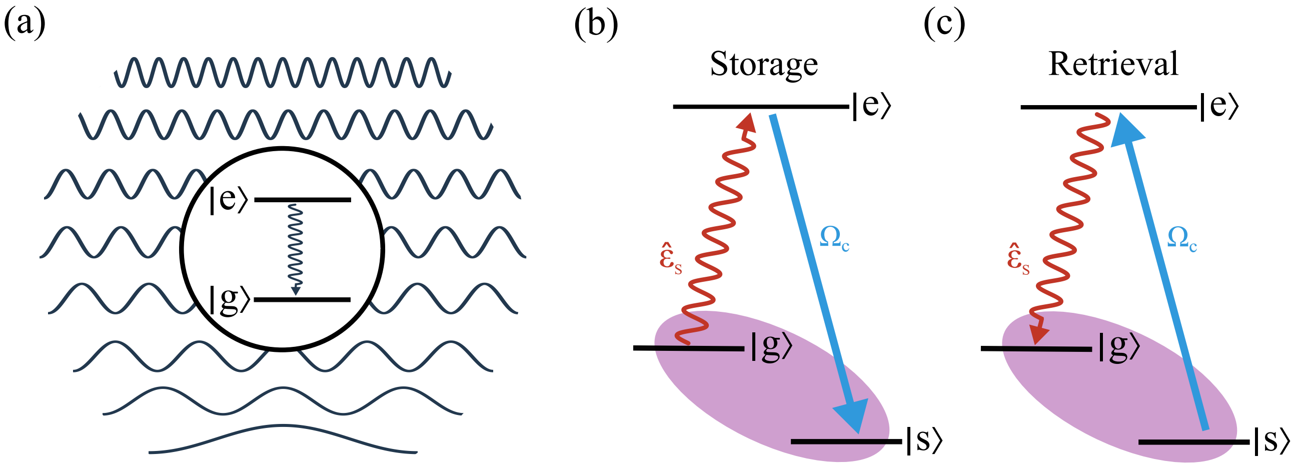

Figure 1.7: (a) Illustration of a two-level system coupled to a continuum of modes. (b) Applying a control field Ω_c and stimulating emission to a dark state, coupling of the emitter to the surrounding reservoir of modes can be suppressed. The purple highlight represents the coherence between the states $|g\rangle$ and $|s\rangle$. (c) The coherence between $|g\rangle$ and $|s\rangle$ can be mapped back to the optical transition by reapplying Ω_c, therefore recoupling the emitter to the reservoir of modes.

photon, the stronger the coupling of the TLS to the reservoir of modes, leading to a faster decay [254]. To overcome this, we can use an auxiliary control laser to transfer the stored coherence (initially between the ground, $|g\rangle$ and excited state, $|e\rangle$), to a coherence between the ground and a third longer lived state, known as the storage state, $|s\rangle$. This is shown in Fig. 1.7b. We can then use a similar control pulse to convert the stored coherence back into an optcial coherence, allowing on-demand readout. Schemes based off this mechanism will be the focus of Chapters 5 and 6.

Secondly, the incident photon is not well mode matched to the dipole of the TLS [108], as discussed in Section 1.3[10]. When exciting a TLS with intense laser light, this is not as important. Yet to have a high probability for one photon to interact with one TLS, we require engineering similar to that used to improve the collection from TLS single photon sources [255]. Surrounding the TLS with a cavity and focusing the incident photon to increase the interaction strength is a viable strategy to realising a quantum memory, though this presents considerable engineering challenges as the TLS must be cooled and trapped within these structures [256,257,258], or contained within a host material which will need to be cryogenically cooled to reduce dephasing

---

[10] The wide angular distribution of the dipole emission from a TLS not only applies to emission, but to any interaction with light.

due to phonons [259].

Single atoms in cavities have shown total efficiencies of 9%, with fidelities of 93% and memory lifetimes of 180 μs [256]. Trapped ions demonstrated slightly larger fidelities of 95% but with a heralded efficiency below 0.5%, even with high numerical aperture collection optics [260]. Single NV centers in diamond have reported entanglement between a single photon and the electronic [261] or nuclear spin [262] - the latter has potential coherence times on the order of a second. Entanglement over three meters has recently been shown using NV centers [263].

Rather than use a single TLS, we can use an ensemble of TLSs where the input photon only has a low probability of interacting with any one TLS. As we increase the number of TLSs the overall interaction increases and so we can approach unity coupling of the photon to the ensemble, without the need for cavities or focusing optics [264]. During storage, every TLS participates in the interaction, with each one retaining the spatial phase information resulting from the interference of the signal and control fields. After the control field is turned back on, constructive interference between the stored coherence and the control field result in retrieval of the stored photon into a well-defined mode.

Let's consider an ensemble of atoms with a Λ-configuration of energy levels, as shown in Fig. 1.7b and c, where the input photon is resonant with levels $|g\rangle \rightarrow |e\rangle$, and the control field is co-propagating with the signal field, as well as being resonant with the transition $|s\rangle \rightarrow |e\rangle$. If we consider energy conservation, absorption of the input photon is accompanied by one atom in the ensemble transitioning to $|e\rangle$. Transfer of the coherence from $|g\rangle\langle e|$ to $|g\rangle\langle s|$ is accompanied by stimulated emission of a photon into the control field, causing the excited atom to transition to state $|s\rangle$. Since every atom contributes to the interaction, the ensemble is in a collective superposition were each atom has some probability of being in state $|s\rangle$. The atomic excitation is said to be de-localised across the ensemble. Mathematically we can write the collective state of the ensemble containing N atoms after storage as[11],

$$|\psi\rangle = \frac{1}{\sqrt{N}} \sum_{j=1}^{j=N} e^{i(\boldsymbol{k}_s - \boldsymbol{k}_c)\cdot \boldsymbol{r}_j} \, |g_1, g_2, ...s_j, ..., g_N\rangle \ , \tag{1.7}$$

where $\boldsymbol{k}_s$ and $\boldsymbol{k}_c$ represent the wavevectors of the signal and control field respectively, and r_j denotes the position of the j'th atom. After the retrieval control field with wavevector $\boldsymbol{k}'_c$, the atoms are returned to the collective state $|\psi\rangle = \frac{1}{\sqrt{N}} \sum_{j=1}^{j=N} e^{i(\boldsymbol{k}_s - \boldsymbol{k}_c + \boldsymbol{k}'_c - \boldsymbol{k}'_s)\cdot \boldsymbol{r}_j} \, |g_j\rangle$, with $\boldsymbol{k}'_s$ the wavevector of the retrieved photon. The probability of emission into the direction defined by $\boldsymbol{k}'_s$ is given by,

$$P(\boldsymbol{k}'_s) = \frac{1}{N} \sum_{j=1}^{j=N} \sum_{l=1}^{l=N} e^{i(\boldsymbol{k}_s - \boldsymbol{k}_c + \boldsymbol{k}'_c - \boldsymbol{k}'_s)\cdot(\boldsymbol{r}_j - \boldsymbol{r}_l)} \ , \tag{1.8}$$

which becomes significant only if $\boldsymbol{k}'_s = \boldsymbol{k}_s - \boldsymbol{k}_c + \boldsymbol{k}'_c$. Hence, by manipulating $\boldsymbol{k}_c$ and $\boldsymbol{k}'_c$ we can control the direction of re-emission. In the literature, it is common to refer to forward retrieval as $\boldsymbol{k}'_c = \boldsymbol{k}_c$ resulting in $\boldsymbol{k}'_s = \boldsymbol{k}_s$ (the retrieved photon propagates in the same direction as the initial photon). Backward retrieval is where $\boldsymbol{k}'_c = -\boldsymbol{k}_c$ and so $\boldsymbol{k}'_s = -\boldsymbol{k}_s$ (the retrieved photon propagates in the opposite direction to the initial photon).

An ensemble also has the advantage of being inherently multimoded [243, 244, 245, 246, 248, 249, 250]. We can see that the above treatment[12] allows for multiple spatially separated excitations which will remain spatially separated upon retrieval [243]. Some protocols, as will be discussed later in this section, use an inhomogeneously broadened ensemble to facilitate storage [248, 265, 266, 267, 268, 269, 270]. In this case, different frequency modes can also be stored.

Memories based upon ensembles of TLSs have received a huge amount of interest through the years. A multitude of different physical systems have been considered, including rare-earth ion-doped solids (REIDS), diamond colour centers, alkali metal vapours and molecules. As well as different platforms, there are multiple different memory protocols employed. Memory protocols typically fall into two main approaches: photon-echo and optically controlled (like the scheme described above).

---

[11] We have assumed that each atom is equally likely to interact with the photon, which in reality is never true. The spatial mode of the signal photon/control field or any inhomogenous broadening of the atoms, will result in different atoms experiencing differing strengths of coupling to the photon.

[12] This is valid provided the number of excitations is small compared to the number of atoms.

Photon-echo

Photon-echo based protocols rely on applying an inhomogeneous broadening across the ensemble to the transition resonant with the incoming photon, see Fig. 1.8a. As the photon is absorbed, generating a coherence between the ground and excited states, different frequency classes (located at different spatial positions within the ensemble) undergo dephasing at a different rate, leading to a suppression of re-emission. By controlling when the atoms rephase, we can control when the photon is re-emitted, known as a photon-echo [273].

Gradient echo memory (GEM) [271] applies a continuous inhomogeneous broadening along the propagation direction of the photon. After the photon is absorbed, the ensemble is allowed to dephase for some time T, before the applied broadening is flipped, causing the different frequency classes to accumulate phase in the opposite direction. The atoms will then rephase after a total time $2T$ and the signal is retrieved. This is illustrated in Fig. 1.8b, where the position of the arrow on the circle circumference represents the relative phase of a particular frequency class. When the phases re-align, the different frequency classes interfere constructively and the stored photon is emitted.

Efficiencies of up to 87% have been demonstrated using GEM in a warm rubidium vapour, with a memory lifetime of a few μs [266]. There was no added noise observed on the output, verified by heterodyne detection, though the input light was bright pulses with peak powers of less than 2 mW. In cold atoms, the memory lifetime was increased to 195 μs, while maintaining a high efficiency of 80% [265]. The downside of this protocol is that to absorb a high bandwidth photon, the inhomogeneous broadening needs to be spread across the entire photon spectrum. So to have a sufficient number of atoms in each frequency class to absorb the photon with high efficiency, requires a large optical depth. Typically only MHz bandwidth signals have been stored efficiently and so β is limited. GEM has also shown utility in quantum sensing, allowing a more precise measurement of the frequency separation between two spectrally overlapped photons [228].

Rather than a continuous inhomogeneous broadening, an atomic frequency comb (AFC) uses a periodic spectrum of absorption lines, each separated by a predetermined amount, δ. This

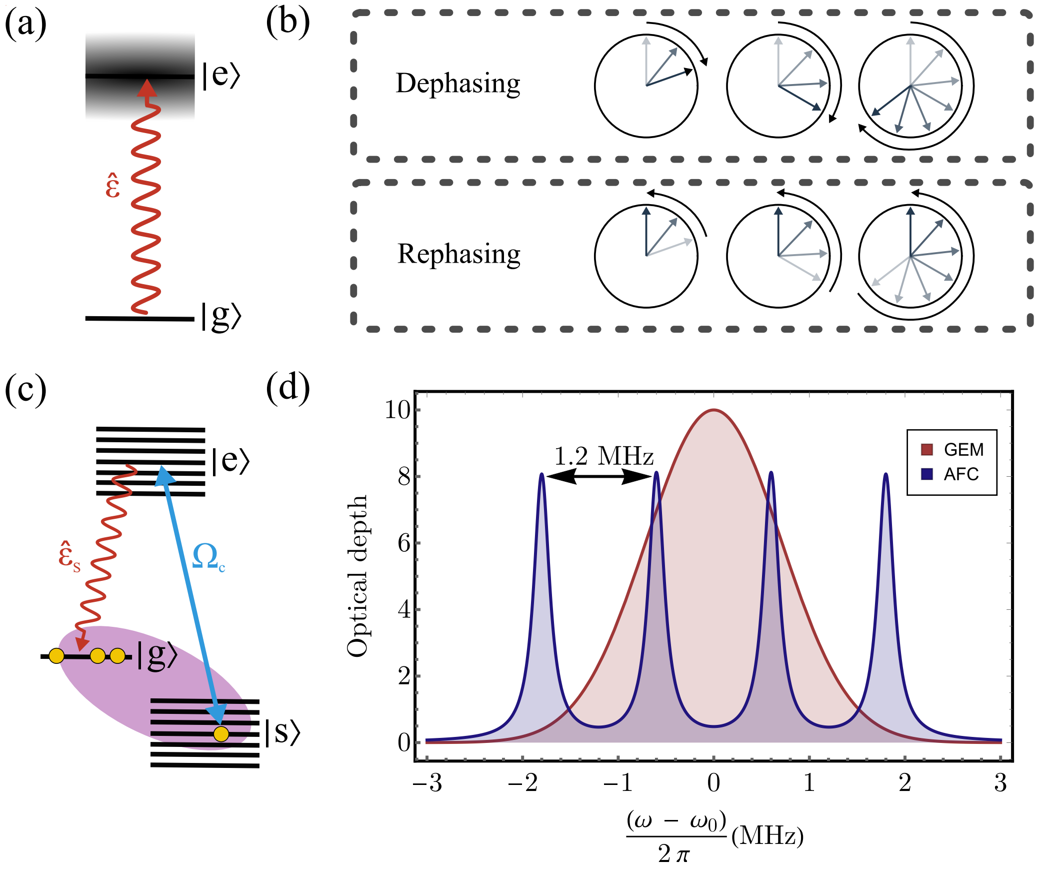

Figure 1.8: (a) Illustration of an ensemble of two level systems (TLSs), with an inhomogeneous broadening. (b) Representation of the phase evolution experienced by different frequency classes within the inhomogeneous broadening. The black arrows around the circumference of the circles denote the direction of phase evolution for increasing time. Within the circles, the darkest blue arrows indicate the phase after some time T. Atoms with a more detuned transition frequency experience a faster phase precession. Reversing the inhomogeneous broadening, causes the phase to precess in the opposite direction, ending with the ensemble rephasing at time $2T$ and emitting a photon. (c) An ensemble with a periodic inhomogeneous broadening. An auxiliary control laser Ω_c can be applied to map the coherence to between two dark states, effectively freezing any phase precession. (d) A mock absorption spectrum that might be observed when employing gradient echo memory (GEM) [228,265,266,271] and atomic frequency comb (AFC) [247,270,272] memory protocols. For the AFC spectrum, the pictured splitting of $\delta = 1.2$MHz will result in periodic rephasing every $5.2\,\mu$s.

is illustrated in Fig. 1.8c and d. Due to the periodicity, the ensemble will rephase every $2\pi/\delta$ seconds.

AFC has been implemented in REIDS [247], as well as recently in a room temperature cesium vapour [270], and efficiences of 58% have been demonstrated [272]. To use AFC in an on-demand manner, after storage an auxiliary control field can be applied to transfer the excitation to a optically dark state, effectively freezing the rephasing process, shown in Fig. 1.8c. When required, the control field can trasfer the coherence back to the original transition, and the rephasing continues. This is sometimes refered to as the full AFC protocol [274, 275, 276] and has shown efficiencies up to 12% [277]. Photon-echo memories are also intrinsically multimode [271, 276, 278].

Optically-controlled

For optically-controlled protocols, as the photon is absorbed, generating an atomic coherence, a control field maps the coherence to a longer lived transition. The photon can then be retrieved on demand by reapplying the control field to map the coherence back to the original transition [241, 279, 280, 281, 282].

There are two main regimes of operation, characterised by how detuned the photon is away from resonance, Δ. For near-resonance, $\Delta \sim \Gamma$ where Γ is the linewidth of the transition (see Fig. 1.9a), the control field leads to a transparency window in the absorption profile of the atomic medium. This is illustrated in Fig. 1.9b. By turning off the control field while the photon is contained within the medium, the photon coherence can be mapped to a long-lived atomic coherence [211, 212, 283, 284, 285].

There are two mechanisms behind the transparency window: destructive interference between the two dressed states created by the control field and AC stark splitting [284, 285, 288]. As the intensity of the control is increased, the spectral width of the window is also increased, allowing for higher bandwidths of photon to be stored. For a narrow transparency window (low control field intensities), destructive interference is the dominant mechanism and is accompanied by a strong dispersive feature (shown in Fig.1.9b), leading to an appreciable slowing of the photon

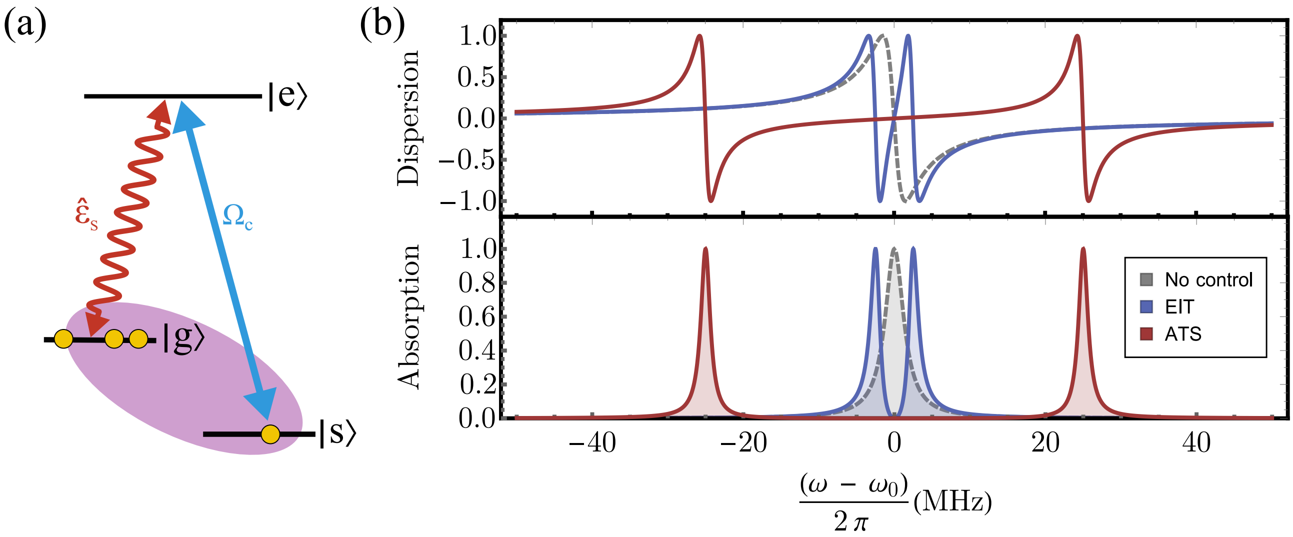

Figure 1.9: (a) Energy level diagram for near-resonant optically controlled memories, such as electromagnetically induced transparency (EIT) [205, 286, 287, 288, 289, 290] and Autler-Townes Splitting [235,288,291] protocols. The input photon is mapped to a collective excitation between the two ground states, indicated by the purple highlight. (b) Plot of normalised dispersion and absorption for the case of no control field applied (grey), and a control field at zero detuning for EIT (blue) and ATS (red) regimes.

group velocity. By adiabatically reducing the control field intensity, the dispersion increases leading to an ever slowing photon until the transparency window is closed and the coherence is mapped to a stationary excitation of the atoms. This is dubbed the electromagnetically induced transparency (EIT) protocol.

For a wide transparency window, AC stark splitting dominates and the dispersion is much smaller. Here the two resulting dressed states absorb the photon coherence. The coherence proceeds by oscillating between the original transition and the long-lived transition. Storage is achieved by sharply turning off the control field when the coherence in the long-lived transition is maximised. This is known as the Autler-Townes splitting (ATS) protocol.

EIT memories have been demonstrated in warm [286] and cold atomic vapours [205, 287] as well as REIDS [289]. Efficiences of 90.6% have been achieved with fidelities exceeding 99% in cooled rubidium atoms [205] and storage times of up to one minute have been reached in REIDS [290]. The EIT protocol has also been extended to invoke Rydberg excitations [292], allowing manipulation of the stored coherence.

ATS has been demonstrated in cold rubidium atoms, showing an efficiency of 23% for a 5 MHz

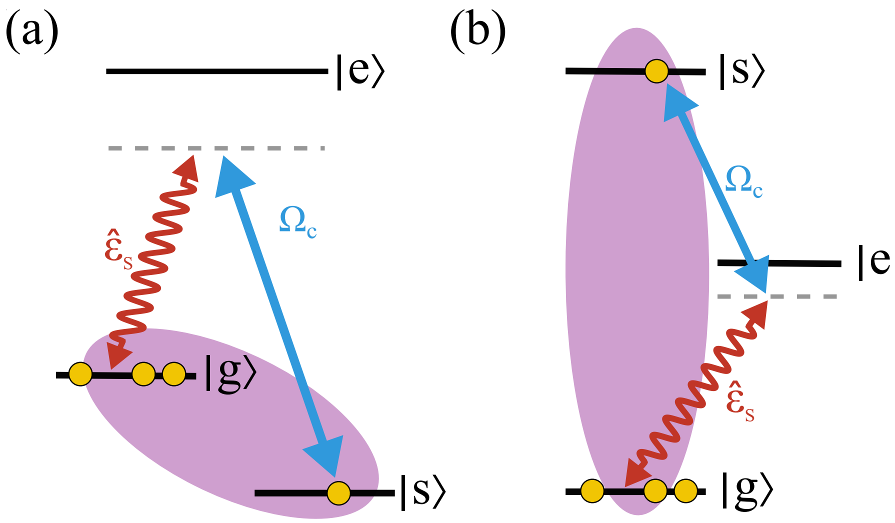

Figure 1.10: Energy level diagram for (a) The Raman [242, 294, 295, 296, 297, 298] memory protcol. The input photon is mapped to a collective excitation between the two ground states, indicated by the purple highlight. (b) The off resonant cascaded absorption (ORCA) [236] protocol, where the photon coherence is mapped to a coherence between the ground state and the double excited orbital state.

bandwidth photon, along with a memory lifetime of 650 ns [235], giving $\beta \approx 20$. Cooling down the atoms even further to form a Bose-Einstein condensate allowed 7 MHz photons to be stored and retrieved with an efficiency of 30% and a memory lifetime of 15 μs [293]. Theoretically ATS is better suited to large bandwidths and should be able to reach the same efficiencies as demonstrated for EIT (above 90%), while requiring a lower optical depth [288, 291]. We will discuss this in more detail in Chapter 5.

For $\Delta \gg \Gamma$, we enter the Raman regime, illustrated in Fig. 1.10a. The Raman regime allows for storage of higher bandwidths at the expense of requiring a higher optical depth and control field intensities [242, 294, 295, 296, 297, 298]. It is also particularly well-suited to room temperature media, where the large detuning overcomes complications arising from the inhomogeneous broadening. Bandwidths of GHz have been stored in warm alkali vapours with efficiencies up to 82% being reported [237]. Bandwidths of THz have been stored in diamond [299], though with efficiencies of only 0.9% and considerable noise. Storage times of 1.5 μs in a warm caesium vapour resulted in $\beta \approx 2500$ [300].

Often near-resonant and Raman memories are plagued by four-wave-mixing noise, which will be discussed in Chapter 5. Recently a Raman protocol has been developed that is immune to such noise processes: off-resonant cascaded absorption (ORCA) [236], also known as fast ladder memory (FLAME) [301]. Here a ladder configuration of levels is used, rather than the traditional $\Lambda-$configuration. This allowed for no change in the photon statistics after the memory process: $g^{(2)}(0) = 0$ before and after [236]. A lifetime of 86 ns was demonstrated in rubidium [301], with a maximum efficiency of 25% for photons of bandwidth 90 MHz, leading to $\beta \sim 50$. We will discuss ladder based memories in more detail in Chapter 6.

Chapter 2

Dibenzoterrylene as a Single Photon Source: Fundamentals

2.1 Theory

In the previous chapter, we discussed how polycyclic aromatic hydrocarbons (PAHs) are a promising candidate for single photon generation. Hosting large PAHs within a solid matrix made up of smaller PAHs allows for stable photo-emission, which is not absorbed by the surrounding host crystal. Provided the dopant is well incorporated into the host matrix, by replacing a few host molecules, and the host matrix is of a high enough purity, photo-bleaching and spectral wandering can be minimised. In this chapter we will look at the PAH dibenzoterrylene (DBT). We will begin by discussing the general properties of DBT, without referring to a specific host crystal. We will then move on to discussing a theoretical framework which when combined with fluorescence measurements will allow us to determine important characteristics of the emitters. Following this, we explain how to perform measurements on these systems.

2.1.1 Dibenzoterrylene

DBT [302] has the formula $C_{38}H_{20}$ and absorbs both blue and red light, thereby appearing green. For single photon generation, we are interested in the red transitions. In particular the transition between the ground S_0 and excited S_1 singlet electronic states, corresponding to a single electron from the pair of outer-most π-electrons, transitioning to a higher energy orbital [303]. Crucially for this transition, the total spin of both π-electrons remains zero and so is dipole allowed. Between the two singlet states lies a triplet state manifold T_1, containing three excited energy levels where the total spin is equal to one[1]. Transitions between singlet states and triplet states are dipole forbidden, making the triplet states typically much longer lived, though transitions can happen and is often referred to as intersystem crossing. For single photon generation using transitions between the two singlet levels, transitions to the triplet state will result in a blinking of the retrieved stream of photons and thus a reduced source efficiency. However, for use as a quantum memory, molecular triplet states are a potential resource [304].

As well as electronic degrees of freedom, intra-molecular vibrations of the guest molecule result in a manifold of vibrational levels for each electronic state [305]. For the n^{th} vibrational mode of electronic level i, we label the state as $S_{i,n}$. Transitions from a vibrational state can either occur non-radiatively to another vibrational mode within the same electronic state, or radiatively, to a vibrational mode in a different electronic state. However, the vibrations of the guest molecule are strongly coupled to the surrounding matrix, which absorbs the vibration on the order of picoseconds, in comparison to typical electronic state lifetimes of order nanoseconds. As a result, the majority of fluorescence originates from $S_{1,0}$[2] [303].

Decays from $S_{1,0}$ to $S_{0,n>0}$ follow a two step process: emission of a photon, followed by fast relaxation of the resulting molecular vibration, which is an incoherent process [306]. The emitted photon is then broadened by the rate of the additional non-radiative decay, and the extra dephasing will cause the photon to be distinguishable from subsequently emitted photons.

---

[1] For two electrons, there are three configurations which give a total spin equal to one. They are $|\uparrow\uparrow\rangle$, $\frac{1}{\sqrt{2}}(|\uparrow\downarrow\rangle + |\downarrow\uparrow\rangle)$ and $|\downarrow\downarrow\rangle$. As for a total spin of zero, there is one state, given by $\frac{1}{\sqrt{2}}(|\uparrow\downarrow\rangle - |\downarrow\uparrow\rangle)$.

[2] This is known as Kasha's rule.

Transitions from $S_{1,0}$ to $S_{0,0}$ occur solely through fluorescence and as a result, the linewidth is only limited by the lifetime of $S_{1,0}$. This spectral line is referred to as the zero phonon line (ZPL) and is suitable for producing indistinguishable photons. The ratio of emission on the ZPL compared with all emission from $S_{1,0}$ is quantified by the Franck-Condon factor [305]. A simplified energy level diagram of DBT embedded in Ac is presented in Fig. 2.1a. In Fig. 2.1b a modelled spectrum is shown, where the dark blue outline illustrates the component of the spectrum originating from vibrational transitions.

In addition to quantised vibrations of the guest molecule, vibrations of the surrounding crystal can also interact with the dopant emitter. Generation of a photon can be accompanied by creation and/or annihilation of lattice phonons, which dephase the coherence between the ground and excited electronic states, reducing the photon indistinguishability. The result is a broader ZPL linewidth and a red shifted fluorescence, referred to as the phonon sideband, with a more continuous characterisitic shape compared with the discrete vibrational lines associated with dopant molecule vibrations [130]. The phonon sideband is shown outlined with dark green in Fig. 2.1b. The total resulting spectrum is shown in grey. The ratio of emission on the ZPL to emission within the phonon sideband is quantified by the Debye-Waller factor [131]. This ratio is temperature dependent. As such, the ZPL only becomes the dominant emission line at cryogenic temperatures.

2.1.2 Resonant spectroscopy

Equations of motion

In this section we will derive a simple theoretical framework which we will use to analyse molecular measurements described later in Chapter 3. We are interested in a single molecule interacting with a classical probe laser. To characterise this interaction, we append the molecular Hamiltonian H_{mol} with the electric dipole Hamiltonian, H_{ED}, describing the interaction of an external light source and an electric dipole, as well as the optical free-field Hamiltonian,

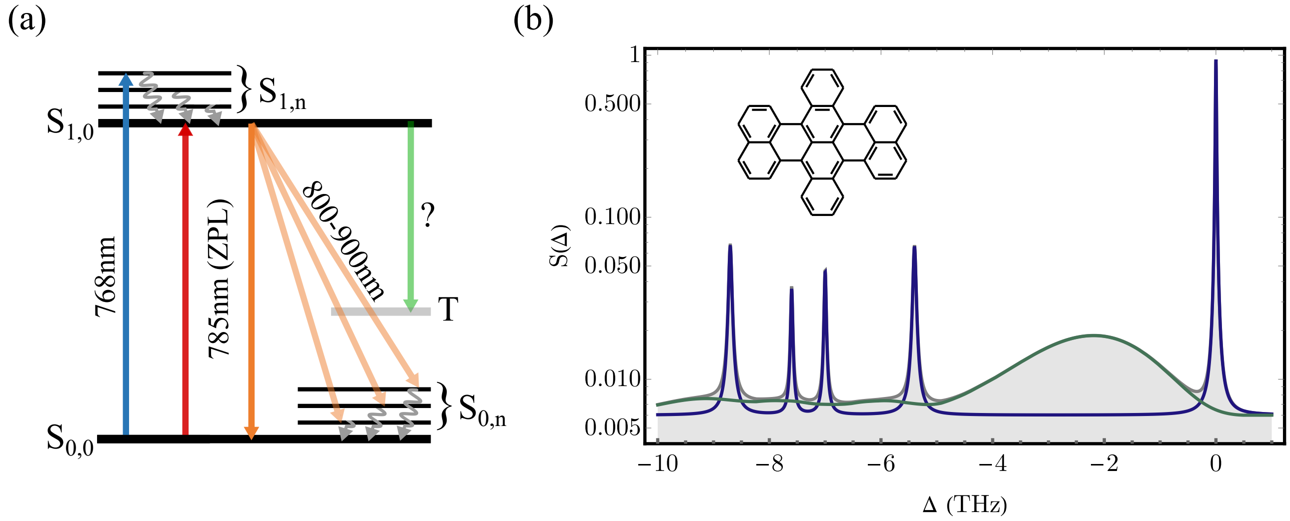

Figure 2.1: (a) Energy level diagram of dibenzoterrylene (DBT) embedded in an anthracene (Ac) host matrix. The singlet electronic level i and vibrational sub-level n are denoted by $S_{i,n}$. Transition wavelengths shown are approximate and vary from molecule to molecule. The triplet level is also included, though the transition wavelength is unknown. The colours of the arrows indicate the different types of transition and do not reflect the relative energies of the transition. Fast picosecond non-radiative decays between the vibrational states are illustrated by the grey arrows. (b) Simulated emission spectrum from a single DBT molecule, shown in grey. Inset is the chemical structure of DBT. The zero-phonon line and molecular vibrational transitions are shown in dark blue, while the contribution from the phonon sideband is shown in dark green, assuming a temperature of $\approx 4\,\mathrm{K}$.

H_L. We can write the full Hamiltonian as,

$$\hat{H} = \hat{H}_{\text{mol}} + \hat{H}_{ED} + H_L \tag{2.1}$$

The Hamiltonian of the molecule is diagonal and given by,

$$\hat{H}_{\text{mol}} = \hbar \sum_j \omega_j \sigma_{jj} \tag{2.2}$$

where ω_j is the resonant frequency of the j'th state and $\sigma_{jj} = |j\rangle \langle j|$ is the population in that state. The electric dipole Hamiltonian is off-diagonal (it couples different states together) and can be written as,

$$H_{ED} = -\hat{\boldsymbol{\mu}} \cdot \boldsymbol{E} \tag{2.3}$$

with the electric dipole operator denoted as $\hat{\boldsymbol{\mu}}$ and the electric field of the laser, $\boldsymbol{E}$. The optical free-field Hamiltonian can be written as,

$$H_L = \frac{\epsilon_0}{2} \int dt(\boldsymbol{E}^{\mathbf{2}} + c^2 \boldsymbol{B}^{\mathbf{2}}) \,, \tag{2.4}$$

where $\boldsymbol{B}$ is the magnetic field of the probe laser and ϵ_0 is the vacuum permittivity.

If we first only consider the states $S_{0,0}$ and $S_{1,0}$, we can write the dipole operator as $\hat{\boldsymbol{\mu}} = \boldsymbol{\mu}_{01}\sigma_{01} + h.c.$[3], where $\sigma_{jk} = |j\rangle \langle k|$ is a flip or transition operator. Assuming that the probe field is sufficiently intense that it is not affected through its interaction with the molecule, we can describe the electric field classically and write,

$$\boldsymbol{E} = \boldsymbol{v}_L E_L \cos(\omega_L t) = \boldsymbol{v}_L \frac{\mathcal{E}_L}{2} \exp[i\omega_L t] + c.c. \tag{2.5}$$

with $\boldsymbol{v}_L$ denoting the polarisation vector of the laser field.

We'll now use the Heisenberg equation to find the time evolution of each σ_{jk}. The Heisenberg

---

[3] For DBT, $\boldsymbol{\mu}$ is real valued and so emitted photons will be linearly polarised, orientated to align with the transition dipole moment [302]

equation reads,

$$\hbar\partial_\tau\sigma_{jk} = i[\sigma_{jk}, H_A + H_{ED} + H_L] \tag{2.6}$$

in which the square brackets denote the commutator. The optical free-field Hamiltonian always commutes with the atomic coherences and so we will not deal with it going forward. Note that we have excluded spontaneous decay and dephasing for now, and will add these in later. This gives us the following initial equations for molecular coherences,

$$\begin{aligned}
\hbar\partial_t\sigma_{11} &= -i\boldsymbol{E}\cdot(\boldsymbol{\mu}_{01}^*\sigma_{10} - h.c.)\\
\hbar\partial_t\sigma_{01} &= i\hbar\omega_{10}\sigma_{10} - i\boldsymbol{E}\cdot\boldsymbol{\mu}_{10}^*(\sigma_{00} - \sigma_{11})\\
\partial_t\sigma_{00} &= -\partial_t\sigma_{11}\\
\partial_t\sigma_{10} &= \partial_t\sigma_{01}^*\,.
\end{aligned} \tag{2.7}$$

In the equation for $\partial_t\sigma_{01}$, the leading term $i\hbar\omega_{10}\sigma_{10}$ describes a rapid oscillation. The laser field is also oscillating rapidly and so the resulting dynamics will contain terms oscillating at the sum and difference of the two frequencies. We are considering near resonant spectroscopy, so the detuning of the laser frequency from the molecule resonant frequency is small and the resulting sum frequencies will be many orders of magnitude larger than the difference frequencies. Over our timescales of interest, these sum frequencies will average to zero and can be ignored. This is known as the rotating wave approximation.

We will move to a frame rotating with the laser frequency, ω_L by defining the rotating coherences,

$$\begin{aligned}
\widetilde{\sigma}_{jk} &= \sigma_{jk}\exp[-i\omega_L t]\\
\partial_t\widetilde{\sigma}_{jk} &= (\partial_t\sigma_{jk})\exp[-i\omega_L t] - i\omega_L\sigma_{jk}\exp[-i\omega_L t]\\
\partial_t\widetilde{\sigma}_{jj} &= \partial_t\sigma_{jj}
\end{aligned} \tag{2.8}$$

which results in the equations,

$$
\begin{aligned}
\hbar\partial_t \sigma_{11} &= -i\boldsymbol{E}\cdot(\mu_{01}^{*}\widetilde{\sigma}_{10} - h.c.)\exp[+i\omega_L t] \\
\hbar\partial_t \widetilde{\sigma}_{01} &= -i\hbar\Delta\widetilde{\sigma}_{01} - i\boldsymbol{E}\cdot\mu_{01}^{*}(\sigma_{00}-\sigma_{11}) \\
\partial_t \sigma_{00} &= -\partial_t \sigma_{11} \\
\partial_t \widetilde{\sigma}_{10} &= \partial_t \widetilde{\sigma}_{01}^{*}
\end{aligned}
\tag{2.9}
$$

where we have defined $\Delta = \omega_L - \omega_{10}$ as the laser detuning from the $S_{0,0} \rightarrow S_{1,0}$ transition.

Now including the expression for $\boldsymbol{E}$, we find terms where the oscillating exponentials cancel and those which oscillate at $2\omega_L$ which we neglect,

$$
\begin{aligned}
\partial_t \sigma_{11} &= \frac{i}{2}\Omega(\widetilde{\sigma}_{01} - \widetilde{\sigma}_{10}) \\
\partial_t \widetilde{\sigma}_{01} &= -i\Delta\widetilde{\sigma}_{01} + \frac{i}{2}\Omega(\sigma_{11}-\sigma_{00}) \\
\partial_t \sigma_{00} &= -\partial_t \sigma_{11} \\
\sigma_{00} + \sigma_{11} &= 1 \\
\widetilde{\sigma}_{10} &= (\widetilde{\sigma}_{01})^{*}\,.
\end{aligned}
\tag{2.10}
$$

The coupling strength of the laser field to the molecule is characterised by the Rabi frequency $\Omega = \frac{\mu_{01}^{*}\cdot\boldsymbol{v}_L\mathcal{E}_L^{*}}{\hbar}$ which we will assume is real. In general the Rabi frequency is a complex number representing the magnitude and phase of the electric field. For the equations we have just derived, phase variation due to detuning of the laser field from the resonant transition is accounted for by the term $-i\Delta\widetilde{\sigma}_{01}$. By forcing the Rabi frequency to be real, we have assumed no other phase variation, such as from sidebands or chirping of the laser field.

We now need to include decay from spontaneous emission and dephasing due to coupling to the environment. We will also include the vibrational states of the molecule. Since we are near resonant with the molecule transition, it is reasonable to ignore the excited state vibrational manifold for now (the vibrational states are typically separated by THz [121, 130, 307]), but decays from the excited state to the vibrational manifold of the ground electronic state need to be included [306]. We represent the population in $S_{0,n>0}$ as σ_{nn} and decays from $S_{1,0}$ to $S_{0,n}$

are denoted by $\Gamma_{1,n}$. Dephasing of the coherence $\widetilde{\sigma}_{01}$ is given by [130]

$$\Gamma_2 = \sum_n \left(\frac{\Gamma_{1,n}}{2} + \Gamma_2^* \right) \tag{2.11}$$

where n is summed over all vibrational transitions and Γ_2^* is the pure dephasing rate, related to the magnitude of energy fluctuations in the system. Γ_2^* is temperature dependent which for molecules doped into organic crystals, can be modelled as [308, 309],

$$\Gamma_2^*(T) = A \exp\left(\frac{-E_a}{\mathrm{k_B} T} \right) \tag{2.12}$$

with T as temperature, $\mathrm{k_B}$ the Boltzmann constant, E_a the activation energy associated with creation/annihilation of local phonons and A is a proportionality constant quantifying the electron-phonon interaction. Adding in the ground electronic state vibrational manifold, decay and dephasing, we arrive at [310],

$$\begin{aligned}
\partial_t \sigma_{11} &= \frac{i}{2}\Omega(\widetilde{\sigma}_{01} - \widetilde{\sigma}_{10}) - \sum_n \Gamma_{1,n}\sigma_{11} \\
\partial_t \sigma_{nn} &= \Gamma_{1,n}\sigma_{11} - \Gamma_n \sigma_{nn} \\
\partial_t \sigma_{00} &= -\frac{i}{2}\Omega(\widetilde{\sigma}_{01} - \widetilde{\sigma}_{10}) + \Gamma_n \sum_n \sigma_{nn} + \Gamma_{1,0}\,\sigma_{11} \\
\partial_t \widetilde{\sigma}_{01} &= -(\Gamma_2 + i\Delta)\widetilde{\sigma}_{01} + \frac{i}{2}\Omega(\sigma_{11} - \sigma_{00}) \\
\sigma_{00} + \sigma_{11} &+ \sum_n \sigma_{nn} = 1 \\
\widetilde{\sigma}_{10} &= (\widetilde{\sigma}_{01})^*\,,
\end{aligned} \tag{2.13}$$

where we have defined the decay from vibrational state σ_{nn} as Γ_n. Typically for molecules,

$\Gamma_n \gg \Gamma_{1,n}$ [303] and we can reduce the above equations to,

$$\begin{aligned}
\partial_t \sigma_{11} &= \frac{i}{2}\Omega(\widetilde{\sigma}_{01} - \widetilde{\sigma}_{10}) - \Gamma_1 \sigma_{11} \\
\partial_t \sigma_{00} &= -\partial_t \sigma_{11} \\
\partial_t \widetilde{\sigma}_{01} &= -(\Gamma_2 + i\Delta)\widetilde{\sigma}_{01} + \frac{i}{2}\Omega(\sigma_{11} - \sigma_{00}) \\
\sigma_{00} + \sigma_{11} &= 1 \\
\widetilde{\sigma}_{10} &= (\widetilde{\sigma}_{01})^* ,
\end{aligned} \tag{2.14}$$

in which we have defined $\Gamma_1 = \sum_n \Gamma_{1,n}$ leaves us with the usual optical-Bloch equations for a two-level system but with modified decay.

Steady state solution

We can find the steady state solutions of Eqs. 2.14 by setting $\partial_t \sigma_{jk} = 0$ for all j and k, to give [310],

$$\begin{aligned}
\sigma_{11} &= \frac{1}{2}\frac{S}{(\Delta/\Gamma_2)^2 + 1 + S} \\
\sigma_{00} &= 1 - \sigma_{11} \\
\sigma_{01} &= -\frac{1}{2}\frac{\Gamma_1}{\Omega}\frac{S}{(\Delta/\Gamma_2)^2 + 1 + S}\left(\frac{\Delta}{\Gamma_2} + i\right) \\
\widetilde{\sigma}_{10} &= (\widetilde{\sigma}_{01})^* ,
\end{aligned} \tag{2.15}$$

where we have defined the saturation parameter $S = \frac{|\Omega|^2}{\Gamma_1\Gamma_2} = \frac{I\cos^2(\theta)}{I_{\text{sat}}}$, with θ as the angle between the molecule dipole moment $\boldsymbol{\mu}_{01}$ and $\boldsymbol{v}_L$, and $I_{\text{sat}} = \frac{\epsilon_0 c\hbar^2}{2}\frac{\Gamma_1\Gamma_2}{|\mu_{01}|^2}$ is the saturation intensity of the transition.

The spontaneous emission rate, R, is then simply,

$$R = \Gamma_1 \sigma_{11} = \frac{\Gamma_1}{2}\frac{S}{(\Delta/\Gamma_2)^2 + 1 + S} \tag{2.16}$$

The steady state solutions given by Eqs. 2.15 are plotted in Fig. 2.2a. Initially population in the excited state increases linearly with S but then saturates at $\sigma_{11} = 0.5$ as $S \to \infty$. We can also see how R has a Lorentzian lineshape, where the peak counts (at $\Delta = 0$) follows a saturation curve,

$$R_{\Delta=0} = R_{\infty}\frac{S}{1+S}\,, \tag{2.17}$$

where $R_{\infty} = \eta_{col}\Gamma_1/2$, which is the collection efficiency multiplied by the maximum spontaneous emission rate for resonant excitation. The width of the Lorentzian is given by,

$$\Delta\omega = 2\Gamma_2\sqrt{1+S}\,. \tag{2.18}$$

The increase in linewidth as the intensity of the laser field is increased is termed power broadening. As S is increased, for laser light resonant with the transition, the population begins to saturate. For the same S, detuned light will cause less saturation, so the returned counts will see a bigger increase for the same increse in S, resulting in a broader lineshape. Fig. 2.2b shows how the Lorentzian lineshape changes with S, while Fig. 2.2c and Fig. 2.2d show R and $\Delta\omega$ plotted against S respectively.

This relatively simple model is useful in the lab for measuring the properties of an emitter. By resonantly exciting a molecule with a continuous wave (cw) laser, we can collect the returned fluorescence and filter out the excitation laser, leaving behind only the red shifted fluorescence originating from decays to $S_{0,n>0}$. Varying the laser power then allows us to determine Γ_2 and I_{sat} from the above relations. We can also determine the maximum count rate from the emitter, R_{∞}, which can be useful in characterising the collection efficiency.

Second-order correlation function

In Section 1.3.1 we discussed how measurement of the second-order correlation function at zero time delay $g^{(2)}(0)$ is a useful measure of the single photon purity. For cw excitation, the statistical properties of the system are constant and we can express $g^{(2)}$ as a function of time delay between detection events, τ,

$$g^{(2)}(\tau) = \frac{\langle \hat{a}^{\dagger}(t)\hat{a}^{\dagger}(t+\tau)\hat{a}(t+\tau)\hat{a}(t)\rangle}{(\langle \hat{a}(t)\rangle)^2} \tag{2.19}$$

where $\hat{a}^{\dagger}$ and $\hat{a}$ are the photon creation and annihilation operators respectively. For $\tau = 0$, this

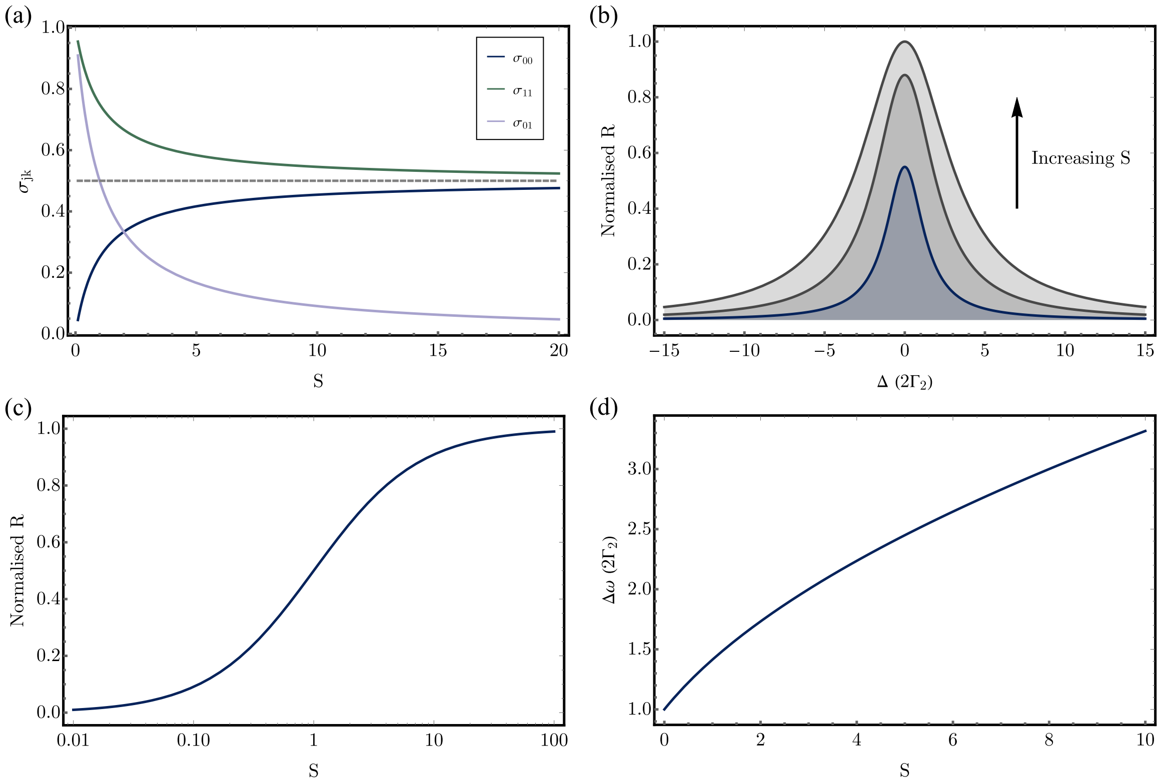

Figure 2.2: (a) Plot showing how the steady state of each σ_{jk} varies with the saturation parameter S. (b) Spontaneous emission rate R as a function of laser detuning Δ, normalised to $R_\infty = \eta_{col}\Gamma_1/2$, where η_{col} is the photon collection efficiency and Γ_1 is the excited state population decay rate. Shown is the characteristic Lorentzian lineshape for a particular S. As S is increased, we see the maximum count rate increase as well as the Lorentzian width increasing demonstrating power broadening.(c) Saturation curve (again normalised to R_∞), showing the maximum count rate as S is increased on a log scale. (d) Power broadening of the resonance linewidth $\Delta\omega$ as S is increased.

reduces to,

$$g^{(2)}(\tau) \approx \frac{2P(2, \tau \in T)}{P(1, \tau \in T)}\,, \tag{2.20}$$

where T is the time interval given by the experimental resolution and $P(n, T)$ is the probability of finding n photons within a time interval T. We require T to be small enough such that $g^{(2)}(T/2) \approx g^{(2)}(0)$, which requires $T \ll 1/\Gamma_1$. After detection of a photon, the molecule is projected to the ground state, so $g^{(2)}(\tau)$ is proportional to the excited state population $\sigma_{11}(\tau)$ given initial condition $\sigma_{11}(0) = 0$.

The steady state solutions derived previously deal with molecule dynamics over time scales longer than lifetime of excited state. To derive an expression for $g^{(2)}(\tau)$ we require equations of motion for the transient behaviour of DBT. We can then write,

$$g^{(2)}(\tau) = \frac{\sigma_{11}(\tau)}{\sigma_{11}(\infty)}\,, \tag{2.21}$$

where $\sigma_{11}(\infty)$ is the steady state value of σ_{11}.

We set $\Delta = 0$ and define,

$$\begin{aligned} u &= \widetilde{\sigma}_{01} + \widetilde{\sigma}^*_{01} = \widetilde{\sigma}_{01} + \widetilde{\sigma}_{10} \\ v &= -i(\widetilde{\sigma}_{01} - \widetilde{\sigma}^*_{01}) \end{aligned} \tag{2.22}$$

which are the real and imaginary components of σ_{01} respectively[4]. This leads to,

$$\begin{aligned} \partial_t \sigma_{11} &= \frac{\Omega}{2} v - \Gamma_1 \\ \partial_t v &= -\Omega(\sigma_{11} - \sigma_{00}) - \Gamma_2 v \\ \partial_t \sigma_{00} &= -\sigma_{11}\,. \end{aligned} \tag{2.23}$$

We can use the Laplace transform to remove the partial differentials and then solve the resulting algebraic equations [198, 311]. Applying the inverse Laplace transform, we arrive at the

---

[4] We can also understand u and v as the components of the induced molecular dipole that are in-phase or $\pi/2$ out of phase in the rotating frame.

expressions,

$$\begin{aligned}
\sigma_{11} &= \frac{1}{2}\frac{\Omega^2}{\Gamma_1\Gamma_2+\Omega^2}\left(1-\frac{p+q}{2q}\exp\left[-(p-q)\tau\right]+\frac{p-q}{2q}\exp\left[-(p+q)\tau\right]\right)\\
\sigma_{00} &= 1-\sigma_{11}\\
\sigma_{01} &= -\frac{i\Omega\Gamma_1}{\Gamma_1\Gamma_2+\Omega^2}\left(1+\frac{d-q}{2q}\exp\left[-(p-q)\tau)\right]-\frac{d+q}{2q}\exp\left[-(p+q)\tau\right]\right)\\
\widetilde{\sigma}_{10} &= \left(\widetilde{\sigma}_{01}\right)^*,
\end{aligned} \tag{2.24}$$

where we have defined,

$$\begin{aligned}
d &= \frac{\Omega^2}{\Gamma_1}-\frac{\Gamma_1-\Gamma_2}{2}\\
p &= \frac{\Gamma_1+\Gamma_2}{2}\\
q &= \sqrt{\left(\frac{\Gamma_1-\Gamma_2}{2}\right)^2-\Omega^2}\,,
\end{aligned} \tag{2.25}$$

The transient solution for σ_{11} is plotted in Fig. 2.3a. We see the populations approach 0.5 for time scales longer than the lifetime of the excited state, as we found in the steady state solutions. However, on shorter time scales, we see an oscillatory behaviour known as Rabi oscillations, caused by absorption and subsequent stimulated emission. This becomes more pronounced at higher S. Over time, spontaneous emission and coupling to the environment cause the dephasing of the transition dipole, which causes the oscillations to be damped. This is shown in Fig. 2.3b where σ_{11} is plotted for different magnitudes of dephasing.

Using the transient solution of σ_{11} we can derive an expression for $g^{(2)}$ under resonant excitation [202],

$$g^{(2)}(\tau) = 1-\frac{p+q}{2q}\exp\left[-(p-q)|\tau|\right]+\frac{p-q}{2q}\exp\left[-(p+q)|\tau|\right]\,. \tag{2.26}$$

In Fig. 2.3c, simulated $g^{(2)}(\tau)$ curves are plotted as S is increased, leading to a narrowing of the central antibunching dip due to an increasing likelihood of quickly re-exciting the emitter. We also see the signature of Rabi oscillations. Shown in Fig.2.3d are simulated $g^{(2)}(\tau)$ curves as Γ_2 is increased and any Rabi oscillations are washed out. As Γ_2 is temperature dependent, in order to see Rabi oscillations the emitter must be at cryogenic temperatures. Notice that $g^{(2)}(0) = 0$ for any choice of parameters, signifying a single photon emitter. By experimentally

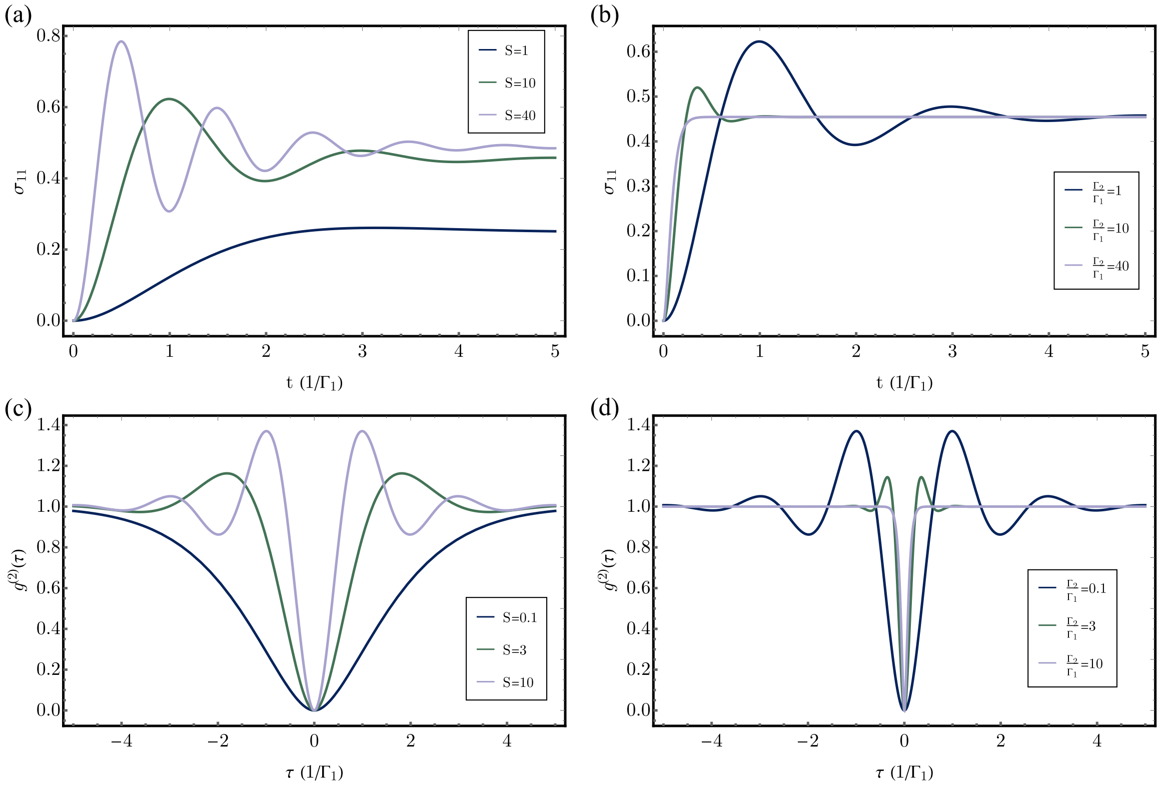

Figure 2.3: Plot showing transient solution of excited state population σ_{11} as a function of time (a) for differing saturation parameter values S while $\Gamma_2/\Gamma_1 = 1$, and (b) for differing levels of dephasing Γ_2 relative to the spontaneous emission rate Γ_1, with $S = 10$. Plots showing second-order correlation function $g^{(2)}(\tau)$ (c) while varying S for $\Gamma_2/\Gamma_1 = 1$, and (d) while varying Γ_2/Γ_1 with $S = 10$.

measuring $g^{(2)}(\tau)$, we can deduce S, Γ_1 and Γ_2.

2.1.3 Non-resonant spectroscopy

So far, we have dealt with resonantly exciting the molecule on the ZPL line. Instead, we may excite to a third state – an excited vibrational state of the excited electronic state, $S_{1,\nu>0}$. As mentioned in Section 2.1.1, excitation to $S_{1,\nu}$ leads to fast non-radiative decay to $S_{1,0}$, followed by fluorescent decay to the ground electronic state manifold, where the photons will be emitted with minimal time uncertainty [312]. Photons emitted on the ZPL transition will also be spectrally distinguishable from the excitation laser, which makes it experimentally easier to isolate the emitted photons. To describe the resulting dynamics, we now need to include the third state.

Three-level equations

We label the third state $S_{1,\nu}$ as $|2\rangle$, with a corresponding population $\sigma_{22} = |2\rangle\langle 2|$. The non-radiative decay Γ_{nrad} from $S_{1,\nu} \to S_{1,0}$ is incoherent, so if we assume that the molecule begins in the ground state and is only excited to $S_{1,\nu}$, we can set the coherences $\sigma_{21} = \sigma_{10} = 0$. We can further simplify our equations by noting that the decay from $|2\rangle \to |1\rangle$ is much faster than $|2\rangle \to |0\rangle$, and so we may neglect decay from $|2\rangle$ to $|0\rangle$. This leads to the following modified set of equations,

$$\begin{aligned}
\partial_t \sigma_{22} &= \frac{i}{2}\Omega_{\text{blue}}(\widetilde{\sigma}_{20} - \widetilde{\sigma}_{02}) - \Gamma_{nrad}\sigma_{22} \\
\partial_t \sigma_{11} &= \Gamma_{\text{nrad}}\sigma_{22} - \Gamma_1\sigma_{11} \\
\partial_t \sigma_{00} &= -\frac{i}{2}\Omega_{\text{blue}}(\widetilde{\sigma}_{02} - \widetilde{\sigma}_{20}) + \Gamma_1\sigma_{11} \\
\partial_t \widetilde{\sigma}_{02} &= -(\Gamma_{2,\text{blue}} + i\Delta)\widetilde{\sigma}_{02} + \frac{i}{2}\Omega_{blue}(\sigma_{22} - \sigma_{00}) \\
&\sigma_{00} + \sigma_{11} + \sigma_{22} = 1 \\
&\widetilde{\sigma}_{20} = (\widetilde{\sigma}_{02})^*\,,
\end{aligned} \tag{2.27}$$

where $\Gamma_{2,\text{blue}} = \frac{\Gamma_{\text{nrad}}}{2} + \Gamma^*_{2,\text{blue}}$ is the decoherence rate of state $|2\rangle$, with $\Gamma^*_{2,\text{blue}}$ the temperature dependent pure dephasing rate of this transition, analogous to Γ^*_2 in the previous section. We have also defined $\Omega_{\text{blue}} = \frac{\boldsymbol{\mu}_{02}\cdot\boldsymbol{v}_L\mathcal{E}_L}{2}$, with μ_{02} denoting the transition dipole moment between states $|0\rangle$ and $|2\rangle$.

We are mainly interested in σ_{11}, as this is the only population that gives rise to photons. The steady state solution is,

$$\sigma_{11} = \frac{S_{\text{blue}}}{1 + S_{\text{blue}}\left(\frac{2\Gamma_1}{\Gamma_{\text{nrad}}} + 1\right) + \left(\frac{\Delta}{\Gamma_{2,\text{blue}}}\right)^2} \tag{2.28}$$

for $S_{\text{blue}} = \frac{\Omega_{\text{blue}}^2}{\Gamma_1 \Gamma_{2,\text{blue}}}$. At cryogenic temperatures, $\Gamma_{\text{nrad}} \gg \Gamma_{2,\text{blue}}^*$ so the Lorentzian width becomes $2\Gamma_{2,\text{blue}}\sqrt{1+S_{\text{blue}}} \to \Gamma_{\text{nrad}}\sqrt{1+S_{\text{blue}}}$ (i.e. much broader than the resonant linewidth). Through non-resonant excitation, we can reach full population inversion ($\sigma_{11} = 1$) in the steady state due to the fast dephasing of σ_{02} preventing stimulated emission. The caveat of this is that $S_{\text{blue}} \approx (\Gamma_2/\Gamma_{\text{nrad}})S$ and so to reach the same saturation as resonant pumping, we require much larger laser intensities.

Transient solution

Equations 2.27 can be solved using the Laplace transform as in the previous section. However a simpler solution can be found by noting that $\Gamma_{\text{nrad}} \gg \Gamma_1$ and so over the timescales of interest, any coherence will have dephased. This leaves us with the following rate equations for the populations,

$$\begin{aligned} \partial_t \sigma_{22} &= \Gamma_1 S_{\text{blue}} \sigma_{00} - \Gamma_{\text{nrad}} \sigma_{22} \\ \partial_t \sigma_{11} &= \Gamma_{\text{nrad}} \sigma_{22} - \Gamma_1 \sigma_{11} \\ \partial_t \sigma_{00} &= -\Gamma_1 S_{\text{blue}} \sigma_{00} + \Gamma_1 \sigma_{11}\,, \end{aligned} \tag{2.29}$$

Given that $\Gamma_{\text{nrad}} \gg \Gamma_1$, we can write the transient solution as,

$$\sigma_{11}(t) = \frac{S_{\text{blue}}}{1 + S_{\text{blue}}} \left(1 - \exp\left[-\Gamma_1(1 + S_{\text{blue}})t\right]\right) \tag{2.30}$$

which results in the non-resonant pumping second-order correlation function $g_{\text{blue}}^{(2)}(\tau)$,

$$g_{\text{blue}}^{(2)}(\tau) = 1 - \exp\left[-\Gamma_1(1 + S_{\text{blue}})|\tau|\right] \tag{2.31}$$

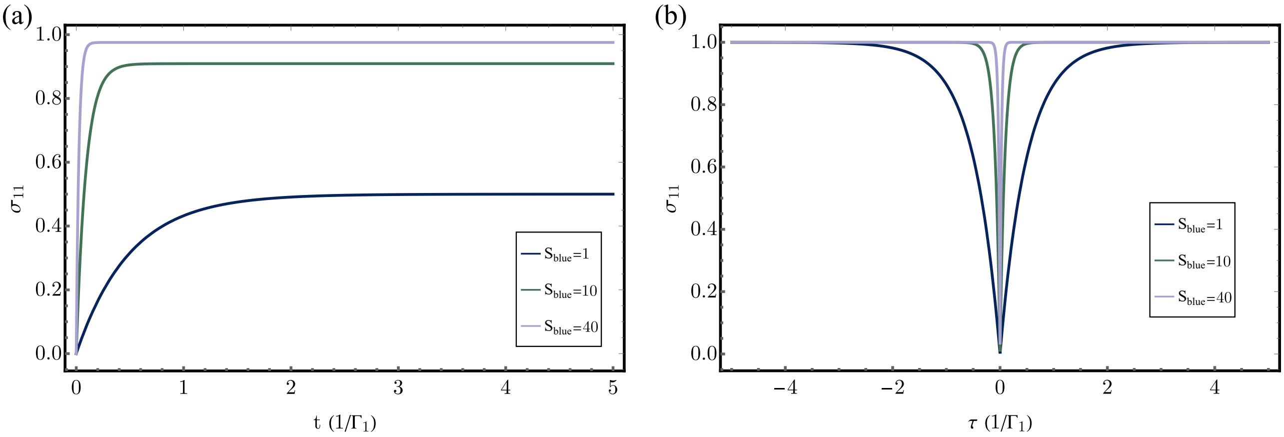

Figure 2.4: (a) Plot showing excited state population σ_{11} as a function of time for varying saturation parameter values S_{blue}, where the excitation laser is resonant with a higher vibrational mode of the excited state. (b) Plot of second-order correlation function $g^{(2)}(\tau)$ resulting from this excitation scheme, for varying S_{blue}.

Note that Eq. 2.26 for resonant pumping $g^{(2)}(\tau)$ tends to Eq. 2.31 as dephasing $\Gamma_2 \to \infty$.

Fig. 2.4a shows a simulation of how the excited state population σ_{11} varies in time, as S_{blue} is increased. In Fig. 2.4b we see how the antibunching feature of $g^{(2)}_{\text{blue}}(\tau)$ narrows for larger S_{blue}, due to an increase in the likelihood of a molecule being re-excited in a shorter period of time. As a result of a large $\Gamma_{2,\text{blue}}$, we do not see any Rabi oscillations.

2.2 Measurement

In this section, we describe the general experimental details of probing fluorescenece from DBT molecules. We begin by describing the workings of a confocal microscope, the workhorse for much of the data presented in the next chapter.

2.2.1 Confocal microscopy

In all the experiments described in the Chapter 3, we used confocal microscopy to characterise the emitters. We used one of three home-built confocal microscope setups: one for room temperature measurements and two for cryogenic temperature measurements. In all cases, the general setup is the same and is illustrated in Fig. 2.5. Individual component details will be given in the next chapter when discussing specific experiments.

Fluorescence confocal microscopy is a common technique used to study solid state single photon sources. It relies on two paths: an excitation path and a collection path. For excitation, a collimated laser is focused onto the sample by means of of an objective lens (L3 in Fig. 2.5). The position of the laser spot relative to the sample can be varied through either translating the sample or by changing the angle of the laser incident on the objective. Any fluorescence from the sample, along with any scattered laser light, is then collected and focused back through the objective lens. A second imaging lens is used to focus the collected light onto the image plane, as shown in the inset of Fig. 2.5. By placing a pinhole in the imaging plane, any out of focus signal is rejected, increasing the axial resolution of the microscope beyond what can be achieved through spatially selective excitation of a laser spot.

The excitation is provided from one of several laser sources available in the lab (the exact source will be detailed when the data is presented). Around 1% of the light from the excitation beam is split onto a photodiode by a beam-splitter (BS1) to monitor and correct for power fluctuations. A polariser (Pol.) is used to clean up the laser polarisation and a half-wave plate (HWP) is used to set the polarisation at the sample. A bandpass filter (F1) is used to remove any light other than the laser, such as Raman scattering from the fibre. The light is then directed to a $90:10$ beamsplitter (or potentially a dichroic mirror for some experiments) which is used to overlap the collection and excitation paths. This results in 90% of the excitation light being thrown away but this can easily be compensated for by turning up the laser power.

A pair of steering mirrors GM (Scanning Galvo Mirror System, Thorlabs) are used to control the angle and position of the laser into a 4-f lens configuration, made up of L1 (focal length of f_1) and L2 (focal length of f_2). The distance from GM to L1 is f_1, from L1 to L2 is $f_1 + f_2$ and from L2 to the back aperture of the objective lens L3 is a distance of f_2. The 4-f configuration allows for the angle of the laser beam to be varied while still passing through the centre of the objective lens.

Signal light from the sample is focused through L3 and travels back along the same path as

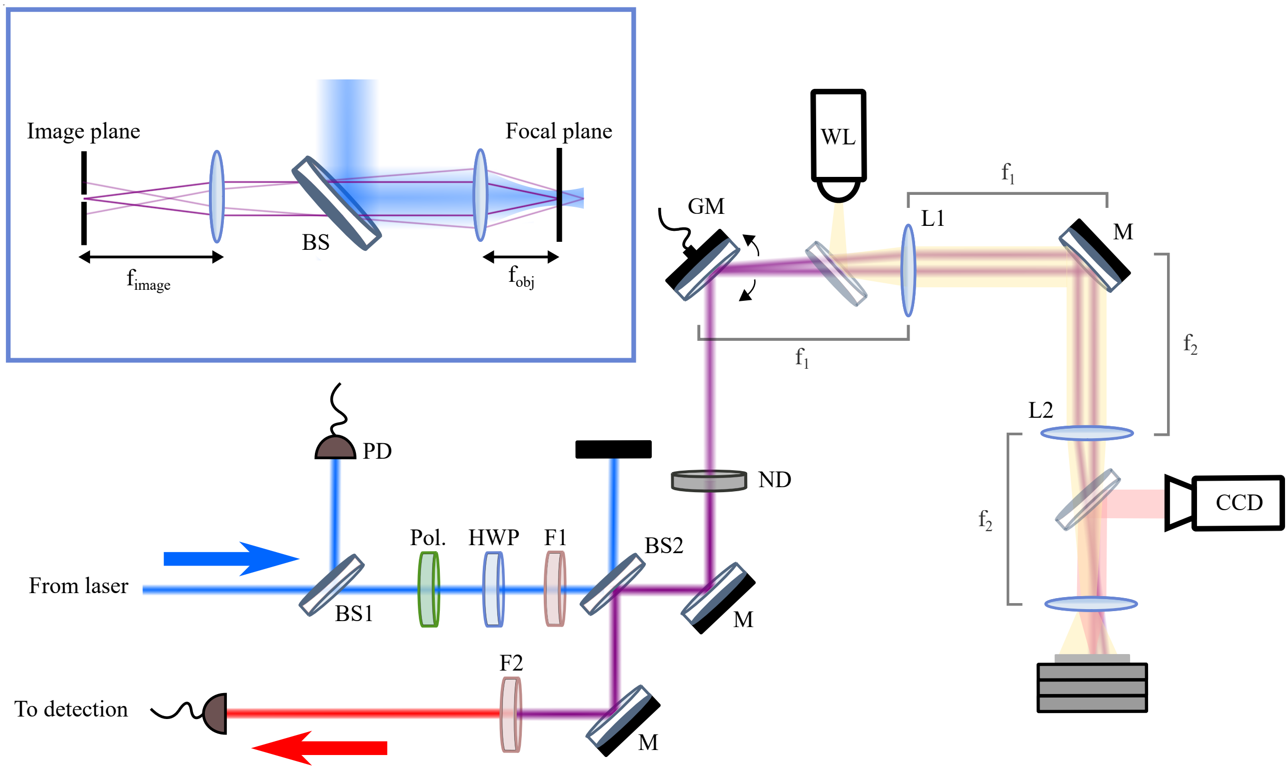

Figure 2.5: The main image sketches the standard layout of the confocal microscopes used in the Chapter 3. Blue represents the excitation light, purple the overlap of excitation and collected light and red the fluorescence after the excitation light has been removed through spectral filtering. White light illumination is also shown in yellow, and the collected light in pink. BS: beam-splitter, PD: photodiode, HWP: half-wave plate, Pol: linear polariser, F: filter, M: mirror, GM: scanning galvo mirrors, WL: white light source, L:lens, CCD: charge-coupled device camera. Inset illustrates the working principle of a confocal microscope. The excitation laser (shown in blue) is focused by an objective lens. The resulting fluorescence (thin purple lines) is collected by the objective lens and focused by an imaging lens onto the image plane where a pinhole is placed. Fluorescence originating from outside the focal plane is rejected by the pinhole.

the excitation light until reaching BS2 (the 90 : 10 beamsplitter). Here 90% of the collected light is directed to the detection part of the setup, with the remaining 10% lost. The collected light then propagates through a long pass filter, to remove any elastic scattering of the pump light, before being collected by an optical fibre - the fibre mode acting as the required pinhole for confocal imaging. For measuring count rates, the collected light can be detected by a silicon single-photon avalanche diode, SPAD (SPCM-AQRH, Perkin Elmer), which quotes a detection efficiency of around 50% for 800 nm. Alternatively, the fluorescence can be sent to a spectrometer (Shamrock 303i, Andor) and an electron-multiplying charge-coupled device (CCD) camera (iXon, Andor) for detection. This allows for an integrated spectrum of fluorescence to be constructed, with a resolution of 0.2 nm.

Inelastic scattering of the excitation beam, such as from other dopant molecules or from Raman scattering in the surrounding crystal, can result in light resonant with emitted fluorescence that cannot be filtered out spectrally. This background can be kept to a minimum by operating at low laser powers, corresponding to an $S \sim 1$. Also operating at cryogenic temperatures and using resonant excitation reduces I_{sat}, meaning lower laser powers can be used to achieve $S \sim 1$. By scanning the laser power and frequency over the molecular resonances, the resulting fluorescence can be fitted to the equations derived earlier in this chapter in order to extract Γ_2 and I_{sat}.

In addition to laser excitation, we can perform white light imaging, useful for identifying structures and finding the focal plane. The white light source WL is placed f_1 away from L1 and is directed into the system by means of a temporary pellicle beam splitter BS3 which is removed when performing single photon measurements to maximise the number of photons transmitted through the setup. Back scattered light from the sample is directed by another temporary pellicle beam splitter BS4 onto a variable zoom lens CCD camera. The whole sample stage can be re-positioned by means of a 3-axis positioning system , which is used for relocating the white light or laser spot in between scans.

2.2.2 Second-order correlation function

For measuring $g^{(2)}(\tau)$, the collection fiber is sent to a $50:50$ fibre beam-splitter (Thorlabs) and the two output ports are sent to two SPADs. A time-correlator card (Time-Harp 260, PicoQuant) is triggered when a photon is detected at one of the SPADs, and records the time delay until the other SPAD records a photon. Provided the count rate is low enough and the probability of multi-photon generation is small, this measure closely approximates $g^{(2)}(\tau)$ [313,314].

For fitting to Eq. 2.26 and Eq. 2.31, we must include a visibility term ($\mathcal{V}$) to include contributions from background light and fluorescence from other nearby molecules. The equations then become,

$$g^{(2)}(\tau) = 1 - \mathcal{V}\frac{p+q}{2q}\exp\left[-(p-q)|\tau|\right] + \mathcal{V}\frac{p-q}{2q}\exp\left[-(p+q)|\tau|\right] , \tag{2.32}$$

for resonant pumping and,

$$g^{(2)}(\tau) = 1 - \mathcal{V}\exp\left[\Gamma_1(1+S)|\tau|\right] , \tag{2.33}$$

for non-resonant pumping.

To account for timing jitter of the SPADs, the above $g^{(2)}(\tau)$ equations must be convolved with a Gaussian of $1/e$ width equal to the detector jitter. For the detectors used in this thesis, we use a Gaussian width of 320 ps, derived from separate measurements of a laser pulse using the same setup.

As well as the single photon purity, when combined with fluorescence measurements while the laser power and frequency are scanned, $g^{(2)}(\tau)$ allows Γ_1 to be extracted.

2.2.3 Time-correlated single photon counting

Another method for determining Γ_1 is to measure the lifetime of the excited state via a time-correlated single photon counting (TSPC) measurement. Here a timing card measures the time delay between a laser pulse and the detected DBT fluorescence. Performing the measurement many times, a histogram can be constructed with number of detection events as a function of delay time. The likelihood of detection is directly proportional to the excited state population.

Chapter 3

Dibenzoterrylene: Experiments

In this chapter we will use the theoretical framework developed in Chapter 2 to examine Dibenzoterrylene (DBT) in two different host matrices: Anthracene (Ac) and *para*-Terphenyl (pT). For DBT in Ac, we will investigate different mechanisms for tuning the emission wavelength and methods for deterministically interfacing DBT doped Ac crystals into photonic structures. The second section will deal with a novel host matrix pT and characterise the optical properties of DBT in pT nanocrystals.

3.1 Dibenzoterrylene in Anthracene

In this section, we place DBT in an Ac (formula $C_{14}H_{10}$, shown in Fig. 3.1a) host matrix. Ac forms a solid at room temperature and pressure, which is weakly held together by van der Waals forces. This leads to a relatively low melting point of 217 °C and poor electrical conductivity. An Ac unit cell is illustrated in Fig. 3.1c, where the lattice constants along the a, b and c axes are 8.56 Å, 6.04 Å and 11.16 Å respectively, with an angle of 124.7 ° between the a and c axes [303].

DBT inserts into one of two sites within Ac: the main site and the red site [302]. For the main site, occupied 1000 times more frequently than the red site, DBT replaces three Ac molecules

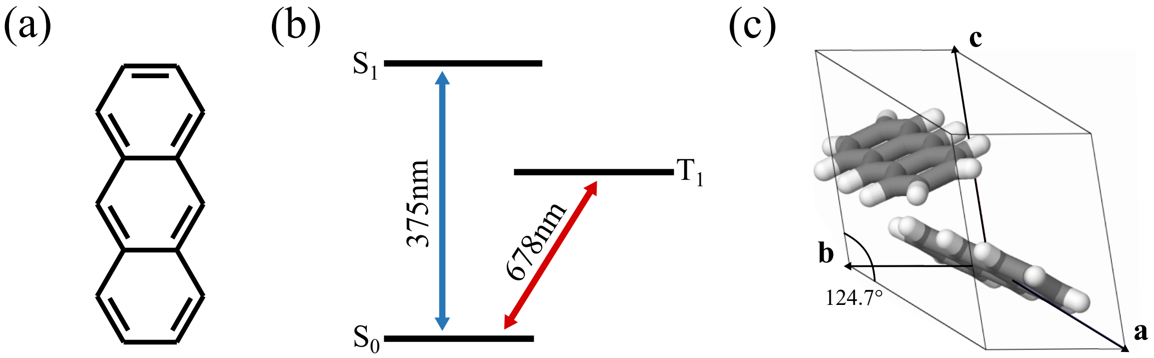

Figure 3.1: (a) Anthracene (Ac) molecular structure. (b) Energy level diagram for the outermost $\pi-$electrons of Ac, showing the ground single S_0 and first excited singlet states S_1, as well as the first triplet state T_1. (c) Ac unit cell.

along the crystallographic b-axis. This results in a transition dipole moment aligned along the b-axis and thus the emitted photons have linear polarisation orientated to this axis. The singlet transition in DBT is centered at 785 nm, with an inhomogeneous broadening of around 3 nm and an excited state lifetime of 4 ns. For the red insertion site, DBT replaces two Ac molecules along the b-axis and one of the neighbouring molecules along the a-axis, producing a singlet transition at 794 nm, with an inhomogeneous broadening of around 12 nm. The red site features more interactions with the surrounding Ac host when compared with the main site, leading to greater dephasing for the same temperature. Strains in the host crystal, such as from structural defects originating from dislocations, grain boundaries or crystal edges, act to reduce photo-stability and increase dephasing for both sites. The nature and frequency of these defects will depend on the growth method used, which will be discussed in more in Section 3.1.1.

The singlet transition, in both the main and the red site, fluoresces at energies well below the singlet transition in Ac, which has a wavelength of 375 nm as shown in Fig. 3.1b, making Ac transparent to photons produced from DBT. The DBT singlet transition also energetically lies below the triplet state in Ac. This reduces the probability of singlet to triplet energy transfer from guest to host, which would otherwise increase the rate of transition to the DBT triplet state, reducing the photon generation efficiency of the DBT [303]. As it happens, the inter-system crossing probability for DBT doped Ac is very small, on the order of 10^{-7} [302], with the lingering probability as a result of spin-orbit coupling allowing for weak transitions between S_1 and T_1. These weak transitions, if radiative, could be accessed through intense laser light, allowing an excitation of DBT to be stored for the lifetime of the triplet state, around $40\,\mu$s [302]. However to date, due to the weak coupling between S_1 and T_1, the exact energy of T_1 in DBT/Ac has not been determined.

As well as electronic transitions, we also have the vibrational manifold of DBT, originating from the normal mode oscillations of the nuclei. The vibrational levels are very short lived, decaying on the order of picoseconds to the ground vibrational state through coupling to the surrounding crystal [303]. On top of this, interaction with phonons from the surrounding host matrix result in a phonon side band. For DBT in Ac, the branching ratio (ratio of fluorescence on the ZPL to all other emission) $\alpha \approx 32\%$ [205, 312], depending on the growth method and local environment of the DBT molecule.

At cryogenic temperatures, DBT/Ac shows Fourier-limited emission on the zero-phonon line (ZPL), with a bandwidth of $40-50\,$MHz [302]. We can resonantly excite on this transition and collect decays from $S_{1,0} \rightarrow S_{0,n>0}$, in order to spectrally filter out the pump. While these photons are not indistinguishable, these tranistions can be useful for characterising the molecule. To collect light emitted from the ZPL while still pumping resonantly, filtering of the pump light must be accomplished by spatially decoupling excitation and collection, or using cross polarisers, where the excitation light polarisation is aligned as close as possible to 90° from the Ac b-axis, allowing polarisers to filter out most of the pump light from the emitted photons.

Alternatively we can excite to a higher vibrational mode of the excited state $S_{1,n>0}$. Since the vibrational decay is several orders of magnitude faster than the electronic state decay [312], there is little time-uncertainty in the preparation of $S_{1,0}$. Typically for DBT, we excite to $S_{1,3}$ for non-resonant pumping as this has a higher transition dipole-moment than the other vibrational lines - not including the ZPL [315]. This corresponds to a wavelength of $768\,$nm for main site DBT, easily separable from the ZPL at $785\,$nm. The fast decay of the $S_{1,3}$ state results in a excitation linewidth of $25-40\,$GHz compared with the $\sim 40\,$MHz resonant excitation linewidth: a factor of 1000 increase in pump power is needed to achieve the same level of saturation.

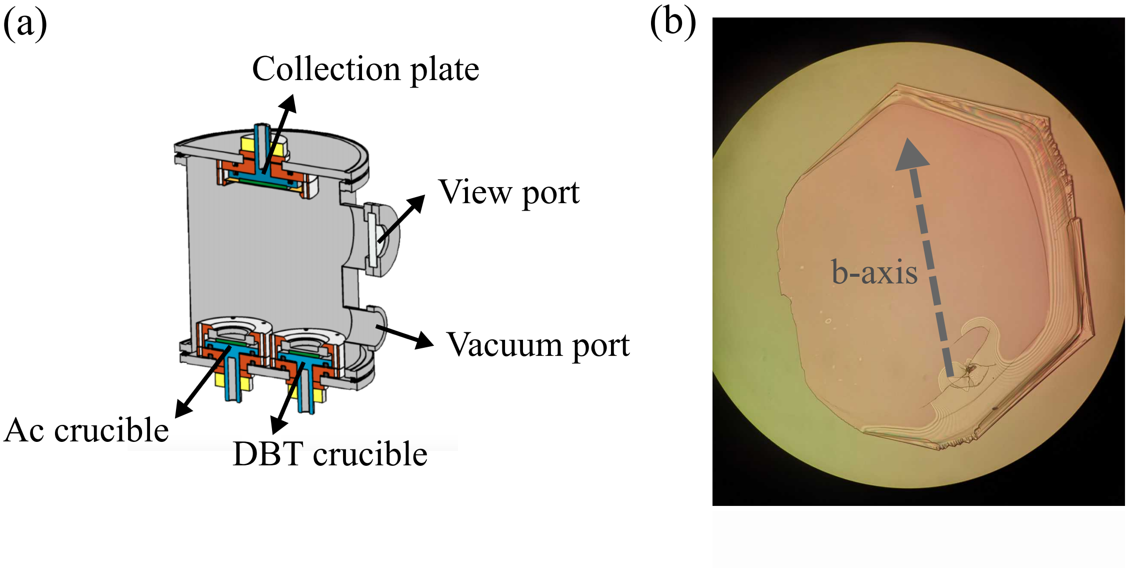

Figure 3.2: Cut-through of the co-sublimation chamber, modified from Ref. [200]. Ac: Anthracene, DBT: Dibenzoterrylene. (b) Photograph of typical Ac crystal grown using co-sublimation with the crystallographic b-axis indicated.

3.1.1 Growth methods

We use three methods for preparing DBT doped Ac in the group, depending on the application. These methods were developed by other members of the group and are described below.

Co-sublimation

Co-sublimation growth [200] involves heating Ac and DBT powders in a low pressure chamber, causing them both to sublime and accumulate on a collection plate placed above the sublimating chambers. This produces Ac crystals that have mm^2 surface areas and that are micrometers thick. Through varying the temperature of the Ac, the growth rate and overall morphology of the Ac crystals can be controlled, while adjusting the DBT temperature controls the doping. The doping and size of the crystals are also affected by the temperature of the collection plate and the pressure of the chamber. The shape of the macroscopic crystals produced corresponds to the Ac unit cell structure allowing the crystallographic axes to be determined using optical microscope images and thus the polarisation alignment of the emitted photons. A typical crystal is shown in Fig. 3.2b with the b-axis labelled.

A diagram of the cosublimation chamber, developed by other members of the group before the start of my PhD [200], is shown in Fig. 3.2a. At the bottom of the chamber sit two aluminium crucibles, one filled with Ac (ReagentPlus 99% purity, Sigma-Aldrich) and the other with DBT (PAH Research Institute, Greifenberg, Germany). At the top of the chamber, around 25 cm above the two crucibles, sits a copper collection plate. Oxygen during the growth process can become incorporated within the Ac crystals and lead to photo-bleaching of the DBT emitters, so beforehand, the atmosphere within the chamber is first evacuated using a roughing pump and then purged with dry-nitrogen to remove oxygen and humidity. The pump and purge process is repeated three times, before setting the internal pressure to 225 mbar. The temperatures of the Ac and DBT crucibles are controlled through resistive heaters and peltier elements for coarse and fine tuning respectively. The body of the chamber is also heated to prevent deposition on the walls.

The chamber and collection plate are heated to around 80 °C and 50 °C respectively. The Ac crucible is heated to 140 °C and the DBT crucible is set in the range $170 - 260\,^{\circ}\mathrm{C}$, depending on the doping required. A typical growth takes one to two hours and the resulting crystals are removed from the collection plate using tweezers. The crystals are placed on a substrate and then coated with PVA (around 200 nm thick) to prevent sublimation of the Ac, protect the crystal from the surrounding environment, as well as adhere the crystal to the substrate. Even without the PVA, the crystal adheres to substrate quite well through weak van der Waals forces, indicating a good thermal coupling. Crystals grown in this fashion show an inhomogeneous broadening of around 0.3 nm centered on 785.5 nm [302]. The narrow inhomogeneous broadening points to a very homogeneous crystal and the stability of the DBT dopants is typically very high for crystals grown in this way. However, the collection efficiency is usually poor, partly because of the spatial mode of the dipole emission, as discussed in Section 1.3 but also due to total internal reflection at the crystal boundary.

Melt growth

Another method for producing a bulk crystal matrix is through melt-growth [207]. Here microfluidic channels are first patterned within a substrate and then filled with a molten Ac and DBT mixture, which is allowed to crystallise by cooling the sample to room temperature. A before

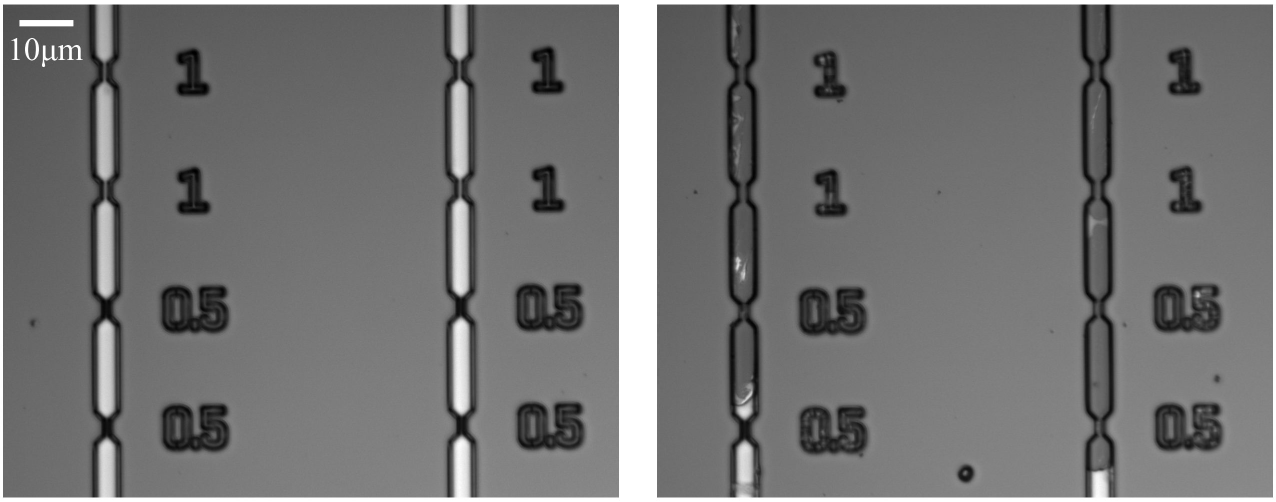

Figure 3.3: White light images showing micro-capillaries (left) unfilled, (right) after filling with doped anthracene. The white regions correspond to unfilled parts of the channel.

and after image is shown in Fig. 3.3, where micro-capillaries are initially unfilled on the left and then predominantly filled on the right. The channels can be used to fill specific regions of photonic structures with DBT/Ac.

The filling is done in a nitrogen purged environment, with typically $< 0.5\%$ O_2 concentration and humidity $< 4\%$ [315]. The DBT/Ac mixture is made by heating up DBT and Ac powders above the melting point of Ac. Since DBT is soluble in liquid Ac, the result is a uniformly doped solid when allowed to cool back down to room temperature. Grinding the cooled material results in a DBT/Ac powder. To fill the channels, the powder is placed at the entry to the channels and the substrate heated. This causes the DBT/Ac mixture to fill the channel through capillary forces. The substrate must be heated past the melting point of Ac (usually to around 220 °C), however near this temperature Ac sublimes rapidly and so the overall time spent here must be kept as short as possible. To do so, a combination of hotplate and peltier is used for additional heating power near the Ac melting point. After filling, the sample is cooled at a rate $5\,^{\circ}\mathrm{Cs}^{-1}$ and any excess DBT/Ac that is not deposited in the channels is cleaned off with toluene. The correct cooling rate is vital for obtaining stable DBT. Too fast and the Ac crystal becomes highly disordered, leading to poor DBT stability. Too slow, and impurities in the Ac are driven towards the edges of the crystal, resulting to DBT close to surface edges and therefore poor stability.

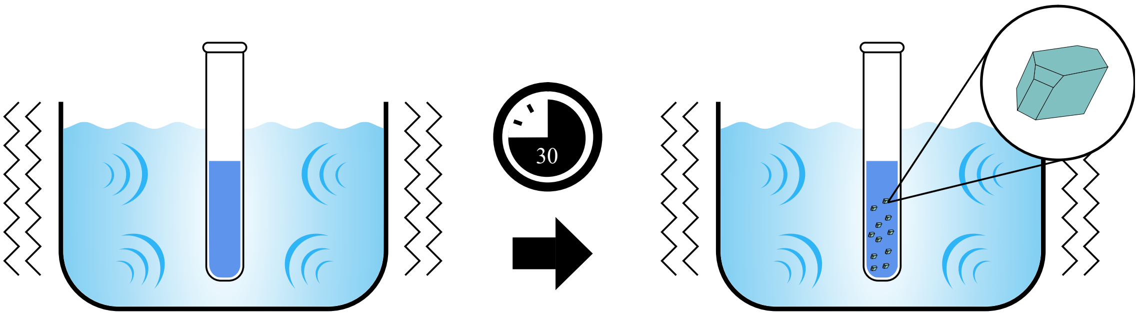

Figure 3.4: Diagram detailing the dibenzoterrylene (DBT) doped anthracene (Ac) nanocystal growth procedure. 250 μL of DBT/Ac in acetone/toluene solution is added to 5 mL of distilled and degassed water. The combined solution is then sonicated for 30 minutes at 37 kHz, leading to the formation of nanocrystals.

This growth method produces a broader inhomogeneous broadening than co-sublimated crystals, equal to 4 nm with a centre wavelength around 783 nm, though the central wavelength shifts to longer wavelengths for smaller channels. Provided the filled channels are wide enough, the DBT shows good spectral stability, with photon emission aligned predominantly in one direction (most likely the Ac b-axis though this has not been confirmed) [315]. Since the capillaries can be used to integrate DBT molecules with photonic structures, the collection efficiency can be larger than for bare co-sublimated crystals.

Re-precipitation growth

The re-precipitation growth method [316] forms crystals with side lengths ranging from sub-micron to 100 nm, ideal for integration into photonic structures. Firstly, a solution of DBT in toluene is added to Ac in acetone. Through varying the concentration of DBT in the toluene, the doping in the final crystal can be adjusted. The combined solution is added to degassed and distilled water, which is then placed inside a sonication bath, where the acoustic waves form cavities in the solution that promote crystal growth. The high frequency of the cavity formation results in a high rate of nanocrystal formation in the solution [317] and the procedure is illustrated in Fig. 3.4. These crystals can then be filtered to control the final size distribution of the nanocrystals. The final filtered solution is deposited onto a substrate and left to evapourate, leaving behind solid nanocrystals. Just as for crystals grown through co-sublimation, a 200 nm layer of PVA is applied to protect the crystals and help adhere them to the substrate surface. However in contrast to macroscopic crystals, nanocrystals require PVA to produce narrow emission at cryogenic temperatures, due to an increase in surface effects [311].

Typical concentrations of DBT in toluene used are $10-25\,\mu$M, which is added to 10 ml of 5 mM Ac in acetone. Of the resulting solution, $250\,\mu$L is added to 5 mL of degassed, distilled water, which is then sonicated at 37 kHz for 30 min at a temperature of 50 °C. Without filtering, the nanocrystals vary from sub-micron down to ~ 100 nm in size.

Nanocrystals show a similar inhomogeneous broadening and center wavelength to the melt growth [311]. Compared to the co-sublimated crystals, they also demonstrate an improved collection efficiency due to less internal reflection. Because of their small size, the doping of DBT can be reduced to the point of having one DBT molecule on average per nanocrystal.

Rather than applying a coating of PVA, the nanocrystals can instead be coated with a polymethyl methacrylate (PMMA) shell, during the sonication growth [311]. The resulting nanocapsules do not require coating with PVA for protection or to achieve narrow linewidths at cryogenic temperatures. The added PMMA shell results in the nanocapsules having a larger size than uncoated nanocrystals, ranging from around 500 nm to 1500 nm, with a mean of 960 ± 20 nm, which is around a factor two increase in particle volume. It may be possible to reduce the PMMA thickness and thus the size of the nanocapsules, while still maintaining the advantages that come with the polymer shell.

3.1.2 Tuning

Due to the differing local environments around each DBT molecule, the photon emission from two different DBT molecules will be spectrally distinguishable. The resulting overall distribution of emission frequencies for the entire ensemble is termed inhomogeneous broadening[1]. We would like a method that allows us to vary the emission frequency of a DBT molecule, without affecting any other optical properties, in order to compensate for this spectral randomness.

---

[1] Note that this does not mean that the lineshape of an individual emitter is broadened, just that the ensemble will display a distribution of emission frequencies. Broadening of an individual emitters lineshape, such as through interactions with surrounding phonons leading to dephasing, is referred to as homogeneous broadening.

Also, for interfacing molecules with other systems, such as an ensemble of atoms, control over the emission frequency could be advantageous to improve the coupling of the two systems.

DC-Stark tuning

Applying an electric field causes the electronic states of an emitter to change due to a modification of the overall Hamiltonian. This can be done using a DC electric field, or an AC electric field as is the case for light. Here we will only discuss the application of DC electric fields, but we will come back to AC Stark tuning when considering atomic quantum memories in Chapters 5 and 6.

Applying a static external electric field E_{DC}, modifies the molecule Hamiltonian H_{mol} as in Chapter 2,

$$\begin{aligned} H &= H_{\mathrm{mol}} + H_{DC} \\ H &= H_{\mathrm{mol}} - \hat{\boldsymbol{\mu}} \cdot \boldsymbol{E}_{DC} \,. \end{aligned} \tag{3.1}$$

Provided the perturbation is small compared with the electric fields of the bound atoms, we can find the shift in energy levels by second-order perturbation theory,

$$\Delta E_j = -\boldsymbol{d}_j \cdot \boldsymbol{E}_{DC} - \frac{\hat{\boldsymbol{\alpha}}_j}{2} \cdot |\boldsymbol{E}_{DC}|^2 \tag{3.2}$$

with $\boldsymbol{d}_j$ the permanent dipole-moment and $\hat{\boldsymbol{\alpha}}_j$ the polarisability tensor, for the j'th state. The two terms in Eq. 3.2 result in a linear and quadratic Stark shift respectively.

We are interested in the relative frequency shift of the ground and excited singlet states in DBT, which is given by the difference in permanent dipole-moments ($\delta\boldsymbol{d} = \boldsymbol{d}_1 - \boldsymbol{d}_0$) and polarisabilities ($\delta\hat{\boldsymbol{\alpha}} = \hat{\boldsymbol{\alpha}}_1 - \hat{\boldsymbol{\alpha}}_0$),

$$\Delta\omega = -\frac{\delta\boldsymbol{d}}{\hbar} \cdot \boldsymbol{E}_{DC} - \frac{\delta\hat{\boldsymbol{\alpha}}}{2\hbar} \cdot |\boldsymbol{E}_{DC}|^2 \,, \tag{3.3}$$

where 0 labels the ground state and 1 the excited state. For the ZPL transition in DBT, $\delta\boldsymbol{d} \approx 0$ as DBT is centrosymmetric and the two states involved have a well defined parity, leaving us with a predominantly quadratic Stark shift [302].

The Stark coefficiencts of DBT in Ac have previously been measured [302] where the electric

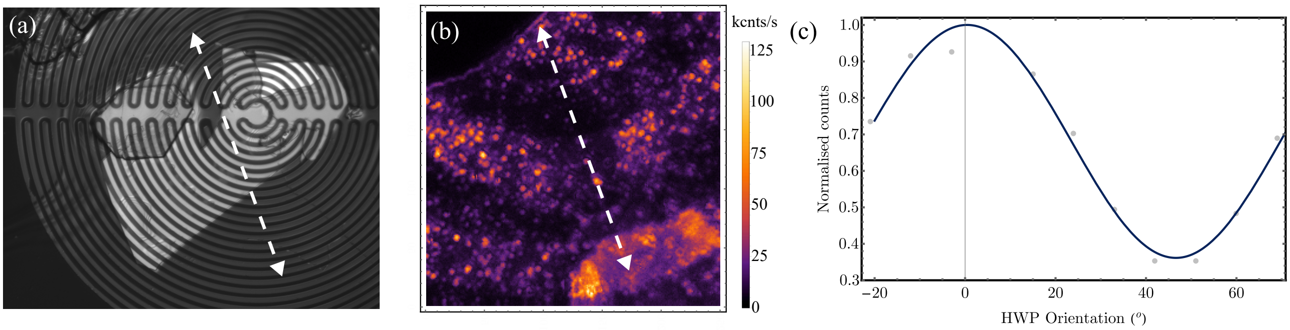

Figure 3.5: (a) White light image showing a co-sublimated crystal (lighter portion of the image) on top of interdigitated spiral electrodes, with the b-axis indicated by the white dashed line. (b) Confocal raster scan of small region of the electrodes. Bright spots correspond to fluorescence from DBT and the white dashed line indicates the direction of the b-axis. (c) Normalised counts averaged over a raster scan, plotted against half-wave plate (HWP) angle θ and fitted with a $\cos^2(\theta)$ curve with the additional of an offset.

field was applied at an angle of 60° to the b-axis, measuring an average scalar polarisability of $-0.4\,\mathrm{MHz}/(\mathrm{kVcm}^{-1})^2$. A large tuning range has also been shown over hundreds of GHz for DBT molecules embedded in a PVA film by having electrodes separated by only $\sim 600\,\mathrm{nm}$ [132].

Here we aimed to map out the dependence of the polarisability tensor on the relative angle between the static electric field and the b-axis of the crystal. To do so, we placed a highly doped Ac crystal, grown using cosublimation, onto a substrate consisting of interdigitated gold circular electrodes (ED-IDRA1-Au, Micrux) and applied a layer of PVA on top. By selecting molecules at different positions along the curved electrodes, we were able to vary the relative angle between the electric field and the b-axis. Shown in Fig. 3.5a is a white light image of the electrodes with the Ac crystal placed on top and the direction of the b-axis indicated - determined through averaged fluorescence polarimetry measurements described later. The sample was cooled to 4.7 K in a closed cycle cryostat (Cryostation, Montana Instruments) so as to be able to spectrally distinguish multiple molecules occupying the same location.

A raster scan across a portion of the electrodes using a confocal microscope of the same design described in Chapter 2, is shown in Fig. 3.5b . A three axis positioning system (ANP101, attocube) inside the cryostat allowed us to reposition the sample. Optical access to the sample used an objective lens with a numerical aperture (NA) of 0.75 and focal length 1.65 mm (LD EC Epiplan-Neofluar, Zeiss). For an excitation beam of diameter 1.5 mm, this objective lens results in a beam waist at the sample of $\sim 275\,\text{nm}$. The excitation beam was provided by a continuous wave (cw) laser (Solstis, Msquared) which was set to 783.5 nm and filtered through a $780 \pm 10\,\text{nm}$ band pass filter (Thorlabs). Each of the two lenses used in the 4f-configuration had a focal length of 250 mm. The collected light was filtered through a combination of 792 nm and 800 nm longpass filters (Chroma Technolgies) and focused by an asphere (Thorlabs) with focal length 10 mm into a multi-mode fibre of core diameter $62.5\,\mu\text{m}$ (Thorlabs)[2]. A silicon avalanche photodiode (APD, Count T, Laser Components) was used for photon detection.

We first performed polarimetry on the sample to determine the orientation of the b-axis. By performing raster scans across a portion of the electrodes and rotating the half-wave plate (HWP) in the excitation arm, we could observe the total collected fluorescence vary with angle. We excited with a low power of 154 nW, allowing the fluorescent count rate, given by Eq. 2.16, to be approximated by,

$$R \sim \cos^2(\theta)\,, \tag{3.4}$$

where θ is the angle between the laser polarisation and transition dipole moment of the DBT. The measured fluorescence as a function of HWP angle is plotted in Fig. 3.5c, showing a clear $\cos^2$ dependence, along with an offset. This allowed us to determine the orientation of the b-axis in Fig. 3.5a and b. The required offset results from unpolarised background light, such as scatter from the gold surface.

A stable molecule was identified at 783.58 nm and linescans were performed as the laser power was increased. The linescans at each power were fitted with lorentzians (Fig. 3.6a) to determine their widths, peak heights and background. Fig. 3.6b shows the maximum count rate as a function of power, which when fitted to a saturation curve (Eq. 2.17) gives $R_\infty = 275 \pm 11\,\text{kcnts}^{-1}$ and a $p_{sat} = 640 \pm 60\,\text{nW}$, where $S = p/p_{sat}$ for laser power p. After taking into account losses through the setup, this corresponds to $I_{sat} = 0.9 \pm 0.1\,\text{Wcm}^{-2}$. The linewidth as a function of power is shown in Fig. 3.6c, which can be fit using Eq. 2.18 to find a zero-power linewidth of $2\Gamma_2 = 290 \pm 20\,\text{MHz}$ and $p_{sat} = 620 \pm 50\,\text{nW}$, consistent with the value obtained from the saturation fit.

---

[2] For the objective lens and asphere used here, a dipole emitter would occupy $4\,\mu\text{m}$ in the image plane and so no additional axial resolution is provided by the the $62.5\,\mu\text{m}$ pinhole.

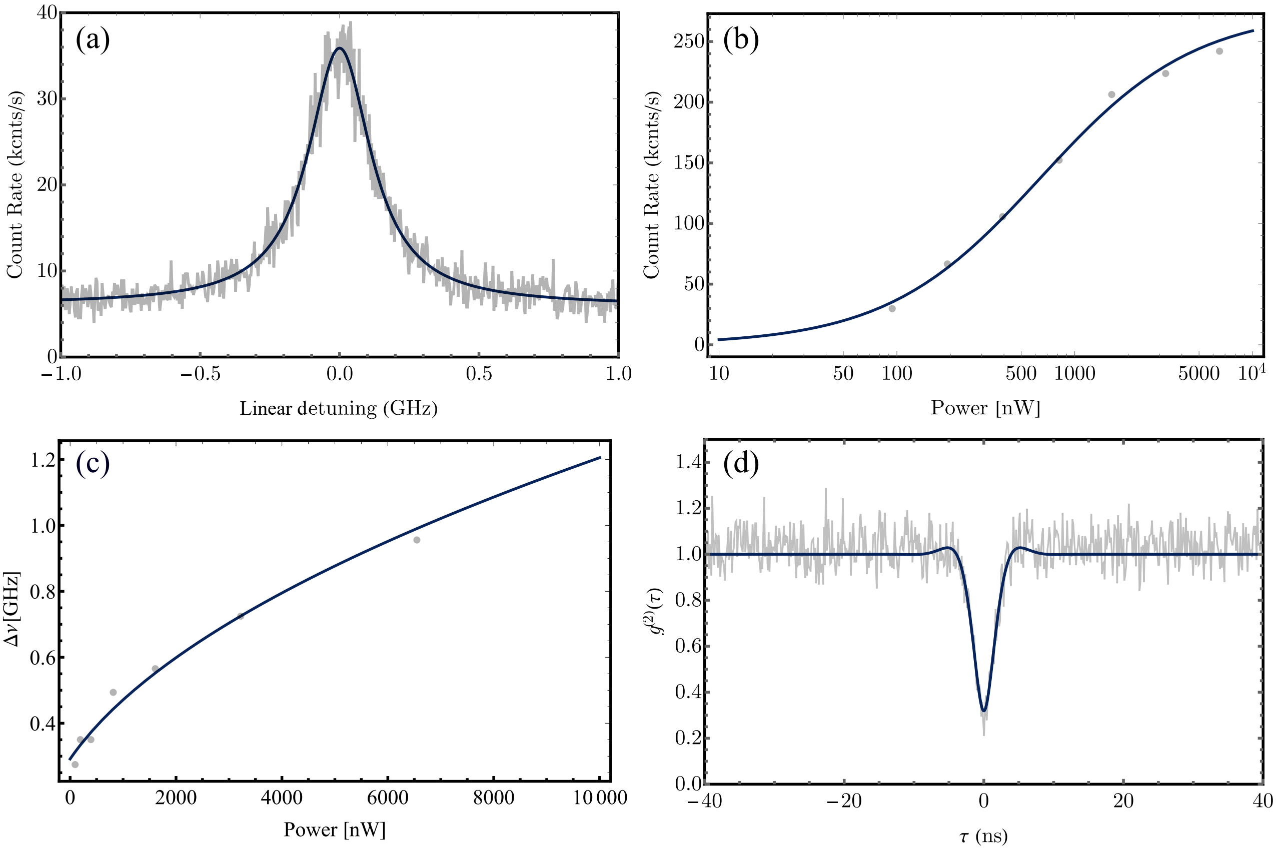

Figure 3.6: (a) Measured fluorescence (grey) as a function of laser detuning, fitted with a Lorentzian (dark blue). (b) Peak count rate (grey) as laser power is increased, determined from Lorentzian fits to linescans. Eq.2.17 is fitted (dark blue) with $R_\infty = 275 \pm 11\,\mathrm{kcnts}^{-1}$ and $p_{sat} = 640 \pm 60\,\mathrm{nW}$. (c) Resonance linewidth (grey) as laser power is increased, determined from Lorentzian fits to linescans. Eq 2.18 is fitted (dark blue) with $2\Gamma_2 = 290 \pm 20\,\mathrm{MHz}$ and $I_{sat} = 0.87 \pm 0.07\,\mathrm{Wcm}^{-2}$. (d) Second-order correlation function $g^{(2)}(\tau)$ (grey) taken with $I = 1.35\,\mathrm{Wcm}^{-2}$, corresponding to an $S = 1.5$, showing characteristic anti-bunching dip, along with a small amount of Rabi oscialltion. Fitted is Eq. 2.26 (dark blue), with $S = 1.5$ and $2\Gamma_2 = 290 \pm 20\,\mathrm{MHz}$ held constant.

We then measured the second-order correlation function $g^{(2)}(\tau)$ with a power of 962 nW, corresponding to $S = 1.5$. Fig. 3.6d shows the measured $g^{(2)}(\tau)$ which was fitted with Eq. 2.32 after convolving with a Gaussian characterising the 320 ps detector timing-jitter. Γ_2 and S were determined from the power-broadening measurements, leaving just Γ_1 and $\mathcal{V}$ as free parameters. The data in Fig. 3.6d has been normalised to 1.0 in the wings of the plot, assuming that for photons emitted after many lifetimes of the molecule, there will be no correlation with photons emitted at zero time[3]. We measured a $\Gamma_1 = 52.9 \pm 0.3\,\mathrm{MHz}$, corresponding to a lifetime of $3.0 \pm 0.2\,\mathrm{ns}$, and $\mathcal{V} = 70\%$. Typically for an isolated DBT, we would expect to measure a higher visibility. The deviation from unity is likely to stem from the large doping concentration, leading to some neighbouring molecules being weakly excited and some of the emitted light being collected. Additionally, the gold electrodes resulted in a larger background which could also contaminate the $g^{(2)}(\tau)$ measurement. The ratio of $\Gamma_1/2\Gamma_2 = 0.37$ is also lower than what would be typically measured in this cryostat, and implies a temperature at the molecule of $\sim 8.5\,\mathrm{K}$ [202]. The extra heating is likely to have originated from the greater thickness of the electrode sample compared to the usual sample wafers used, as well as the electrode wires adding additional heat load. This is supported by the distribution of linewidths shown in Fig. 3.7a where we see a mean linewdith of 371 MHz after fitting with a Weibull distribution [307].

To investigate Stark tuning, we first picked a point on the sample, in between two electrode annuli, and scanned a large portion of the inhomogeneous broadening ($780-784\,\mathrm{nm}$) at a power of $\sim 170\,\mathrm{nW}$ ($S < 1$). We selected the largest and most isolated peaks, and repeatedly scanned 5 GHz either side of each peak as the electrode voltage was varied from $-30\,\mathrm{V}$ to $30\,\mathrm{V}$ in steps of 5 V. An example density plot of laser frequency against applied voltage in shown in Fig. 3.8a, where we can see two initially separated molecules which can be tuned on resonance with one another due to their different tuning rates. We see no evidence of linewidth broadening with voltage, implying no current flow between the electrodes which would otherwise cause heating.

---

[3] Note that if there were significant blinking of the molecule emission, such as due to significant probability of inter-system crossing to the triplet state, and we measured the second-order correlation function to timescales comparable to the triplet state lifetime, we would see anti-bunching in the wings of the plot and therefore normalising the wings of the plot to 1.0 would be invalid. Also if significant Rabi oscillations were present in the entire plot, it would not be valid to normalise the wings to 1.0.

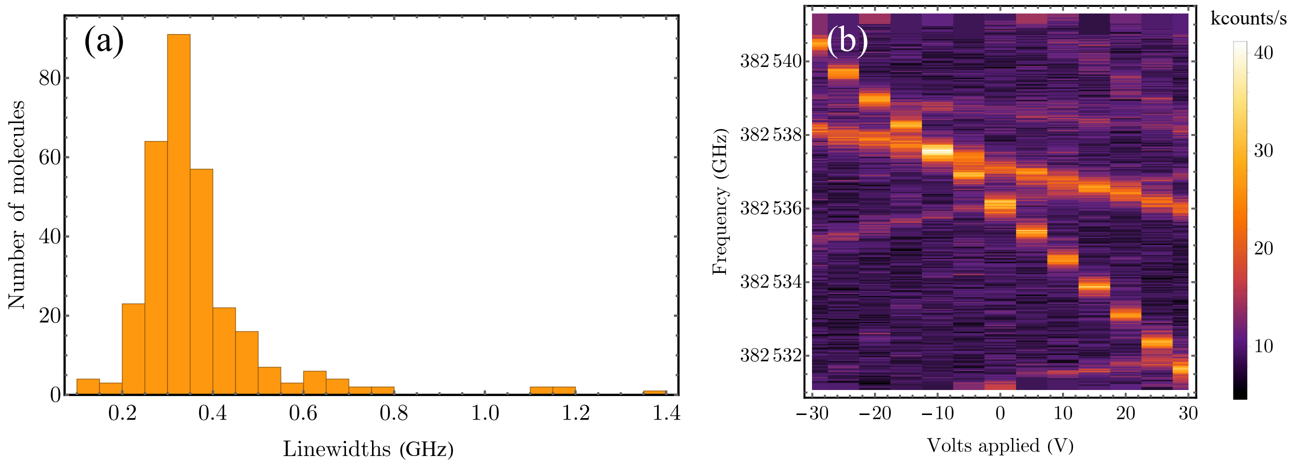

Figure 3.7: (a) Zero-power linewidths for 409 DBT molecules. (b) Density plot showing two bright molecular resonances tuning with applied voltage. The molecules are initially separated but can be spectrally overlapped by applying approximately −10 V.

Each molecular emission was fit with a 2D Lorentzian of the form,

$$L_{2D} = \frac{A}{(\nu - [kV^2 + mV + d])^2 + \left(\frac{\Gamma_2}{2}\right)^2} + B\,, \tag{3.5}$$

where A is the amplitude, ν is the frequency in hertz, V is the applied voltage and B is the background. The term in the square brackets is the quadratic shifting of the central frequency, with coefficients k, m and d characterising the curve, gradient and zero voltage central frequency respectively.

We found that the fit was only successful if good initial parameters, particularly for m, were provided. The parameters A, B, d and Γ_2 could be determined from one dimensional Lorentzian fits to the 0 V case. For a starting point for m, we performed a modified Radon transform, see Appendix A. Overall, curves were fitted to a total of 409 molecules.

We then had to convert voltage to the local electric field at the molecule. Each annulus on the electrode sample was 10 μm wide with a 10 μm gap. A simulation of the electric field between the annuli and up to a 1 μm above the sample (the typical thickness of a co-sublimated crystal) showed an electric field entirely parallel to the crystal plane, provided molecules were not chosen on the edge of the electrodes, and that the electric field strength was constant across the gap. The strength of the field was also found to agree with the simple relation $|\boldsymbol{E}| = V/d$

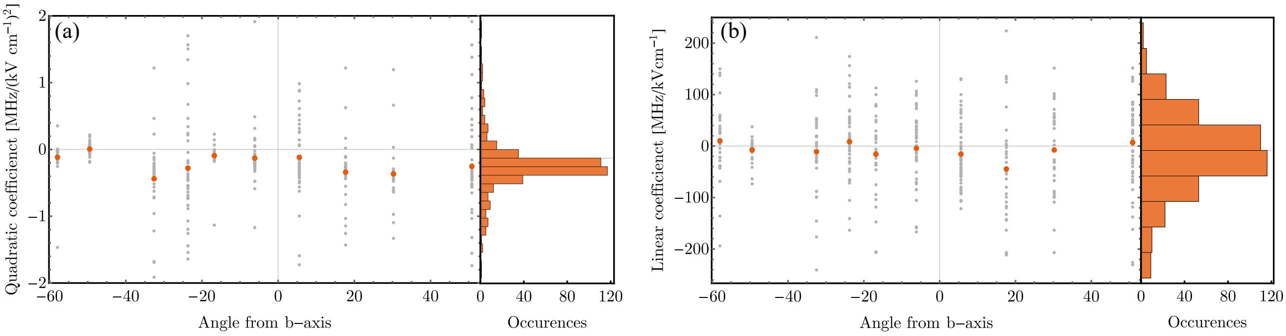

Figure 3.8: (a) Plot of quadratic Stark coefficients against the angle of applied electric field relative to the b-axis of the antracene (Ac) crystal. Orange points represent the mean of the fitted coefficients at that angle, shown in grey. On the right is a histogram showing the total distribution. (b) Plot of linear Stark coefficients against the angle of applied electric field relative to the b-axis of the Ac crystal. On the right is a histogram showing the total distribution.

where d is the distance between the electrodes. In the calculation of the electric field, we have ignored any local field correction due to interaction of the Ac matrix with the external field. The resulting histograms of quadratic and linear Stark coefficients are shown in Fig. 3.8a and Fig. 3.8b respectively, along with plots showing the angular dependence.

The linear components of the Stark shift are centered around zero, as is to be expected for a molecule with no permanent dipole moment. The FWHM of a fitted normal distribution is $195 \pm 7\,\mathrm{MHz/kVcm^{-1}}$, is a factor of two larger than that reported in the literature [302], possibly due to a more inhomogeneous crystal or becuase of the larger range of angles considered. This corresponds to dipole-moment changes of up to 390 mD. The quadratic Stark components centre about $-0.21 \pm 0.06\,\mathrm{MHz/(kVcm^{-1})^2}$ with a width of $2.87 \pm 0.09\,\mathrm{MHz/(kVcm^{-1})^2}$, where the centre is consistent with values reported in the literature, though the width is roughly an order of magnitude greater.

For the relative angle between the electric field and b-axis, the linear Stark coefficient shows little angular dependence, although a non-zero mean is observed for angles around ±17°. The larger mean for +17° is likely to be a result of outliers in the distribution and so is probably an exaggerated effect. The quadratic coefficient shows a small symmetrical increase when the electric field is either side of the b-axis - though the variation in the data obscures any trend. We observed no correlation between quadratic and linear coefficients. Additionally, we saw

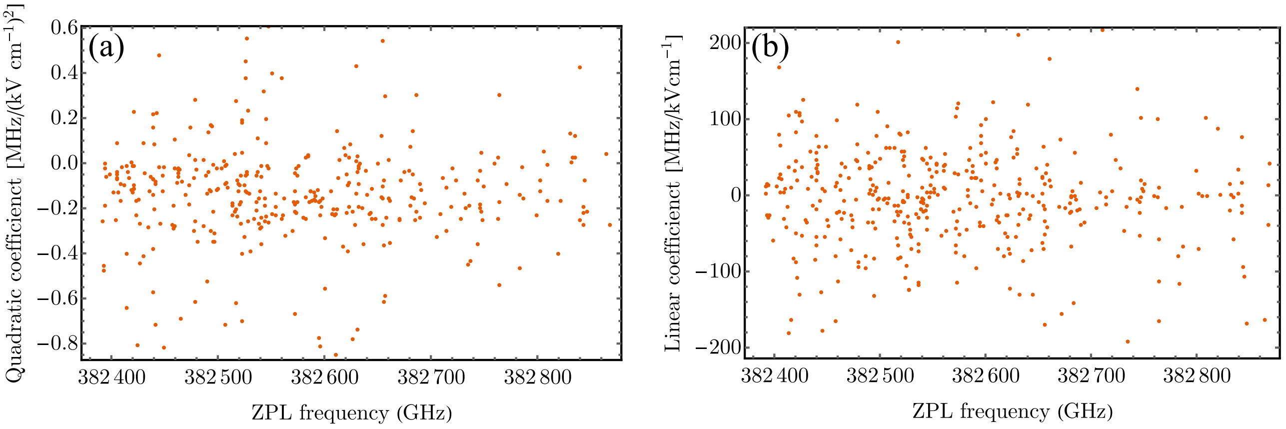

Figure 3.9: (a) Plot of quadratic Stark coefficients against the central emission frequency. (b) Plot of linear Stark coefficients against the central emission frequency.

no correlation, over the > 400 GHz range of central frequencies investigated, between central frequency and linear or quadratic coefficients, as shown in Fig. 3.9. The width of the ZPL also had no relation to any of the coefficients.

Strain

An alternative method to Stark tuning is to apply strain to the Ac crystal. Here the deformation of the molecule and surrounding host matrix acts to alter the relative energy gap between the ground and excited states. In previous work, the effects of strain have been studied through increasing the pressure surrounding the host crystal [318, 319], and through modulating the fluorescence through acoustic waves [320]. In this work, published in Ref. [135], we adhere a co-sublimated DBT/Ac crystal to a 150 μm polished glass layer with PVA, which was attached to a bending piezoelectric strip (EB-T-320, RS PRO). Application of a voltage across the piezoelectric strip causes the Ac crystal to compress, in the case of positive voltage, or decompress, in the case of negative voltage, as depicted in Fig. 3.10b. In order to isolate any potential Stark effect from strain induced tuning, a second strip was made up, identical to the first, except that it had been heated to 320 °C for two hours prior to placing a DBT/Ac crystal on top. The heat treatment acts to depolarise the piezoelectric material, thereby removing any voltage induced bending motion.

We cool the sample down to 2.6 K in a helium bath cryostat (OptiStat, Oxford Instruments) with the top side of the crystal grounded to the inner side of the chamber. A cw excitation laser (Solstis, MSquared) is set to 780 nm and passes through a 785 ± 5 nm band-pass filter (Semrock). For the 4f-lens arrangement, both lenses had focal lengths of 150 mm. An objective lens with a NA= 0.7 and focal length 3.1 mm (C330TMD-B, Thorlabs) resulting in a excitation spot size of 370 nm at the sample. In the collection arm, we placed a 800 nm long pass filter (Semrock) before coupling the fluorescence into a 62.5 μm core multi-mode fibre (Thorlabs) and detecting with a silicon avalanche photodiode (APD, Laser Components, Count T).

To determine the relative orientation of the Ac b-axis to the bending axis of the piezo, we monitor the average fluorescence (taken from four bright spots), as the HWP angle is stepped. We find the b-axis of the Ac crystal to lie $\sim 10^\circ$ to the piezo axis. For verifying the presence of narrow ZPLs, we perform power broadening measurements for 32 molecules. A histogram of zero power linewidths is plotted in Fig. 3.10a. We fit the results with a Weibull distribution and find a mean value of 57.2 MHz with a standard deviation of 17.4 MHz, consistent with Fourier-limited emission.

In Fig. 3.10c we see an example of tuning molecules while applying a positive voltage (compression). In contrast to Stark tuning, we observe only linear tuning over the voltage range measured, with each molecule showing a similar tuning rate. Compression of the crystal leads to a red shifting of the ZPLs, and decompression to a blue shifting. A histogram of tuning rates is shown in Fig. 3.10d. The distribution is best fit by a Student T distribution (used for modelling a small number of samples taken from a normal distribution) with mean -10.42 ± 0.05 MHz/V and a width of 0.45 ± 0.05 MHz/V. Also shown in Fig. 3.10d are the tuning rates from the inactive piezo strip. There is very little variation in the ZPL frequency, with a mean of -0.32 ± 0.07 MHz/V and a width of 0.30 ± 0.06 MHz/V, when fitted with the same distribution as the active sample. These results are consistent with density functional theory simulations performed by Anastasios Fasoulakis [135].

Laser induced

In Colautti et al. [321] a further scheme for tuning the ZPL of DBT was demonstrated that did not require any additional sample fabrication beyond depositing DBT containing Ac crystals on a substrate. By exposing a molecule to intense laser light the ZPL frequency was observed to

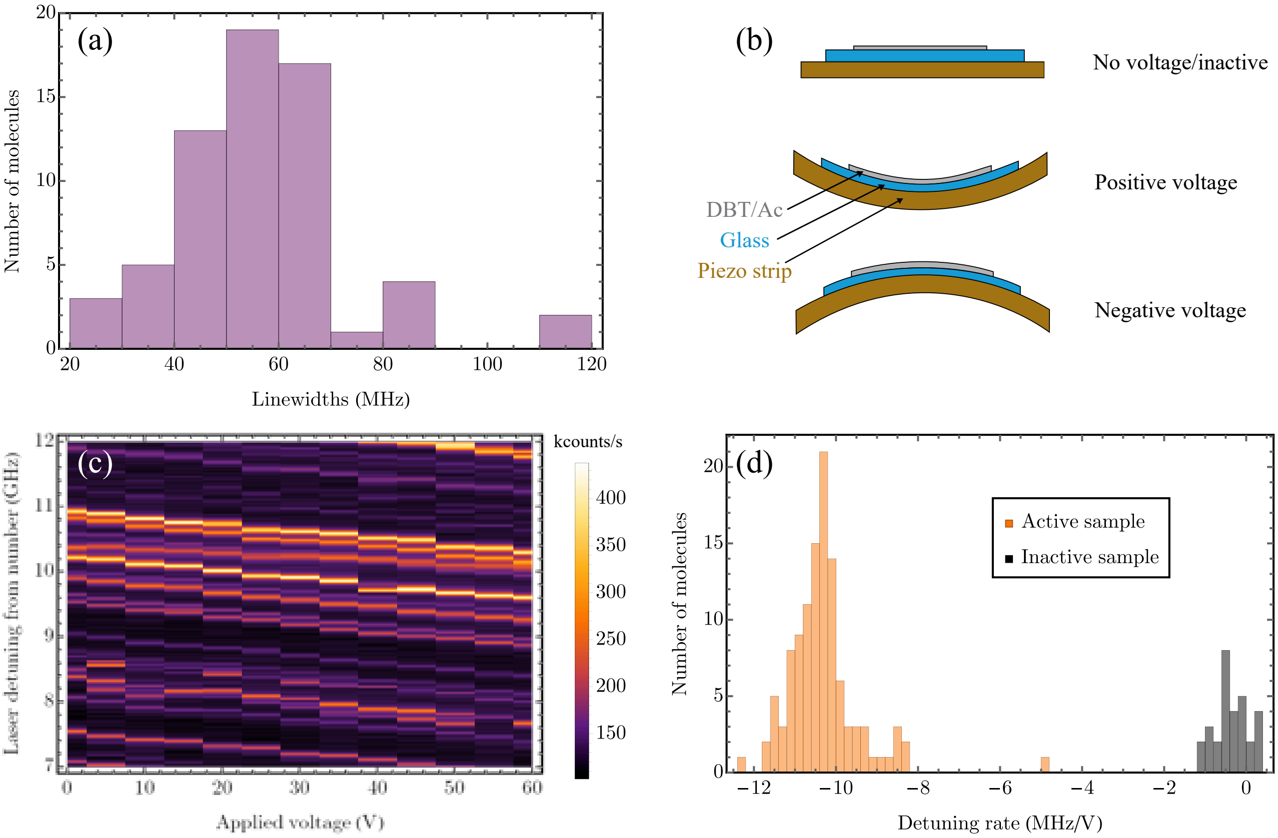

Figure 3.10: (a) Histogram showing the zero power line widths for 32 Dibenzoterrylene (DBT) molecules with no strain applied, extracted from power broadening measurements. (b) Illustration of the mechanism for strain, where application of a positive voltage caused the active piezoelectric strip to bend and compress the DBT and Anthracene (Ac) crystal. On the other hand, application of a negative voltage resulted in a decompression of the DBT/Ac crystal. (c) Density plot showing the intensity of the collected light as a function of laser detuning, while the voltage applied to the piezoelectric strip was varied. (d) Histogram showing the tuning rates for the active and inactive piezoelectric strip.

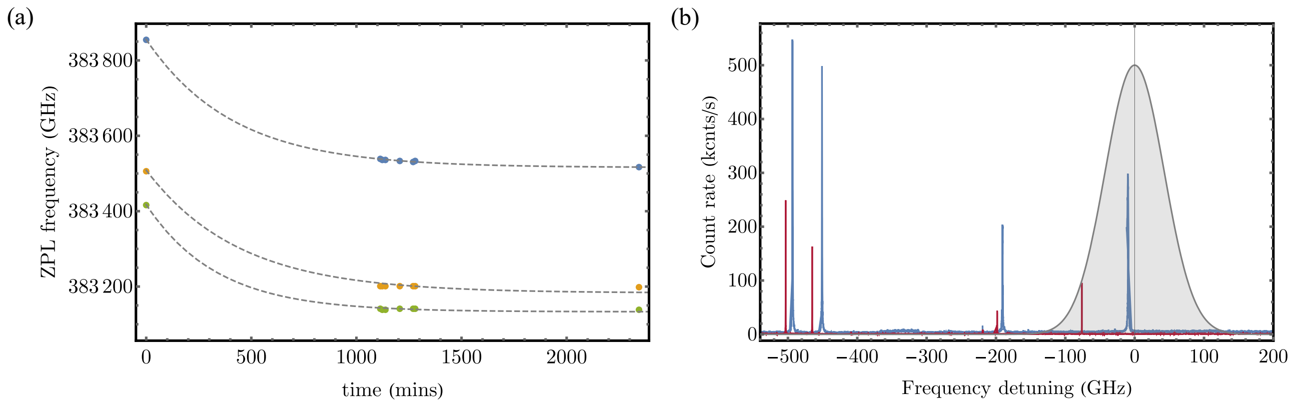

Figure 3.11: (a) Plot showing the central frequency of four dibenzoterrylene (DBT) molecules, excited with the same laser spot at 390355 GHz (768 nm) over two days. The dashed grey curves are fitted decaying exponentials. (b) Spectra of a different set of four DBT molecules, where the initial spectra is shown in blue. In red, the spectra after 20 minutes of exposure with a resonant pulsed laser centered on 384005 GHz (780.7 nm) with a full width at half maximum bandwidth of 100 GHz, shown in grey, where we have normalised the peak power to 500 kcnts/s. The pulsed laser peak power was set to 98 μW, corresponding to full population inversion of the molecule located at ~ 0 GHz detuning.

red shift over time. The exact mechanism isn't fully understood, but the authors of Ref. [321] suggest a two photon transition, which results in one of the outer π-electrons from DBT being ejected into the surrounding Ac matrix. The resulting hole in the DBT is filled via a different electron donated from the Ac crystal. The final state is a separated hole and electron in the Ac, far enough apart such that the recombination probability is very small, leading to an extremely long lifetime. The resulting charge separation shifts the ZPL through the Stark effect. In this study, the authors measured the ZPL over the course of 250 minutes of exposure.

We performed preliminary measurements, with the same confocal microscope used for the Stark tuning measurements, to determine whether the laser-induced frequency tuning saturates. Four DBT molecules, spatially overlapped but with different ZPL wavelengths, were exposed with 768 nm light over two days. Shown in Fig. 3.11a we see a clear saturation behaviour and that the frequency shift appears to be stable. We also observed no significant change in the ZPL widths.

The shift occurs for both resonant and non-resonant pumping, with resonant appearing to require less laser power, supporting the claim that it is a two photon transition. We carry out resonant pulsed laser excitation with a 100 GHz wide pulse at 780.3 nm. The peak pulse power was increased until a resonant molecule achieved full population inversion (98 μW) and the sample was left exposed for 20 minutes. The spectra before (blue) and after (red) are shown in Fig. 3.11b, and the laser pulse spectral shape is shown in grey. We see tuning for all molecules in the scan range, with the largest tuning for the resonant molecule. Contrary to the cw case, we see a decrease in counts for the exposed DBT, though this may be due to non-optimal realignment when switching between laser sources.

While laser induced tuning has the potential to be an extremely useful tool, allowing multiple emitters to be tuned onto resonance without the need for any additional sample fabrication, it is a problem for experiments requiring repeated excitation over the course of hours. For pulsed excitation, it is possible that decreasing the bandwidth of the excitation pulse, thereby allowing lower peak intensities to be used, could allow for full population inversion while keeping tuning of the molecule ZPL to a minimum.

Alternatively, with an improved understanding of the mechanism responsible for the tuning, additional lasers or DC electric fields could be employed to encourage recombination of the separated electron-hole pair. Another possible solution is other host crystals with lower charge mobility, thereby preventing the charge separation.

3.1.3 Photonic Structures

The dipole emission pattern of DBT has a poor overlap with single mode fibres or waveguides, which are needed for interfacing single photon sources with fibre networks or photonic processing elements on a chip. One solution is to use nanophotonic structures to modify the photonic environment seen by an emitter. This results in a redirection of the emission pattern, and can cause a speed up in the decay rate on the ZPL.

There are a huge variety of nanophotonic structures currently being considered. A common theme amongst all of them is that, for an efficient coupling of an emitter to the photonic structure, we require a good overlap between the emitter and the mode of the structure. Therefore, we require the emitter to be well placed inside the structure. Recent work in the group demon-

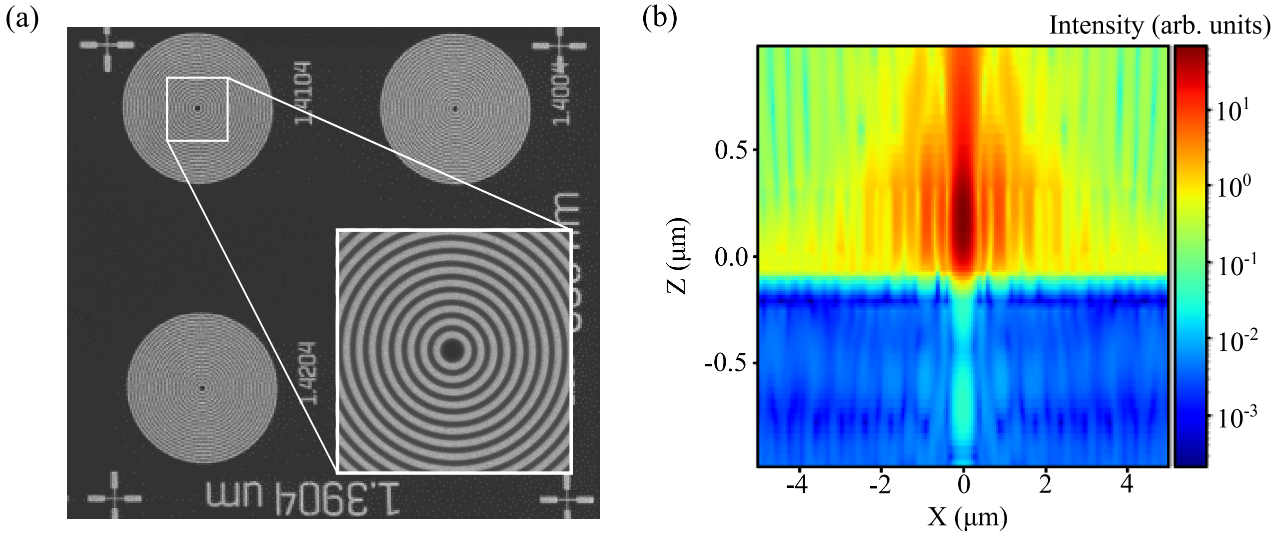

Figure 3.12: (a) Scanning electron microscope image showing several bullseye gratings. Also shown is a zoom in of the centre of one of the gratings. (b) Simulated electric field as a function of distance from the central disk (X) and height above the grating (Y). The electric field intensity is plotted on a log scale in arbitrary units.

strated coupling of DBT molecules to waveguides using the melt growth method [207], where capillaries were made to intersect with the middle of the waveguides. Through filling the capillaries with highly doped DBT/Ac, the probability of finding a DBT molecule well coupled to the waveguide could be increased.

Another promising photonic structure is the circular Bragg grating or bullseye grating, where a scanning electron microscopy (SEM) image is shown in Fig. 3.12a. Bullseye gratings feature concentric rings of material with alternating refractive index, which act as an effective mirror. The resulting cavity causes a modest enhancement to the decay rate but efficiently redirects emission out of the plane into a Gaussian mode, which can be efficiently coupled to a single mode fibre [153,322,323,324]. An example of the electric field intensity as a function of distance from the centre disk and height above the disk, is shown in Fig. 3.12b. For an efficient coupling of the emitter to the bullseye grating, the DBT molecule should be placed in the centre of the structure, where the electric field intensity is at its highest.

One way of ensuring that DBT molecules are located at the centre of the bullseye, is to first grow DBT doped Ac nanocrystals, locate a DBT molecule, and then fabricate the structure around the emitter. Preliminary work, detailed in Ref. [311] aimed to coat the nanocrystals with a thin PVA film and use electron beam lithography to pattern bullseye gratings into the PVA around the nanocrystals. Repeated exposure to SEM imaging resulted in no narrow emission from DBT molecules. However, for a sample that was imaged a single time using SEM, narrow emission from DBT persisted. Bullseye gratings were patterned around DBT/Ac nanocrystals. While the bullseye grating was not successively centered on the nanocrystal, therefore providing no emission enhancement, the DBT molecules showed no discernible difference in their optical properties when compared to unexposed DBT/Ac. The DBT molecules also survived thermal cycling between cryogenic and room temperature, though a $\sim 4\,\mathrm{GHz}$ shift in the ZPL was observed [311].

Perhaps a better approach is to incorporate nanocrystals into bullseye structures made of materials with a higher refractive index, such as titanium dioxide ($\mathrm{TiO_2}$), with a refractive index of around 2.35, compared with the PVA refractive index of 1.5. A higher refractive index results in a greater confinement of the electric field in the guided mode. However, in sputtering $\mathrm{TiO_2}$ on a sample, we require temperatures upwards of $300\,^{\circ}\mathrm{C}$ and high vacuum [325]. A layer of PVA would prevent the inclusion of the DBT into the $\mathrm{TiO_2}$ structure but nanocapsules (nanocrystals coated in PMMA) allow the structure to be fabricated around them. Initial tests showed that DBT in nanocapsules continued to fluorescence after $\mathrm{TiO_2}$ sputtering, but this was only measured at room temperature and so it remains to be seen whether there is still narrow emission [311].

Alternatively, rather than pattern the structure around the emitter, we could pre-pattern the bullseye and then deposit the DBT doped nanocrystal at the centre of the bullseye. Fabricating channels through the bullseye structure interupts the grating and would reduce the overall efficiency. Moreover, while the melt growth and capillary filling technique confines the DBT/Ac crystal in two dimensions, a filling method with control over all three dimensions is desirable. Here we present a method to deterministically place nanocrystals inside holes fabricated on a substrate, using capillary self-assembly. These holes could be located at the centre of a bullseye grating, allowing the nanocrystal to be placed at the electric field maximum of the bullseye mode (the hole also allows the DBT to sit in the plane of the device, rather than on top of it).

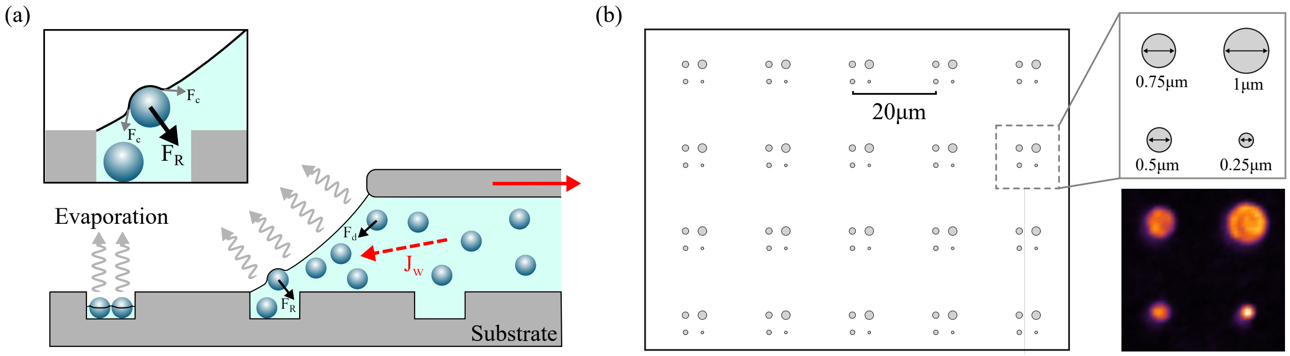

Figure 3.13: (a) Diagram showing capillary filling of holes patterned into a substrate. Through controlling the temperature of the substrate, the convective flow J_w of the suspended particles towards the meniscus can be adjusted. At the meniscus, a capillary force acts on the particle, the direction of which is determined by the angle between the meniscus and the substrate, referred to as the contact angle. (b) Schematic of a chip with holes patterned in an array. On the top right side is pictured the four sizes of holes, with a confocal raster scan below showing fluorescence originating from only within the holes.

Deterministic capillary nanocrystal placement

The general principle is illustrated in Fig. 3.13a, where a droplet of a colloidal suspension is sandwiched between the substrate and a retracting slide. The substrate is heated, allowing the rate of evaporation at the droplet meniscus to be controlled. The evaporation creates a convective flow (J_w) which drives the suspended particles towards the contact line. Depending on the velocity of the retracting slide and hydrophobicity of the substrate, there are two regimes of interest for particle deposition [326, 327, 328]. The first is convective assembly, and occurs when the contact angle is below $\sim 20°$, which typically occurs on hydrophillic surfaces. Here the shallow profile of the meniscus leads to vertical confinement of the colloids. When the solution film reaches a comparable thickness to the colloid diameter, the colloids begin to form a homogeneous layer or multi-layer of closely packed particles.

The second regime is capillary assembly, where the contact angle is $> 20°$ and the meniscus now provides a horizontal force large enough to prevent particles from depositing on a flat substrate. The more hydrophobic the surface, the larger the horizontal force. However, if the meniscus is dragged over a structure such as a hole, the walls of the hole can overcome the horizontal force, leading to selective deposition in only the hole.

For our case, DBT/Ac nanocrystals are suspended in a distilled and degassed water solution.

Several substrates of silicon dioxide were fabricated and coated with a PMMA (hydrophobic) resist into which holes were etched using electron-beam lithography. Each chip consisted of four arrays of holes arranged in a 2 × 2 grid, with each grid separated by $20\,\mu$m. Each array had a side length 1.5 mm and contained grids of 60 × 60 elements, where each element consisted of four holes of diameters: $0.25\,\mu$m, $0.5\,\mu$m, $0.75\,\mu$m and $1\,\mu$m arranged in a square. A schematic of the chip is shown in Fig. 3.13b.

The substrate was mounted on a pelitier heater with thermal grease and preheated to a temperature between $29 - 30\,^{\circ}$C. A solution containing DBT/Ac nanocrystals was filtered through a $0.45\,\mu$m filter and a $250\,\mu$L droplet was placed on the substrate. The top slide was lowered to 500μm above the substrate surface, forming the meniscus. The top slide was retracted at velocities ranging from $0.5\,\mu\mathrm{m\,s^{-1}}$ to $0.75\,\mu\mathrm{m\,s^{-1}}$, using a motorised linear actuator (Newport, 850G-HS). Once the deposition had been completed ($\sim$ 40 minutes), the sample was coated in PVA to prevent sublimation of the Ac.

To determine the filling fraction of the holes and to see how selective the deposition was, we performed room temperature fluorescence confocal microscopy. The holes were first located by white light imaging and a set of four holes were moved to the centre of the scan. We then switched to pulsed laser excitation at 755 nm (Picoquant) which was passed through a 760 nm band-pass filter, a 4f-lens setup with $f_1 = 75\,$mm $f_1 = 250\,$mm and a 0.9 NA objective lens (PlanApo 100x, Nikon) which resulted in a beam waist of 610 nm. The excitation laser was raster scanned over the four holes, the collected fluorescence was filtered through 770 nm and 780 nm long pass filters and collected by a multimode fibre to be detected by an APD. An example raster scan is shown to the bottom right of Fig. 3.13b.

We compared the fluorescence for both DBT containing nanocrystals and nanocrystals without DBT. No fluorescence was observed from the deposition without DBT. We find the best parameters to be a substrate temperature of $31\,^{\circ}$C and retraction speed of $0.75\,\mu\mathrm{m\,s^{-1}}$, though the trend suggests higher temperatures and speeds would perform better, which were not investigated. We observed a constant filling fraction over the array, up until the edge of the chip where the droplet eventually fully evaporated, depositing any remaining nanocrystals.

To investigate the emission properties of the nanocrystals contained within the holes, we cooled the sample down to 5 K in a closed cycle cryostat (Cryostation, Montana Instruments). While fluorescence continued to be observed, no narrow spectral lines were able to be measured as a cw laser was scanned across the inhomogeneous broadening of DBT/Ac. This most likely results from the emission being too broad, due to large amounts of dephasing. Previous measurements in the group have found nanocrystals require a coating of PVA to yield narrow single photon emission. While the samples in these experiments were coated in PVA, the PVA would struggle to surround the nanocrystals deposited in the holes. One solution to this would be to use a less viscous PVA solution, or to instead deposit nanocrystals coated with a PMMA shell.

3.2 Dibenzoterrylene in *para*-Terphenyl

An alternative host material for DBT is *para*-Terphenyl (pT), pictured to the left of Fig. 3.14a, which is another small PAH similar to Ac, with similar physical properties [329]. Some of the first experiments studying single photon emission from pentacene [330] used pT as a host material and later on, single photon emission from terrylene embedded in pT was demonstrated [331]. An energy level diagram of DBT/pT is shown to the right of Fig. 3.14a, which was deduced from the measurements detailed in this section.

The solubility of pT in water and acetone is similar to that of Ac, suggesting that the reprecipitation technique used to grow DBT/Ac nanocrystals can be adapted to grow DBT/pT nanocrystals. We used the same recipe as previously discussed for Ac, but increased the growth time from 30 to 45 minutes. A histogram of pT nanocrystal root mean squared side lengths is plotted in Fig. 3.14b. These were determined using Mathematica image recognition filters to first ascertain the area, the square root of which is displayed. The inset of Fig. 3.14b shows an SEM image of a typical nanocrystal. The side lengths follow a Weibull distribution, which without any filtering gives a mean of 490 nm and a variance of 350 nm. As with Ac, to prevent sublimation of the pT nanocrystals, we applied a layer of PVA, around 150 nm thick.

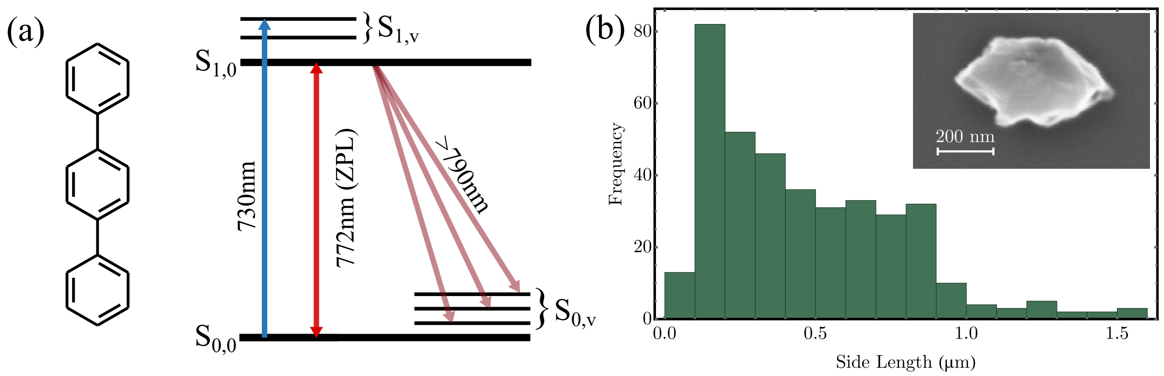

Figure 3.14: (a) On the left, the chemical structure of *para*-Terphenyl (pT), the right shows an energy level diagram of dibenzoterrylene (DBT) in pT. (b) Histogram of pT nanocrystal side length distribution taken from scanning electron microscope images, an example of which is shown in the inset.

3.2.1 Characterisation

Room temperature

To first verify the presence of DBT in the pT nanocrystals, we placed a highly doped sample into the same room temperature confocal microscope used for the hole filling measurements. The molecules were pumped using a cw Ti:Sapphire laser (Solstis, MSquared) at 730 nm with a spot size of 720 nm in order to excite them to a higher lying vibrational state. The resulting red shifted fluorescence was collected and sent through a 750 nm long pass filter to remove the 730 nm light. By scanning the two galvo mirros, we measured a raster scan of the molecules and the fluorescence from a randomly chosen bright spot was sent to a spectrometer (Shamrock 303i with Newton EMCCD, Andor). The obtained spectrum is shown in Fig. 3.15a, where the sharp step at 750 nm is due to the cutoff of the longpass filter (Thorlabs). We find the central wavelength to be 772.1 ± 0.2 nm, which is close to the resonance of the potassium D1 line [332] as well as higher lying transitions in rubidium [333].

To measure the lifetime of the excited state, a 730 nm pulsed Ti:Sapphire laser (Tsunami, Spectra Physics) set to 1 mW was used to excite a bright spot, and the resulting fluorescence was sent to an avalanche photodiode (APD Count-T LaserComponents) and timing card (Hydraharp, PicoQuant) to perform a time-correlated single photon counting (TCSPC) measurement, as described in Section 2.2.3. Fitting the resulting histogram with a decaying single exponential

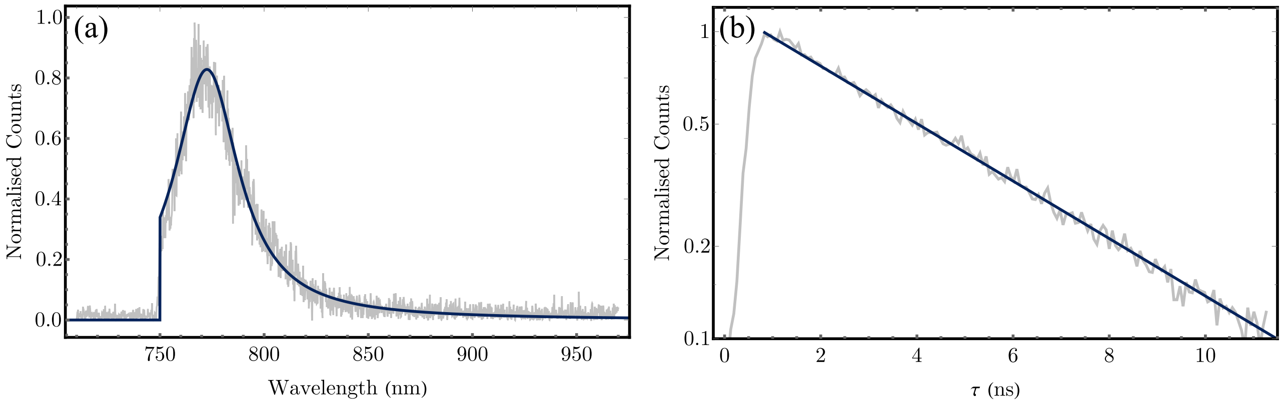

Figure 3.15: (a) In grey is the combined emission for many dibenzoterrylene (DBT) molecules taken at room temperature. The sharp edge at 750 nm is due to a long-pass filter. A fitted Lorentzian is shown in dark blue, where a step function was introduced to model the filter. We find a central wavelength of 772 ± 0.2 nm. (b) Time-correlated single photon counting measurement plotted in grey, measured after excitation of the DBT with a 730 nm laser pulse. The y-axis is on a log-scale and a fitted decaying exponential is shown in dark blue which gives a lifetime of 4.60 ± 0.02 ns.

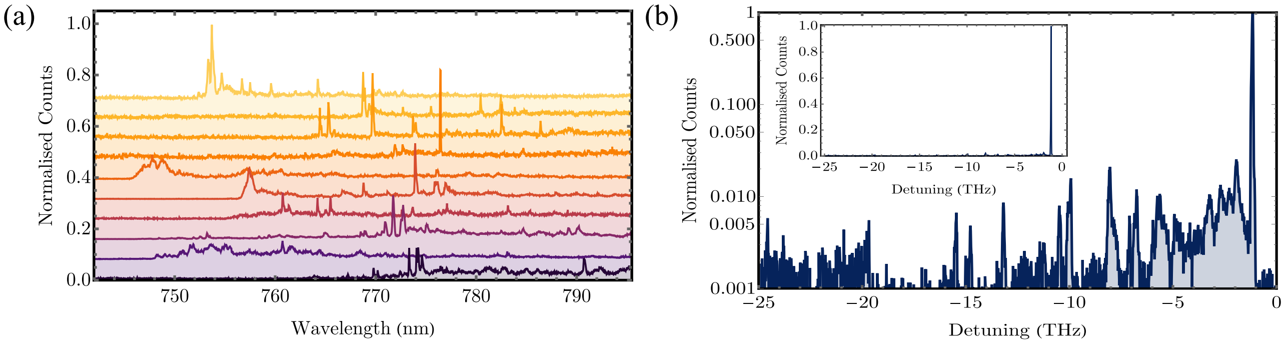

Figure 3.16: (a) Spectra from 10 nanocrystals (b) Frequency spectrum of single dibenzoterrylene (DBT) molecule, excited by 745.7 nm light and where detuning is taken from 388282 GHz (772.1 nm), plotted on a log scale. Inset: same spectrum plotted on a linear scale.

allows us to extract an excited state lifetime of 4.60 ± 0.02 ns, which is consistent with DBT/Ac.

Cryogenic

For cryogenic characterisation we performed another nanocrystal growth which we filtered through a 1200 nm pore size syringe filter. 5 μL of the filtered solution was deposited onto a silicon substrate which had been coated with gold and silica. The gold and silica layers act as a back reflector to redirect emission and increase the collection efficiency. The sample was coated in PVA and cooled to 5 K.

Again pumping using 730 nm light and collecting the fluorescence from a total of 10 nanocrystals, after filtering with a 745 nm long pass filter, we observe the spectrum shown in Fig. 3.16a. We see multiple emission peaks, some centered around 772 nm but also many resembling ZPL emission tens of nanometers away. Some of the observed lines, particularly those in the $780-790$ nm region, could be attributed to vibrational transitions. Others may be due to multiple insertion sites, resulting in different emission wavelengths and variable spectral stability, as has been shown in previous work involving pentacene [330] or terrylene [331] doped in pT.

To test whether this was the case here, we began by measuring the spectrum of a molecule with ZPL centered on 772.1 nm, by exciting with 745.7 nm light. The spectrum is shown in Fig. 3.16b, on both a log scale (main figure) and linear scale (inset), after having the background subtracted and being normalised to the maximum count of the ZPL. We can pick out vibrational transitions at lower frequencies, as well as a broad phonon sideband. The spectrum can be integrated to estimate the overall branching ratio, i.e. the ratio of emission on the ZPL compared to all other emission. This is only an estimate however, as there are vibrational transitions outside the range of frequencies captured in Fig. 3.16b, though they are likely to have little contribution due to their small transition dipole moment. With this method, we find a branching ratio $\alpha_{pT}=0.55$, larger than the branching ratio of DBT/Ac calculated in the same way ($\alpha_{Ac}=0.46$). This calculation was performed on only one molecule and so may not be representative of the DBT/pT in general. The same method can be used to compute the Debye-Waller factor $\alpha_{DW,pT}=0.79\pm0.03$, compared with the slightly lower value of $\alpha_{DW,Ac}=0.70\pm0.06$ for DBT in Ac. The phonon sideband is completely captured by the spectrum in Fig. 3.16b so this may be a more accurate comparison.

We next performed power broadening measurements and fitted Lorentzian functions to determine the linewidth and peak count rate at each power. An example linescan is shown in Fig. 3.17a for an excitation laser power of 1680 nW, where we see a stable Lorentzian response. The power-dependent linewidth is plotted in Fig. 3.17b from which we can determine the zero power linewidth of $2\Gamma_2 = 2\pi\times 65\pm4$ MHz and a saturation power of $p_{sat} = 350\pm54$ nW, which corresponds to a saturation intensity $I_{sat}=0.50\pm0.06\,\mathrm{Wcm}^{-2}$. In Fig. 3.17c we fit the peak count rate as a function of laser power (plotted in red), finding a maximum count rate

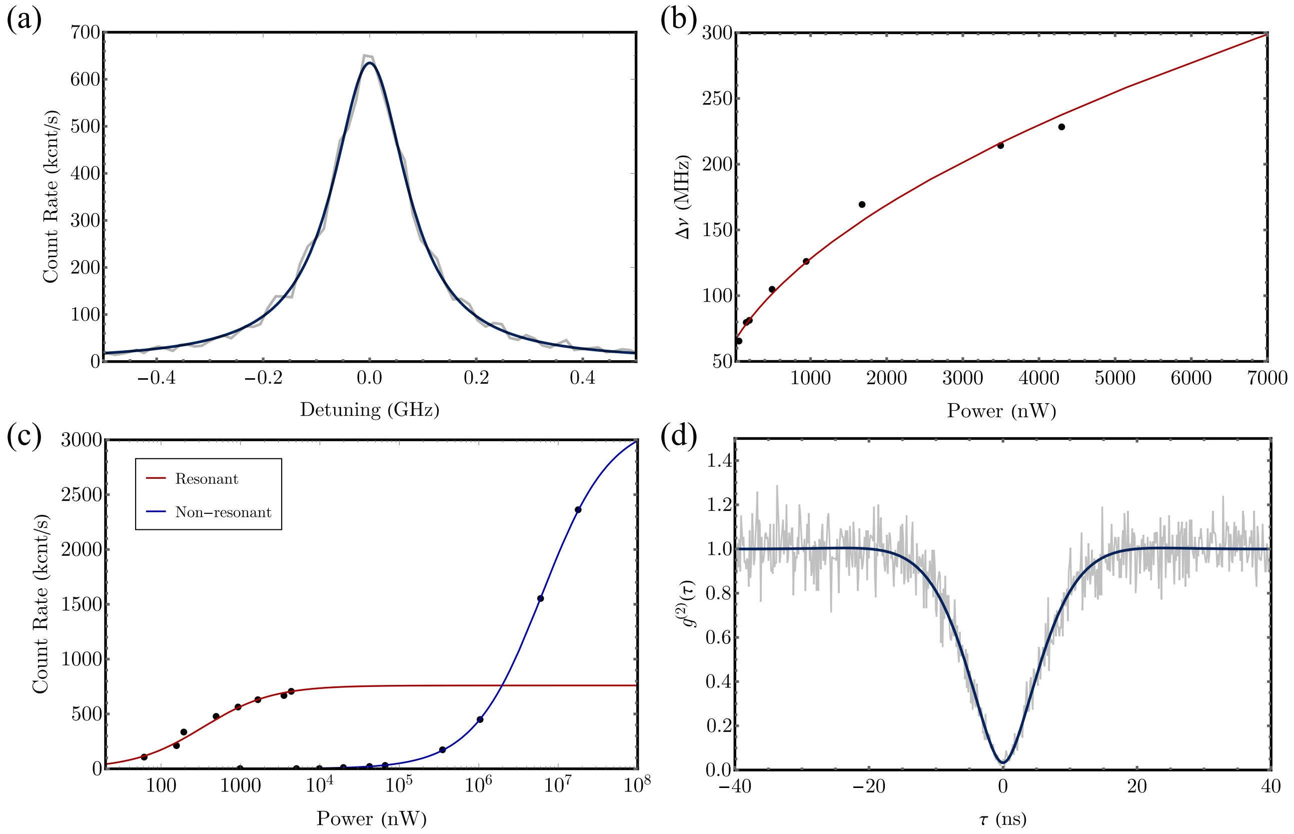

Figure 3.17: (a) Detected fluorescence (grey) as a function of laser detuning, with 0 detuning corresponding to 388282 GHz (772.1 nm). A Lorentzian function has has been fitted (dark blue). (b) Linewidth (black) as laser power is increased for resonant excitation and fitted with Eq. 2.18. A zero-power linewidth of $2\Gamma_2 = 2\pi \times 65 \pm 4$MHz and a saturation power of $p_{sat} = 350 \pm 54$ nW were extracted from the fit. (c) Peak count rate (black) as laser power is increased, fitted with Eq. 2.17 for resonant (red) and non-resonant 745.7 nm (blue) excitation. A maximum count rate of $R_\infty = 760 \pm 30$kcnts^{-1} and $p_{sat} = 340 \pm 40$ nW were obtained for resonant pumping. For non-resonant pumping $R_\infty = 3280 \pm 8$kcnts^{-1} and $p_{sat} = 6260 \pm 40\,\mu$W. (d) Second-order correlation function $g^{(2)}(\tau)$ (grey) taken with 120 nW excitation power. The data was fit with Eq. 2.32, from which we find a decay rate of $\Gamma_1 = 2\pi \times 40 \pm 2$MHz and a visibility of $\mathcal{V} = 0.97 \pm 0.02$.

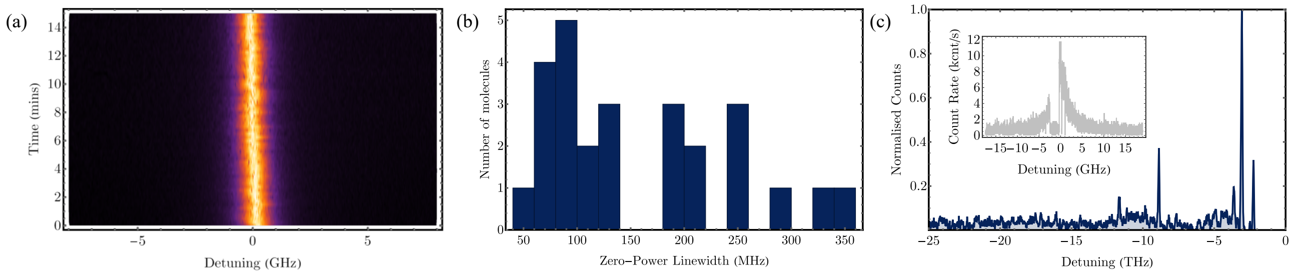

Figure 3.18: (a) Repeated linescans of molecule zero-phonon line (ZPL), centred at 388282 GHz (772.1 nm), taken over 15 mins and showing long term stability. (b) Histogram of zero-power linewidths for 26 molecules. (c) Single molecule spectrum, with a ZPL at 393428 GHz (762 nm). Inset: Excitation linescan over ZPL, performed at 1 GHz/s, showing instability of the molecule.

$R_\infty = 760 \pm 30\,\mathrm{kcnts}^{-1}$ and $p_{sat} = 340 \pm 40\,\mathrm{nW}$, consistent with the value derived from power broadening measurements.

To determine the single photon purity of the molecule, we measured a $g^{(2)}(\tau)$ at $S = 0.35$ ($P = 120\,\mathrm{nW}$), shown in Fig. 3.17d, where we have normalised the wings of the plot to 1.0 as in Fig. 3.6d. We fit the $g^{(2)}(\tau)$ measurement with Eq. 2.26, with S and Γ_2 known from the power broadening measurements, and find a $\Gamma_1 = 2\pi \times 40 \pm 2\,\mathrm{MHz}$, corresponding to a lifetime $4.0 \pm 0.2\,\mathrm{ns}$. This is shorter than the lifetime measured for the room temperature molecule using TCSPC but within the usual range found for DBT in Ac. The $g^{(2)}(\tau)$ visibility is $\mathcal{V} = 0.97 \pm 0.02$, showing an excellent single photon purity. The deviation from unity visibility is likely due to unsuppressed background and detector dark counts. The ratio of $\Gamma_1/2\Gamma_2 = 0.61$ is less than unity, implying that the molecule emission is not lifetime limited. This is consistent with thermal dephasing at a temperature of $\sim$ 5K. Cooling the DBT/pT crystal to $\sim$ 3K should allow for fourier-limited emission.

We then switched to pumping with 745.7 nm, in order to excite to a higher lying vibrational state $S_{1,n>0}$. To measure the change in count rate as the excitation power was increased, we performed spatial scans rather than spectral scans, due to the factor $\sim$ 1000 greater linewidth than the resonant case. The background, measured from a point on the sample free of molecules, was subtracted and the peak count rate versus laser power is fit in Fig. 3.17c (plotted in blue). From this we calculate $R_\infty = 3280 \pm 8\,\mathrm{kcnts}^{-1}$, approximately a factor four increase from the resonant case and $p_{sat} = 6260 \pm 40\,\mu\mathrm{W}$ ($I_{sat} = 9.38 \pm 0.06\,\mathrm{kWcm}^{-2}$).

Switching back to resonant excitation, repeated scanning of the ZPL over ~ 15 minutes, plotted in Fig. 3.18a, demonstrated continuous stable emission, with a slight variation in the central frequency, possibly due to a similar tuning mechanism as that responsible for laser tuning DBT/Ac. However, any variation remains much less than the ZPL width.

For the ZPLs in the range $768 - 776$ nm, we saw consistent stable emission. Power broadening measurements were performed for a total of 26 molecules within this range, and a histogram of the zero-power linewidths is shown in Fig. 3.18b. Around 40% displayed linewidths below 100 MHz, showing the potential for fourier-limited emission at lower temperatures. Some of the molecules investigated within the 'stable' $768 - 776$ nm region showed bleaching soon after excitation, possibly because of proximity to a crystal surface or defect. This behaviour is also seen in DBT/Ac. The overall stability may be improved by adjustment of the crystal growth parameters, or by using a co-sublimation growth to produce larger more homogeneous crystals.

For the majority of the features outside the $768 - 776$ nm range, we were unable to detect red shifted fluorescence. However for some lines, we were able to detect fluorescence and perform linescans, though the transition appeared unstable over the 30 seconds it takes to perform a linescan, most likely due to the DBT dopant being poorly included in the pT matrix. An example is shown in the inset of Fig. 3.18c, for a ZPL at 762 nm. The spectrum of this molecule is pictured in the main part of Fig. 3.18c, showing a ZPL at 762 nm, which is comparatively weaker than the spectrum shown in Fig. 3.16b. A couple of vibrational transitions can be seen, as well as the phonon side band.

3.3 Conclusions

In this chapter, we have demonstrated several ways to tune the emission frequency of doped DBT molecules. We began with DC-Stark tuning where we were able to tune individual DBT molecules at differing rates, thereby allowing us to tune DBT molecules onto resonance with each other, such as shown in Fig. 3.7b. The tuning was shown to be quadratic on average, as expected from a centrosymmetric molecule like DBT, and the quadratic and linear coefficients were found to be consistent with what had previously been seen in the literature [302]. We also investigated if there was any angular dependence of the applied electric field on the rate of tuning and found no conclusive evidence of a relationship, though the large variation in the data may have obscured a small angular dependence. Following this, we studied strain tuning of DBT molecules, where the macroscopic Ac crystal was adhered to a bending piezo. The frequency tuning showed a linear dependence on the voltage applied to the bending piezo. The final tuning method we investigated was laser tuning, where we demonstrated that the effect saturated over time, together with showing that pulsed excitation also displayed significant tuning. This presents a significant challenge needed to be overcome if DBT is to be used as an indistinguishable on-demand photon source.

We then moved on to describe photonic structures intended to improve the emission of DBT, and identified one of the key challenges in integrating DBT molecules with these structures, namely incorporating DBT at the correct position in photonic structures to show maximal enhancement. A method to deterministically place DBT/Ac nanocrystals was developed and showed excellent and repeatable results for depositing nanocrystals in prepatterned holes. However, this method failed to produce DBT with narrow spectral lines at cryogenic temperatures, implying high amounts of dephasing. This was most likely due to increased surface effects due to the PVA coating struggling to surround the nanocrystals in the holes. Using a less viscous PVA solution, or encasing the nanocrystals in a PMMA shell before deposition are two possible solutions.

The final section of this chapter investigated DBT doped into nanocrystals synthesised from a novel host matrix, pT [307]. We showed narrow stable emission with high single photon purity, at wavelengths compatible with the potassium D1 line, as well as higher lying transitions in rubidium. Measurements suggested a more favourable branching ratio for DBT/pT when compared with DBT/Ac.

Chapter 4

Warm Rubidium Vapour

Having discussed dibenzoterrylene as a single photon source, we will now turn our attention to atomic ensembles as a medium for a quantum memory. Vapours of alkali metals are good candidates for quantum memories, owing to their long-lived ground state coherence, large light-matter coupling and high room temperature vapour pressures, resulting in large optical depths for modest cell lengths [213, 334].

Rubidium (Rb) is an alkali, commonly placed within a vapour cell and employed as a frequency reference [335, 336, 337, 338], due to transitions available in the near-infrared where there are a huge amount of laser sources, detectors and optics available. Rb has also been used extensively in experiments for spectral filtering [339], accelerometers [340], magnetometry [341] and quantum memories [44, 205, 237, 266, 293, 297, 298]. Additionally, higher lying transitions in Rb are compatible with the telecommunication (telecom) bands, commonly used for commercial fibre optic data transfer, and these transitions have been used to show telecom wavelength conversion [342], as well as storage of telecom single photon level pulses [343]. Many of these experiments have been conducted using cold Rb atoms, trapped in a magneto-optical trap (MOT). While Rb is relatively simple to trap and cool, MOT setups add additional complexity and overhead which we would ideally like to avoid. The subject of this chapter will be warm vapours, which are technically much simpler and can reach much higher atomic number densities than a MOT.

A model predicting the absolute absorption of a Rb vapour is useful for determining the occupation of different levels, overall number density and temperature of the Rb, all of which are important parameters for memory performance, as will be discussed in Chapters 5 and 6. Also, understanding the dynamics of the atom-light interaction can aid in optimising the signal used for frequency stabilisation of a laser [335,344] ('laser locking') or for atomic clocks [345].

Doppler broadening of hyperfine transitions prevents direct monitoring of the energy levels involved. Techniques to resolve sub-Doppler features exist for room-temperature ensembles but traditionally these use high probe laser intensities when compared to single photon level probes [346,347,348]. In this chapter, we will present a model for a modified sub-Doppler spectroscopy technique using a single-photon level probe and an independent counter-propagating bright pump laser. This is a step towards interfacing tunable Dibenzoterrylene from the previous chapter with rubidium vapours. We then compare an experimentally measured spectrum with the simulated spectrum from our model and find excellent agreement. These results are published in Ref. [119]. Following this, we use the verified model to investigate different optical pumping regimes of Rb, for preparing a warm atomic ensemble for quantum memory protocols.

4.1 Theory

In Chapter 2, we could assume that the intense probe light was not significantly affected by interaction with the emitters. Here, we are attempting to describe the interaction of single photons with room temperature alkali vapour, made up of billions of atoms.

We will begin by assuming that all beams propagate along the z-axis, with negligible divergence, such that we may treat our system as one dimensional. This is the paraxial approximation and we can neglect divergence provided the central wavelengths of the light fields involved are much smaller than the transverse area of the beams, which is true for the transitions we will be considering in Rb. In one dimension, the change in intensity of a weak cw probe beam, propagating in the +z-direction of a dilute atomic gas, follows the Beer-Lambert relation [349],

$$\frac{dI(\omega,z)}{dz} = -N_v\sigma(\omega)I(\omega,z) \tag{4.1}$$

where N_v represents the number density of Rb atoms, $\sigma(\omega)$ is the frequency dependent absorptive cross section, with ω representing angular frequency, and $I(\omega,z)$ is the probe laser intensity at frequency ω and longitudinal position z. The intensity exiting a medium of length L is therefore,

$$I(\omega,L) = I(\omega,0)\exp[-d(\omega)]\,, \tag{4.2}$$

where we have introduced the optical depth $d(\omega) = N_v\sigma(\omega)L$. The aim of this derivation is to compute the optical depth (or equivalently cross section) for the combined system, which will depend on the temperature of the Rb, as well as on the population of the ground and excited state. An incident probe beam monitors the change in absorption of the medium, due to the counter-propagating pump beam modifying the populations.

4.1.1 Rubidium

Rb has 37 electrons with one in the outer shell, which is the only electron involved in the transitions used in this thesis. Since the transition dynamics are the result of only one electron, Rb has a relatively simple electronic structure. There are two naturally occuring isotopes: ^{87}Rb [350] and ^{85}Rb [351], with ^{85}Rb the only stable one, though the decay rate of ^{87}Rb is so slow, with a half-life of 48.8 billion years, that it may be considered stable. Typical vapour cells will contain both isotopes in their natural abundances: 0.2785 and 0.7215 for ^{87}Rb and ^{85}Rb respectively [350, 351].

Number density

We can determine the number density from the vapour pressure p of the Rb, using the relation,

$${}^{\mathcal{I}}N_v = \frac{\mathcal{P}_{\mathcal{I}}}{\mathrm{k_B}T} \times 133.323 \times p\,, \tag{4.3}$$

where $\mathcal{P}_{\mathcal{I}}$ is the fraction of isotope $\mathcal{I}$, $\mathrm{k_B}$ is the Boltzmann constant and T is the temperature in kelvin. The vapour pressure in Eq. 4.3 is in units of torr and the factor of 133.323 is to convert from torr to pascal. An estimate of p can be found from the vapour-pressure model given in [352],

$$\log_{10}(p_y) = \begin{cases} -94.04825 - (\frac{1961.258}{T}) - 0.03771678 \times T + 42.57526\log_{10}(T), & \text{for } T < 312.45\,\mathrm{K} \\ 15.88253 - (\frac{4529.535}{T}) + 0.00058663 \times T - 2.99138\log_{10}(T), & \text{for } T \geq 312.45\,\mathrm{K}, \end{cases} \tag{4.4}$$

where $T = 312.45\,\mathrm{K} = 39.3\,°\mathrm{C}$ is the melting point of Rb. In Fig. 4.1a we have plotted N_v as a function of temperature up to a limiting value of 100 °C. While vapour cells can survive being heated to much higher temperatures than this, Rb vapour can react with the vapour cell walls and the number density will decrease over time [353,354,355]. Additionally, pressure broadening can begin to have a substantial effect at higher number densities, which we will neglect in the derivations provided in this thesis. Also indicated with a grey dashed line is the typical number density in a high density MOT [356]. Compared to a MOT we see an advantage at temperatures upwards of 54 °C for ^{85}Rb and above 64 °C for ^{87}Rb. However the increased temperature leads to substantial Doppler broadening, effectively spreading out the optical depth for a range of frequencies, δ_{DB}, which denotes the Doppler width expressed as a linear frequency.

The Maxwell-Boltzmann distribution of a one dimensional velocity vector (as we are considering propagation only along the z-axis) is given by,

$$f_{\mathrm{MB}}(v) = \sqrt{\frac{m}{2\pi k_B T}} \exp\left[\frac{-mv^2}{2k_B T}\right], \tag{4.5}$$

where m and v are the mass and velocity of a Rb atom. In the limit of $\delta_{\mathrm{DB}} \gg \Gamma$, where Γ is the excited state decay rate, δ_{DB} is well approximated by the full-width half-maximum of Eq. 4.5,

$$\delta_{\mathrm{DB}} = \sqrt{\frac{8\mathrm{k_B}T\ln(2)}{mc^2}}\, f_0\,, \tag{4.6}$$

for central frequency f_0 and c is the speed of light in a vacuum.

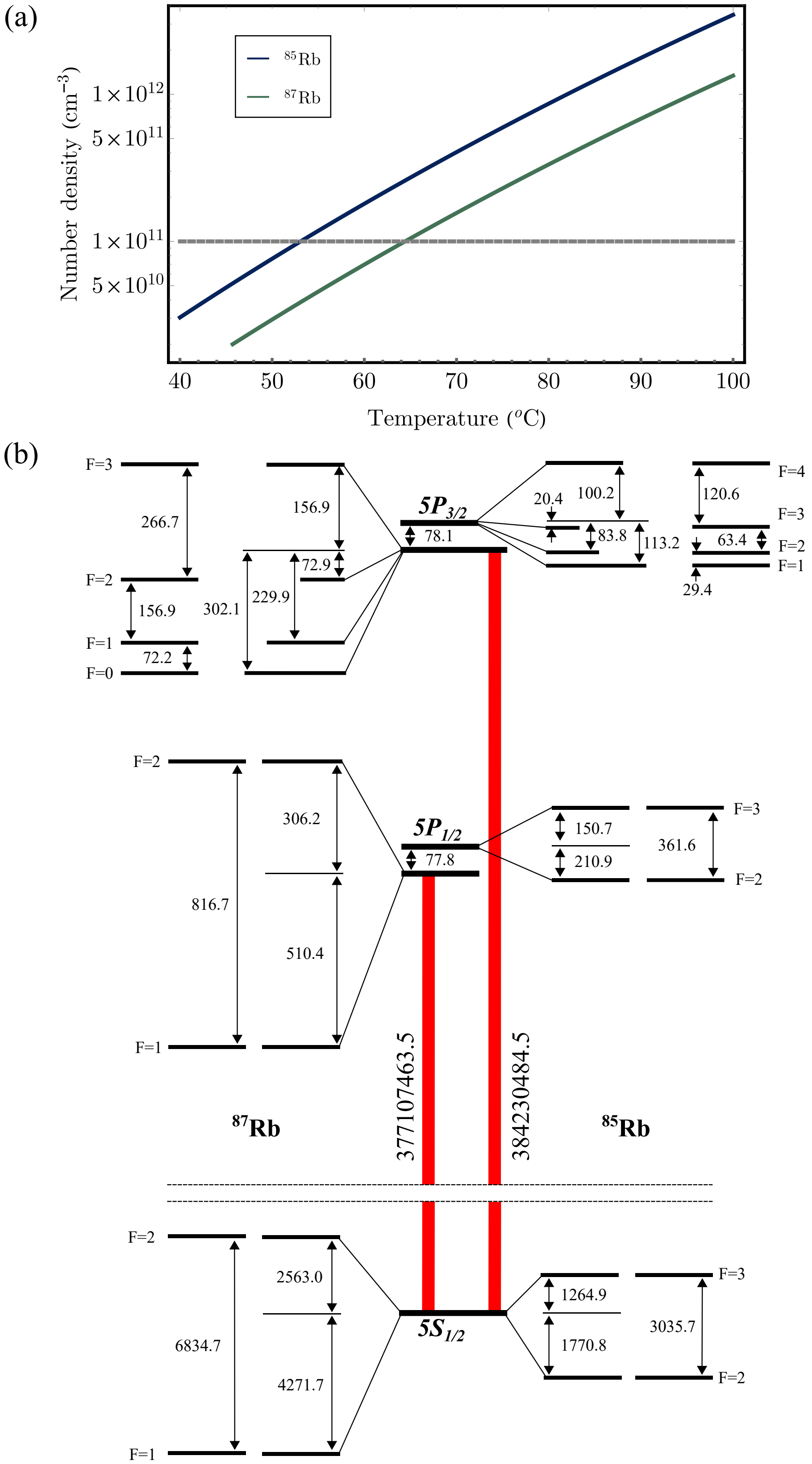

Figure 4.1: (a) Number density of ^{85}Rb (blue) and ^{87}Rb (green) with natural abundance. Shown in dashed grey is a typical density of a high density magneto-optical trap [356]. (b) Hyperfine structure of ^{87}Rb [350] (left) and ^{85}Rb [351] (right), with values given in MHz.

Level structure

The full electronic structure of Rb is $1s^2 2s^2 2p^6 3s^2 3p^6 3d^{10} 4s^2 4p^6 5s$, with only the outer electron contributing to the atoms orbital angular momentum and therefore transition probabilities. For denoting the state of this electron, we will use the standard nomenclature nL_J where n labels the electronic shell, L the angular momentum orbital and $J = |\boldsymbol{J}|$ the total electron angular momentum. The total electron angular momentum is given by $\boldsymbol{J} = \boldsymbol{L} + \boldsymbol{S}$, for spin angular momentum $\boldsymbol{S}$. The ground state of Rb corresponds to $5S_{1/2}$. Commonly used for light-matter interactions in alkali metals are the 'doublet' lines, D_1 and D_2, which for Rb occur at wavelengths 795 nm and 780 nm respectively and are illustrated in Fig. 4.1b. These transitions correspond to $5S_{1/2} \rightarrow 5P_{1/2}$ for the D_1 line and to $5S_{1/2} \rightarrow 5P_{3/2}$ for the D_2 line. The D_2 line is often employed as a cycling transition used for trapping and cooling.

The $5S_{1/2}$ ground state has zero orbital angular momentum ($\boldsymbol{L} = 0$) and so the electron wavefunction extends into the nucleus, leading to a strong magnetic dipole coupling between the nuclear and electronic spin. This interaction causes the ground state to split into two hyperfine states, depending on the total *atomic* angular momentum $\boldsymbol{F} = \boldsymbol{I} + \boldsymbol{J}$, where $\boldsymbol{I}$ is the nuclear angular momentum. For ^{87}Rb, $|\boldsymbol{I}| = 3/2$, which when combined with the electron spin angular momentum $|\boldsymbol{S}| = 1/2$, results in two ground states with $|\boldsymbol{F}| = 1$ or $|\boldsymbol{F}| = 2$ with a splitting of 6.835 GHz. For ^{85}Rb, $|\boldsymbol{I}| = 5/2$ resulting in $|\boldsymbol{F}| = 2$ or $|\boldsymbol{F}| = 3$, separated by 3.035 GHz. Both splittings are illustrated in Fig. 4.1b. At room temperature, $\delta_{\mathrm{DB}} \approx 500$ MHz, and so the ground states can be easily distinguished through absorption spectroscopy with a cw laser.

The excited P states have non-zero orbital angular momentum and so $|\boldsymbol{F}|$ can take a greater range of values. However, the larger angular momentum means that less of the electron wavefunction overlaps with the nucleus, making the hyperfine magnetic dipole interaction smaller. The result is a splitting on the order of 100 MHz, which at room temperature is obscured by the Doppler broadening. The individual splittings of the excited hyperfine states are shown in Fig. 4.1b in MHz.

Beyond the doublet lines, some other useful transitions are to higher lying D states. The $5P$ to $4D$ state transitions are compatible with telecom wavelengths and have been used to realise a telecom compatible quantum memory [343], which we will explore in more detail in Chapter 6.

Within each hyperfine level, there is a manifold of $2|\boldsymbol{F}| + 1$ degenerate sub-levels, labelled by m_F, corresponding to the relative orientation of $\boldsymbol{F}$ to a defined quantisation axis. The application of an external magnetic field will cause the degeneracy to be lifted and is termed Zeeman splitting.

A single plane-wave photon has spin equal to the reduced Planck's constant, $\pm\hbar$ (corresponding to left and right circularly polarised light from the point of view of the receiver) and so absorption of a photon by an atom leads to an increase in the orbital angular momentum by one (units of $\hbar$). This means that only transitions resulting in $\Delta\boldsymbol{L} = \pm 1$ are allowed (i.e. $S \to P$ but not $S \to S$ or $S \to D$). In addition, the projection of $\boldsymbol{F}$ along some quantisation axis can change depending on the polarisation of the light. In Fig. 4.2 we show how light travelling in the $+z$-direction, with different polarisation, changes the projection of $\boldsymbol{F}$ along the $+z$-axis, labelled by m_{Fz}.

A $\Delta m_{Fz} = \pm 1$ corresponds to left and right circularly polarised light respectively. Light of linear polarisation is a superposition of left and right circularly polarised light and will cause the atom to be in a superposition of $\Delta m_{Fz} = \pm 1$. For a quantisation axis defined orthogonal to the z-axis, represented by the x-axis in Fig. 4.2, linear polarised light polarised parallel to the x-axis and propagating in the $+z$-direction, will drive $\Delta m_{Fx} = 0$

When combined, we arrive at the transition selection rules,

$$\begin{aligned}
&\Delta|\boldsymbol{L}| = \pm 1 \\
&\Delta|\boldsymbol{S}| = 0 \\
&\Delta|\boldsymbol{J}| = 0,\ \pm 1 \ (\text{but not } J = 0 \to J' = 0) \\
&\Delta|\boldsymbol{F}| = 0,\ \pm 1 \\
&\Delta m_F = 0,\ \pm 1 \ (\neq 0 \text{ if } \Delta|\boldsymbol{F}| = 0)\,.
\end{aligned} \tag{4.7}$$

While for no application of an external magnetic field, any Δm_F will result in the same transition frequency, the transition strengths are not identical. The strength of the transition between

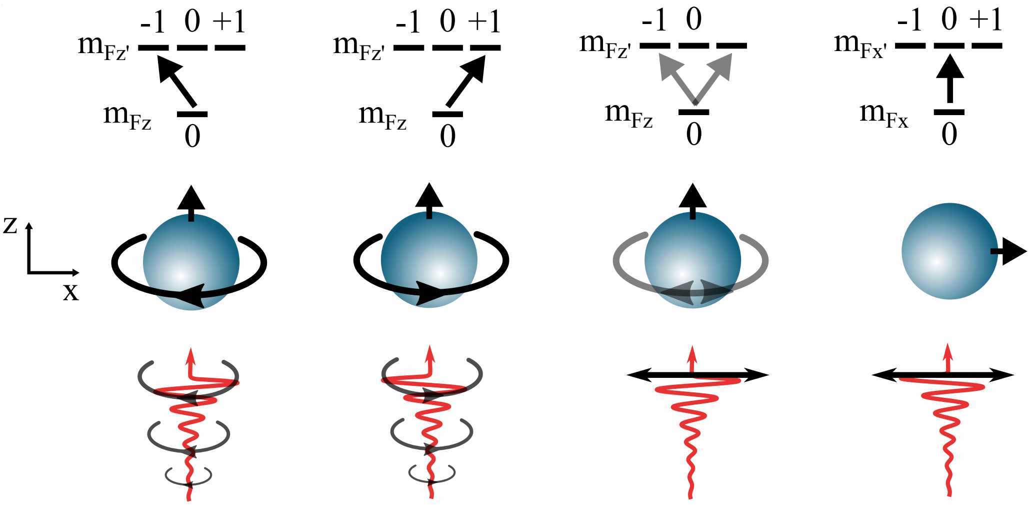

Figure 4.2: Incoming photons of a defined polarisation drive transitions in an atom relative to a quantisation axis. For the three left illustrations, the quantisation axis is taken to be in the propagation direction of the light: $+z$-direction. Furthest left, we have right circularly polarised light (RCP) with respect to the receiving atom, which reduces the projection of $\boldsymbol{F}$ along the $+z$-axis ($\Delta m_{Fz} = -1$). To the immediate right, we have left circularly polarised (LCP) light which results in $\Delta m_{Fz} = +1$. To the right again, we have linearly polarised light, which can be though of as a superposition of RCP and LCP light. This drives the atom into a superposition of both transitions. On the far left, we have the same linearly polarised light, but we have taken the quantisation axis to be along the $+x$-direction (orthogonal to the $+z$-direction). In this frame, the light causes no change to the projection of $\boldsymbol{F}$, resulting in $\Delta m_{Fx} = 0$.

states $|F_j, m_{F_j}\rangle \rightarrow |F_k, m_{F_k}\rangle$ is characterised by the dipole matrix element [357],

$$\mu_{jk} = \langle F_j, m_{F_j}|\, er_q\, |F_k, m_{F_k}\rangle = e \int \psi_j^*(\boldsymbol{r}) r_q \psi_k(\boldsymbol{r}) d^3\boldsymbol{r} \tag{4.8}$$

where $\boldsymbol{r}$ is the electron position, q labels the component of $\boldsymbol{r}$ in the spherical basis: $q = 0$ for linearly polarized light, $q = +1$ for left hand circular and $q = -1$ for left hand circular. We can factor out the angular dependence to give [350, 357],

$$\begin{aligned} \langle F_j, m_{F_j}|\, er_q\, |F_k, m_{F_k}\rangle &= C(F_j, m_{F_j}, F_k, m_{F_k}) \langle F_j|\,|e\mathbf{r}|\,|F_k\rangle \\ &= W(F_j, J_j, F_k, J_k, I) C(F_j, m_{F_j}, F_k, m_{F_k}) \langle J_j|\,|e\mathbf{r}|\,|J_k\rangle \end{aligned} \tag{4.9}$$

where $C(F_j, m_{F_j}, F_k, m_{F_k})$ is the Clebsch-Gordan coefficient, $W(F_j, J_j, F_k, J_k, I)$ represents the Wigner $6-j$ symbol[1] and $\langle J_j|\,|e\mathbf{r}|\,|J_k\rangle$ represents the reduced dipole moment, related to the

---

[1] Typically, Eq. 4.9 features some additional prefactors, which we will take to be within the definition for the Wigner $6-j$ symbol.

decay, Γ, of the excited state by,

$$\langle J_j| \, |e\mathbf{r}| \, |J_k\rangle = \sqrt{\frac{2J_k+1}{2J_j+1}\frac{3\epsilon_0 \hbar c^3 \Gamma}{2f_0^3}}\,, \tag{4.10}$$

where ϵ_0 is the vacuum permittivity. The Clebsch-Gordan coefficents and Wigner $6-j$ symbol may be calculated, or alternatively can be obtained from Ref. [358]. To obtain the total strength of a hyperfine transition, we need to sum over all m_F sub-level transitions.

4.1.2 Cross section

We now move on to deriving an expression for the cross section. We will consider low laser powers, allowing non-linear effects to be discounted and cw lasers over timescales much longer than the decay rate of Rb so we may consider the steady state and neglect coherence effects.

While the treatment used during Chapter 2 involving the optical Bloch equations would also be appropriate for deriving the equations from this section, we instead choose to use Einstein A and B coefficients as this was the method I originally obtained the expressions detailed in Ref. [119].

We can write the absorption cross section for the electric dipole transition from $|g\rangle \rightarrow |e\rangle$ for an atom travelling at velocity v as,

$$\sigma(\omega) = \frac{\hbar\omega_{ge}}{c}(B_{ge}n_g - B_{eg}n_e)L_{ge}(\omega, v) \tag{4.11}$$

where B_{ge} and B_{eg} are the Einstein coefficients for absorption and stimulated emission, n_g and n_e are the fractional populations of the ground and excited state, respectively, and $\hbar\omega_{ge}$ is the energy difference between the ground and excited state. The Lorentzian line shape $L_{ge}(\omega, v)$ is defined as,

$$L_{ge}(\omega, v) = \frac{\Gamma/2\pi}{(\omega-\omega_{ge}-kv)^2+(\Gamma/2)^2} \tag{4.12}$$

In Eq. 4.11, we have defined B_{ge} such that the rate of absorption is $B_{ge}\rho_{ge}(\omega, v)$ where $\rho_{ge}(\omega, v) = L_{ge}(\omega, v)I/c$ is the spectral energy density of a monochromatic laser field; the rate of stimulated emission is defined analogously.

The B coefficients are given by [359],

$$B_{ge} = \frac{\pi}{\epsilon_0 \hbar^2 \mathcal{D}_g} \sum_{m_F} |\mu_{ge}|^2 = \frac{\mathcal{D}_e}{\mathcal{D}_g} B_{eg} \,, \tag{4.13}$$

where $\mathcal{D}_j$ is the number of degenerate sub-levels in $|j\rangle$. Often a factor of $1/3$ is added to Eq. 4.13 to average over the three possible orientations of the atom for the case of no quantisation axis. In our case, the laser light defines our quantisation axis and we assume linear polarisation, so we may neglect the factor of $1/3$.

We can define saturation intensity I_{ge} in the same way as in Chapter 2, (the intensity needed to reach a population difference in a two-level system of $1/2$) which can be shown to be [349],

$$I_{ge} = \frac{1}{3} \frac{\pi c \Gamma^2}{4 \mathcal{D}_g B_{ge}} \tag{4.14}$$

where the factor of $1/3$ is because we are considering only linearly polarised light.

Open two-level system

We now need to compute the dynamic fractional populations: n_g and n_e. These populations will be modified by the counter-propagating pump beam. Let us consider three level system shown in Fig. 4.3a. As well as absorption and stimulated emission, we have spontaneous decay from the excited state, as we had in the two level system in Chapter 2. In contrast to the two level system we had for DBT, we now have an open two level system, where spontaneous decay can not only occur on the $|e\rangle \rightarrow |g\rangle$ transition, but on the $|e\rangle \rightarrow |d\rangle$ transition (where $|d\rangle$ represents the other hyperfine ground state), which is far from detuned from our laser. After decay to the dark state $|d\rangle$, these atoms stop interacting with the light. The ratio of decay between the two pathways can be determined via the Clebsch-Gordan coefficients as,

$$\begin{aligned} \Gamma_{ge} &= \frac{\sum_{m_F} C_{ge}^2}{\sum_{m_F} C_{ge}^2 + \sum_{m_F} C_{de}^2} \Gamma \\ \Gamma_{de} &= \frac{\sum_{m_F} C_{de}^2}{\sum_{m_F} C_{ge}^2 + \sum_{m_F} C_{de}^2} \Gamma \,. \end{aligned} \tag{4.15}$$

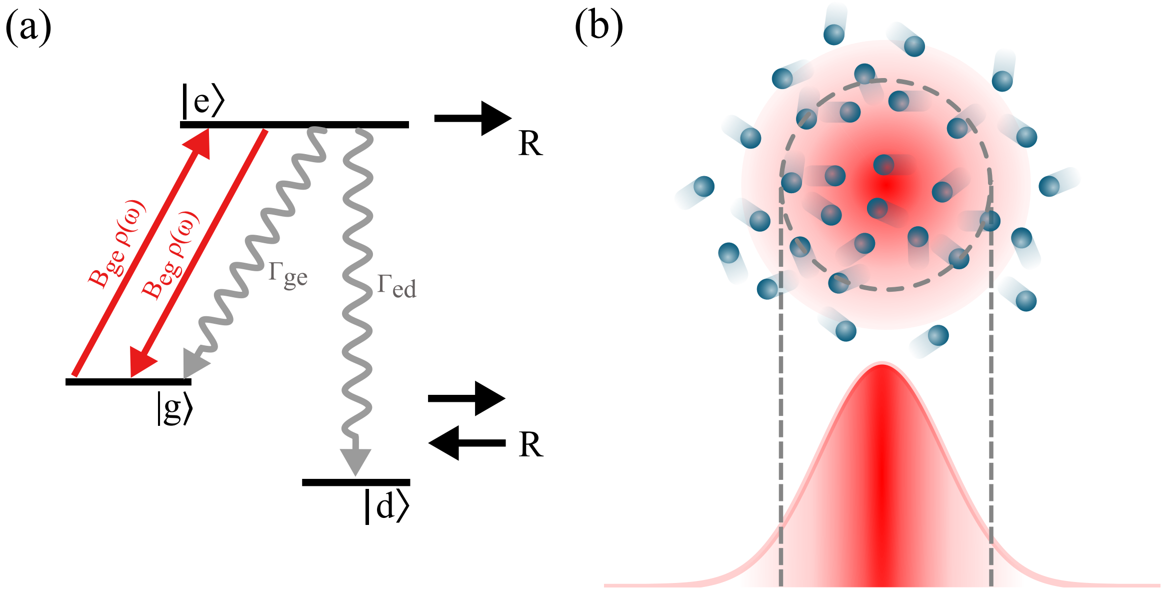

Figure 4.3: (a) Open two level system, showing absorption and stimulated emission in red, at rates $B_{ge}\rho_{ge}(\omega, v)$ and $B_{eg}\rho_{ge}(\omega, v)$ respectively. Spontaneous decay is represented by the wavy grey arrows and can occur either to the original ground state $|g\rangle$ or to the other dark ground state $|d\rangle$. Atoms enter and leave the beam at a rate of R, entering with an unpumped population distribution. (b) Cut through of a gaussian mode laser as it propagates through an atomic vapour. Illustrated in dashed grey is the $1/e^2$ diameter. While this captures most of the intensity in the beam, atoms may still be optically pumped in the outer intensity tail.

Initially, the atomic populations will be in equilibrium with the thermal background, which at room temperature corresponds to a frequency of ∼THz. While the excited state in Rb is close to 400 THz away, the ground state splitting is a few GHz. The initial equilibrium population in each ground state is proportional to the ratio of sublevels in each,

$$\begin{aligned} \mathcal{N}_g &= \frac{\mathcal{D}_g}{\mathcal{D}_g + \mathcal{D}_d} \\ \mathcal{N}_d &= \frac{\mathcal{D}_d}{\mathcal{D}_g + \mathcal{D}_d}\,, \end{aligned} \tag{4.16}$$

with $\mathcal{N}_g + \mathcal{N}_d = 1$.

Another consideration in our system is that the atoms are moving, and so can move into and out of the beam, at a transit rate R. We will assume that atoms drifting into the beam enter with the original unpumped equilibrium population distribution. We can initially take R to be,

$$R_0 = \frac{v_p}{2r}\,, \tag{4.17}$$

with $v_p = \sqrt{2k_BT/M}$ denoting the most probable speed of an atom in one dimension and r is the $1/e^2$ radius of the pump beam, pictured in Fig. 4.3b. However, this estimate does not take into account atoms interacting with the wings of the pump laser. We will return to derive a more accurate expression for R in later in this section.

We now arrive at the rate equations,

$$\begin{aligned} \dot{n_g} &= -n_g B_{ge}\rho_{ge} + n_e[B_{eg}\rho_{ge} + \Gamma_{ge}] + R(\mathcal{N}_g - n_g) \\ \dot{n_e} &= n_g B_{ge}\rho_{ge} - n_e[B_{eg}\rho_{ge} + \Gamma + R] \\ \dot{n_d} &= n_e\Gamma_{ed} + R(\mathcal{N}_d - n_d)\,, \end{aligned} \tag{4.18}$$

where we have assumed that any laser field does not transfer significant population from $|d\rangle \rightarrow |e\rangle$, as the bandwidth of a cw laser ($\sim$ MHz) is much less than the GHz splitting of the Rb ground states.

We can draw some parallels between Eqs. 4.18 and the optical-Bloch equations derived in Chapter 2. The decay term appears with the same form, but the coherence terms have been replaced by rates involving Einstein B coefficients, spectral densities and populations. If we were to set the time derivatives of the equations pertaining to coherence in Eqs 2.13 and reduce the equations to be in terms of only populations, we would be able to relate the Einstein B coefficients and spectral density to the Rabi frequency Ω, detuning Δ, decay rate Γ_1 and decoherence rate Γ_2, defined in Chapter 2. The remaining term in Eqs. 4.18 involving R did not appear in Chapter 2 as there we were considering solid state media where there was no transit into or out of the beam.

The steady state solutions to Eqs. 4.18 are,

$$n_g = \frac{n_e[B_{eg}\rho_{ge} + \Gamma_{ge}] + \mathcal{N}_g R}{B_{ge}\rho_{ge} + R} \tag{4.19}$$

$$n_e = \frac{n_g B_{ge}\rho_{ge}}{B_{eg}\rho_{ge} + \Gamma + R} \tag{4.20}$$

$$n_d = \frac{n_e\Gamma_{ed} + \mathcal{N}_d R}{R}\,. \tag{4.21}$$

Substituting Eq. 4.20 into Eq. 4.19 results in,

$$n_g = \frac{\mathcal{N}_g}{1 + \alpha_{ge}\beta_{ge}} \tag{4.22}$$

$$n_e = n_g \alpha_{ge} \tag{4.23}$$

with the saturation parameter α_{ge} defined as,

$$\alpha_{ge} = \frac{B_{ge}\rho_{ge}}{B_{eg}\rho_{ge} + \Gamma + R} \tag{4.24}$$

and the optical pumping parameter β_{ge} defined as,

$$\beta_{ge} = 1 + \frac{\Gamma - \Gamma_{ge}}{R} \, . \tag{4.25}$$

The saturation parameter quantifies the ratio of processes adding population to $|e\rangle$ (absorption) to all processes removing population from $|e\rangle$ (stimulated emission, decay, atoms moving out of the interaction region). In the two level system considered in Chapter 2, we saw that the excited state population saturated at half due to competition between absorption and stimulated emission. We can see that in Eq. 4.22, for $\beta_{ge} = 1$, as $\rho_{ge} \to \infty$, $\alpha_{ge} \to \mathcal{D}_e/\mathcal{D}_g$, which for $\mathcal{D}_e = \mathcal{D}_g$, leads to $n_g = \mathcal{N}_g/2$. If the number of sublevels in the excited state is larger than the ground state, the rate of stimulated emission is lowered and the ground state population can be reduced further still. The larger the decay rate and shorter the transit time (larger R), the higher the laser intensity needed to approach this bound.

The optical pumping parameter captures the effect of the dark state. Decays to the dark state reduce the rate of stimulated emission while absorption remains unaffected. The longer atoms spend in the beam ($R \to 0$), the higher the chance of absorption followed by emission to the dark state ($\beta_{ge} \to \infty$), allowing the ground state population to approach zero and all population to accumulate in the dark state.

The three fractional populations are plotted in Fig. 4.4a as a function of α_{ge}, where the dashed lines represent the populations in the limiting case of $\beta = 1$ and the solid lines the case of

$\beta = 10$ (for Rb this corresponds to an $R \approx 600\,\text{kHz}$). In both cases, $D_g = D_e = 1$. The dashed lines are observed to tend towards 0.5 at high saturation, as we expect for a two level system. Decay to the dark state causes population to be lost from $|g\rangle$ and build up in $|d\rangle$. Once in $|d\rangle$ there is no way for the population to make it back to $|g\rangle$ through interacting with the laser. Only through transitions into and out of the beam is the population in $|g\rangle$ replenished, leading to a limiting value of $n_g = n_e \approx 0.1$ for $\beta = 10$, as saturation is increased.

Inserting Eq. 4.22 and Eq. 4.23 into Eq. 4.11 for the cross section gives us,

$$\sigma(\omega) = \frac{\hbar\omega_{ge}}{c} B_{ge} \mathcal{N}_g \, \Delta N_g(v) L_{ge}(\omega, v)\,, \tag{4.26}$$

where we have defined,

$$\Delta N_g(v) = \frac{1 - \frac{\mathcal{D}_g}{\mathcal{D}_e}\alpha_{ge}(v)}{1 + \alpha_{ge}(v)\beta_{ge}}\,, \tag{4.27}$$

which is related to the difference in the population of states $|g\rangle$ and $|e\rangle$ with the level degeneracy taken into account. We plot $\Delta N_g(v = 0)$ as a function of α_{ge} for different values of optical pumping parameter in Fig. 4.4b. For $\beta_{ge} = 1$, as the populations n_g and n_e tend to 0.5, $\Delta N_g \to 0$, reducing the cross section to zero as it is equally likely that a photon is lost to absorption as it is to gain a photon from stimulated emission. The result is all incident light will be transmitted. As optical pumping is increased, ΔN_g approaches zero much faster.

For a dilute gas of atoms we must integrate over the full velocity distribution, weighted by the occupation probability corresponding to each velocity class. This gives an absorption cross section of,

$$\sigma(\omega) = \frac{\hbar\omega_{ge}}{c} \int_{-\infty}^{\infty} B_{ge} \mathcal{N}_g \, \Delta N_g(v) L_{ge}(\omega, v) f(v) dv\,, \tag{4.28}$$

which for $\Delta N_g = 1$ results in a Voigt profile (convolution of the Lorentzian atomic lineshape and Gaussian Doppler broadening), shown in Fig. 4.4d in blue. The introduction of a counter-propagating pump beam, on resonance with the stationary $|g\rangle \to |e\rangle$, causes saturation of the transition and optical pumping of population to the dark state, leading to a reduction in the ground state population for atoms with velocities close to zero [2], as shown in Fig. 4.4c, where

---

[2] By close to zero, we mean slow enough such that the Doppler shift is within the linewidth of the transition.

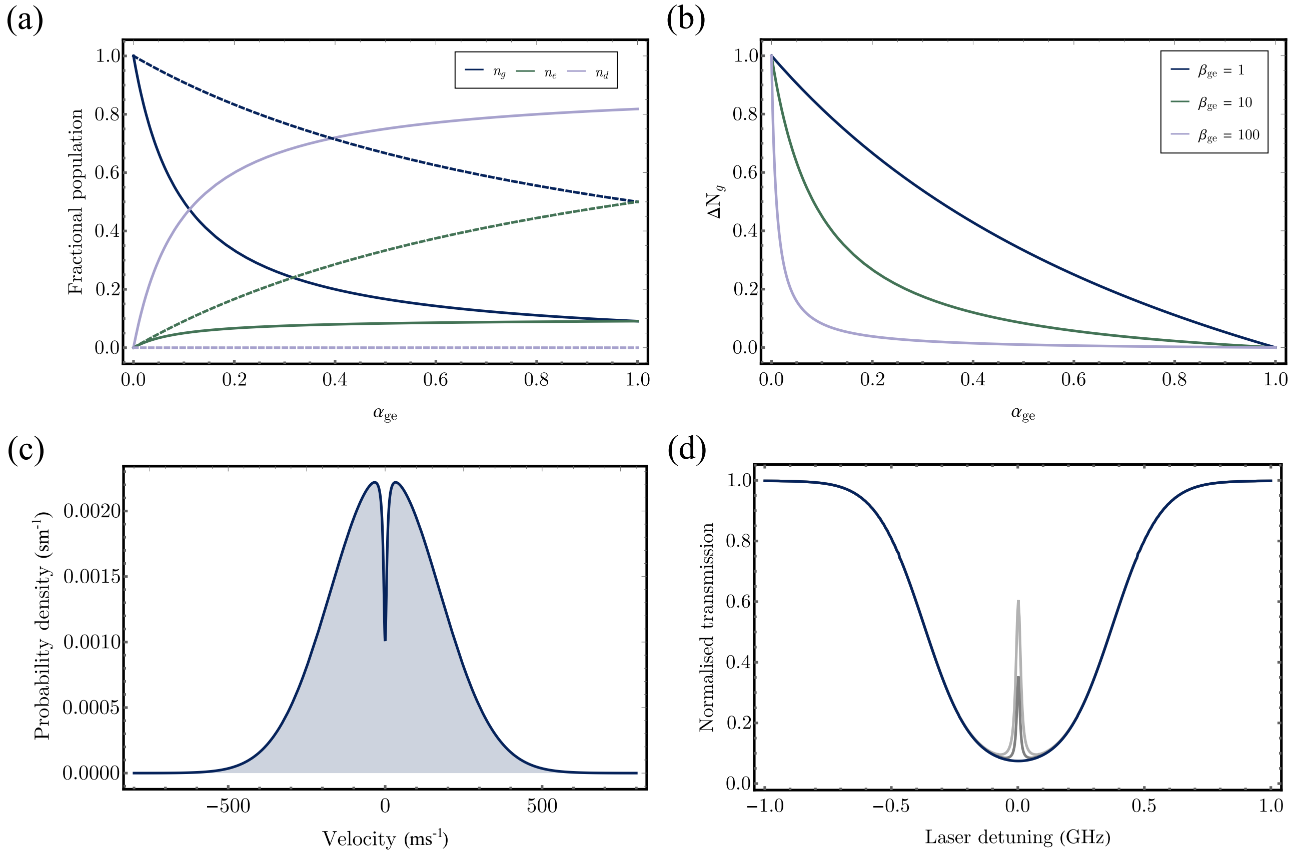

Figure 4.4: (a) Fractional populations as the saturation parameter α_{ge} is increased, with (solid lines) and without (dashed lines) optical pumping. (b) Plot of ΔN_g, related to the population difference in states $|g\rangle$ and $|e\rangle$, with varying α_{ge} and for increasing optical pumping parameter β_{ge}. (c) Velocity distribution for the ground state of a ^{87}Rb vapour at 40 °C, where positive velocity is taken to be travelling in the same direction as the probe beam. Illustrated is a hole in the distribution caused by a laser beam pumping the population out of $|g\rangle$ for the simple case of one transition, and for a pump beam perfectly on resonance with the transition. (d) Plot of the corresponding Doppler broadened spectra, without (dark blue line) and with pump beam (grey), showing the emergence of a sub-Doppler feature at the centre. Both grey peaks correspond to the same pump laser intensity but the smaller darker peak has $\beta_{ge} = 40$ while the taller peak has $\beta_{ge} = 160$, consistent with a beam radius increase of a factor four.

positive velocity refers to travelling in the direction of the probe beam (resulting in a red Doppler shift). Typically in vapours of alkalis, optical pumping dominates over saturation [360]. The result in the spectrum is the emergence of a sub-Doppler feature in the centre of the Doppler broadened absorption dip, plotted in Fig. 4.4d in grey, with the both grey lines originating from a pump beam of the same intensity but the smaller darker grey line was simulated with a $\beta_{ge} = 40$ while the taller peak was simulated with $\beta_{ge} = 160$. This change in β_{ge} is consistent with an decrease in R by a factor four.

Transit rate

It is important that we determine an accurate value for R, as this has a large affect on the degree of optical pumping, as illustrated in Fig. 4.4d. Our initial expression in Eq. 4.17 fails to consider that the absorption of one photon is enough to cause an atom to be pumped to the dark state, and so optical pumping can continue well into the wings of the pump laser. From this argument we can see that stronger transitions will likely see a larger effective beam radius and so we should scale R depending on the transition being interrogated. As in Himsworth et al. [346], we apply a scaling to R_0 relative to the reduced saturation intensity I_{ge}^R,

$$I_{ge}^R = \frac{I_{ge}}{\Gamma}\left(\frac{\Gamma + R_0}{2 + (\Gamma - \Gamma_{ge})/R_0}\right) , \tag{4.29}$$

which is a modified saturation intensity for open two level system. We then redefine the transit rate for the $|g\rangle \rightarrow |e\rangle$ transition R_{ge} as,

$$R_{ge} = \frac{R_0}{\sqrt{\frac{1}{2}\ln(I_P/I_{ge}^R)}} , \tag{4.30}$$

which effectively rescales the radius from $1/e^2$ to where the pump intensity equals I_{ge}^R.

Extension beyond three levels

We can extend the previous treatment to include the full hyperfine structure of the Rb excited state manifold by summing over all excited states, indexed by k,

$$n_g = \frac{\mathcal{N}_g}{1 + \sum_k \alpha_{gk}\beta_{gk}} \tag{4.31}$$

$$n_k = n_g \alpha_{gk} \,, \tag{4.32}$$

which gives,

$$\sigma(\omega) = \frac{\hbar\omega_{ge}}{c} \int_{-\infty}^{\infty} \mathcal{N}_g \, \Delta N_g(v) \sum_k B_{gk} L_{gk}(\omega, v) f(v) dv \,, \tag{4.33}$$

with $\Delta N_g(v)$ amended to,

$$\Delta N_g(v) = \frac{1 - \sum_k \frac{\mathcal{D}_g}{\mathcal{D}_k} \alpha_{gk}(v)}{1 + \sum_k \alpha_{gk}(v)\beta_{gk}} \,. \tag{4.34}$$

For completeness we will include a sum over the ground state manifold as well (indexed by i), accounting for any off resonant absorption and stimulated emission on the dark state transition,

$$\sigma(\omega) = \frac{\hbar\omega_{ge}}{c} \int_{-\infty}^{\infty} \sum_i \left(\mathcal{N}_i \, \Delta N_i(v) \sum_k B_{ik} L_{ik}(\omega, v) \right) f(v) dv \,. \tag{4.35}$$

In Fig. 4.5b we have plotted the resulting spectrum while scanning a low intensity probe beam across a Doppler broadened transition resulting from two excited states, while an overlapped pump laser counter-propagates. We see a total of three sub-Doppler peaks. The outer two originate from the probe and pump laser interacting with the same transition. The middle peak is a crossover feature. In Fig. 4.5a we can see that the velocity distribution causes the saturation and optical pumping of multiple transitions at once. As the probe beam is scanned across the Doppler broadening, it too interacts with multiple transitions. For Fig. 4.5 we see a ‘true’ sub-Doppler feature when the probe beam is blue (red) shifted onto resonance and interrogates the same transition as the pump beam which is red (blue) shifted onto resonance. In contrast to the traditional case of saturation absorption spectroscopy (SAS), which has both beams scanning with the same frequency (often derived from the same laser), these sub-Doppler features will not necessarily occur at the frequency of the stationary transition. The crossover feature occurs when the probe and pump are interacting with different transitions that share the same ground state and so are still subject to the same saturation and optical pumping.

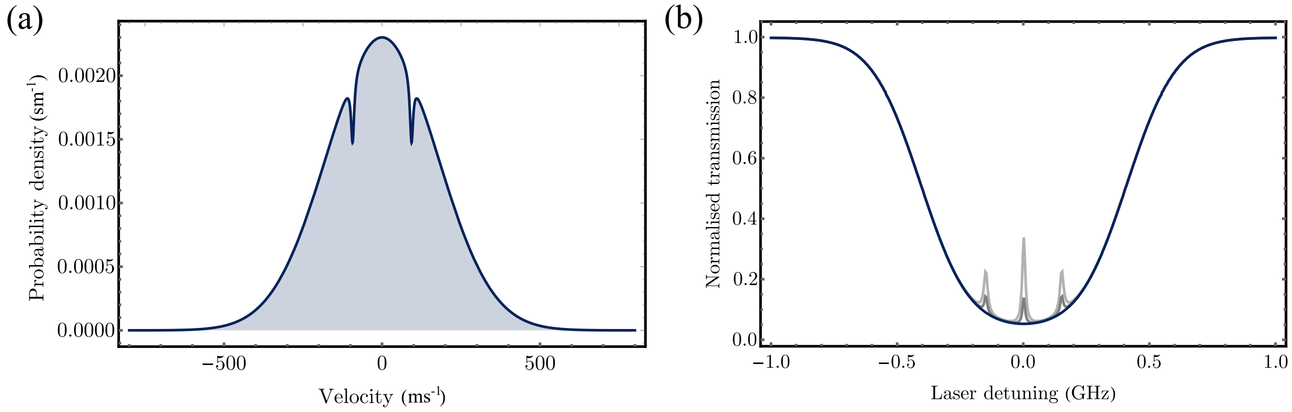

Figure 4.5: (a) Velocity distribution of ground state. The pump beam is set to a frequency half way between the two ground to excited state transitions, resulting in two dips in the velocity distribution, corresponding to velocities which Doppler shift the pump beam onto resonance with the two transitions. (b) The corresponding probe transmission spectrum, showing the Doppler broadened absorption without (dark blue line) and with pump beam (grey), showing the emergence of a sub-Doppler features. Both grey peaks correspond to the same pump laser intensity but the smaller darker peak has $\beta_{ge} = 40$ while the taller peak has $\beta_{ge} = 160$, consistent with a beam radius increase of a factor four. The two outer peaks originate from the probe laser interacting with the same transition as the pump beam, and therefore seeing a reduction in population. The middle peak is a crossover feature, where the probe beam is at the same frequency as the pump laser (half way between the two transitions) and so interacts with both velocity dips created by the pump, resulting in a larger peak.

For the system presented in Fig. 4.5, this occurs when the probe in equidistant between the two transitions, where it experiences a greater transmission due to interacting with two sets of holes in the velocity distribution at once.

Fluorescence

We now have an expression to compute the change in intensity of a probe laser, where the cross section is a function of the counter-propagating pump beam. For SAS measurements, where the probe beam is usually in the microwatt range, this plus an additional background is sufficient to describe the measurement. However, as the probe beam approaches the single photon level, the spontaneous emission of the atoms becomes a non-negligible contribution to the spectrum and so to accurately describe the experiment, we must include an additional fluorescence term.

The total fluorescence collected from the ensemble, assuming no significant re-absorption is,

$$I_{\text{fluor}}(\omega_p, v) = \eta_{\text{fluor}} \Gamma N_v \pi r^2 L \left(\int_{-\infty}^{\infty} f(v) \sum_i \frac{\mathcal{N}_i \sum_k \frac{\mathcal{D}_i}{\mathcal{D}_k} \alpha_{ik}(\omega_p, v)}{1 + \sum_k \alpha_{ik}(\omega_p, v) \beta_{ik}} \right), \tag{4.36}$$

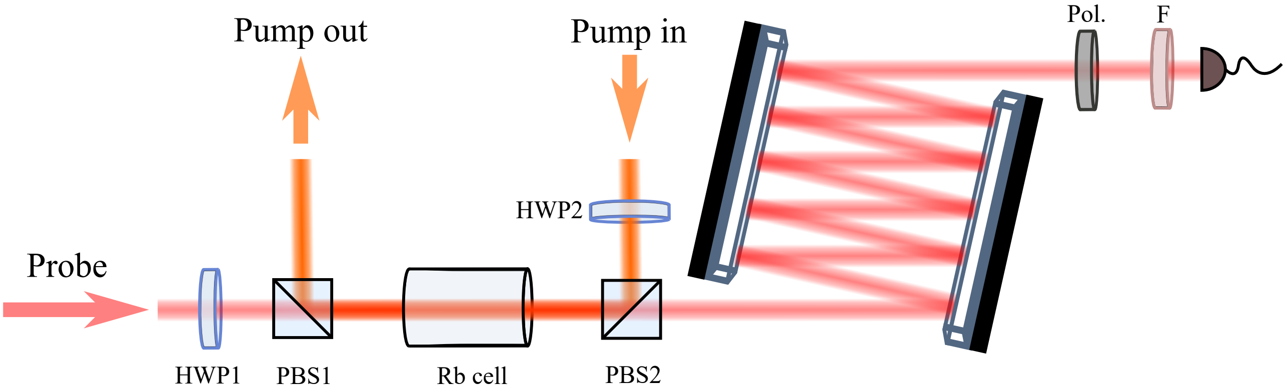

Figure 4.6: Schematic of experimental setup. The single photon level probe beam (shown in red) has a linear polarization set by the first half-wave plate (HWP1) such that it is transmitted through each polarizing beam splitter (PBS1 and PBS2). The linear polarization of the pump beam (shown in orange) is rotated by HWP2 such that it is reflected from each PBS2 and PBS1. Each of these beams may be tuned independently. Once transmitted through the Rb cell and PBS2, the probe beam is reflected many times between to planar mirrors to increase the distance of propagation to the avalanche photo-diode. This reduces the amount of background fluorescence recorded by the APD. To further reduce this background signal a polariser (Pol.) is use to filter out the randomly polarized fluorescence, as well as a long pass filter F ($> 770\,\mathrm{nm}$), which rejects any scattered light outside the Rb transition being investigated.

where the term inside the brackets is the total fractional population in the excited manifold. The fluorescence collection efficiency η_{fluor} accounts for the solid angle overlap between the collection fibre and the isotropically emitted fluorescence.

4.2 Experiment

4.2.1 Setup

The experimental setup, similar to SAS, features two counter-propagating lasers shown in Fig. 4.6: the pump beam which causes a redistribution of the atomic population and a probe field to measure this change in population. Both fields are independently tuned in frequency. An attenuated continuous-wave (cw) Ti:sapphire laser (MSquared SolsTiS) is used as the single-photon level photon probe and its polarisation is adjusted by a half-wave plate (HWP1) such that it is transmitted through both polarizing beam splitters (PBS1 and PBS2) before being coupled into a multimode fibre of core diameter $62.5\,\mu\mathrm{m}$ (Thorlabs) and detected by a silicon avalanche photodiode (SPCM-AQR-14-FC, Excelitas). The polarisation of the pump beam is controlled via HWP2 and enters through the top port of PBS2, travelling in the opposite direction through the cell to the probe beam with an orthogonal polarisation, before being reflected from PBS1.

Interaction with the pump beam causes the atoms to fluoresce at all polarisations, a signal which is many times larger than the probe signal. To minimise the fluorescence detected by the single photon detector, we propagate the probe approximately two metres by repeatedly bouncing between two mirrors, thereby reducing the solid angle overlap by around 10^{-10}. We further filtered the scattered pump light through a polariser immediately before the APD, along with a 780 ± 10 nm bandpass filter (Thorlabs) to reject any scattered room light. A temperature controller (TC200, Thorlabs) is used to regulate the temperature of the 7.5 cm long Rb vapor cell (quartz vapor reference cell, Thorlabs) to 40 °C. No attempt is made to protect the Rb cell from magnetic fields.

We independently scan the frequency of the probe and pump lasers between $384.2267-384.2302$ THz to measure a two dimensional Doppler free absorption spectrum. Both beams are kept at constant powers with acousto-optic modulators, regulated by analogue proportional-integral-derivative controllers (SIM960). The probe beam is attenuated down to 2.5 ± 0.1 Mcnts/s before the cell and the pump beam is set to $791 \pm 2\,\mu$W. At each point of the scan, we integrate for 20 ms to ensure that a steady-state population has been reached.

4.2.2 Results

The simulated and experimentally measured spectra are shown in Fig. 4.7a and b respectively. The experimental data was been corrected for slow drifts of the probe and pump frequencies over the course of the scan - approximately two hours. The probe frequencies were corrected using the Doppler-broadened absorption features in each horizontal scan and the pump frequencies were corrected to ensure the sub-Doppler features remained parallel and separated by the known hyperfine splitting [350, 351].

After these corrections, the simulated and measured spectra show close agreement. We quantify the agreement over N pixels with the mean absolute percentage error,

$$MAPE = \frac{1}{N}\sum_{j,k}\left|\frac{S_{j,k} - M_{j,k}}{S_{j,k}}\right| , \tag{4.37}$$

where $S_{j,k}$ and $M_{j,k}$ denote the j'th row and k'th column of the simulated and measured spectrum respectively. We choose to take the absolute value in Eq. 4.37, rather than the square, to reduce the affect of 'outliers' in the measured data, which we discuss in the final paragraph of this section.

Recall that the vapour pressure obtained from Eq. 4.4 is an estimate, and so for the simulation shown in Fig. 4.7b the Rb number density was allowed to vary (while maintaining the ratio of natural abundances of the isotopes) to minimise the $MAPE$. The $MAPE$ was optimised over a few selected slices of the data due to lengthy computation involved in calculating the full spectrum. We find value of $2.688 \pm 0.003 \times 10^{10}\,\mathrm{cm}^{-3}$ for ^{85}Rb and $1.037 \pm 0.001 \times 10^{10}\,\mathrm{cm}^{-3}$ for ^{87}Rb. If the vapour pressure in Eq. 4.4 is assumed to be exact, then these number densities correspond to a temperature of $38.76 \pm 0.01\,^{\circ}\mathrm{C}$. This discrepancy (from $40\,^{\circ}\mathrm{C}$) could be explained by a combination of a systematic offset of the temperature controller probe, as well as a temperature gradient between the heated portion of the cell and the Rb. The fluorescence prefactor was also extracted from the data and found to be $\eta_{fluor} = 1.2 \times 10^{-9}$, consistent with the earlier 10^{-10} estimatation. With these three extracted values, we calculate on overall $MAPE = 3.11\%$.

For the case of the pump being off resonance with the Doppler broadened transition, scanning the probe across the two isotopes shows Doppler-broadened absorption, plotted in Fig. 4.7c. As the pump beam approaches resonance, we see an increase in the background, caused by fluorescence, shown for a fixed probe frequency in Fig. 4.7d. Scanning the probe laser across the transition while the pump laser is resonant, we see the addition of sub-Doppler peaks within the absorption dip, three of which are crossover peaks.

For increasing pump laser frequency, the sub-Doppler peaks shift to lower probe frequencies,

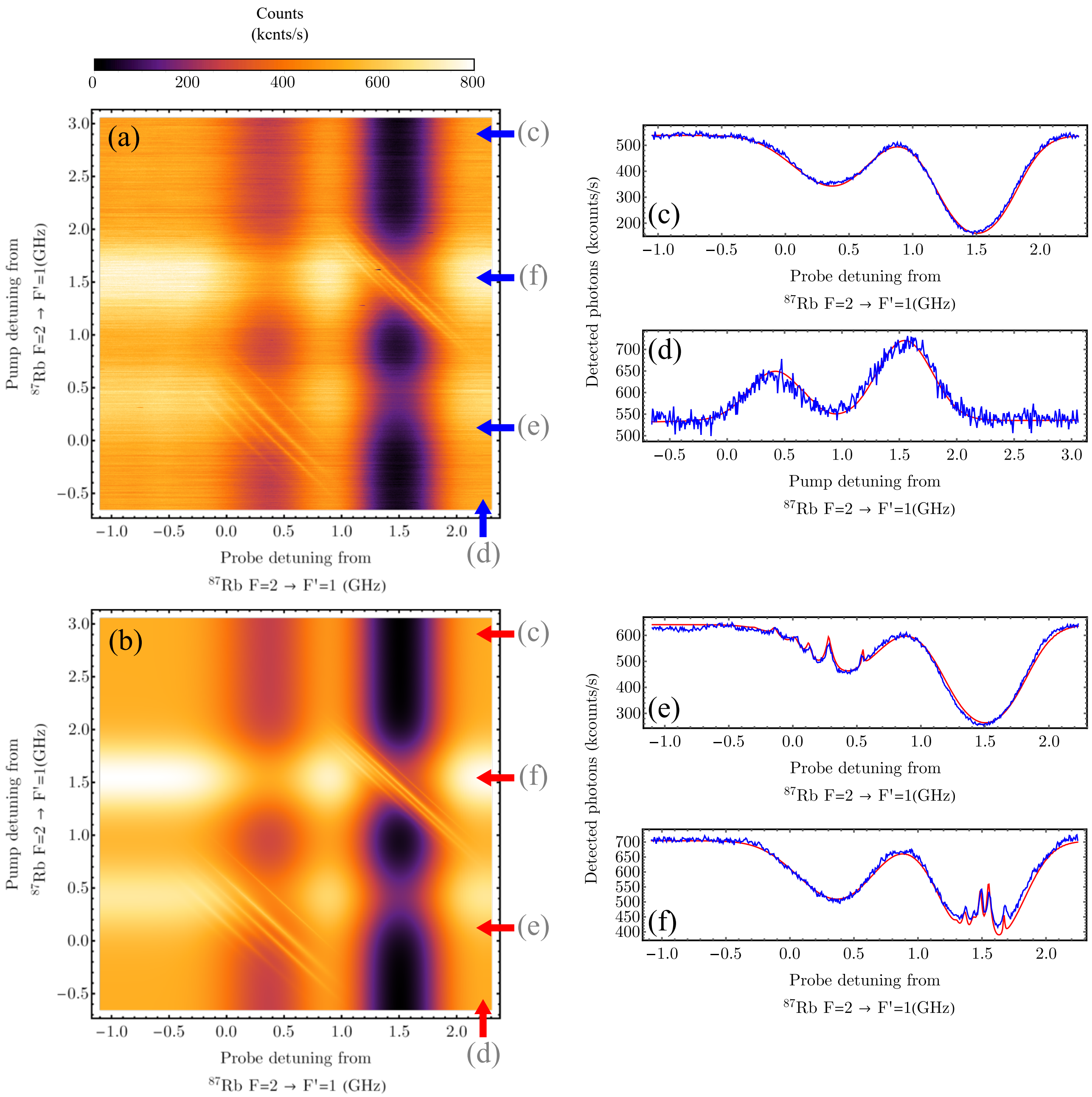

Figure 4.7: Density plots of the number of transmitted probe photons through the Rb cell with varying probe laser detuning on the x-axis and varying pump laser detuning on the y-axis. The antidiagonal sub-Doppler features towards the bottom left result from the ^{87}Rb D$_2$ $F = 2 \rightarrow F' = 1, 2, 3$ transitions and the features towards the top right result from ^{85}Rb D$_2$ $F = 2 \rightarrow F' = 2, 3, 4$ transitions. (a) Experimental data. (b) Simulation. Cuts through of the experimental (blue) and simulated (red) density plots, with the positions of the cuts through indicated on the density plots. (c) Horizontal slice showing the room-temperature Doppler-broadened spectra. (d) Vertical slice showing the fluorescence produced by the pump beam. (e) Horizontal slice showing the sub-Doppler features of ^{87}Rb. (f) Horizontal slice showing the sub-Doppler features of ^{85}Rb.

forming the anti-diagonal lines observed in Fig. 4.7a and b. This is a result of the velocity classes that shift the pump laser onto resonance, apply the opposite shift to the probe. The traditional spectrum obtained from SAS can be found by taking the slice along the diagonal of Fig. 4.7a and b. There are some faint diagonal lines seen in Fig. 4.7a, which are the ‘outliers’ we referred to previously. These diagonal lines are due to reflections of the pump beam from optical faces in the setup, which result in a faint pump beam co-propagating with the probe. The features do not lie along the diagonal and so are not measured in normal SAS. The simulated spectrum does not include these features and so they result in a small addition to the calculated $MAPE$.

4.3 Optical pumping

As we will see in the next chapter, the efficiency of a quantum memory is proportional to optical depth. Initially, the population in a warm alkali vapour is split between both ground states and so not all of the atoms are interacting with the input photon. As well as for determining an accurate number denisty and temperature, we can use the theory developed in this chapter to model optical pumping from one ground state to the other, thereby increasing the optical depth and memory efficiency. However, for lambda quantum memories where the atomic excitation is stored in a ground state, perhaps a more important consideration is that the state used for storage be unoccupied before the memory protocol is begun. Any remaining population in the storage state will contribute noise to the stored coherence and so to have a high fidelity memory, we need to completely empty the storage state (at least for the velocity classes involved in the memory interaction).

In Fig. 4.8 we show how the population of the ^{87}Rb ground states vary for a 1 mm radius pump laser resonant with $F = 2 \rightarrow F = 2'$ transition for differing laser powers, as well as the associated spectrum that would be measured using the setup shown in Fig. 4.6, with the background and fluorescence subtracted. We have plotted the case of no pump laser in light grey, and then pump powers of 500 μW, 200 mW and 800 mW in dark blue, dark green and purple respectively. At these high powers, the fluorescence background will have a large contribution

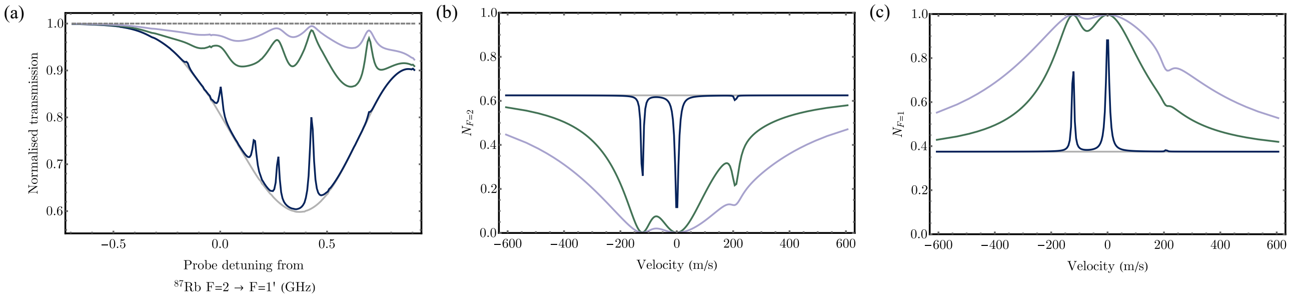

Figure 4.8: (a) Simulated probe transmission spectrum, with fluorescence and background subtracted. The atoms were set to 40 °C. In light grey is the case with no pump beam. For a pump beam of radius 1 mm, dark blue corresponds to a pump power of 500 μW, dark green to 200 mW and purple to 800 mW. (b) Ground state $F = 2$ population across the atomic velocity distribution. (c) Ground state $F = 1$ population across the atomic velocity distribution.

to the spectrum and may necessitate the probe beam being propagated for a longer distance than that used to measure Fig. 4.7 in order to distinguish the signal. Alternatively a higher intensity probe beam may be used, where it may be necessary to include the probe intensity in the calculation of ΔN_i.

For the spectrum plotted in Fig. 4.8a, the probe transmission tends towards 100% as the population is optically pumped out of the $F = 2$ ground state, shown in Fig. 4.8b. We can see the population reaching effectively zero for a narrow band of velocities at a laser power of 200 mW, with the hole in the velocity distribution widening further for 800 mW. Even when the majority of the population was been pumped away around $v = 0$, there is still some residual absorption of the probe beam caused by the tails of higher velocity classes remaining in $F = 2$. The majority of the pumped population accumulates in the $F = 1$ ground state, as shown in Fig. 4.8c. The dips seen in $N_{F=1}$ at high intensities are due to transitions $F = 2 \rightarrow F = 3'$ (occurring at $v \approx 200$ m/s) which cannot decay to $F = 1$. For storage of a photon with bandwidth ≈ 100 MHz, a 200 mW pump laser would appear to be sufficient.

Hollow core photonic crystal fibres filled with Rb atoms have shown promise for integrating memories with fibre networks. The smaller mode diameter ($\sim 60\,\mu$m) allows for higher intensities to be reached, though the transit decay rate is significantly increased. In Fig. 4.9 we plot the simulated spectrum and ground state populations, using the same laser intensities as in Fig. 4.8 but reducing the beam radius to 30 μm. Implicit in this simulation is the assumption that the atoms return after contacting the fibre walls with the initial population distribution.

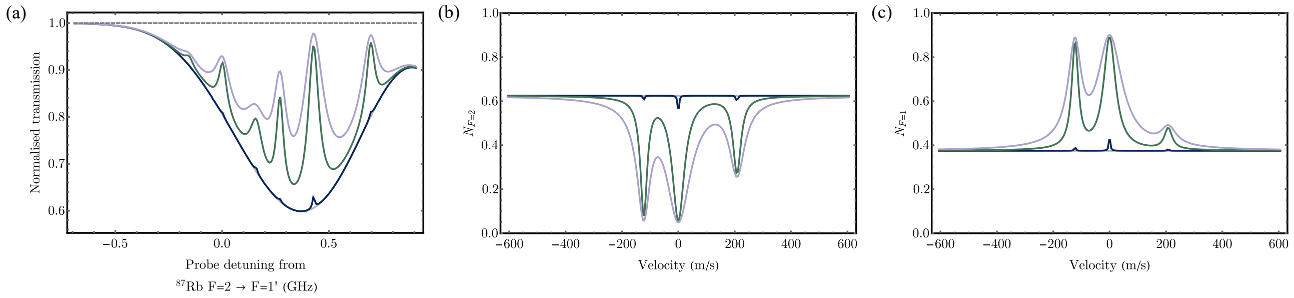

Figure 4.9: (a) Simulated probe transmission spectrum, with fluorescence and background subtracted. The atoms were set to 40 °C. In light grey is the case with no pump beam. For a pump beam of radius 30 μm, dark blue corresponds to a pump power of 450 nW, dark green to 180 μW and purple to 720 μW. (b) Ground state $F = 2$ population across the atomic velocity distribution. (c) Ground state $F = 1$ population across the atomic velocity distribution.

The simulation shows the higher transit decay rate resulting in less efficient optical pumping.

In Chapter 5 we will discuss how the preparation of particular m_F states can aid in removing unwanted transitions from the memory interaction, reducing noise and increasing efficiency. The treatment described in this chapter can also be extended to optical pumping of individual m_F sublevels and is left to future work.

Chapter 5

Light-Matter Interaction

In this chapter, we will derive Maxwell-Bloch equations to describe the coherent interaction of light with an ensemble of atoms. We will begin with near resonant storage using a $\Lambda-$level configuration of levels: two ground states and an excited state, shown in Fig. 5.1a. Our goal is to store an input photon, near resonant with the transition $|g\rangle \rightarrow |e\rangle$ as a long lived atomic coherence. We will mediate the transfer of photon coherence to atomic coherence by using a classical control field. Following this, we will derive analytical expressions characterising the efficiency of storing and retrieving photons, before describing a technique to optimise the temporal shape and phase of the control field. Next, we begin to make our system more realistic by adding in four-wave mixing noise, then extending our derived equations to describe multiple hyperfine excited states. Finally we will investigate how the derived optimums scale to warm vapour temperatures.

The initial part of the derivation will resemble the treatment used for single dibenzoterrylene (DBT) molecules from Chapter 2, though with an additional quantum light field included to describe the input signal the photon. We will then sum up the contributions from all of the atoms in the ensemble, culminating in an increased interaction strength, quantified by the ensemble optical depth. Note that the treatment from Chapter 4 is not suitable here as we are for from the steady state regime and cannot neglect the atomic coherences.

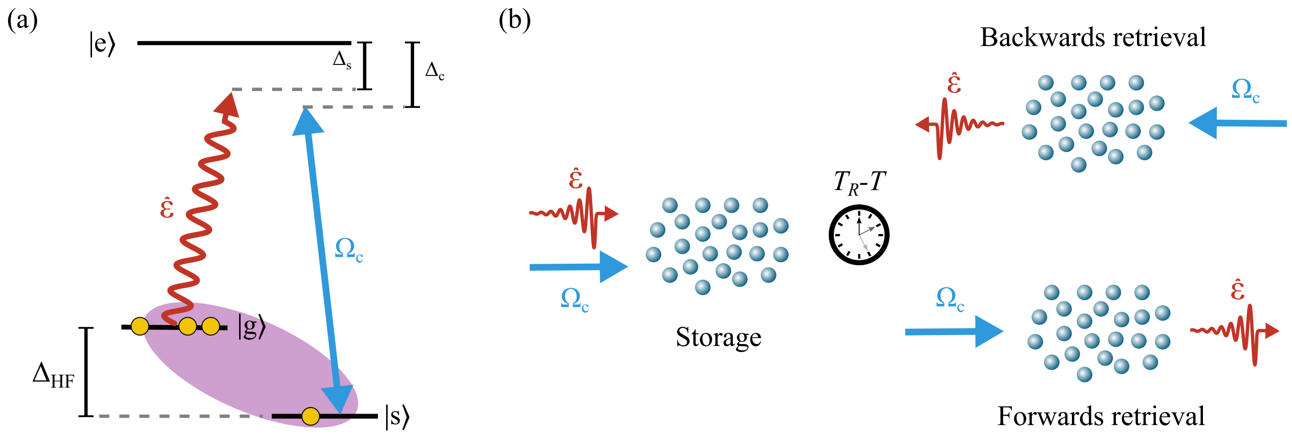

Figure 5.1: (a) Λ-configuration of energy levels, where a quantum photon field is near-resonant to the $|g\rangle \rightarrow |e\rangle$ transition, with a detuning of Δ_s. A classical control field is near-resonant with the $|s\rangle \rightarrow |e\rangle$ transition, with a detuning of Δ_c. The photon coherence is mapped to an atomic coherence between the two ground hyperfine ground states, referred to as the spin wave (represented by the purple oval), where the hyperfine splitting is denoted by Δ_{HF}. (b) The photon and control field arrive from the same direction and in the same spatial mode (not shown). After the photon coherence is transferred to the spin wave at time T, sometime later at time T_R the photon may be recovered by applying the retrieval control field in the same direction as the storage control field, resulting in the photon travelling in the same direction as the initially stored photon and referred to as forward retrieval. Alternatively, the control field may be applied in the reverse direction, causing the retrieved photon to propagate in the opposite direction to the initial photon, referred to as backward retrieval.

5.1 Near-resonant $\Lambda-$system

The general scheme is pictured in Fig. 5.1a. Initially, all atoms are assumed to be optically pumped to the ground state $|g\rangle$. A photon, near resonant with the transition from $|g\rangle$ to excited state $|e\rangle$, without the presence of any other fields, will induce an atomic polarisation on this transition, represented by the operator $\sigma_{ge} = |g\rangle\langle e|$. This coherence will decohere at a rate $\gamma_e = \Gamma_e/2$, where Γ_e is the population decay rate of the excited state. Unlike with DBT hosted in an organic crystal, the atomic ensemble has no additional dephasing from phonon coupling to the environment, however there are other mechanicsms which can lead to additional decoherence, such as atom-atom or atom-wall collisions, as well as motional dephasing. We will discuss these other mechanisms in more detail in Section 5.5, but for now we will just include γ_e as the decoherence rate due to excited state decay. The stronger the interaction between the photon and the $|g\rangle \rightarrow |e\rangle$ transition, the larger the decoherence rate, so we would like to couple σ_{ge} to another atomic coherence: one which is much longer lived.

A second light field, referred to as the control field, is intense enough to modify the overall Hamiltonian, and is near resonance with the storage state $|s\rangle$ (empty second ground state) and excited state $|e\rangle$. This field will couple σ_{ge} to an atomic coherence between the two ground states $\sigma_{gs} = |g\rangle\langle s|$, termed the spin wave. There is no dipole moment coupling $|g\rangle$ and $|s\rangle$ and so neglecting any additional dephasing mechanisms, $\gamma_s = 0$, with γ_s the decoherence rate of σ_{gs}. We can therefore store the photon using σ_{gs} and retrieve the atomic coherence back as a photon by reversing the process. The photon may be retrieved in the forwards or backwards direction, as illustrated in Fig. 5.1b, depending on the direction of the retrieval control field.

Memory protocols based on near-resonant Λ−systems are often referred to as electromagnetically induced transparanency (EIT) protocols, due to early experiments and theoretical treatment of stopped light in atomic ensembles [286, 287]. EIT storage uses the control field to adiabatically map the photon coherence directly to the spin wave, with negligible atomic polarisation σ_{ge} [284, 285, 288]. This typically leads to strong dispersion of the photon wavepacket. However, not all protocols based on this system feature EIT. Recently the Autler-Townes splitting (ATS) protocol demonstrated single photon level storage [235]. The ATS protocol uses the control field to split the $|g\rangle \to |e\rangle$ resonance using the AC Stark effect. The resulting split resonance absorbs the photon and the coherence oscillates between σ_{ge} and σ_{gs}, with storage achieved by switching off the control field when the spin wave coherence is maximised [288]. The period of the oscillation is determined by the strength of the control field, which if left on, leads to the output photon wavepacket exhibiting a periodic echo-like behaviour. In reality, the storage and retrieval mechanism is often a hybrid of the two regimes.

The Maxwell-Bloch equations derived in the next section, encompass all near-resonant Λ−system protocols, regardless of the underlying mechanism used for storage. The derivation will closely follow the derivations found in Refs. [232, 264, 361, 362].

5.1.1 Equations of motion

Hamiltonian

Similarly to Chapter 2, we begin with the modified Hamiltonian,

$$H = H_A + H_{ED} + H_L \,, \tag{5.1}$$

with $H_A = \hbar \sum_j \omega_j \sigma_{jj}$ the atomic Hamiltonian where σ_{jj} is the population in state $|j\rangle$ and $H_{ED} = -\hat{\boldsymbol{\mu}} \cdot \boldsymbol{E}$ is the electric dipole Hamiltonian, with $\hat{\boldsymbol{\mu}}$ the atomic transition dipole operator and $\boldsymbol{E}$ is the total electric field. H_L is the optical free-field Hamiltonian of the control and photon fields and can be written as [264],

$$H_L = \frac{\epsilon_0}{2} \int dt (\boldsymbol{E_c^2} + c^2 \boldsymbol{B_c^2}) + \int d\omega \, \hbar\omega \left(\hat{a}^\dagger(\omega) \hat{a}(\omega) + 1/2 \right) \,. \tag{5.2}$$

The first integral term pertains to the classical control field, where ϵ_0 is the vacuum permittivity, c is the speed of light, and $\boldsymbol{E_c}$ and $\boldsymbol{B_c}$ refer to the control electric and magnetic field respectively. The second term is due to the photon field, with $\hat{a}^\dagger(\omega)$ and $\hat{a}(\omega)$ denoting the narrowband creation and annihilation operators for a photon of frequency ω.

For the $\Lambda-$system, we can write $\hat{\boldsymbol{\mu}} = \boldsymbol{\mu}_{ge} \sigma_{ge} + \boldsymbol{\mu}_{se} \sigma_{se} + h.c.$, since the transition $|g\rangle \leftrightarrow |s\rangle$ is not dipole allowed, with $\sigma_{jk} = |j\rangle \langle k|$ the transition operator.

The total electric field $\boldsymbol{E} = \boldsymbol{E}_c + \boldsymbol{E}_s$ is made up of the classical control field $\boldsymbol{E}_c$ and a quantum signal field $\boldsymbol{E}_s$, which we will assume only propagates along the z-axis with negligible divergence such that we can invoke the paraxial approximation[1] [232]. We write our control field with central angular frequency ω_c as,

$$\boldsymbol{E}_c = \boldsymbol{v}_c \frac{\mathcal{E}_c(z,t)}{2} \exp[i\omega_c(t - z/c)] + c.c. \,, \tag{5.3}$$

with $\boldsymbol{v}_c$ denoting the polarisation vector of the control field and $\mathcal{E}_c$ is the slowly-varying[2] spatio-temporal field amplitude, where we have included a factor of $1/2$ so that the amplitude of $\boldsymbol{E}_c$ is $\mathcal{E}_c$ due to the addition of the complex conjugate, *c.c.*.

---

[1] As in the previous chapter, this is reasonable given that the transverse area of the light fields is much larger than the wavelength squared.

[2] We have made the slowly-varying envelope approximation, where we assume the pulse envelope varies slowly compared to the central frequency of the field, i.e. the bandwidth of the field is much smaller than its central frequency.

The signal field requires a quantum mechanical description, which we write as [232],

$$\boldsymbol{E}_s = i\boldsymbol{v}_s \int g(\omega)\hat{a}(\omega)\exp[-i\omega z/c]d\omega + h.c.\,, \tag{5.4}$$

where $\boldsymbol{v}_s$ is the polarisation vector of the signal field and $g(\omega) = \sqrt{\hbar\omega/4\pi\epsilon_0 c}$ is the photon mode amplitude. Substituting $\hat{a}(\omega,t) = \hat{a}(\omega)\exp[i\omega t]$ and making the slowly varying envelope approximation, we can write the signal field in a similar form to the control,

$$\boldsymbol{E}_s = i\boldsymbol{v}_s g_s \frac{\mathcal{E}_s(z,t)}{2}\exp[i\omega_s(t-z/c)] + h.c.\,, \tag{5.5}$$

in which we have defined $g_s = \sqrt{2\pi}g(\omega_s)$ and the slowly varying broadband annihilation operator $\mathcal{E}_s(z,t)$,

$$\mathcal{E}_s(z,t) = \frac{\exp[-i\omega_s(t-z/c)]}{\sqrt{2\pi}}\int d\omega\hat{a}(\omega,t)\exp[-i\omega z/c]\,. \tag{5.6}$$

Optical-Bloch equations

Following the same procedure as Chapter 2, we now find how the atomic coherences σ_{jk} evolve in time using the Heisenberg equation,

$$\hbar\partial_t\sigma_{jk} = i[\sigma_{jk}, H_A + H_{ED} + H_L]\,. \tag{5.7}$$

We can take advantage of the fact that H_L always commutes with σ_{jk} and so does not affect $\partial_t\sigma_{jk}$. This results in the following equations for atomic populations,

$$\begin{aligned}\hbar\partial_t\sigma_{gg} &= -i\boldsymbol{E}\cdot(\boldsymbol{\mu}_{ge}\sigma_{ge} - h.c.)\\ \hbar\partial_t\sigma_{ss} &= -i\boldsymbol{E}\cdot(\boldsymbol{\mu}_{es}\sigma_{es} - h.c.)\\ \hbar\partial_t\sigma_{ee} &= -\partial_t(\sigma_{gg} + \sigma_{ee})\,,\end{aligned} \tag{5.8}$$

and the following for atomic coherences,

$$\begin{aligned}
\hbar\partial_t\sigma_{ge} &= i\hbar\omega_{eg}\sigma_{ge} - i\boldsymbol{E}\cdot\left(\boldsymbol{\mu}_{ge}^*(\sigma_{gg}-\sigma_{ee}) + \boldsymbol{\mu}_{es}\sigma_{gs}\right)\\
\hbar\partial_t\sigma_{gs} &= i\hbar\omega_{sg}\sigma_{gs} - i\boldsymbol{E}\cdot\left(\boldsymbol{\mu}_{es}^*\sigma_{gs} - \boldsymbol{\mu}_{ge}^*\sigma_{es}\right)\\
\hbar\partial_t\sigma_{es} &= i\hbar\omega_{se}\sigma_{es} - i\boldsymbol{E}\cdot\left(\boldsymbol{\mu}_{es}^*(\sigma_{ee}-\sigma_{ss}) - \boldsymbol{\mu}_{ge}\sigma_{gs}\right),
\end{aligned} \tag{5.9}$$

where $\omega_{jk} = \omega_j - \omega_k$.

To begin simplifying these equations, for an ensemble containing many atoms, where all of the atoms begin in $|g\rangle$, the absorption of one photon will not lead to a significant change in population, so we can set $\sigma_{gg} = 1$ and $\sigma_{ee} = \sigma_{ss} = 0$, and ignore the equations for atomic population.

We proceed to transform each of the coherences to a frame rotating at the corresponding resonance frequency, $\widetilde{\sigma}_{jk} = \sigma_{jk}\exp[-i\omega_{kj}\tau]$, where $\tau = t - z/c$ is the retarded time. With this transformation we have,

$$\begin{aligned}
\hbar\partial_\tau\widetilde{\sigma}_{ge} &= -i\boldsymbol{E}\cdot\left(\boldsymbol{\mu}_{ge}^*\exp[-i\omega_{eg}\tau] + \boldsymbol{\mu}_{es}\widetilde{\sigma}_{gs}\exp[-i\omega_{es}\tau]\right)\\
\hbar\partial_\tau\widetilde{\sigma}_{gs} &= -i\boldsymbol{E}\cdot\left(\boldsymbol{\mu}_{es}^*\widetilde{\sigma}_{ge}\exp[+i\omega_{es}\tau] - \boldsymbol{\mu}_{ge}^*\widetilde{\sigma}_{es}\exp[-i\omega_{eg}\tau]\right)\\
\hbar\partial_\tau\widetilde{\sigma}_{es} &= +i\boldsymbol{E}\cdot\left(\boldsymbol{\mu}_{ge}\widetilde{\sigma}_{gs}\exp[+i\omega_{eg}\tau]\right).
\end{aligned} \tag{5.10}$$

Next we insert the full expression for $\boldsymbol{E}$, assuming that the signal field only couples to the $|g\rangle \to |e\rangle$ transition, the control field only couples to $|s\rangle \to |e\rangle$, and only keep terms oscillating at the difference frequencies (the rotating wave approximation),

$$\begin{aligned}
\hbar\partial_\tau\widetilde{\sigma}_{ge} &= -i\boldsymbol{\mu}_{ge}^*\left(i\boldsymbol{v}_s g_s\frac{\mathcal{E}_s}{2}\exp[+i\Delta_s\tau]\right) - i\boldsymbol{\mu}_{es}\widetilde{\sigma}_{gs}\left(\boldsymbol{v}_c\frac{\mathcal{E}_c}{2}\exp[+i\Delta_c\tau]\right)\\
\hbar\partial_\tau\widetilde{\sigma}_{gs} &= -i\boldsymbol{\mu}_{es}^*\widetilde{\sigma}_{ge}\left(\boldsymbol{v}_c^*\frac{\mathcal{E}_c^*}{2}\exp[-i\Delta_c\tau]\right) + i\boldsymbol{\mu}_{ge}^*\widetilde{\sigma}_{es}\left(i\boldsymbol{v}_s g_s\frac{\mathcal{E}_s}{2}\exp[+i\Delta_s\tau]\right)\\
\hbar\partial_\tau\widetilde{\sigma}_{es} &= +i\boldsymbol{\mu}_{ge}\widetilde{\sigma}_{gs}\left(-i\boldsymbol{v}_s^* g_s\frac{\mathcal{E}_s^\dagger}{2}\exp[-i\Delta_s\tau]\right),
\end{aligned} \tag{5.11}$$

where we have defined $\Delta_s = \omega_s - \omega_{eg}$ and $\Delta_c = \omega_c - \omega_{es}$. We can make a further simplification by only keeping terms that are linear in coherence: any atomic coherence in the system will have originated from the photon coherence, so the multiplication of an atomic coherence by the photon coherence is second order and can be assumed to be small [232]. This leaves us with two equations for the atomic coherences,

$$\begin{aligned}\hbar\partial_\tau\widetilde{\sigma}_{ge} &= \frac{\boldsymbol{\mu}^*_{ge}\cdot\boldsymbol{v}_s g_s\mathcal{E}_s}{2}\exp[+i\Delta_s\tau] - \frac{i\boldsymbol{\mu}_{es}\cdot\boldsymbol{v}_c\mathcal{E}_c\widetilde{\sigma}_{gs}}{2}\exp[+i\Delta_c\tau]\\ \hbar\partial_\tau\widetilde{\sigma}_{gs} &= -\frac{i\boldsymbol{\mu}^*_{es}\cdot\boldsymbol{v}^*_c\mathcal{E}^*_c\widetilde{\sigma}_{ge}}{2}\exp[-i\Delta_c\tau]\,.\end{aligned} \tag{5.12}$$

Note that we have not yet included decoherence due to spontaneous emission.

Photon propagation

We have derived equations describing the evolution of the atomic coherences and now need to describe how the photon propagates through the medium. To do so, we start with Maxwell's equation for an electric field travelling through a medium,

$$\nabla^2\mathbf{E}_s = \mu_0\partial_t^2\mathbf{D}_s\,, \tag{5.13}$$

where $\mathbf{D}_s = \epsilon_0\mathbf{E}_s + \mathbf{P}_s$ is the displacement field associated with the photon electric field and the component of atomic polarisation which acts as a source for $\mathbf{E}_s$. This leads to the wave equation,

$$\Big(\nabla^2 - \frac{1}{c^2}\partial_t^2\Big)\mathbf{E}_s = \mu_0\partial_t^2\mathbf{P}_s\,. \tag{5.14}$$

Now inserting our expression for the photon electric field, as well as defining the slowly varying atomic polarisation $\boldsymbol{P}_s = \widetilde{\boldsymbol{P}}_s\exp[+i\omega_s\tau]$ we arrive at,

$$\Big(\nabla^2 - \frac{1}{c^2}\partial_t^2\Big)(iv_s g_s\frac{\mathcal{E}_s}{2}\exp[i\omega_s\tau]) = \mu_0\partial_t^2\widetilde{\mathbf{P}}_s\exp[+i\omega_s\tau]\,, \tag{5.15}$$

which after expanding the derivatives leads to,

$$\left(\nabla_\perp^2 + \left(\partial_z^2 - \frac{1}{c^2}\partial_t^2\right) - \frac{2i\omega_s}{c}\left(\partial_z + \frac{1}{c^2}\partial_t\right)\right)\frac{\mathcal{E}_s}{2} = -i\frac{\mu_0}{g_s}v_s^*\left(\partial_t^2 + 2i\omega_s\partial_t - \omega_s^2\right)\widetilde{\mathbf{P}}_s\,, \tag{5.16}$$

where we have defined $\nabla_\perp = \partial_x + \partial_y$. We can set $\nabla_\perp = 0$ with the paraxial approximation (negligible divergence) and invoke the slowly varying envelope approximation to remove the second order derivatives, leaving,

$$\Big(\partial_z + \frac{1}{c}\partial_t\Big)\mathcal{E}_s = -\frac{\mu_0\omega_s^2}{g_s k_s}\boldsymbol{v}_s^* \cdot \widetilde{\boldsymbol{P}}_s \,. \tag{5.17}$$

We now need to relate the macroscopic polarisation $\widetilde{\mathbf{P}}_s$ with the single atomic coherence σ_{ge}.

Macroscopic coherences

Let's consider a cylindrical element of volume δV containing many atoms such that $N_v \delta V \gg 1$, where N_v is the atomic density per unit volume, while its length in the direction of photon propagation satisfies $\delta L \ll \lambda_s$ with λ_s the central wavelength of the photon, allowing us to assume a constant phase in each element. We also require that the cylindrical element has a transverse area $\delta A \gg \lambda_s^2$, so that the density of atoms is small enough to ignore any atom-atom interactions [232]. If we index the coherence such that an individual atom a, has a coherence σ_{ge}^a, the macroscopic polarisation may be written as,

$$\begin{aligned}
\boldsymbol{P}_s &= \frac{1}{\delta V}\sum_{a(r)}(\mu_{ge}\sigma_{ge}^a + h.c.)\\
\boldsymbol{P}_s &= \frac{1}{\delta V}\sum_{a(r)}(\mu_{ge}\widetilde{\sigma}_{ge}^a \exp[+i\omega_{eg}\tau] + h.c.)\\
\widetilde{\mathbf{P}}_s &= \frac{1}{\delta V}\sum_{a(r)}(\mu_{ge}\widetilde{\sigma}_{ge}^a \exp[+i\Delta_s\tau] + h.c.)\\
\widetilde{\mathbf{P}}_s &= \sqrt{N_v}\mu_{ge}\Big(\frac{1}{\sqrt{N_v}\delta V}\sum_{a(r)}\widetilde{\sigma}_{ge}^a \exp[-i\Delta_s\tau]\Big)\,,
\end{aligned} \tag{5.18}$$

where in the last line we have removed terms oscillating at the sum rather than difference frequency. From the above equation for $\widetilde{\boldsymbol{P}}_s$ we can define the macroscopic polarisation operator,

$$P_{ge} = \frac{1}{\sqrt{N_v}\delta V}\sum_{a(r)}\widetilde{\sigma}_{ge}^a \exp[-i\Delta_s\tau] \tag{5.19}$$

and a similar operator for the macroscopic spin wave,

$$S_{gs} = \frac{1}{\sqrt{N_v}\delta V}\sum_{a(r)}\widetilde{\sigma}_{gs}^a \exp[-i(\Delta_s - \Delta_c)\tau]\,. \tag{5.20}$$

We have defined these operators in this way, such that they obey bosonic commutation relation,

$$
\begin{aligned}
[F_{jk}(r,t), F^{\dagger}_{jk}(r,t)] &= \frac{1}{\sqrt{n\delta V}} \sum_{a(r)} \sum_{b(r')} [\widetilde{\sigma}^{a}_{jk}, \widetilde{\sigma}^{a}_{kj}] \\
&= \begin{cases} \frac{1}{\delta V}(\sigma_{jj} - \sigma_{kk}) & \text{if } r \wedge r' \in \delta V \\ 0 & \text{otherwise,} \end{cases}
\end{aligned}
\tag{5.21}
$$

where as $\delta V \longrightarrow 0$ the operator F_{jk} describes the annihilation of an atomic excitation in the state $|k\rangle$ at position r [232].

We can now write down equations of motion for the macroscopic operators and the photon field,

$$
\begin{aligned}
\Big(\partial_z + \frac{1}{c}\partial_t\Big)\mathcal{E}_s &= -\frac{\kappa^*_{ge}}{2} P_{ge} \\
\partial_\tau P_{ge} &= -i\Delta_s P_{ge} + \frac{\kappa_{ge}}{2}\mathcal{E}_s - \frac{i}{2}\Omega_{es} S_{gs} \\
\partial_\tau S_{gs} &= -i(\Delta_s - \Delta_c) S_{gs} - \frac{i}{2}\Omega^*_{es} P_{ge}
\end{aligned}
\tag{5.22}
$$

where,

$$
\begin{aligned}
\kappa_{ge} &= \frac{\mu^*_{ge} v_s \sqrt{N_v} g_s}{\hbar} = \frac{\mu^*_{ge} v_s}{\hbar}\sqrt{\frac{\hbar\omega_s N_v}{2\epsilon_0 c}} \\
\Omega_{es} &= \frac{\mu_{es} v_c \mathcal{E}_c}{\hbar}
\end{aligned}
\tag{5.23}
$$

Since the macroscopic coherence operators behave as bosons, we can include decoherence into the equation for P_{ge} due to spontaneous emission by adding the decoherece rate γ_e along with a Langevin noise operator, which describes fluctuations in the decay of P_{ge} that preserve the bosonic commutation relation in Eq. 5.21. Provided that the number of atoms in the states $|e\rangle$ and $|s\rangle$ remains approximately zero, the expectation value of these noise operators is zero and so we can neglect them going forward. With decoherence included the equations become,

$$
\begin{aligned}
\Big(\partial_z + \frac{1}{c}\partial_t\Big)\frac{\mathcal{E}_s}{2} &= -\kappa^*_{ge} P_{ge} \\
\partial_\tau P_{ge} &= -(\gamma_{ge} + i\Delta_s) P_{ge} + \frac{\kappa_{ge}}{2}\mathcal{E}_s - \frac{i}{2}\Omega_{es} S_{gs} \\
\partial_\tau S_{gs} &= -i(\Delta_s - \Delta_c) S_{gs} - \frac{i}{2}\Omega^*_{es} P_{ge}\,.
\end{aligned}
\tag{5.24}
$$

We can further simplify these equations by transforming to the reference frame co-propagating with the photon and control field, and writing our constants in a dimensionless form. The co-propagating frame, allows us to write both the control field and photon field as functions of $\tau = t - z/c$. The derivatives are modified to,

$$\partial_z|_t + \frac{1}{c}\partial_t|_z \rightarrow \partial_z|_\tau \tag{5.25}$$

$$\partial_t|_z \rightarrow \partial_\tau|_z \,, \tag{5.26}$$

where $|_x$ indicates that the variable x is held constant. We will normalise τ by γ_e and z by the length of the atoms L. This results in the following rescaling of variables,

$$\tau\gamma_{ge} \rightarrow \tau \tag{5.27}$$

$$\frac{z}{L} \rightarrow z \tag{5.28}$$

$$\frac{\partial_\tau}{\gamma_{ge}} \rightarrow \partial_\tau \tag{5.29}$$

$$\partial_z L \rightarrow \partial_z \tag{5.30}$$

$$\frac{\Delta_j}{\gamma_{ge}} \rightarrow \Delta_j \tag{5.31}$$

$$\frac{\Omega_{es}}{\gamma_{ge}} \rightarrow \Omega_{es} \tag{5.32}$$

$$\frac{|\kappa_{ge}|^2 L}{\gamma_{ge}} \rightarrow d \tag{5.33}$$

$$\frac{\mathcal{E}_s}{\sqrt{\gamma_{ge} L}} \rightarrow \mathcal{E}_s \tag{5.34}$$

$$P_{ge} \rightarrow P_{ge} \tag{5.35}$$

$$S_{gs} \rightarrow S_{gs} \tag{5.36}$$

Finally we have,

$$\partial_z \mathcal{E}_s = -\sqrt{\frac{d}{2}} P_{ge} \tag{5.37}$$

$$\partial_\tau P_{ge} = -(1 + i\Delta_s) P_{ge} + \sqrt{\frac{d}{2}} \mathcal{E}_s - \frac{i}{2} \Omega_{es} S_{gs} \tag{5.38}$$

$$\partial_\tau S_{gs} = -i(\Delta_s - \Delta_c) - \frac{i}{2} \Omega^*_{es} P_{ge} \tag{5.39}$$

where we have taken κ_{ge} to be real. For the simple three level system described here this is fine, however when extending our treatment to multiple excited excited states later in this chapter, we will need to remember the complex nature of κ_{ge}. The treatment so far has assumed the atoms to be stationary. We will extend this model to warm vapours in the end of this chapter.

Simulation

We numerically solve the Eqs. 5.37-5.39 using the method of lines. Both the τ and z dimensions are discretised, for the photon coherence $\mathcal{E}_s$ and the atomic coherences: τ with regular spacing and z with Chebyshev points, illustrated in Fig. 5.2a for an example simulation with photon bandwidth $32.97\gamma_e = 2\pi \times 100\,\text{MHz}$ for ^{87}Rb. The atomic coherences are initialised at $\tau = 0$ with,

$$P(z, 0) = S(z, 0) = 0 \tag{5.40}$$

and the photon coherence is initialised with,

$$\mathcal{E}_s(0, \tau) = \sqrt{\frac{2}{\tau_c}} \exp\left[-\frac{(\tau - \tau_0)}{\tau_c}\right], \tag{5.41}$$

where τ_0 is the arrival time of the photon at the beginning of the cell and τ_c is the time taken for the exponential decay to reach $1/e$ - in this example $\tau_c = 1/(32.97\gamma_e)$. The photon envelope, plotted in Fig. 5.2b, has an amplitude that is fixed by $\int_0^T d\tau\, \mathcal{E}^*_s(0, \tau)\mathcal{E}_s(0, \tau) = 1$, where T is the end of the storage simulation, i.e. only one photon is input into the system at once. The exponential decay corresponds to the temporal envelope of a photon emitted from a two-level system, like DBT. In reality, the initial sharp edge should be convolved with the shape of the excitation pulse used to excite the two-level system, though for an excitation pulse much shorter than the lifetime of the emitter, we found that this did not alter the simulation or later optimisations significantly.

At each point in time, Eq. 5.37 is solved using a spectral method [232]. The atomic coherences are then propagated using a fourth order Runge-Kutta method. We can calculate the storage efficiency η_{storage} by,

$$\eta_{\text{storage}} = \int_0^1 dz\, S^*(z,T)S(z,T) \tag{5.42}$$

where any loss comes from decoherence or photon field leaking out of the cell without being stored.

For retrieval beginning at time $T_R > T$, we can map the spin wave back to the photon field in either the forward (propagating in the same direction as the initial photon) or backward direction (opposite to the initial photon). Emission in the backwards direction is caused by reversing the direction of the control field for retrieval. For forward retrieval, the initial conditions of the retrieval simulation are simply,

$$\begin{aligned} P(z,0) &= 0 \\ \mathcal{E}_s(0,\tau) &= 0 \\ S(z,T_R) &= S(z,T)\,, \end{aligned} \tag{5.43}$$

where T_R is the start time and we have assumed that there is no spin wave decay between T and T_R. For backwards retrieval, we flip the spin wave boundary condition, so that in the simulation space all propagation is in the forwards direction. We can then flip the retrieval simulation back if we wish to concatenate it with the storage simulation, as shown in Fig. 5.2c,d and e. The amended boundary condition for backwards retrieval becomes,

$$S(z,T_R) = S(1-z,T)\,. \tag{5.44}$$

Note that we have implicitly assumed in Eq. 5.44 that the ground and storage states are degenerate in energy, i.e. $\Delta_{HF} = 0$ in Fig. 5.1a. In reality, it is often beneficial to have these states be different hyperfine ground states and so the signal and control will have differing wave vectors, thereby imparting some momentum onto the spin wave. We will discuss the effect of a

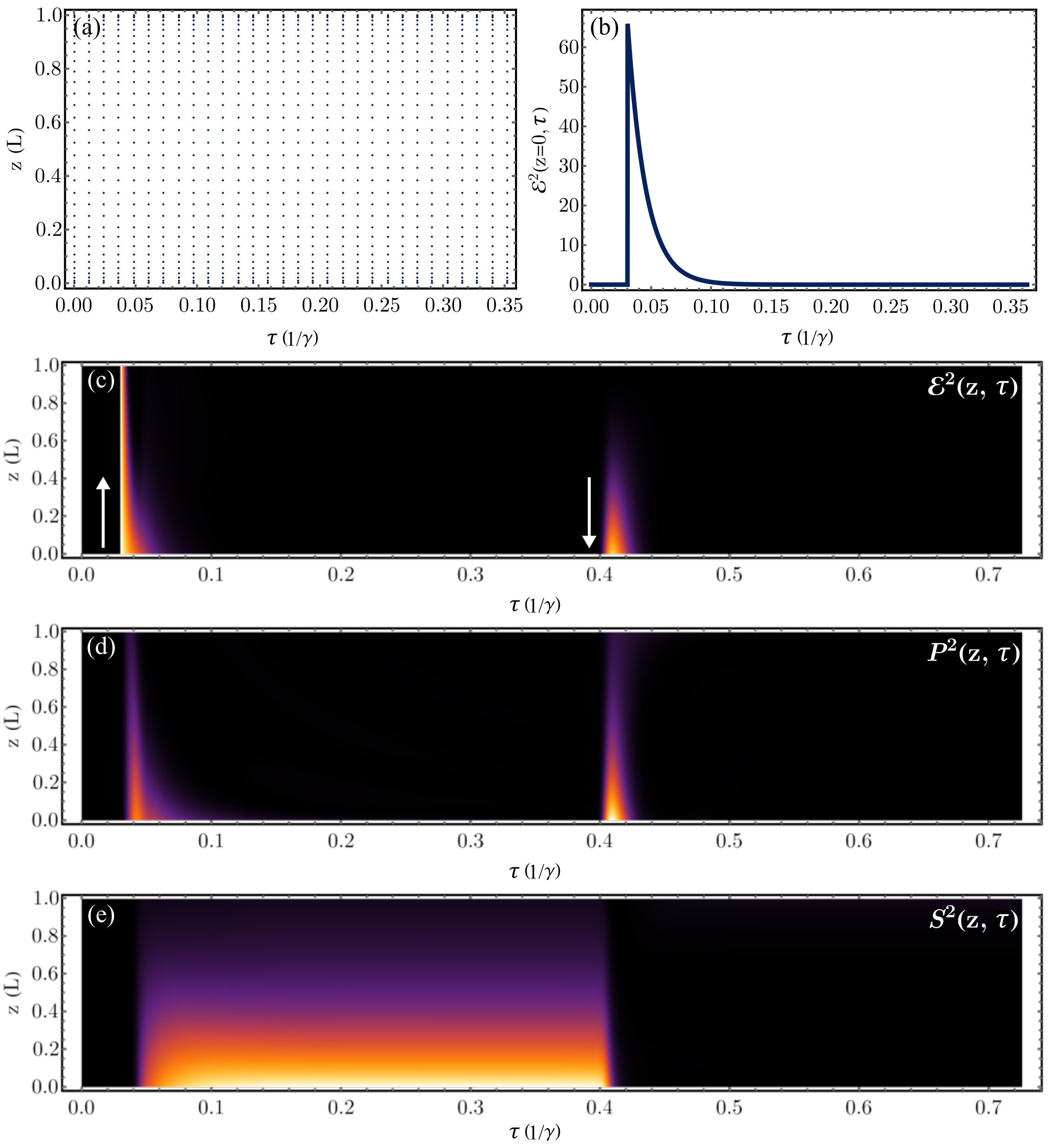

Figure 5.2: (a) Example discretisation of the simulation space, where points along τ are regularly spaced and points along z are distributed as Chebyshev points [232] (more closely spaced at the boundaries). (b) Input signal photon, with bandwidth $32.97\gamma_e = 100\,\mathrm{MHz}$, used as an initial boundary condition. To enforce the criteria of only one input photon, the integral $\int_0^T d\tau\, \mathcal{E}_s^*(0,\tau)\mathcal{E}_s(0,\tau) = 1$ which sets the maximum amplitude. Simulated storage and backward retrieval, with plots of the (c) photon electric field squared $\mathcal{E}_s^2(z,\tau) = \mathcal{E}_s^*(z,\tau)\mathcal{E}_s(0z,\tau)$, where the white arrows indicate the photon propagation direction, (d) atomic polarisation squared $P_s^2(z,\tau) \sim \sigma_{ge}^\dagger \sigma_{ge}$ and (e) the atomic spin wave squared $S_s^2(z,\tau) \sim \sigma_{gs}^\dagger \sigma_{gs}$.

spin wave with finite momentum in Section 5.4 but for now we will assume that the spin wave is momentumless. We can compute the total efficiency η_{total} with,

$$\eta_{\text{total}} = \int_{T_R}^{T_{\text{end}}} d\tau\, \mathcal{E}_s^*(1,\tau)\mathcal{E}_s(1,\tau)\,, \tag{5.45}$$

with T_{end} the end cutoff time in the simulation. We can similarly define the retrieval efficiency as,

$$\eta_{\text{retrieval}} = \frac{\int_{T_R}^{T_{\text{end}}} d\tau\, \mathcal{E}_s^*(1,\tau)\mathcal{E}_s(1,\tau)}{\int_0^1 dz\, S^*(z,T)S(z,T)}\,, \tag{5.46}$$

which reduces to Eq. 5.45 if the spin wave is renormalised before retrieval.

5.1.2 Optimisation

We would like to optimise the overall efficiency of storage and then retrieval of a photon, emitted from a two-level system, like DBT. It is possible to optimise the memory by either varying the photon temporal shape or the control field. The photon temporal shape from DBT (or indeed any two-level emitter) is a decaying exponential, and so we will focus on optimising the memory using the control pulse temporal shape.

It is possible to analytically derive the optimal control shape from Eqs. 5.37-5.39 in the adiabatic and non-adiabatic limits, defined by $Td \gg 1$ and $Td < 1$ respectively (T is in units of $1/\gamma_{ge}$). However, for experimentally realisable optical depths in cold atomic ensembles and available photon sources, we require a general optimisation method for in between these regimes. It is also worth investigating the strictness of the inequalities.

Before describing the general optimisation technique, we will first derive some important results regarding the memory interaction: what parameters the memory efficiency depends on and upper limits in achievable memory efficiencies.

Optimal efficiency

Firstly we will consider retrieval. We would like to find the spin wave that maximises the retrieval efficiency defined in Eq. 5.46, where we will enforce the spin wave to be normalised.

Following Gorshkov et al. [280], taking the Laplace transform of Eq. 5.37 with $z \to u$ and setting the input electric field to zero (since we are dealing with retrieval), we have,

$$\widetilde{\mathcal{E}}_s(u,\tau) = -\frac{\sqrt{d}}{u\sqrt{2}}\widetilde{P}(u,\tau)\,, \tag{5.47}$$

where the tilde denotes the transformed function. Taking the Laplace transform of Eq. 5.38 and subbing in Eq. 5.47 we arrive at,

$$\partial_\tau \widetilde{P}(u,\tau) = -\left(1 + \frac{d}{2u} + i\Delta_s\right)\widetilde{P}(u,\tau) - \frac{i}{2}\Omega\widetilde{S}(u,\tau)\,. \tag{5.48}$$

Here we see that, if we could perfectly map coherence from $S \to P$, decay from P is into two modes with a fixed branching ratio: a rate of γ_{ge} ($= 1$ in normalised units) due to decoherence and a rate of $\gamma d/(2u)$ into the desired photon mode. The retrieval efficiency becomes,

$$\eta_r = \mathcal{L}^{-1}\left[\frac{d}{2uu'}\int_0^\infty \widetilde{d\tau} P(u,\tau)\widetilde{P}^*(u',\tau)\right]\,, \tag{5.49}$$

where we have set $T_R = 0$ and $T_{end} = \infty$. We now wish to write this it terms of the spin wave. By combining Eq. 5.48 and the Laplace transform of Eq. 5.39 we arrive at the identity,

$$\partial_\tau\left[\widetilde{P}(u,\tau)\widetilde{P}^*(u',\tau) + \widetilde{S}(u,\tau)\widetilde{S}^*(u',\tau)\right] = -\left(2 + \frac{d}{2u} + \frac{d}{2u'}\right)\widetilde{P}(u,\tau)\widetilde{P}^*(u',\tau)\,, \tag{5.50}$$

which we can rearrange to get,

$$\begin{aligned}\frac{d}{2uu'}\int_0^\infty \widetilde{P}(u,\tau)\widetilde{P}^*(u',\tau) =& \widetilde{P}(u,\infty)\widetilde{P}^*(u',\infty) - \widetilde{P}(u,0)\widetilde{P}^*(u',0)\\ &+ \widetilde{S}(u,\infty)\widetilde{S}^*(u',\infty) - \widetilde{S}(u,0)\widetilde{S}^*(u',0)\\ =& \frac{d}{4uu' + d(u+u')}\widetilde{S}(u,0)\widetilde{S}^*(u',0)\,.\end{aligned} \tag{5.51}$$

Taking the inverse Laplace transform results in the expression,

$$\eta_r = \int_0^1 dz \int_0^1 dz' K_r(1-z, 1-z')S(z,0)S^*(z,0) \tag{5.52}$$

with the retrieval kernel $K_r(z, z')$ defined as,

$$K_r(z, z') = \frac{d}{4} \exp\left[-d(z + z')/4\right] I_0(d\sqrt{zz'}) \tag{5.53}$$

where I_0 is the modified Bessel function. The kernel $K_r(z, z')$ quantifies the mapping between spin wave and output light field, in the case of perfect control field. It only depends on optical depth and so the maximum memory efficiency is entirely parameterised by d. To find the optimum spin wave and efficiency for backwards retrieval, at each d, we numerically solve the eigenvalue problem,

$$\eta_r S(z) = \int_0^1 dz K_r(1 - z, 1 - z')S(z)\,, \tag{5.54}$$

in which the optimum spin wave is the eigenvector of Eq. 5.54 with the largest corresponding eigenvalue η_r (the retrieval efficiency for $S(z)$).

One numeric method for solving such a problem is to begin with some trial $S(z)$ and insert it into equation Eq. 5.54. The result, after renormalisation, then becomes the new trial solution, which is inserted back into Eq. 5.54. At each iteration, the method is tested to see if the result has converged. The final result is then the optimum spin wave which can then be combined with the kernel to extract the associated eigenvalue or retrieval efficiency.

The optimum spin wave for retrieval in the backwards direction ($z < 0$) is plotted in Fig. 5.3a against z while varying the optical depth. The associated eigenvalues are $\eta_r = 0.05,\ 0.33,\ 0.97$ for $d = 0.1,\ 1,\ 100$ respectively. The limiting case of $S(z) = \sqrt{3}(1 - z)$ for $d \to \infty$ is plotted in dashed grey. For $d \to 0$, the ideal spin wave is flat as it is best to have the entire ensemble contributing to maximise the coupling between the matter and light modes, and the emission from all atoms to interfere constructively. However, as d increases, the optimum begins to accumulate a larger amplitude towards the beginning of the ensemble. The constructive interference builds up through the ensemble but the more atomic medium the excitation propagates through, a greater proportion of the excitation is lost to the decoherence decay channel. Therefore, it is best to have as little amplitude at $z = 1$ as possible, and have the spin wave amplitude slowly build up as we approach $z = 0$.

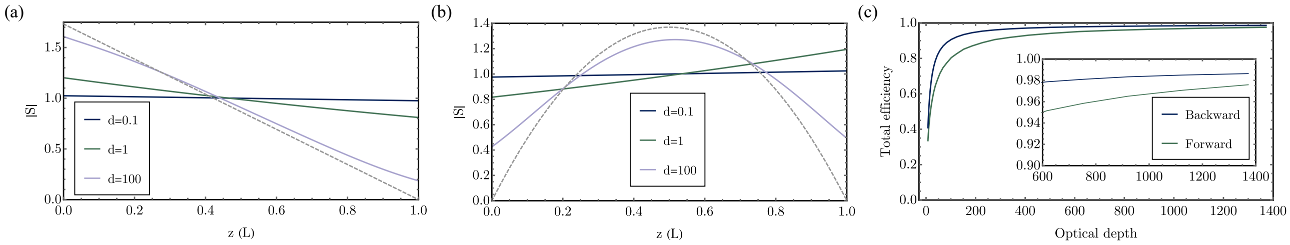

Figure 5.3: Plots of optimal spin waves (absolute value) at different optical depths as a function of distance through the atomic ensemble, for (a) backwards retrieval (b) forwards retrieval, where the dashed grey lines are the limiting case of $d \to \infty$. (c) Total efficiency as a function of optical depth for forwards and backwards retrieval.

The same argument applies to the-time reverse, that is the optimal spin wave for storage is exactly those plotted in Fig 5.3a, where for large optical depths we maximise the spin wave amplitude at the beginning of the ensemble, thereby minimising decay. Note that the optimum spin wave for storage and retrieval are only equal to each other for the case of backwards retrieval where the total efficiency $\eta_{\text{total}} = \eta_r^2(d)$ found from Eq. 5.54, and is plotted in Fig 5.3c in dark blue.

For the case of forward retrieval, a compromise is needed between the optimum spin wave for storage and for retrieval. We can employ the same time reverse argument, but we must now reverse the whole process of storage and forward retrieval - the optimum spin wave will flip after time reversal. We can reformulate the eigenvalue problem as,

$$\sqrt{\eta_{\text{total}}} S(z) = \int_0^1 dz K_r(z, 1-z') S(z) \tag{5.55}$$

where η_{total} is now for the forwards direction. However, unlike for backwards retrieval, storage efficiency will always be greater than the retrieval efficiency for forwards retrieval [280]. The optimum spin waves are plotted in Fig 5.3b. The scaling of η_{total} with optical depth is plotted in Fig 5.3c in green.

All of the results derived in this section set an upper limit on the possible efficiency for a given optical depth, provided that we can perfectly map to the optimal spin wave. We will now look to use gradient ascent to determine the control field that most faithfully reproduces this mapping for an input photon mode of a decaying exponential. We will examine how the optimum changes while transitioning between the adiabatic and non-adiabatic regimes and what physical parameters are needed to realise an efficient memory. We will focus on backwards retrieval, as this can reach higher potential efficiencies for lower optical depth. The optimisation procedure that we derive in the following can be equally applied to forward retrieval [241].

Gradient ascent

We have bounded the maximum possible efficiency for both forwards and backwards retrieval. However, the previous derivation gave no insight into what temporal shape (or phase) of control field achieves this efficiency and did not indicate whether all input photon modes can reach this efficiency. It is possible to derive analytical solutions in the adiabatic and non-adiabatic limits. In general, the choice of photon source and atomic medium may not fall into these limits and we must find an alternative way to optimise the control pulse.

Our goal will be to optimise the storage efficiency, as this will optimise the overall efficiency for backward retrieval. To do so we will use a gradient ascent algorithm, initially presented in Gorshkov et al. [241] and further developed in Rakher et al. [363]. The method proceeds by incrementing a trial solution using a gradient derived from a metric J which is to be maximised while obeying some constraints. A trial solution for the control field $\Omega_j(\tau)$ is incremented as,

$$\Omega_{j+1}(\tau) \leftarrow \Omega_j(\tau) + \alpha \frac{\delta J}{\delta \Omega(\tau)} \,, \tag{5.56}$$

where $\Omega_{j+1}(\tau)$ is the next trial, with α determining the step size. The gradient, taken with respect to the control field, is a function of τ and so the control field will be updated for every time step.

Our metric is a functional consisting of the storage efficiency, plus our constraints which are the equations of motion of our system (Eqs. 5.37-5.39). We can write this as,

$$
\begin{aligned}
J = &\int_0^1 dz\, S_{gs}^*(z,T) S_{gs}(z,T) \\
&+ \int_0^1 dz \int_0^T d\tau \bar{P}_{ge}^*[-\partial_\tau P_{ge} - (\gamma_{ge} + i\Delta)P_{ge} + \sqrt{d}\mathcal{E}_s - i\Omega_{es}S_{gs}] + c.c. \\
&+ \int_0^1 dz \int_0^T d\tau \bar{S}_{gs}^*[-\partial_\tau S_{gs} - i\Omega_{es}^* P_{ge}] + c.c. \\
&+ \int_0^1 dz \int_0^T d\tau \bar{\mathcal{E}}_s^*[-\partial_z \mathcal{E}_s - \sqrt{d}P_{ge}] + c.c.\,,
\end{aligned}
\tag{5.57}
$$

where c.c. stands for the complex conjugate and we have set $\Delta_s = \Delta_c = \Delta$. We have also introduced the co-functions: $\bar{P}_{ge}(z,\tau)$, $\bar{S}_{gs}(z,\tau)$, $\bar{\mathcal{E}}_s(z,\tau)$. These are analogous to the Lagrange multipliers commonly seen in optimisation problems. To deal with the complex nature of the coherences, it is sufficient to treat the coherences and their complex conjugates as independent. With this convention, the functional derivative is given by,

$$
\frac{\partial J}{\partial \Omega_{es}^*(\tau)} = i \int_0^1 dz \left(\bar{P}_{ge} S_{gs}^* - \bar{S}_{gs}^* P_{ge} \right) \,, \tag{5.58}
$$

which in general is complex. Allowing the control field to be complex allows for the phase of the control field to be optimised as well as its amplitude. We can instead force the control field to be real, in which case the gradient becomes,

$$
\frac{\partial J}{\partial \Omega_{es}(\tau)} = -2 \int_0^1 dz\, \mathrm{Im}\left[\bar{P}_{ge} S_{gs}^* - \bar{S}_{gs}^* P_{ge} \right] \,. \tag{5.59}
$$

Both expressions for the gradient feature the co-functions and so we must derive equations of motion for these. To do so, we use the fact that the metric must be stationary with respect to variations in all dynamic parameters, allowing us to write,

$$
\begin{aligned}
\delta J = &\int_0^1 dz S_{gs}(z,T)\delta S_{gs}^*(z,T) + \delta S_{gs}(z,T) S_{gs}^*(z,T) \\
&+ \int_0^1 dz \int_0^T d\tau \bar{P}_{ge}^*[-\delta\partial_\tau P_{ge} - (\gamma_{ge} + i\Delta)\delta P_{ge} + \sqrt{d}\delta\mathcal{E}_s - i\Omega_{es}\delta S_{gs}] + c.c. \\
&+ \int_0^1 dz \int_0^T d\tau \bar{S}_{gs}^*[-\partial_\tau \delta S_{gs} - i\Omega_{es}^*\delta P_{ge}] + c.c. \\
&+ \int_0^1 dz \int_0^T d\tau \bar{\mathcal{E}}_s^*[-\partial_z \delta\mathcal{E}_s - \sqrt{d}\delta P_{ge}] + c.c.\,.
\end{aligned}
\tag{5.60}
$$

Performing integration by parts gives us,

$$
\begin{aligned}
\delta J = &\int_0^1 dz S_{gs}(z,T)\delta S_{gs}^*(z,T) + \delta S_{gs}(z,T) S_{gs}^*(z,T) \\
&+ \Bigg(\int_0^1 dz(\bar{P}_{ge}^*(z,0)\delta P_{ge}(z,0) - \bar{P}_{ge}^*(z,T)\delta P_{ge}(z,T)) \\
&+ \int_0^1 dz \int_0^T d\tau \partial_\tau \bar{P}_{ge}^* \delta P + \bar{P}_{ge}^*[-(\gamma_{ge} + i\Delta)\delta P_{ge} + \sqrt{d}\delta\mathcal{E}_s - i\Omega_{es}\delta S_{gs}] + c.c. \Bigg) \\
&+ \int_0^1 dz(\bar{S}_{gs}^*(z,0)\delta S_{gs}(z,0) - \bar{S}_{gs}^*(z,T)\delta S_{gs}(z,T)) \\
&+ \int_0^1 dz \int_0^T d\tau \partial_\tau \bar{S}_{gs}^* \delta S_{gs} + \bar{S}_{gs}^*[-i\Omega_{es}^*\delta P_{ge}] + c.c. \\
&+ \int_0^1 d\tau(\bar{\mathcal{E}}_s(0,\tau)\delta\mathcal{E}_s(0,\tau) - \bar{\mathcal{E}}_s(L,\tau)\delta\mathcal{E}_s(L,\tau)) + \int_0^1 dz \int_0^T d\tau\ \partial_z \bar{\mathcal{E}}_s^* \delta\mathcal{E}_s + \bar{\mathcal{E}}_s^*[-\sqrt{d}\delta P_{ge}] + c.c.
\end{aligned}
\tag{5.61}
$$

We have $\delta S_{gs}(z,0) = \delta P_{ge}(z,0) = \delta \mathcal{E}_s(0,\tau) = 0$ as our initial conditions are fixed, leading to,

$$
\begin{aligned}
\delta J = &\int_0^1 dz S_{gs}(z,T)\delta S^*_{gs}(z,T) + \delta S_{gs}(z,T) S^*_{gs}(z,T) \\
&\Bigg(- \int_0^1 dz \bar{P^*_{ge}}(z,T)\delta P_{ge}(z,T) \\
&+ \int_0^1 dz \int_0^T d\tau \partial_\tau \bar{P}^*_{ge} \delta P_{ge} + \bar{P}^*{}_{ge}[-(\gamma_{ge} + i\Delta)\delta P_{ge} + \sqrt{d}\delta\mathcal{E}_s - i\Omega_{es}\delta S_{gs}] + c.c. \Bigg) \\
&- \int_0^1 dz \bar{S^*_{gs}}(z,T)\delta S_{gs}(z,T) \\
&+ \int_0^1 dz \int_0^T d\tau \partial_\tau \bar{S}^*_{gs} \delta S_{gs} + \bar{S}^*{}_{gs}[-i\Omega^*_{es}\delta P_{ge}] + c.c. \\
&- \int_0^1 d\tau \bar{\mathcal{E}}_s(L,\tau)\delta\mathcal{E}_s(L,\tau) + \int_0^1 dz \int_0^T d\tau \ \partial_z \bar{\mathcal{E}}^*_s \delta\mathcal{E}_s + \bar{\mathcal{E}}^*_s[-\sqrt{d}\delta P_{ge}] + c.c.
\end{aligned}
\tag{5.62}
$$

The optimum storage efficiency requires that $\delta J = 0$ for any small parameter variation and so we can collect terms multiplying δX (where X represents some parameter) and set the results to zero. This results in the following equations of motion for the co-functions,

$$\partial_z \bar{\mathcal{E}}_s = -\sqrt{d}\bar{P}_{ge} \tag{5.63}$$

$$\partial_\tau \bar{P}_{ge} = (\gamma_{ge} - i\Delta)\bar{P}_{ge} + \sqrt{d}\mathcal{E}_s - i\Omega_{es}S_{gs} \tag{5.64}$$

$$\partial_\tau \bar{S}_{gs} = -i\Omega_{es}\bar{P}_{ge} \tag{5.65}$$

and the associated boundary conditions,

$$\bar{\mathcal{E}}_s(L,\tau) = 0 \tag{5.66}$$

$$\bar{P}_{ge}(z,T) = 0 \tag{5.67}$$

$$\bar{S}_{gs}(z,T) = S_{gs}(z,T) \tag{5.68}$$

These are precisely the same equations as Eqs. 5.37-5.39 except the decay is replaced with growth. The Eqs. 5.63-5.65 are the time and spaced reverse of Eqs. 5.37-5.39. To see this, transforming the co-function equations as $\tau \to T - \tau$ and $z \to L - z$ (and remembering to take the complex conjugate for time reversal) will result in precisely Eqs. 5.37-5.39, except for $\bar{\mathcal{E}}_s$

replaced by $-\bar{\mathcal{E}}_s$ due to the i in the definition Eq. 5.5. The gradient therefore originates from the difference in the memory interaction, solved before and after time (and space) reversal. Put another way, the most efficient memory is one in which the dynamics for storage and backward retrieval are as similar as possible, which agrees well with the optimal spin waves derived earlier in this section.

The optimisation algorithm proceeds by first solving Eqs. 5.37-5.39 for storing a photon described by Eq. 5.41 using an initial trial $\Omega(\tau)$. This determines the boundary condition for Eq. 5.68 and Eqs. 5.63-5.65 are solved (these equations run backward in time and space). The results from the two simulations are then used to compute the gradient at each time step and update the control field. This is repeated until the efficiency has converged within the desired tolerance. While in general, gradient ascent methods can become trapped at local maxima, in Gorshkov et al. [241] they showed that in the limiting cases where there exists an analytical solution, the gradient ascent method presented here converged to the global optima in all cases. This suggests that this method always yields the global optimum.

Overall, this method is very efficient, requiring only two memory runs to improve the control field over the entire temporal domain. Even more efficient algorithms exist such as Krotov's method [364], which was originally used to optimise the landing of a spacecraft onto the surface of a planet. However for this thesis, we will stick to the slightly less optimal but simpler gradient ascent.

Example optimisation

We are primarily interested in using Rb as a medium for a quantum memory, with all of the population beginning in one of the hyperfine ground states and the other empty ground state used for storage. For ^{87}Rb, the ground state splitting is 6.8 GHz, so to reduce the coupling of the control field with the $|g\rangle \rightarrow |e\rangle$ transition (which in deriving the equations Eqs. 5.37 - 5.39 we assumed was zero) the control bandwidth should be much less than the hyperfine splitting. Even so, this coupling will not be zero and we will revisit this undesired coupling when discussing four-wave mixing in Section 5.3. For now, we will restrict ourselves to optimising photons of bandwidth ≤ 1 GHz, as the bandwidth of the corresponding control pulse will be of a similar

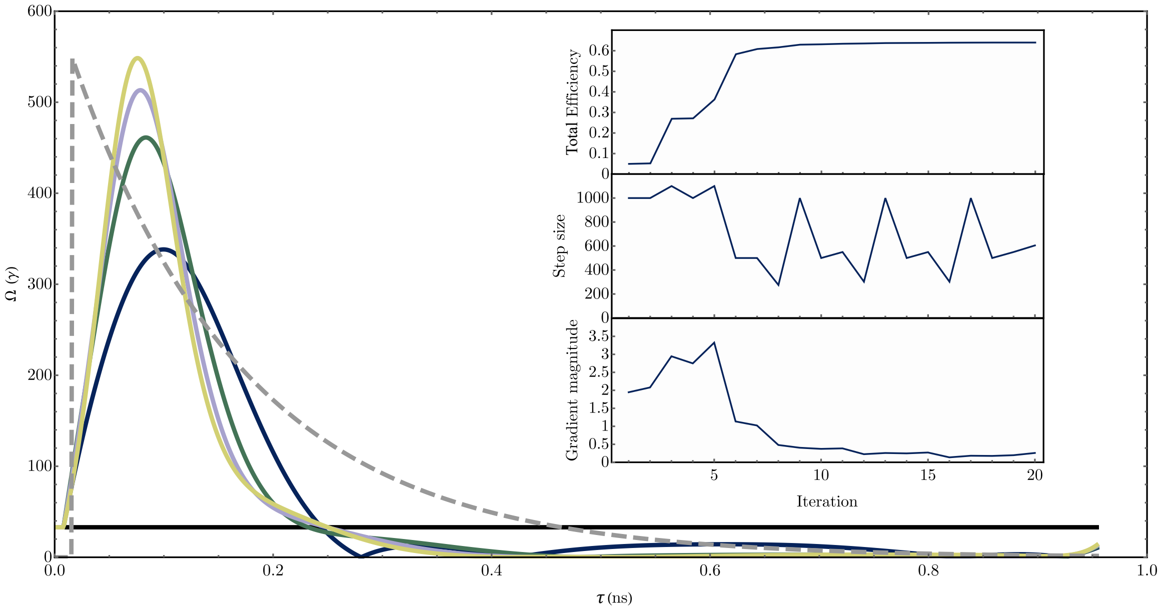

Figure 5.4: Typical gradient ascent optimisation. The photon temporal shape is shown in dashed grey and has been normalised to the maximum control field amplitude. The initial control $\Omega(\tau) = 1/(10\tau_c)$ is shown in black. The control field at iterations 5, 10, 15 and 20 is pltoted in dark blue, green, purple and yellow respectively. Inset: Total efficiency, step size and gradient magnitude in the direction of travel over the 20 total iterations of the gradient ascent.

order.

In particular, we will optimise three bandwidths of photon: 1 MHz, 100 MHz and 1 GHz. Narrowband sources with bandwidths on the order of 1 MHz include high quality factor cavity sources [276, 365], photon sources such as DBT and colour centres often produce lifetime limited photons in the $10-100$ MHz range [189, 202] and quantum dots typically have bandwidths on the order of 1 GHz [81, 147]. To begin with, we set the photon and control field on resonance ($\Delta_s = \Delta_c = 0$). As for optical depths, high density magneto-optical traps (MOTs) have been demonstrated with $d \lessapprox 1000$ [366]. We will consider optical depths up to 2500 in the following, thereby encompassing current capabilities and future improvements. In warm Rb vapours, higher optical depths can be obtained and will be investigated at the end of this chapter.

We set the initial control field to $\Omega(\tau) = 1/(10\tau_c)$ with a starting step size of $\alpha = 1000$. When the gradient is computed at each iteration, the step is tested to see if it satisfies the Wolfe conditions, see Appendix B.3.1. The Wolfe conditions set a lower and upper bound on an appropriate step, increasing or decreasing the step size geometrically if the current iteration falls outside of these bounds. A typical optimisation run is shown in Fig. 5.4. The photon temporal shape (rescaled to the maximum height of the control field) is shown in dashed grey and the initial control is shown in black. The control field at iteration 5, 10, 15 and 20 is shown in dark blue, green, purple and yellow respectively, where convergence to 0.01% took 20 iterations total (a total of just 40 simulation runs). The inset shows the storage efficiency, step size and gradient magnitude (in the direction of the steepest ascent) over the 20 iterations, showing the gradient ascent converges quickly to within a few percent after < 10 iterations. As the gradient approaches zero, the step size is adjusted to allow for better convergence.

5.2 Three level results

The results of the full complex optimisations for $\Delta = 0$ are shown in Fig. 5.5. The total efficiency against optical depth is plotted in Fig. 5.5a for 1 MHz (dark blue), 100 MHz (green) and 1 GHz (purple) bandwidth photons. In dashed grey are the efficiencies obtained from the eigenfunctions of Eq. 5.54. We see that the optimisation for 1 MHz photons very quickly approaches the upper efficiency limit. For higher bandwidths, the process becomes less adiabatic and the efficiency suffers. As the optical depth is increased, we begin to enter the adiabatic regime again and the efficiencies converge with the dashed grey line.

In Fig. 5.5b, c and d we have plotted the optimised spin waves for $d = 40, 110$ and 850 respectively. In dashed grey are the optimum spin waves obtained from the eigenvectors of Eq. 5.54 with the coloured lines corresponding to the same bandwidths as in Fig. 5.5a. We see that the optimised spin waves obey the qualitative argument that most of the spin wave should be located at the entrance to the ensemble, and in Fig. 5.5b the spin wave that corresponds to the 1 MHz photon follows the optimal very closely. As the bandwidth is increased, and the efficiency drops, we observe that the photon cannot be mapped to the optimum spin wave. For higher optical depths, the spin waves relating to higher bandwidths begin to resemble the optimum more closely.

We plot the optimum control field shapes in Fig. 5.5e with the amplitudes normalised to one in order to better compare the shapes. For zero detuning, the control field is real, so only the

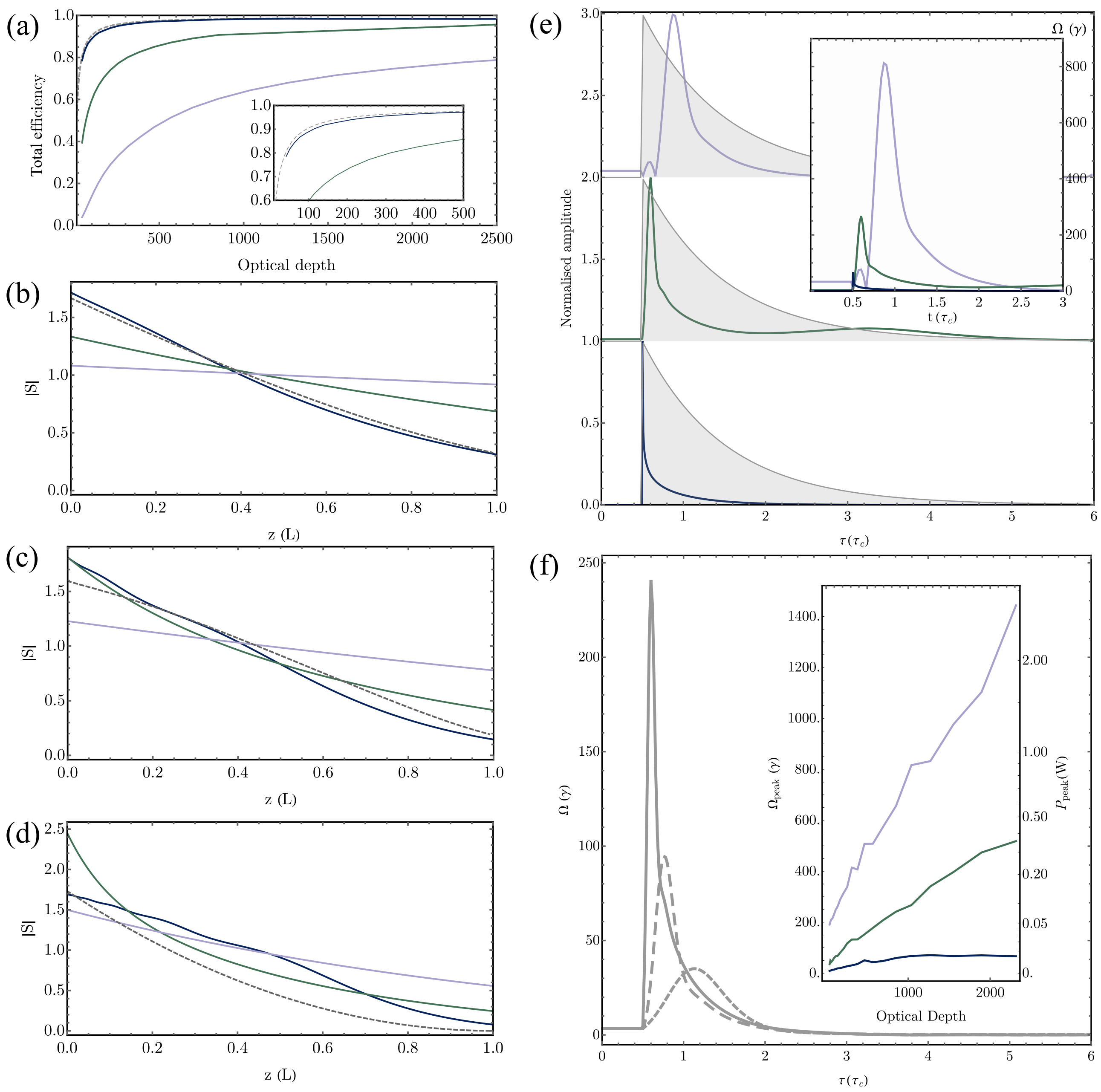

Figure 5.5: Optimisation results for input photon bandwidths 1 MHz (blue), 100 MHz (green) and 1 GHz (purple). (a) Plot of optimised total efficiency as a function of optical depth. The theoretical upper bound is shown is dashed grey. The resulting absolute values of the optimised spin waves as a function of distance through the atomic ensemble are plotted, for an optical depth of (b) $d = 40$, (c) $d = 110$, (d) $d = 850$. The theoretical optimum is shown in dashed grey, derived from Eq. 5.54. (e) Optimised control shapes, normalised to an amplitude of 1, and plotted as a function of the characteristic decay time of the input photon, with the input photon shown in solid grey. Inset: True amplitude of opitmised control fields in units of Rabi frequency. (f) Optimum control field for a 100 MHz input photon and optical depths of $d = 40, 110$ and 850, where a higher peak amplitude corresponds to a higher optical depth. Inset: Peak Rabi frequency of the control fields as optical depth is increased. On the left axis, the peak amplitude is given in terms of Rabi frequency, while on the right it is given in terms of watts, where we have assumed a control beam radius of 1 mm and a dipole moment of 3.584×10^{-29} Cm.

amplitudes are plotted. The adiabatic case resembles a decaying exponential, though with a steeper initial drop off. This results in the photon coherence being mapped directly to the spin wave, with very little excitation of the atomic polarisation (P_{ge}), which resembles EIT storage. As we move away from the adiabacity criterion, the centre of mass of the control field shifts to after the photon has arrived. The photon coherence is first allowed to induce an atomic polarisation P_{ge} which is then mapped by the control field to the spin wave. This more closely resembles ATS storage. The true amplitudes of the control fields are shown in the inset of Fig. 5.5e, where we can see the increase in peak Rabi frequency required for higher bandwidths.

In Fig. 5.5f we show how increasing the optical depth results in the optimum approaching the adiabatic case, for an input photon of 100 MHz. Here the increasing amplitude of the grey lines relate to an increasing optical depth, of values $d = 40, 110$ and 850. The inset shows how the peak Rabi frequency scales with optical depth for the three bandwidths considered, with the corresponding peak power shown on the right axis, assuming a control beam radius of 1 mm and a dipole moment of 3.584×10^{-29} Cm [350].

Non zero-detuning

In Fig. 5.6, we plot the real valued optimisation results on the left for an input photon bandwidth of $2\pi \times 100$ MHz, at three photon detunings, $\Delta_s/(2\pi) = 0$, 625 MHz and 2.5 GHz denoted by solid blue, green and purple lines respectively, for an optical depth of 2500. The control field detuning Δ_c was set equal to Δ_s, so the two light fields were on two photon resonance. Plotted with dashed lines, are the amplitudes of the complex results, with the corresponding phases plotted on the right. Only at $\Delta_s = 2\pi \times 2.5$ GHz do we begin to observe a significant deviation between the real and complex shapes, where the complex results appear to be smoother and resemble the adiabatic result from the resonant case.

In terms of efficiency, with complex control fields, each detuning reached roughly the same efficiency, in the range $95 - 96\%$. The same is true for the real valued control fields, except for the $\Delta_s = 2\pi \times 2.5$ GHz case where the efficiency drops to 75%. This could be a physical effect often observed in detuned Raman memories (as will be discussed in more detail in Chapter 6) where increasing the control field power, as is required to achieve the required coupling at

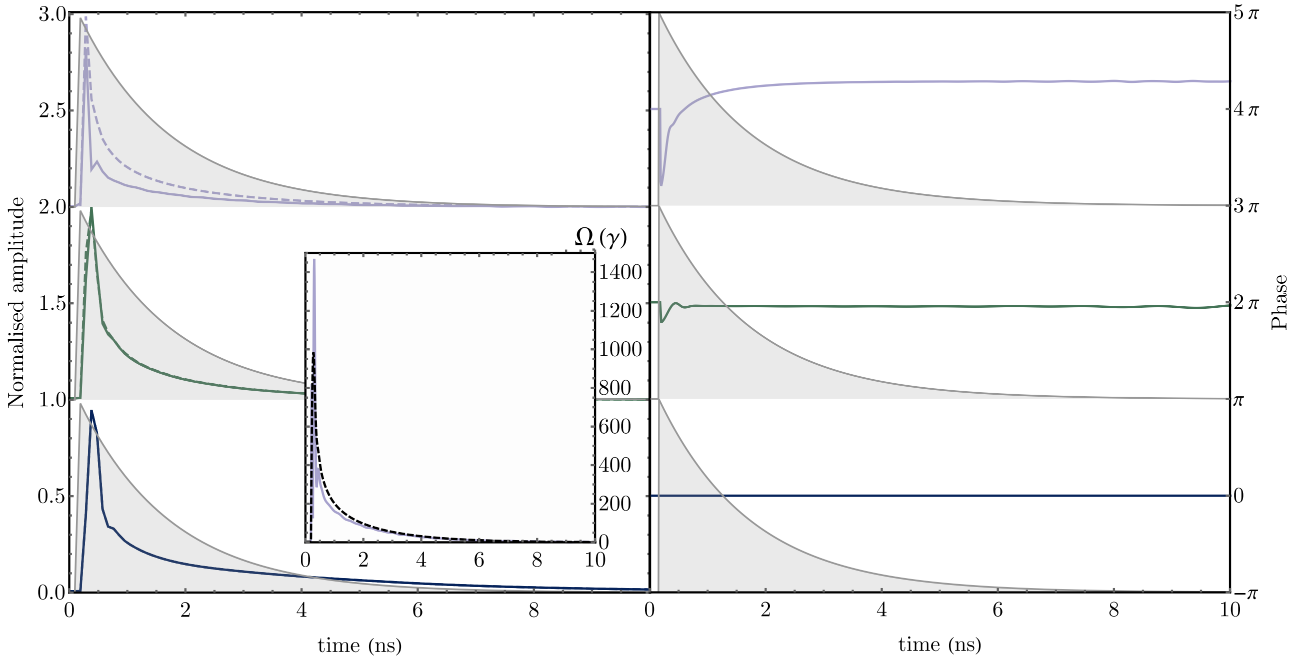

Figure 5.6: Left: Normalised control field amplitudes plotted against time in nanoseconds, for input photon bandwidth of $2\pi \times 100\,\mathrm{MHz}$ at $\Delta = 0$ (blue), $\Delta = 2\pi \times 625\,\mathrm{MHz}$ (green), $\Delta = 2\pi \times 2.5\,\mathrm{GHz}$ (purple), where Δ is the detuning of both the photon and control fields. Solid lines denote the results of the real valued optimisation, and the dashed the result of the complex valued optimisation. Inset: True amplitudes of real and complex control fields for $\Delta = 2\pi \times 2.5\,\mathrm{GHz}$, where the complex amplitude is shown in dashed black. Right: Phase of complex control field.

larger detunings, results in an AC Stark shift of the intermediate and storage states. The consequence is a decrease in efficiency as the control field power is increased beyond a certain point [264, 367]. Through varying the phase, complex control field amplitudes can circumvent this issue. To see this, note that an additional detuning of the control field (from the two photon resonance condition) could be described by incorporating a time dependant phase. Control over the phase also accounts for sidebands and chirping of the control pulse. Alternatively, the lower efficiency could be explained by the gradient ascent algorithm converging too slowly, and may have been prematurely terminated.

In the inset of Fig. 5.6, the true amplitudes of the real and complex control fields are plotted, with the dashed black line representing the complex control field. It appears that the complex field requires less peak power, at the expense of requiring phase control.

We can see in all of the optimisations presented here (decaying exponential input photon), in order to reach above 90% efficiencies, the optical depth has to be high enough to enter the

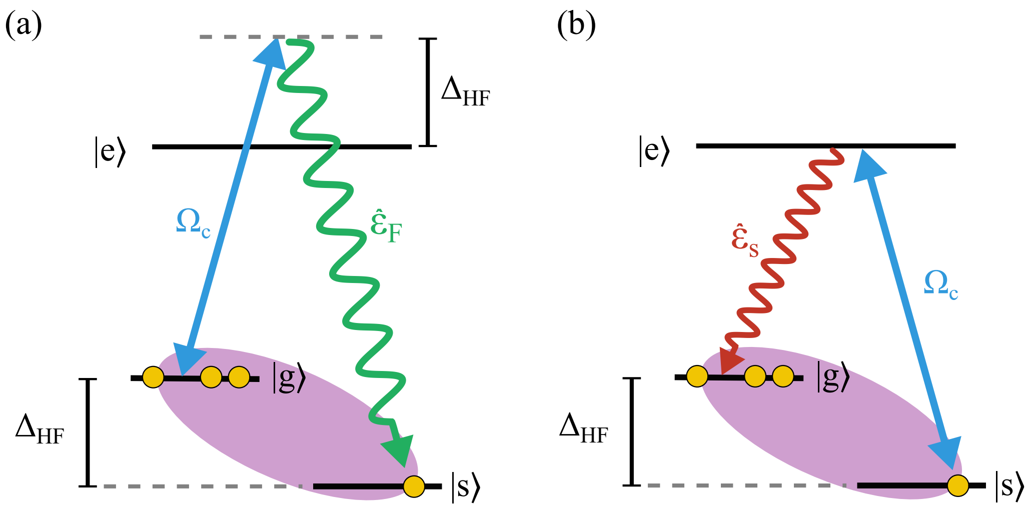

Figure 5.7: (a) Illustration showing unwanted cross coupling of the control field to the signal transition, leading to the creation of a spin wave without the presence of a signal photon. Additionally, coupling of this kind can couple any spin wave to the anti-stokes field $\mathcal{E}_F$, potentially removing stored coherence which was correlated to a signal photon. (b) A spurious spin wave can be readout in the usual retrieval process, producing a field of the same frequency as the signal photon but with no correlation to the input signal.

adiabatic regime. This implies then that the we only need to be able to engineer the limiting adiabatic control pulse shape, with the peak amplitude and duration dictated by the bandwidth and optical depth. While this is true for the simple case of three levels, as we move to more realistic setups we will see the true benefit of this gradient ascent method.

It is worth noting that in Gorshkov et al. [280], it was shown that in the non-adiabatic limit, efficient mapping of a photon to the spin wave is possible for a rising exponential photon. Shaping of the photon may be a promising avenue to achieve high bandwidth memories for attainable optical depths, but we will not discuss it further in this thesis.

5.3 Four-wave mixing noise

In previous derivation, we neglected coupling of control field to the signal transition. In reality, though this transition is very far detuned, the coupling is non zero, especially at high bandwidths and optical depths, which also require high control intensities. The effect of this non-resonant cross-coupling is illustrated in Fig. 5.7.

As well as the desired interaction shown in the previous section, the control field acts to couple population in $|g\rangle$ via a stokes field $\mathcal{E}_F$, to excite a spurious spin wave, even without the presence of a signal photon, as illustrated in Fig. 5.7a. This spin wave can then be read out through coupling of the control field to the desired transition, depicted in Fig.5.7b. The process is termed four-wave mixing (FWM) and does not only act to both add amplitude to the spin wave which is not correlated with the signal photon, but also can couple the spin wave to the photon field $\mathcal{E}_F$ reducing the amplitude of the spin wave.

In Phillips et al. [368] they included the cross-coupling of the control field and derived a modified set of equations that included the Stokes field, under the assumption that the bandwidth and amplitude of the control field are still small enough such that there is minimal population transfer from $|g\rangle$ to $|e\rangle$. The modified equations were shown to agree with experiment well and are,

$$\partial_z \mathcal{E}_s = -\sqrt{\frac{d}{2}} P_{ge} \tag{5.69}$$

$$\partial_z \mathcal{E}_F = \sqrt{\frac{d}{2}} \frac{\Omega_{es}}{\Delta_{\mathrm{HF}}} S_{gs} \tag{5.70}$$

$$\partial_\tau P_{ge} = -(1 + i\Delta_s - 2i\delta_{ls}) P_{ge} + \sqrt{\frac{d}{2}} \mathcal{E}_s - \frac{i}{2} \Omega_{es} S_{gs} \tag{5.71}$$

$$\partial_\tau S_{gs} = -i(\Delta_s - \Delta_c - \delta_{ls}) S_{gs} - \frac{i}{2} \Omega^* P_{ge} - \frac{i}{2} \sqrt{\frac{d}{2}} \frac{\Omega_{es}}{\Delta_{\mathrm{HF}}} \mathcal{E}_F^* \,, \tag{5.72}$$

where Δ_{HF} denotes the hyperfine splitting of the ground states and δ_{ls} refers to the time-dependent light shift $\delta_{ls} = |\Omega_{ge}|^2/\Delta_{\mathrm{HF}}$, with Ω_{ge} referring to control field coupling strength on the $|g\rangle \rightarrow |e\rangle$ transition. As we would expect, increasing Δ_{HF} reduces the FWM, and so alkali vapours with large hyperfine ground splittings such as ^{87}Rb and Cs will offer improved resilience to FWM. Lower optical depths are also beneficial due to the decreased coupling of the control field to the signal transition and the lower Rabi frequency required for optimal control.

In Fig. 5.8a we have plotted the efficiencies obtained when using the optimum control fields from the previous section, after adding in FWM to the system, using $\Delta_{\mathrm{HF}} = 2\pi \times 6.8$ GHz. In contrast to the simple three level system, bandwidths $2\pi \times 100$ MHz (solid green) and $2\pi \times 1$ GHz (solid purple), show a decreasing efficiency at higher optical depths. The dashed lines of the same

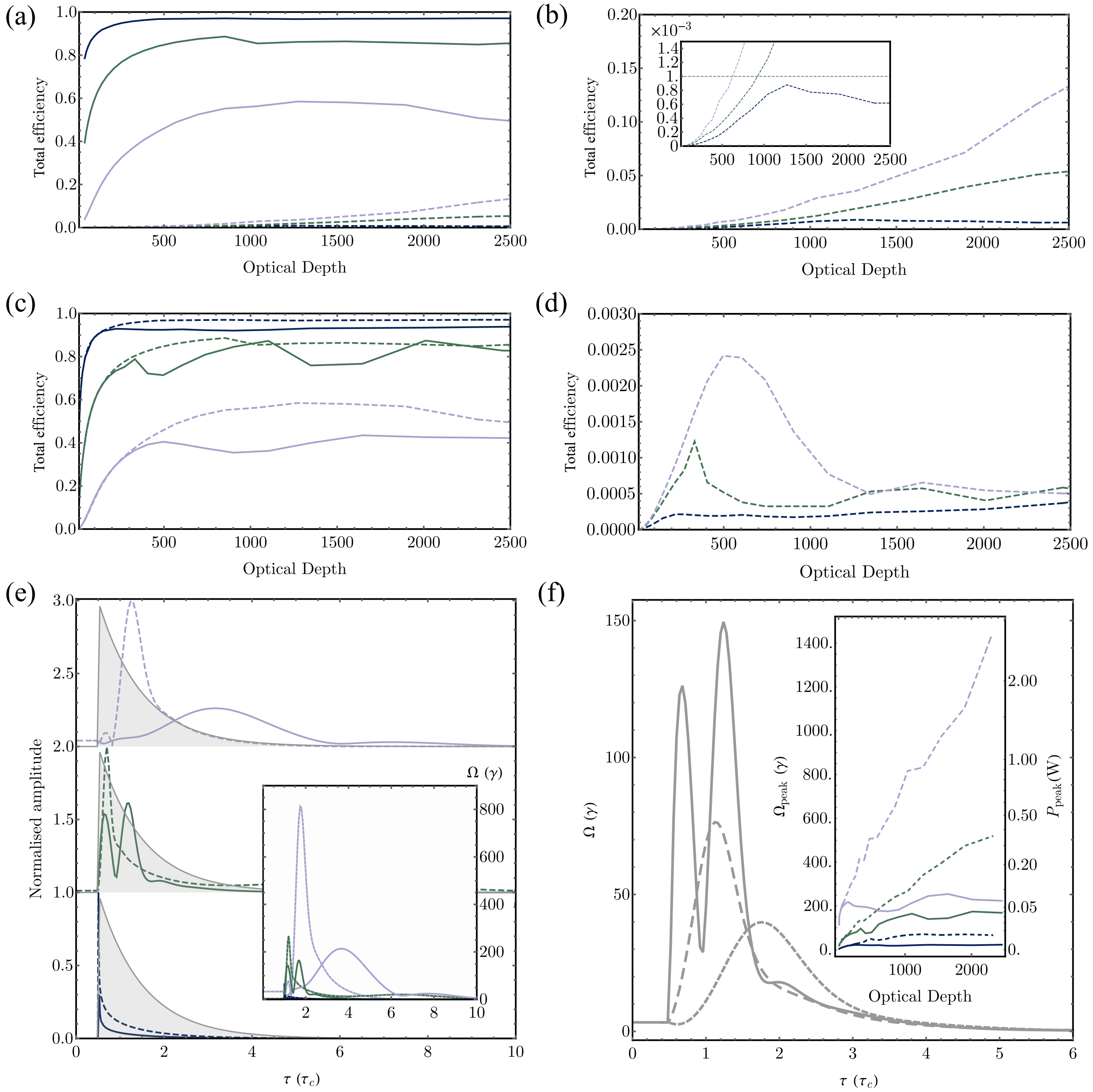

Figure 5.8: Optimisation results for input photon bandwidths $2\pi \times 1\,\mathrm{MHz}$ (blue), $2\pi \times 100\,\mathrm{MHz}$ (green) and $2\pi \times 1\,\mathrm{GHz}$ (purple) (a) Plot of total memory efficiency (solid) against optical depth, using the optima derived in Section 5.2 with four-wave mixing (FWM) included. FWM efficiency, defined as the number of excitations in the stokes field, are plotted as dashed lines. (b) Zoom in of FWM efficiences, with an inset which further zooms in on $2\pi \times 1\,\mathrm{MHz}$ input bandwidth. (c) Shown in colour are the optimisation results using the metric defined in Eq. 5.73, with $\mathcal{F} = 100$, which adds a penalty for FWM noise. Dashed lines are the optima from the metric not including the FWM penalty for comparison. (d) FWM noise from optima derived from the FWM penalising metric. (e) Normalised control field amplitudes, with the original real valued optima shown in dashed and the new optima shown in solid colour. Inset: True amplitudes of control fields. (f) Optimum control fields from the new metric, as optical depth is increased from $d = 40, 110$ and 850. Inset: Peak Rabi frequency of the control fields as optical depth is increased. On the left axis, the peak amplitude is given in terms of Rabi frequency, while on the right it is given in terms of watts. Dashed corresponds to the results from the old metric.

colour show the FWM efficiency, defined as the number of excitations in the stokes field. Note that this does not strictly capture the full effect of gain due to FWM as spurious excitations in the spin wave mode would be indistinguishable from higher efficiency. However, FWM efficiency is a good metric for determining the amount of FWM in the system. In Fig. 5.8b we see a zoom in of the FWM efficiencies Fig. 5.8a, showing how bandwidths $2\pi \times 100\,\text{MHz}$ and $2\pi \times 1\,\text{GHz}$ continue to increase at higher optical depths, exceeding 1% at $d \approx 900$ and $d \approx 600$ respectively. In contrast, $2\pi \times 1\,\text{MHz}$ saturates at around 0.8% before evening off at higher optical depths, which corresponds to the peak Rabi frequency, seen in the inset of Fig. 5.5f, beginning to plateau. The metric of 1% is rather arbitrary here, as it does not directly relate to the fidelity of the output photon state. Nevertheless, it is clear that without correction, the FWM noise introduced will render a quantum memory unsuitable for quantum information.

We can use the gradient ascent optimisation strategy with a modified objective function in order to penalise the introduction of FWM. We write the new objective function,

$$\begin{aligned} J = & \int_0^1 dz\, S^*(z,T)S(z,T)\left(1 - \mathcal{F}\int_0^1 d\tau \mathcal{E}_F^*(L,\tau)\mathcal{E}_F(L,\tau)\right) \\ & + \int_0^1 dz \int_0^T d\tau \bar{P}^*[-\partial_\tau P - (\gamma + i\Delta - 2i\delta_{ls})P + \sqrt{d}\mathcal{E}_s - i\Omega S] + c.c. \\ & + \int_0^1 dz \int_0^T d\tau \bar{S}^*[+i\delta_{ls} - \partial_\tau S - i\Omega^* P - \frac{i}{2}\sqrt{\frac{d}{2}}\frac{\Omega}{\Delta_{HF}}\mathcal{E}_F^*] + c.c. \\ & + \int_0^1 dz \int_0^T d\tau \bar{\mathcal{E}}_s^*[-\partial_z \mathcal{E}_s - \sqrt{d}P] + c.c. \\ & + \int_0^1 dz \int_0^T d\tau \bar{\mathcal{E}}_F^*[-\partial_z \mathcal{E}_F + \sqrt{\frac{d}{2}}\frac{\Omega}{\Delta_{HF}}S] + c.c.\,, \end{aligned} \tag{5.73}$$

where $\mathcal{F}$ is a factor to determine how much to penalise FWM. The new expression gradient and the boundary conditions are given in the Appendix B.3.2.

The resulting efficiencies for a real valued control field and $\mathcal{F} = 100$ are plotted with solid lines in Fig. 5.8c with the efficiencies from Fig. 5.8a plotted in dashed lines for comparison. We see a general plateauing of the efficiency below that of Fig. 5.8a with some oscillation. In Fig. 5.8d we have plotted the associated FWM efficiency which is much reduced when compared with Fig. 5.8b. The oscillations in Fig. 5.8c and Fig. 5.8d coincide, due to the FWM noise increasing to the point where the FWM penalty began to significantly affect the optimum. At this point, efficiency is sacrificed to keep FWM low.

In Fig. 5.5e, the new optimal control pulses are plotted with solid lines, while the original pulses from the previous section are plotted with dashed lines. We see a preference for spreading out the area of the pulse, thereby retaining a similar total pulse energy but with a lower average Rabi frequency. The lower peak heights can be seen in the inset of Fig. 5.5e. The control fields for increasing optical depth ($d = 40, 110$ and 850) are shown in Fig. 5.5f, where the optimum is observed to split into two peaks. The inset shows how the control pulses tend to a maximum peak value. Worth noting is that optimising against FWM is equivalent to optimising for a lower average Rabi frequency. A similar metric to Eq. 5.73 can also be useful for experimental setups where laser power is limited.

From the results of this section, it would appear that high-bandwidth storage in a Λ-scheme quantum memory isn't possible for ^{87}Rb or alkali vapours with smaller ground hyperfine splittings (Cs has a larger splitting of $2\pi \times 9$ GHz and so could allow for higher bandwidths to be stored). However, we have so far neglected the full manifold of levels available in the excited state and the Zeeman sublevels contained within. In the next section, we will discuss how we may choose configurations resistant to FWM and how the optimum pulses and efficiencies change when considering more realistic systems.

5.4 Full excited state manifold

The treatment developed so far considered storage of $2\pi \times 1$ MHz, $2\pi \times 100$ MHz and $2\pi \times 1$ GHz bandwidth photons using only one excited state. However, the excited state splitting in ^{87}Rb is on the order of $2\pi \times 100$ MHz, and the control field Rabi frequency quickly approaches this splitting even for a $2\pi \times 1$ MHz bandwidth photon. As a result, we need to take into account transitions to all states in the excited state manifold, where depending on the dipole matrix elements the transitions may interfere constructively or destructively.

We have also seen how even for the simple three-level system, FWM can prevent storage of

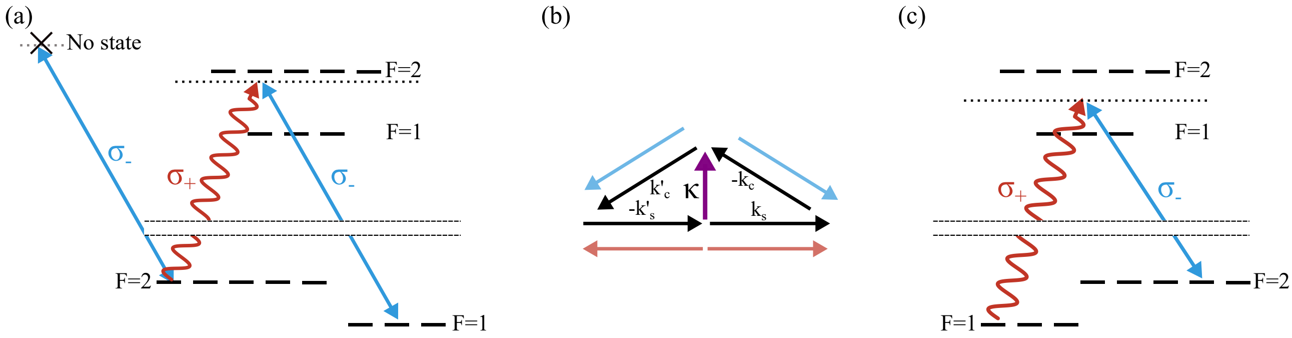

Figure 5.9: (a) Memory scheme using the ^{87}Rb D1 transition, where the population has been prepared in the ground $F = 2$ maximal spin state $m_F = -2$. The signal photon, illustrated by the red wavy line, is near-resonant with the excited hyperfine manifold and drives the σ_+ transition. The control field drives the σ_- transition, thereby coupling the excited state to the $F = 1$, $m_F = 0$ hyperfine ground state. With this configuration, the control field polarisation cannot couple the $F = 2$ state to the excited manifold and so FWM is eliminated. (b) Phase matching diagram for storage and backward retrieval. The black arrows represent the wavevectors of the various fields while the parallel coloured arrows illustrate the propagation direction of the fields. The spin wave wavevector, labelled κ, is given by $\boldsymbol{k}_s - \boldsymbol{k}_c$, where $\boldsymbol{k}_s$ and $\boldsymbol{k}_c$ refer to the input photon and control field wave vectors respectively. The retrieval control field wavevector is represented by $\boldsymbol{k'}_c$ and the retrieved signal photon $\boldsymbol{k'}_s$. (c) Memory scheme where the population has been prepared in the ground $F = 1$ maximal spin state $m_F = -1$, and $F = 2$, $m_F = +1$ is used as the storage state. These two states have the same variation with magnetic field to first order and so the stored coherence is somewhat insensitive to magnetic field fluctuations.

greater than 90%. Increasing the hyperfine ground state splitting is one way to mitigate the off-resonant coupling of the control field, though this restricts the available alkali species. If we consider the full excited state manifold, an alternative approach to mitigate the cross coupling of the control is to select a configuration of levels where the cross-coupled transitions are not dipole allowed. An example of such a scheme on the ^{87}Rb D1 transition is shown in Fig. 5.9a. This transition is compatible with the red insertion site of DBT [302].

The atomic population is initially prepared in the ground $F = 2$ maximal spin state $m_F = -2$. The input photon drives the transition σ_+ while the control field drives σ_-. With this setup, the control field cannot couple to the signal transition as there is no excited state with the appropriate m_F to couple to, thereby eliminating FWM noise. However, in reality polarisers and atomic preparation are not perfect, so some FWM may persist. In the rest of this section we will assume that FWM has been completely eliminated, but effects of weak FWM could be included by extending Eqs. 5.69-5.72 to include all allowed transitions in the system, and adjusting the strength of the couplings to reflect the error in atomic preparation of laser polarisation. Furthermore, for the case of the D2 manifold, which would be compatible with the main insertion site of DBT at 780 nm, the full FWM theory would need to be considered. This is beyond the scope of this thesis.

A feature we have neglected to mention so far is the effect on the spin wave of having signal and control fields with different wave vectors. A larger Δ_{HF} (and thus a larger wave vector mismatch between the signal and control fields) results in more momentum being taken up by the spin wave. We can absorb the additional momentum Δ_k by redefining the macroscopic operators [280] but we must now take care to amend the boundary condition for backwards retrieval (forwards retrieval remains unchanged) to,

$$S(z, T_R) = S(1 - z, T) \exp[-2i\Delta_k z]\,, \tag{5.74}$$

which can cause a significant reduction in efficiency unless $\Delta_k L \ll \sqrt{\frac{d}{2}}$. In Surmacz et al. [243], it was shown that this momentum mismatch may be compensated for by introducing an angle between the signal and control field, as shown in Fig. 5.9b. Typically for the wavevector mismatch acquired from the ground hyperfine state splitting, the angle required is of the order milli-radians.

For the full 2d simulation, provided the control wave vector is larger than that of the signal (as is the case for the scheme presented in Fig. 5.9a to prevent FWM), the memory interaction was shown to remain efficient and agree well with the one dimensional treatment. The justification is that the input and output photon traverse along the same axis and so the entire spin wave contributes to the interaction. In this case, increasing Δk is no longer a problem, though increasing the angle between the signal and control fields reduces the size of the interaction region. To counteract this, we may increase the width of the control beam, though at the cost of requiring a higher laser power to reach the same intensities. For schemes using signal photons with a larger wave vector than the control field it is important to include the phase factor in Eq. 5.74. Provided the length of the ensemble is low, and the optical depth high, possible in a high density MOT, the reduction in efficiency due to the phase mismatch can be kept minimal.

Another factor to consider is magnetic field sensitivity. The spin wave is distributed across two m_F states, in two different ground states. Fluctuations in magnetic field can cause fluctuations in the relative energies of the m_F levels for different atoms, which can lead to a differing phase evolution. The resulting decoherence will lead to a decay in the retrieval efficiency. To combat this, we could use $m_F = 0$ in states $F = 1$ and $F = 2$ as the ground and storage state, which will not fluctuate with magnetic field. While this configuration prevents magnetic dephasing, the polarisations of the signal and control fields now must be identical, making filtering of the control field more difficult. Alternatively, using $m_F = \pm 1$ as $|g\rangle$ and $m_F = \mp 1$ as $|s\rangle$, fluctuations in magnetic field are cancelled out to first order. This scheme is illustrated in Fig. 5.9c. With this configuration, the control and signal beams can be orthogonally polarised, though we now have a signal wave vector which is larger than the control wave vector, preventing us using the scheme shown in Fig. 5.9b. For simulating this magnetically insensitive scheme, it is important to include Eq. 5.74. Both of these magnetically insensitive schemes do not prevent cross-coupling of the control field and so other methods to reduce FWM would likely need to be employed.

It is clear that we cannot satisfy all of these issues (FWM, wave vector mismatch and magnetic field sensitivity) at once in the Λ-scheme. In the next chapter, we will consider ladder schemes which will allow us to satisfy all of these criteria, though at the expense of memory lifetime. For now, we will restrict ourselves to using $|g\rangle = |F = 2, m_F = -2\rangle$, $|s\rangle = |F = 1, m_F = 0\rangle$ and $|e\rangle = |F = 1, 2, m_F = -1\rangle$ on the D1 transition, as shown in Fig. 5.9a and assume no FWM. We will also neglect the non zero momentum of the spin wave, assuming either a short atomic ensemble length or a slight angle between the signal and control field. As for magnetic fields, appropriate $\mu-$metal shielding can protect the atoms from fluctuations [286] so we will not consider this any further.

Expanding Eqs. 5.37-5.39 to include multiple excited states, we arrive at,

$$\partial_z \mathcal{E}_s = \sum_j -(\sqrt{d_j})^* P_j \tag{5.75}$$

$$\partial_\tau P_j = -(\gamma_j + i\Delta_{sj})P_j + \sqrt{d_j}\mathcal{E}_s - i\Omega_j S_{gs} \tag{5.76}$$

$$\partial_\tau S_{gs} = -(\gamma_{gs} + i(\Delta_s - \Delta_c)) - i\sum_j \Omega_j^* P_j \,, \tag{5.77}$$

where the subscript j is used to index the states in the excited manifold. It is important to include the relative sign of $\sqrt{d_j}$ when solving the above equations.

The gradient of our metric for complex valued control field becomes,

$$\frac{\partial J}{\partial \Omega^*(\tau)} = i\int_0^1 dz \left(\sum_j \bar{P}_j\right) S_{gs}^* - \bar{S}_{gs}^* \left(\sum_j P_j\right) \,, \tag{5.78}$$

and real valued control field,

$$\frac{\partial J}{\partial \Omega(\tau)} = -2\int_0^1 dz\, \mathrm{Im}\left[\left(\sum_j \bar{P}_j\right) S_{gs}^* - \bar{S}_{gs}^* \left(\sum_j \bar{P}_j\right)\right] \,. \tag{5.79}$$

In Fig. 5.10a, b and c, we plot how the optimal efficiency changes as a function of detuning, relative to the $F = 2$ excited state, for optical depths $d = 500$, 1000 and 2000 respectively, where the photon and control fields are kept at two photon resonance. The solid lines refer to the real control field and the dashed lines to a complex control field. We see at an optical depth of 500, photon bandwidths of $2\pi \times 1\,\mathrm{MHz}$ and $2\pi \times 100\,\mathrm{MHz}$ (plotted in blue and green respectively) show a reduced efficiency at a detuning of $-2\pi \times 225\,\mathrm{MHz}$ from the excited $F = 2$ state. This is due to destructive interference between the two transitions. For a $2\pi \times 1\,\mathrm{GHz}$ bandwidth, the broader bandwidth prevents the destructive dip from being observed. In contrast, a complex control field appears to be able to mitigate the destructive interference and maintain a reasonably constant efficiency over the full manifold. At higher optical depths, both real and complex control fields are seen to tend to the same efficiency.

In Fig. 5.11 we have plotted the optimised control fields for detunings $-2\pi \times 225\,\mathrm{MHz}$ and

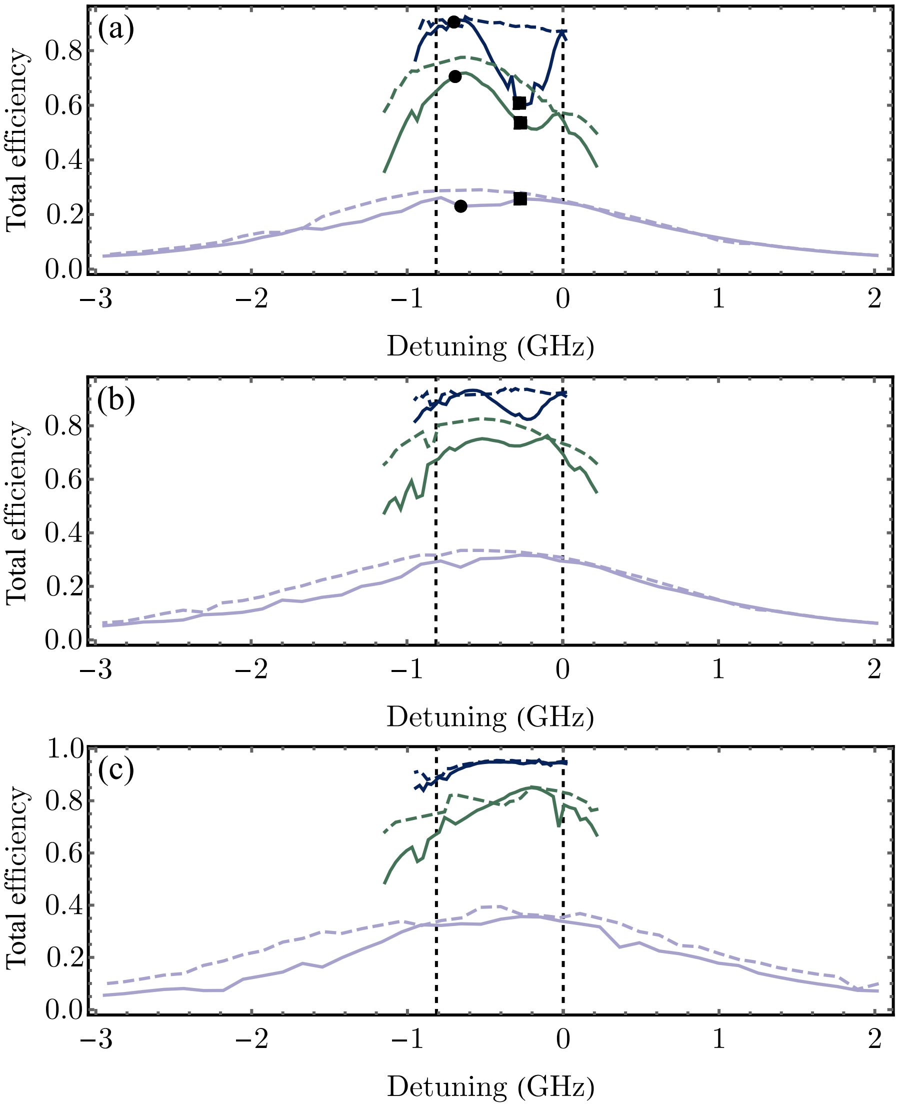

Figure 5.10: Plots of total memory efficiency versus detuning, relative to the $F = 2$ excited state of ^{87}Rb, for signal photons of bandwidth 1 MHz, 100 MHz and 1 GHz shown in blue, green and purple respectively, and with optical depths equal to (a) 500, (b) 1000, and (c) 2000.

$-2\pi \times 700\,\text{MHz}$, corresponding to the efficiencies marked with squares and circles on Fig. 5.10a respectively. For the detuning of $-2\pi \times 225\,\text{MHz}$, where we see a high degree of destructive interference, the control field amplitudes are shown in Fig. 5.11a, with solid lines representing the real optimisation and dashed the result of complex optimisation. The phases of the complex optimisation are shown in Fig. 5.11b. We see that for low bandwidths, we once again recover the same adiabatic shape as the three level case, while for higher bandwidths we begin to deviate from this shape. The real valued control pulse for an input photon of 1 GHz (purple) features a a degree of oscillation on a time scale consistent with the excited hyperfine splitting, most likely to counteract the photon interacting with both excited states. For the complex field, this oscillation is absent from the amplitude and we recover something more similar to the high bandwidth three level case. Instead we have a phase varying within the range of around $\pi/2$ for the period where the control field is of appreciable strength. For the $2\pi \times 1\,\text{MHz}$ (blue) case, the real and complex control fields have similar amplitudes and shapes, but the addition of a phase variation following the control amplitude causes an increase in efficiency from $\approx 60\%$ to 90%.

The control field shapes for detuning of $-2\pi \times 700\,\text{MHz}$ (black circles on Fig. 5.10a), corresponding to the higher efficiency are shown in Fig. 5.11c, along with the phases of the complex controls in Fig. 5.11d. The shapes remain very similar to Fig. 5.11a, with similar oscillations present in the $2\pi \times 1\,\text{GHz}$ (purple) case. Interestingly for the $2\pi \times 1\,\text{MHz}$ (blue) case, the complex optimisation requires around four times as much peak power, perhaps due to the gradient ascent finding two different local maxima. For this bandwidth and detuning, the complex control field doesn't require any significant changes in the phase.

At an optical depth of 2000 (not shown), all control shapes begin to resemble the adiabatic shape seen in the three level case, though with the oscillation in amplitude persisting for high bandwidths and real valued control fields.

From the results presented in this chapter, it is clear that to achieve high bandwidth quantum memories, we require much higher optical depths than those available in MOTs. We will now turn to warm vapours, where much higher optical depths are available.

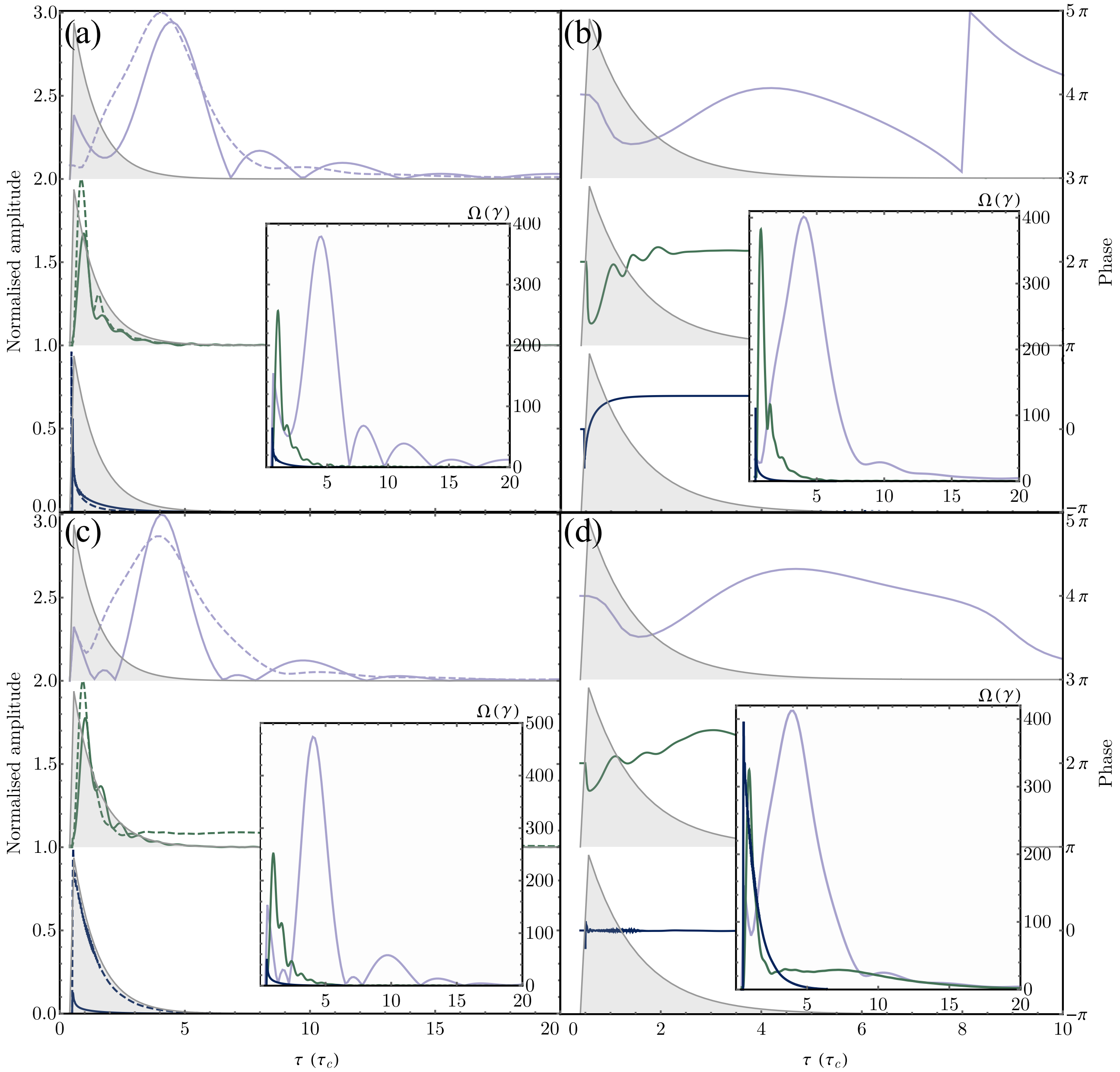

Figure 5.11: For a signal and control field detuning of $-2\pi \times 225\,\mathrm{MHz}$ from the $F = 2$ excited state of the ^{87}Rb D1 transition, and a signal photon of bandwidth $2\pi \times 1\,\mathrm{MHz}$ (blue), $2\pi \times 100\,\mathrm{MHz}$ (green) and $2\pi \times 1\,\mathrm{GHz}$ (purple), we have plotted are the (a) normalised optimal control field amplitudes, against τ in units of the characteristic decay time of the photons. The solid lines are the resulting amplitude from the real valued optimisation and the dashed lines the amplitude of the complex valued optimisation. The inset shows the true amplitudes of the real valued control fields, in units of Rabi frequency. (b) Plots showing the optimal phase from the complex values control, with the inset showing the true amplitudes of the complex valued control fields. For a signal and control field detuning of $-2\pi \times 700\,\mathrm{MHz}$, we have again plotted the (c) normalised control field amplitudes, with the true amplitudes of the real valued control field shown in the inset, and (d) the complex control field phases, along with the unnormalised complex valued control field amplitudes.

5.5 Warm vapour

While warm vapours offer significantly higher optical depths of hundreds of thousands, we must now deal with the non-zero velocity of the atoms. Each atom will Doppler shift the light fields depending on the relevant wavevector and velocity. We will first briefly return to the three-level system with finite temperature, before expanding to the full manifold. The new equations can be written as [280],

$$\partial_z \mathcal{E}_s(z,\tau) = -\sum_v \sqrt{p_v\, d}\, P_{ge}(v,z,\tau) \tag{5.80}$$

$$\partial_\tau P_{ge}(v,z,\tau) = -(\gamma_{ge} + i(\Delta_s - k_s v))P_{ge}(v,z,\tau) + \sqrt{p_v\, d}\mathcal{E}_s(z,\tau) - i\Omega_{es} S_{gs}(v,z,\tau) \tag{5.81}$$

$$\partial_\tau S_{gs}(v,z,\tau) = -(\gamma_{gs} + i\left((\Delta_s - k_s v) - (\Delta_c - k_c v)\right) S_{gs}(v,z,\tau) - i\Omega^*_{es} P_{ge}(v,z,\tau)\,. \tag{5.82}$$

For $k_s \neq k_c$, the addition of velocity results in a velocity dependent two photon detuning $((\Delta_s - k_s v) - (\Delta_c - k_c v))$. Due to the differing energies, over time velocity classes will become out of phase with one another, leading to a reduction in retrieval efficiency.

After storage, when the control field has been turned off at time $\tau = 0$, we can write the spin wave as,

$$S_{gs}(v,z,\tau) = \exp\left[-\frac{\gamma_{gs}}{2}\tau\right] \exp\left[i\left((\Delta_s - k_s v) - (\Delta_c - k_c v)\right)\tau\right] S_{gs}(v,z,0)\,, \tag{5.83}$$

which we can then integrate over the velocity distribution to give,

$$S_{gs}(z,\tau) = \exp\left[-\frac{\gamma_{gs}}{2}\tau - \frac{\mathrm{T}\Delta_{\mathrm{k}}^2\mathrm{k}_{\mathrm{B}}}{2\mathrm{M}}\tau^2\right] \exp\left[i\left(\Delta_s - \Delta_c\right)\tau\right] S_{gs}(v,z,0)\,. \tag{5.84}$$

In the above, T refers to the ensemble temperature, k_{B} the Boltzmann constant, and M is the mass of an atom in the ensemble. We can identify an exponential decay due to γ_{gs}, along with a decay which is shows quadratic exponential decay, termed Doppler dephasing.

In the $\Lambda-$scheme presented in this chapter, the signal and control field wavevectors are similar enough that this Doppler dephasing is negligible, over the timescale of microseconds. However,

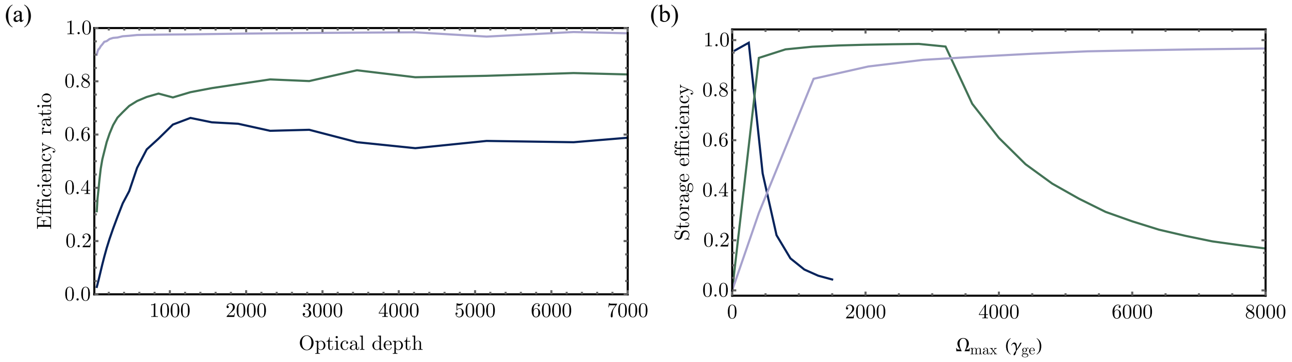

Figure 5.12: (a) Ratio of memory storage efficiency at 400 K to the efficiency at 0 K (using the optima obtained from gradient ascent in Section 5.2), plotted against the optical depth of the atomic medium, for photon bandwidths of $2\pi \times 1\,\mathrm{MHz}$ (blue), $2\pi \times 100\,\mathrm{MHz}$ (green) and $2\pi \times 1\,\mathrm{GHz}$ (purple). (b) Plot of storage efficiency as the control field peak Rabi frequency is increased, for a decaying exponential control field with the same characteristic decay time as the photon.

in Chapter 6 we will investigate systems for which this becomes a significant effect.

Another complication of warm vapours is the now velocity dependent *single* photon detuning $(\Delta_s - k_s v)$. Here, if the photon coherence is first mapped to atomic polarisation, each velocity will begin to evolve with a differing phase. We would therefore expect higher bandwidths to perform better in warm vapours as the shorter timescale of the memory interaction leaves less time for the atomic polarisation to decohere.

In Fig. 5.12a, we plot the ratio of memory storage efficiency at an ensemble temperature of $T = 400\,\mathrm{K}$ (127°C) to the efficiency at 0 K, as we vary the ensemble optical depth, while using the optima derived in Section 5.2. We see that as we approach high optical depths, the optima derived for higher bandwidths of photon tend to the $T = 0\,\mathrm{K}$ case, while lower bandwidths saturate at a lower value, due to the dephasing of atomic polarisation as the photon is absorbed.

However in reality, at temperatures of 400 K, we have optical depths of hundreds of thousands, which will push us well into the adiabatic regime for all of the bandwidths we are considering. We can crudely approximate the adiabatic control shape as a decaying exponential with the same characteristic decay time as the signal photon, where since the optical depth is so large, there is little decrease in efficiency from using the non-optimal shape. It is then sufficient to vary the amplitude to find the peak efficiency. In Fig. 5.12b we have plotted the efficiency as the control field peak Rabi frequency is varied, for a temperature of 400 K and $d = 150000$, which is the typical optical depth of ^{87}Rb at this temperature in a standard vapour cell. For all bandwidths we find that we can reach efficiencies over 90%, though we require much larger Rabi frequencies when compared to the cold system. We find for maximum efficiencies of 98.9%, 98.5% and 96.9%, the required peak Rabi frequency is 250, 2800 and 9500 respectively, in units of γ_{ge}. In comparison, optimal Rabi frequencies of the cold system were on the order of a few hundred γ_{ge} (see Fig. 5.5). For a control beam radius of 1 mm, these Rabi frequencies correspond to 80 mW, 10 W and 120 W respectively. We can see how for large bandwidths, in order to achieve the required intensities, we would need to focus the control field to a smaller beam waist.

It is possible to run the optimisation routine discussed throughout this chapter for warm vapours, though currently the simulation takes too long to run for this to be completed in a reasonable time. A more efficient simulation would allow warm systems to be optimised, while imposing a limit in the available control field intensity, in order to find the best compromise.

Something neglected so far in this section is the loss of atoms from the interaction region, as well as collisions with the vapour cell walls. While vapour cells may be coated to prevent decoherence due to wall collisions, in practice, atoms will be lost from the interaction region on the order of a microsecond in a warm vapour [300], though for smaller radii of control fields, atoms will be lost from the interaction region at a faster rate. This limits the warm vapours use for lower bandwidths such as $2\pi \times 1$ MHz. However, since storing higher bandwidths is desirable due to the larger time-bandwidth product, this is not really a limitation. Going forward, we no longer consider $2\pi \times 1$ MHz input photons.

A further cause for concern is FWM. With the large optical depths and control Rabi frequencies required in warm vapours, we can expect FWM noise to render our quantum memory useless. We will now return to the scheme illustrated in Fig. 5.9a and how the inclusion of the excited state manifold affects the warm vapour results.

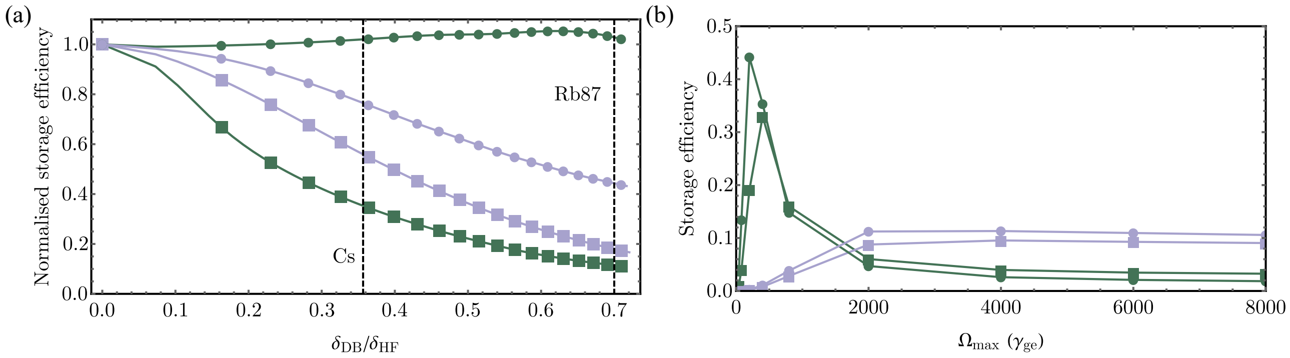

Figure 5.13: (a) Normalised storage efficiency versus the atomic ensemble Doppler width as a linear frequency, $\delta_{\rm DB}$, defined as in Eq.4.6, over the linear frequency splitting between the D1 excited hyperfine states, $\delta_{\rm HF}$. Plotted are photon bandwidths of $2\pi \times 100\,$MHz (green) and $2\pi \times 1\,$GHz (purple), where the efficiencies have been normalised to the $\delta_{\rm DB} = 0$ values. The lines marked by squares refer to a photon detuning of $-2\pi \times 220\,$MHz from the $F = 2$ excited state of the ^{87}Rb D1 transition, indicated by the black squares on Fig. 5.10a. The lines marked by circles refer to a detuning of $-2\pi \times 700\,$MHz, indicated by black circles on Fig. 5.10a. Additionally for convenience, we have marked the corresponding $\delta_{\rm DB}/\delta_{\rm HF}$ ratio for Rb^{87} and Cs at 400 K. (b) Plot of storage efficiency as the control field peak Rabi frequency is varied, for a decaying exponential control field with the same characteristic decay time as the photon.

5.5.1 Manifold

When expanding to the full excited manifold, the issue due to velocity classes becomes more pronounced, as it becomes difficult to isolate which transition the photon will interact with. We again focus on the two detunings labelled by the black squares and circles in Fig. 5.10a, keeping the optical depth fixed at $d = 2000$, but make a toy model atom where we can easily vary the linear Doppler width $\delta_{\rm DB}$ (see Eq.4.6) and/or hyperfine spacing of the two excited D1 hyperfine states, $\delta_{\rm HF}$. As we increase the ratio $\delta_{\rm DB}/\delta_{\rm HF}$, we we observe very different behaviour for the two detunings, plotted in Fig. 5.13a. For a detuning of $-2\pi \times 220\,$MHz (squares), the efficiency drops off very quickly, whereas $-2\pi \times 700\,$MHz (circles) performs better for the both the 100 MHz (green) and 1 GHz (purple) bandwidth photons, with the 100 MHz seemingly improving slightly for certain ratios. The storage efficiency here has been normalised to the $\delta_{\rm DB} = 0$ values shown in Fig.5.10. To compare our toy atom to realistic atoms, we have indicated the $\delta_{\rm DB}/\delta_{\rm HF}$ ratio for the D1 hyperfine states in Rb^{87} and Cs at $T = 400K$, by the labelled vertical black dashed lines.

However, if we set our optical depth to 150000 and again use a decaying exponential control field we find that we cannot reach high efficiencies for any control field amplitude, as shown in Fig. 5.13b. At high optical depth, it appears that the destructive interference between the two excited state transitions prevents efficient storage, at least for the control fields used here. This is where the gradient ascent optimisation method may be most useful, when paired with a faster running simulation, perhaps finding a complex valued control field which could counteract the destructive interference of the two excited state transitions, as was observed in Fig. 5.10a.

Despite this optimisation currently being intractable, a more attainable solution is to far detune from the excited state manifold, as is the case in Raman memories [218, 237, 367]. Here the memory dynamics are dominated by a single photon detuning, which is made many times larger than the hyperfine state splitting and Doppler broadening.

Something else we have failed to discuss so far is how the retrieved photon is practically filtered from the control field. Using polarisers to filter the orthogonally polarised control can achieve rejection on the order of 1000 : 1, but given the control field is likely many milliwatts (which must be filtered to below the single photon level), we need orders of magnitude better filtering. Some spatial filtering may be possible if there is a small angle between the signal and control fields, provided the collection pinhole is very far from the ensemble, though this is also typically insufficient. Generally, many etalon filters are added after the memory setup to spectrally filter out the control field. While these work well, with each one giving around 1000 : 1 rejection again, multiple etalons are still required, with each requiring careful alignment and temperature stabilisation. Additionally, the losses due to each interface concatenate to drastically reduce the end to end efficiency.

Recently, a novel quantum memory protocol was demonstrated, combining a far detuned Raman scheme with a ladder configuration of levels, referred to as off resonant cascaded absorption (ORCA) [236] or fast ladder memory (FLAME) [301]. This scheme boasts immunity from FWM noise as well as counter-propagating beams, making spatially filtering the control field from the retrieved photon trivial. In the next chapter, we will examine the ORCA memory scheme and how the optimisation technique used throughout this chapter may be applied to this new configuration.

Chapter 6

Ladder Scheme

In the previous chapter we optimised the memory efficiency of Λ-type near-resonant memories for cold atoms, such as those contained within a MOT. We showed how available optical depth and four-wave mixing (FWM) noise significantly restrict the bandwidths that are possible to store efficiently and with high fidelity. We then looked at warm vapours, which offer a much improved optical depth, but the large Doppler broadening prevented efficient storage on the ^{87}Rb D1 line due to being unable to isolate a single excited state transition. While it may be possible to overcome this by extending the gradient ascent algorithm to warm vapours (provided the simulation could be sped up) and modulating the phase of the control field, an alternative solution are protocols where the signal photon is far-detuned from the excited state. With the signal photon detuning much larger than the excited state hyperfine splitting and Doppler broadening, the memory dynamics becomes entirely dominated by the photon detuning, allowing us to approximate the excited manifold as a single state. Such a scheme falls under the umbrella of Raman memories.

In this chapter, we will look at the Off-Resonant-Cascaded-Absorption (ORCA) [236] memory scheme (also referred to as fast ladder memory or FLAME) [301], which is a Raman memory implemented using a ladder configuration of energy levels, illustrated in Fig. 6.1a. After discussing the differences between an ORCA memory and the near-resonant Λ-memories investigated last chapter, we will adapt the gradient ascent algorithm to optimise the ORCA scheme. We ex-

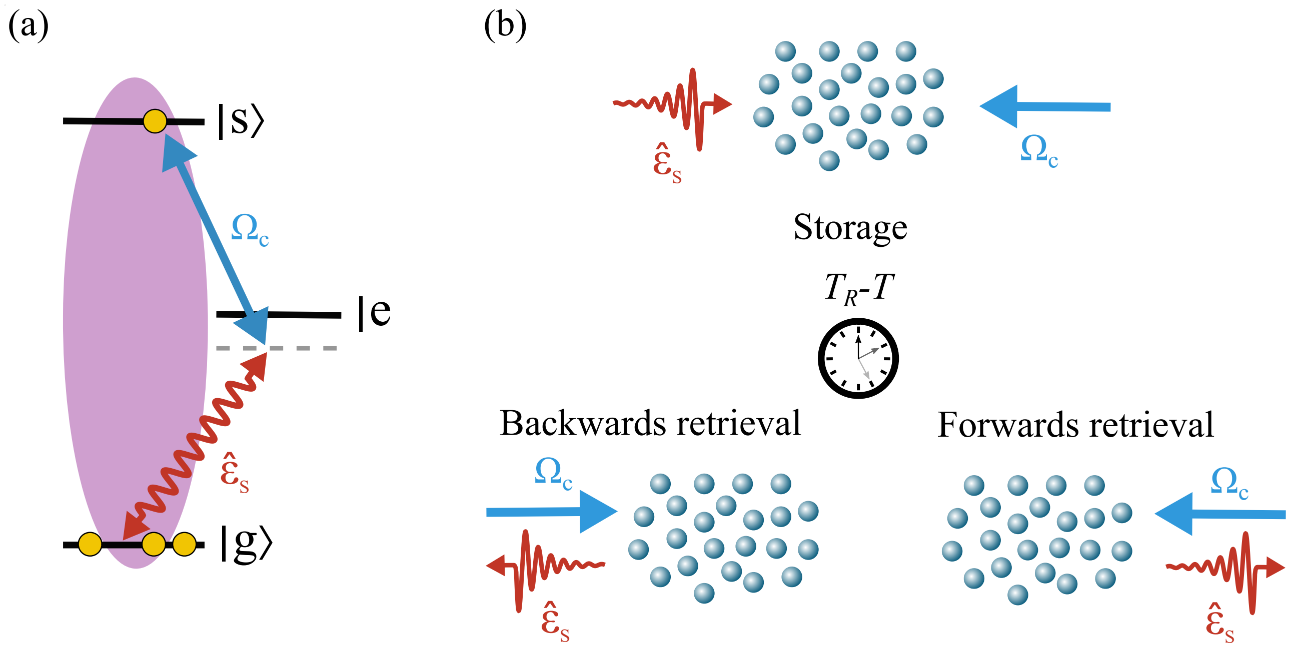

Figure 6.1: (a) Ladder configuration of levels, referred to as the ORCA scheme in the text. A photon $\hat{\mathcal{E}}_s$, detuned from the $|g\rangle \rightarrow |e\rangle$ transition, is coupled to the orbital wave coherence between the states $|g\rangle$ and$|s\rangle$ (represented by the purple oval) via a classical control field Ω_c, detuned from $|e\rangle \rightarrow |s\rangle$. (b) The photon and control field counter-propagate through the ensemble. At time T_R, where the storage interaction was completed at time T, we can either retrieve into the forward or backward direction, depending on the direction of the retrieval control field.

amine how the optima differ and scale compared with that of the lambda system; in particular how the length of the cell and overlap of the optical fields becomes an important consideration. Following this, we will investigate a similar scheme, namely the telecom ORCA (TORCA) protocol [343], which allows the storage of telecommunications wavelengths single photons with Rb. Joining these schemes together, we will see how this also allows for wavelength conversion between telecom and 780 nm light, before briefly discussing ways to extend the lifetimes of the ORCA and TORCA protocols.

6.1 ORCA

Memories based on a Λ-configuration store the coherence between the two ground states. This comes with the benefit of a long coherence lifetime of the spin wave. However we saw in the previous chapter how there are some major drawbacks. First of all is four-wave mixing

(FWM) noise. Due to the cross coupling of the control field to the signal transition, we are severely limited in the bandwidth of photon we can store, unless we employ other techniques to temper FWM, which add further complexity to the system, such as requiring optical pumping. Secondly, due to the signal and control propagating in the same direction, up to some small angle, it can be difficult to filter out the control field to below the single photon level without introducing a lot of loss for the retrieved photons as well. We may also wish to use magnetically insensitive states. Storage using the $m_F = 0$ states required signal and control fields of the same polarisation for the Λ-configuration, which would be difficult to separate. Alternatively, using states $m_F = \pm 1$ and $m_F \mp 1$ for the initial and storage states requires the signal wavevector to be larger than the control wavevector, which may reduce efficiency due to phase mismatching for backwards retrieval. Yet, we do not have to use the two ground states to store the atomic coherence. In principle, any two states with a long enough lifetime (long compared with the photon temporal duration) could constitute a useful quantum memory.

The ORCA scheme [236, 301] overcomes many of the difficulties associated with a Λ-type memory. This scheme uses a ladder configuration of levels, with the control field mapping the photon coherence to an atomic coherence between the initial ground state and a doubly excited state, as shown in Fig. 6.1a - the stored coherence is termed an orbital wave. There are three main differences to the storage interaction between the two memory schemes. Firstly, the absorption of a photon in the Λ-type memory was followed by stimulated emission into the mode of the control field, resulting in a spin wave with a momentum equal to $\boldsymbol{k}_s - \boldsymbol{k}_c$, where $\boldsymbol{k}_s$ refers to the photon wavevector and $\boldsymbol{k}_c$ to the control field wavevector. That meant we required copropagating beams (up to some small angle) to give the smallest resulting spin wave momentum and therefore, the longest lived spin wave, see Eq. 5.84. In contrast, a ladder-type memory absorbs both the input photon and a photon from the control field, forming an orbital wave with momentum of $\boldsymbol{k}_s + \boldsymbol{k}_c$. This necessitates the two optical fields be counter-propagating (again up to some small angle), illustrated in Fig. 6.1b, in order to produce the lowest momentum orbital wave. This allows trivial spatial filtering of the photon from the control field.

Secondly, since the two atomic transitions used are no longer restricted to starting and ending in the same hyperfine manifolds, the photon and control can have a much larger frequency difference. Rather than a few gigahertz separation, limited by the ground hyperfine splitting of whichever alkali metal we chose, the separation can now be many nanometers. As well as allowing for further spectral filtering of the signal photon, this also effectively eliminates FWM noise. As long as the control field remains a shorter wavelength than the signal field, we can always correct the phase matching for backward retrieval by introducing an angle, with no detriment to efficiency, provided we can make our control beam suitably large in diameter.

On top of this, there is no problem in using magnetically insensitive states, other than having to optically pump to prepare the states. If we don't require magnetically insensitive states, unlike the Λ-scheme where we must empty the storage state of all population, in the ORCA scheme, the doubly excited state is already unpopulated, so we don't require any initial state preparation.

The downside to this scheme is the orbital wave decay. The doubly excited state has no single photon transitions to the ground state and so is longer lived than the intermediate excited state, yet even so, the spin wave decays on a much faster timescale when compared with a cold Λ-type memory. For example, the ^{87}Rb state $5D_{5/2}$, used in Finkelstein et al. [301], has an electronic decoherence rate of 240 ns. For applications where the memory lifetime is not as critical, the ORCA scheme offers some significant advantages over Λ-type systems.

6.1.1 Equations of motion

While the equations governing our new configuration appear very similar to the Λ-case, there are nonetheless some subtle differences in the dynamics. For a three level ladder configuration, our equations of motion read,

$$\begin{aligned}
\partial_z \mathcal{E}_s &= -\sqrt{\frac{d}{2}} P_{ge} \\
\partial_\tau P_{ge} &= -(\gamma_{ge} + i\Delta_s) P_{ge} + \sqrt{\frac{d}{2}} \mathcal{E}_s - \frac{i}{2} \Omega_{es}(\tau + 2z/c) S_{gs} \\
\partial_\tau S_{gs} &= -(\gamma_{gs} + i(\Delta_s + \Delta_c)) S_{gs} - \frac{i}{2} \Omega^*_{es}(\tau + 2z/c) P_{ge} \,,
\end{aligned} \tag{6.1}$$

where $\Delta_c = \omega_c - \omega_{se}$ and $\Omega_{es} = \frac{\mu^*_{es} v^*_c \mathcal{E}^*_c}{\hbar}$ have been redefined. See Appendix B.1 for a full derivation.

We have also redefined the macroscopic spin wave operator as,

$$S_{gs} = \frac{1}{\sqrt{n\delta V}} \sum_{a(r)} \widetilde{\sigma}^a_{gs} \exp\left[i(\Delta_s - \Delta_c)\tau + 2ik_c z\right] \; , \tag{6.2}$$

where we have included the longitudinal momentum of the control field in the co-moving reference frame of the signal photon, $2k_c = 2\omega_c/c$.

Apart from the change in definitions, Eqs. 6.1 differ from the Λ-configuration only due to the inclusion of spin wave decay and a control field with a dependence on $\tau + 2z/c$ with $2z/c$ representing the signal and control beam walk off.

If we define a characteristic duration of the control pulse, τ_{control}, then the spatial length of the control pulse is $c\tau_{\text{control}}$. For the case of $c\tau_{\text{control}} \gg L$, where L is the length of the atomic medium, we arrive at the short cell limit, and Eqs. 6.1 reduce to the copropagating case: $\Omega_{es}(\tau + 2z/c) \approx \Omega_{es}(\tau)$. In this limit, all the results from the previous chapter optimisation apply, except without any FWM noise and with the addition of spin wave decay. However in practice this restriction would limit the available optical depth and the bandwidth of photons capable of being stored.

The opposite limit is where optical pulses are much shorter than the medium, either due to very long cells or atoms within an optical fibre, or because of large bandwidth optical fields. In this limit the two optical fields are able to completely pass each other in the medium. One potential benefit of this, would be to allow for multiple temporal modes to be stored at different spatial positions along the memory. While potentially useful for quantum information processing, similar mappings have been used for quantum sensing [228].

Although it is possible to use the ladder scheme while near resonant with the intermediate excited states, in this chapter we will focus on the far-detuned raman case, with the goal of efficiently storing high bandwidth photons in a warm vapour. However, large detuning comes at the cost of requiring much more optical depth and control field power to reach the high efficiencies compared with the near-resonant case. At this far-detuned limit, we can assume that the atomic polarisation adiabatically follows the incident fields and set $\partial_\tau P = 0$ [232, 264, 361, 362]. We can therefore simplify our equations to,

$$\partial_z \mathcal{E}_s = \frac{+i\sqrt{\frac{d}{2}}\Omega_{es}(\tau + 2z/c)S_{gs} - d\mathcal{E}_s}{2(\gamma_e + i\Delta_s)} \tag{6.3}$$

$$\partial_\tau S_{gs} = -\left(\gamma_s + i(\Delta_s + \Delta_c) + \frac{|\Omega_{es}(\tau + 2z/c)|^2}{4(\gamma_e + i\Delta_s)}\right) S_{gs} - \frac{i\sqrt{d/2}\,\Omega^*_{es}(\tau + 2z/c)\mathcal{E}_s}{2(\gamma_e + i\Delta_s)} \tag{6.4}$$

where we have made the substitution $P_{ge} \approx \left(\sqrt{\frac{d}{2}}\mathcal{E}_s - \frac{i}{2}\Omega_{es}S_{gs}\right)/(\gamma_{ge} + i\Delta_s)$. In the above set of equations, we can identify the $|\Omega_{es}|^2$ term as the AC stark shift produced by the control field. The real and imaginary part of the $d\mathcal{E}_s/[2(\gamma_e + i\Delta_s)]$ term refer to absorption and dispersion respectively.

6.1.2 Modification to optimisation

We can construct a similar optimisation metric as the previous chapter,

$$\begin{aligned} J = &\int_0^1 dz S_{gs}(z,T)S^*_{gs}(z,T) \\ &+ \int_0^1 dz \int_0^T d\tau \bar{\mathcal{E}}^*_s \left[-\partial_z \mathcal{E}_s + \frac{+i\sqrt{\frac{d}{2}}\Omega_{es}(\tau + 2z/c)S - d\mathcal{E}_s}{2(\gamma_e + i\Delta_s)} \right] + c.c. \\ &+ \int_0^1 dz \int_0^T d\tau \bar{S}^*_{gs} \left[-\partial_\tau S_{gs} - \left(\gamma_s + i(\Delta_s + \Delta_c) + \frac{|\Omega_{es}(\tau + 2z/c)|^2}{4(\gamma_e + i\Delta_s)}\right) S_{gs} \right. \\ &\left. - \frac{i\sqrt{\frac{d}{2}}\Omega^*_{es}(\tau + 2z/c)\mathcal{E}_s}{2(\gamma_e + i\Delta_s)} \right] + c.c.\,, \end{aligned} \tag{6.5}$$

although we now want to find the gradient of J in the co-moving frame of the *control field*. This equates to finding the gradient $\frac{\partial J}{\partial \Omega_{es}}(\tau + 2z/c)$. To do so, we make the transformation

$y = \tau + 2z/c$ and define the new macroscopic operators,

$$\xi(y,\tau) = \mathcal{E}_s\left(\tau + 2z/c, \tau\right) \tag{6.6}$$

$$\sigma(y,\tau) = S_{gs}\left(\tau + 2z/c, \tau\right) \tag{6.7}$$

Our new equations of motion are,

$$\partial_y \xi(y,\tau) = \frac{+ic\sqrt{\frac{d}{2}}\Omega^*_{es}(y)\sigma - cd\xi}{4(\gamma_e + i\Delta_s)} \tag{6.8}$$

$$\left(\partial_\tau + \partial_y\right)\sigma(y,\tau) = -\left(\gamma_s + i(\Delta_s + \Delta_c) + \frac{|\Omega_{es}(y)|^2}{4(\gamma_e + i\Delta_s)}\right)\sigma - \frac{i\sqrt{\frac{d}{2}}\Omega_{es}(y)\xi}{2(\gamma_e + i\Delta_s)} \tag{6.9}$$

Now taking the Fourier transform in the τ direction, defined as,

$$f'(y,k) = \frac{1}{\sqrt{2\pi}}\int_{-\infty}^{\infty} d\tau f(y,\tau)\exp\left[ik\tau\right] \,, \tag{6.10}$$

results in,

$$\partial_y \xi'(y,k) = \frac{+ic\sqrt{\frac{d}{2}}\Omega^*_{es}(y)\sigma' - cd\xi'}{4(\gamma_e + i\Delta_s)} \tag{6.11}$$

$$\partial_y \sigma'(y,k) = ik\sigma(y,k) - \left(\gamma_s + i(\Delta_s + \Delta_c) + \frac{|\Omega_{es}(y)|^2}{4(\gamma_e + i\Delta_s)}\right)\sigma' - \frac{i\sqrt{\frac{d}{2}}\Omega_{es}(y)\xi'}{2(\gamma_e + i\Delta_s)} \,. \tag{6.12}$$

In these transformed coordinates, the real-valued gradient reads,

$$\frac{\partial J}{\partial \Omega^*}(y) = \int_0^1 dk\ 2\,\mathrm{Im}\left[\sqrt{\frac{d}{2}}\left(\frac{\bar{\xi}^*\sigma' c}{4(\gamma_e + i\Delta_s)} + \frac{\bar{\sigma}\xi'}{2(\gamma_e - i\Delta_s)}\right)\right] \tag{6.13}$$

$$- \Omega_{es}(y)\mathrm{Re}\left[\frac{\bar{\sigma}^*\sigma'}{4(\gamma_e + i\Delta_s)} + \frac{\bar{\sigma}\sigma'^*}{4(\gamma_e - i\Delta_s)}\right] \tag{6.14}$$

With these transformed equations, we can derive expressions for the co-functions,

$$\partial_y \bar{\xi}(y,k) = \frac{-ic\sqrt{\frac{d}{2}}\Omega_{es}^{*}\bar{\sigma} + cd\bar{\xi}}{4(\gamma_e - i\Delta_s)} \tag{6.15}$$

$$\partial_y \bar{\sigma}(y,k) = ik\sigma(y,k) + \left(\gamma_s - i(\Delta_s + \Delta_c) + \frac{|\Omega_{es}|^2}{4(\gamma_e - i\Delta_s)}\right)\bar{\sigma} + \frac{i\sqrt{\frac{d}{2}}\Omega_{es}\bar{\xi}}{2(\gamma_e - i\Delta_s)}\,, \tag{6.16}$$

which are precisely the transformed co-functions of Eqs. 6.3-6.4,

$$\partial_z \bar{\mathcal{E}}_s = \frac{-i\sqrt{\frac{d}{2}}\Omega_{es}(\tau + 2z/c)\bar{S}_{gs} + d\bar{\mathcal{E}}_s}{2(\gamma_e - i\Delta_s)} \tag{6.17}$$

$$\partial_\tau \bar{S}_{gs} = \left(\gamma_s + i(\Delta_s + \Delta_c) + \frac{|\Omega_{es}(\tau + 2z/c)|^2}{4(\gamma_e - i\Delta_s)}\right) S_{gs} + \frac{i\sqrt{\frac{d}{2}}\Omega_{es}^{*}(\tau + 2z/c)\mathcal{E}_s}{2(\gamma_e - i\Delta_s)}\,, \tag{6.18}$$

with the following boundary conditions,

$$\bar{\mathcal{E}}_s(L,\tau) = 0 \tag{6.19}$$

$$\bar{S}_{gs}(z,T) = S_{gs}(z,T) \tag{6.20}$$

So to perform the same optimisation for backwards retrieval as the previous chapter, we must store using our trial control field using Eqs. 6.3-6.4, then solve using Eqs. 6.17-6.18 (with time and space reversed), subject to the boundary conditions described in Eqs. 6.19-6.20. We then transform the coherences to obtain $\xi(y,k)$, $\bar{\xi}(y,k)$, $\sigma(y,k)$ and $\bar{\sigma}(y,k)$ and compute the gradient defined in Eq. 6.14.

The resulting transformations are illustrated in Fig. 6.2. We can see how the transform $\tau + 2z/c \rightarrow y$ results in two axis which each describe the retarded time frame of either the co-propagating photon, or the counter-propagating control field. If we examine the gradient in Eq. 6.14 more closely, we see that the first term resembles the near-resonant co-propagating gradient, in that it compares the coherences before and after time reversal. The second term did not appear in the near-resonant case directly, but is a consequence of adiabatically eliminating P_{ge} from the system, which directly includes the AC stark shift. This second term is an explicit penalty for control field power while coherence is stored in S_{gs}, i.e. informs the optimisation to

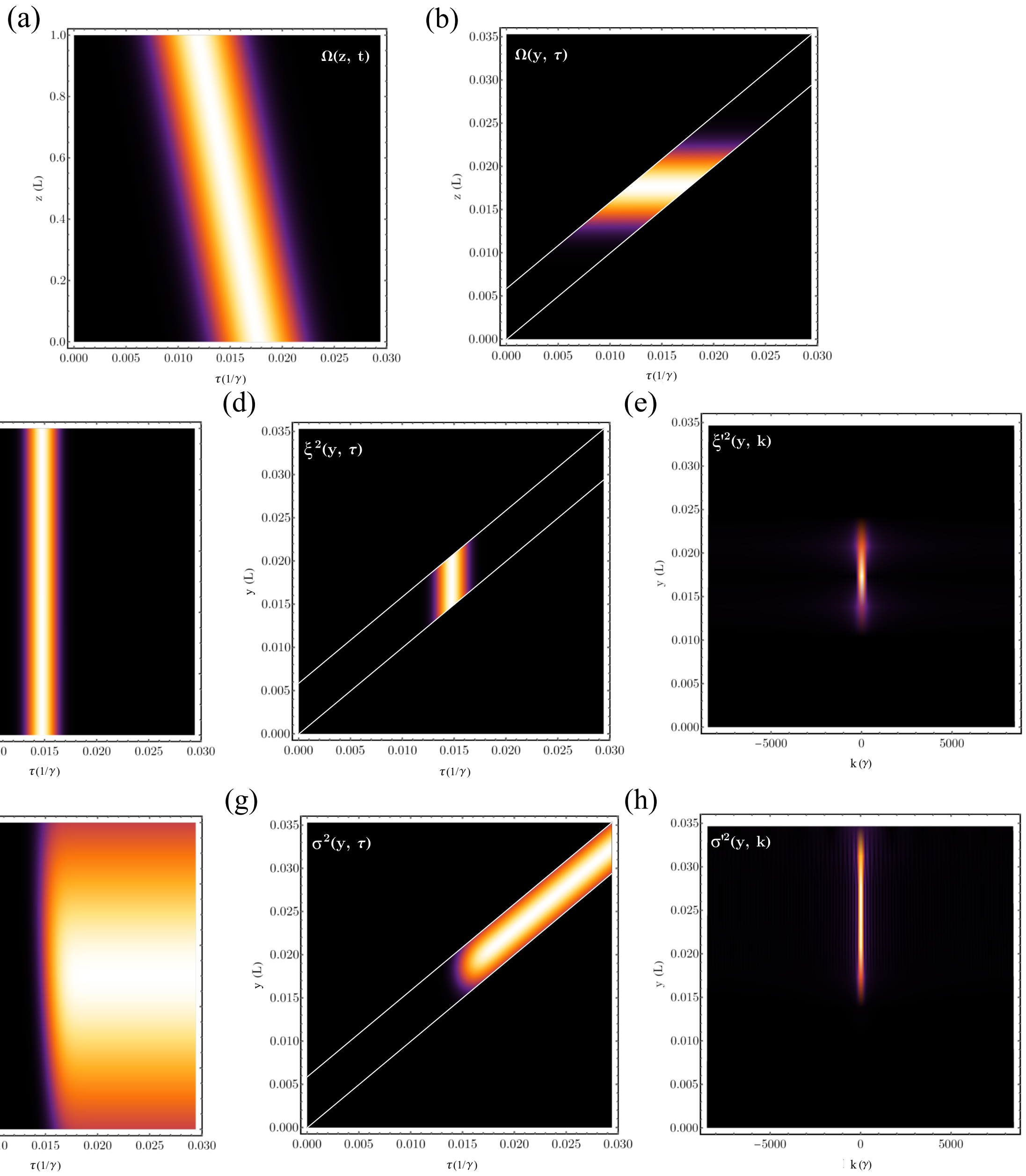

Figure 6.2: Plots showing visually the outcome of the transform $\tau + 2z/c \rightarrow y$, followed by a Fourier transform along τ. Shown are the (a) counter propagating control field $\Omega_{es}(z, \tau)$, (b) and the transformed control field $\Omega_{es}(y, \tau)$, where the diagonal white lines indicate the edge of the ensemble. (c) Plot of the non-transformed square of the photon field $\mathcal{E}_s^2(z, \tau)$ propagating through the ensemble, (d) then transformed to $\mathcal{E}_s^2(y, \tau)$, (e) and finally Fourier transformed along τ to give $\mathcal{E}_s^2(y, k)$, with k the Fourier conjugate variable of τ. (f) Plot of the non-transformed square of the spin ave $S_{gs}^2(z, \tau)$, (g) then transformed to $S_{gs}^2(y, \tau)$ (h) and finally Fourier transformed along τ, resulting in $S_{gs}^2(y, k)$

counteract the AC stark shift.

6.1.3 Results

We examine the two bandwidths from the end of Chapter 5, namely 100 MHz and 1 GHz. Each is detuned by 1.5 GHz and 3 GHz respectively, so as to be well away from the Doppler broadened intermediate excited state and have negligible overlap between the photon bandwidth and the intermediate states, while still maintaining an appreciable atom-light coupling. We also investigate three key lengths of atomic ensemble: 3 cm, comparable to a typical magneto optical trap (MOT), 7.5 cm, the length of a standard Rb vapour cell and 80 cm, to investigate dynamics relevant to fibre based systems. For a 100 MHz photon, 3 cm and 7.5 cm correspond to the short cell regime, and 80 cm resides in the long cell regime. For a 1 GHz photon, we have 3 cm in the intermediate regime, whereas 7.5 cm and 80 cm are in the long cell regime.

For simulating storage, it is now important to ensure that the time frame of the simulation is long enough to allow for the control pulse to completely traverse the atomic ensemble, otherwise we will bias the gradient optimisation to a particular time window, which will in turn bias the resulting optimal spin wave to a region in space, particularly in the long cell regime. We simulate a total time of L/c, with the input photon arriving at time equal to $L/(2c)$. As the length of the cell or bandwidth increases, choosing to solve with too coarse a mesh will result in non-smooth coherences, particularly along a diagonal, which can be exasperated by the interpolation required for the transform $\tau + 2z/c \rightarrow y$, as well as the subsequent Fourier transform.

We optimise the ORCA memory for cold atoms, so that the optimisation runs in a reasonable time frame, but extend the optical depths considered to 15000 due to Raman memories requiring a higher optical depth to reach large efficiencies. While these optical depths are not currently obtainable in cold systems, our goal is to use the derived optimal control fields with warm vapours, and so the high cold optical depth is simply to obtain the adiabatic regime optima.

In contrast to the previous chapter, we found that the best initial condition for the control field

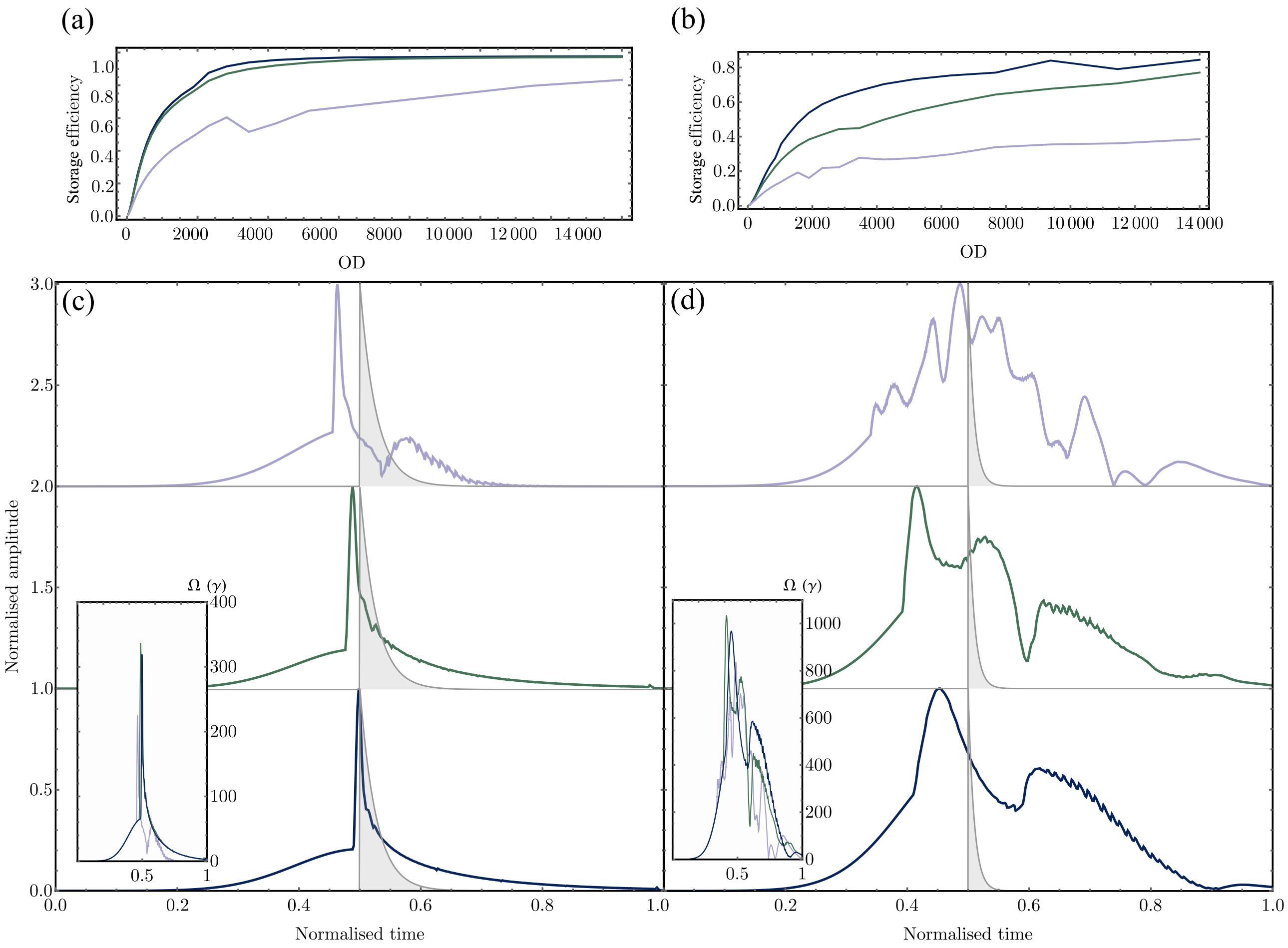

Figure 6.3: Optimisation results for ensembles of length 3 cm, 7.5 cm and 80 cm, shown in blue, green and purple respectively. Plot of optimal storage efficiency as a function of optical depth, for an input photon bandwidth of (a) 100 MHz and (b) 1 GHz. Optimal control fields at the midpoint of the cell for input photon bandwidths of (c) 100 MHz and (d) 1 GHz. The photon temporal shape is shown in grey. Insets show the true amplitudes of the control fields in terms of rabi frequency.

was a Gaussian with a full-width-half-maximum equal to 1/4 of the storage simulation time and an amplitude equal to the bandwidth of the input photon. The control field was initialised and optimised at the midpoint of the cell, and interpolated for each point in z to simulate counter-propagation. The results for the real-valued optimisation are shown in Fig. 6.3.

In Fig. 6.3a we plot the optimised storage efficiency as optical depth is increased, for ensembles of length 3 cm (blue), 7.5 cm (green) and 80 cm (purple). We will examine the total efficiency after returning to warm vapours. For optical depths currently accessible in a MOT (≈ 1000) we see that it was only possible to achieve around 70% storage efficiency, whereas for the three level near-resonant case in the last chapter, the optimum reached 90%. The efficiencies for 3 cm and 7.5 cm are largely indiscernible, as they are both in the short cell regime. As we move to 80 cm, we see a substantial decrease in efficiency as the interaction region (the space-time area where the photon field and control field overlap) is reduced. The results for a 1 GHz input photon are plotted in Fig. 6.3b. For all lengths, this bandwidth is no longer in the short cell regime, leading to a significant reduction in storage efficiency.

The optmised control fields in the short cell regime, (plotted at the midpoint of the cell in Fig. 6.3c) for a photon bandwidth of 100 MHz, lengths of 3 cm and 7.5 cm, both resemble the adiabatic case from near-resonant co-propgating memories, but with slightly higher amplitudes (shown in the inset). As we approach the long cell regime, the peak of the control field moves earlier in time, resulting in the intersection of photon and control field happening at an earlier point in the cell from the perspective of the photon. We also observe a second feature appearing at a later time. The inset of Fig. 6.3c shows this second feature as a second bump, acting to spread out the control pulse area, thereby increasing the interaction region, along with a reduction in the length of the exponential tail, which would otherwise propagate the coherence further through the ensemble, leading to more loss. Note that each length has been normalised to the same duration of time for ease of comparison. The ragged edges seen on this later bump are simulation artifacts from too coarse a computation mesh combined with the transforms required to calculate the gradient. In the inset of Fig. 6.3c we see how there is very little change in the peak amplitudes, with a small reduction as length increased to 80 cm.

In Fig. 6.3d, we have plotted how the control fields change for a photon bandwidth of 1 GHz, where the system is now in the intermediate/long cell regime, along with becoming less adiabatic. For $L = 3$ cm, the control field appears similar to the 100 MHz $L = 80$ cm case, except the initial decaying exponential is somewhat smeared out, similarly to the near-resonant case as we moved away from the adiabatic regime. Additionally, we see a general spreading out of the control pulse when compare to the 100 MHz optima, resulting in an increased interaction region. The oscillations seen for $L = 80$ cm don't significantly alter the efficiency and likely are the result of too few time and space steps used in the optimisation. In the inset, we again see very little change in the Rabi frequencies required, though with an overall higher peak amplitude when compared to the 100 MHz case.

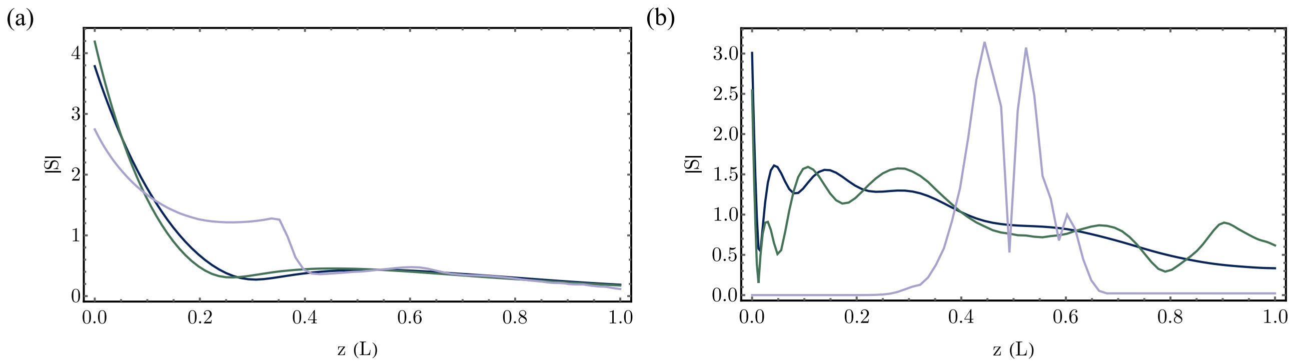

Figure 6.4: Spin waves resulting from optimised real-valued control fields, for ensembles of length 0.03 m (blue), 0.075 m (green) and 1 m (purple), and with an input photon bandwidth of (a) 100 MHz and (b) 1 GHz.

The resulting spin waves from the optimisation are shown in Fig. 6.4. For a photon bandwidth of 100 MHz, (Fig. 6.4a) with $L = 3\,\mathrm{cm}$ and $L = 7.5\,\mathrm{cm}$ (short cell regime), the spin waves agree well with those from the previous chapter, where the majority of the coherence is stored at the entry to the atomic ensemble. As the length is increased, the optimisation still favours this, but there is a resulting sharp drop of in spin wave amplitude at $z \approx 0.4$. For a 1 GHz input photon, further into the long cell limit, the optimum spin waves found deviate from the co-propagating case substantially. There still appears to be some preference for more spin wave amplitude at the entry to the cell for $L = 3\,\mathrm{cm}$ and $L = 7.5\,\mathrm{cm}$, but the optimisation seems to result in the entire length of the ensemble being used. For the most extreme case of $L = 80\,\mathrm{cm}$, the spin wave coherence is well localised in exactly the middle of the ensemble.

6.1.4 Extending to warm vapours and full manifold

We will now look at how the previously derived optima scale to warm vapours. Similarly to the previous chapter, we will investigate how efficiency changes as we increase the ensemble temperature to 400 K, for both a simple three level system as well as after including the full excited state manifold.

In Fig. 6.5a, we plot the ratio of memory storage efficiency at an ensemble temperature of $T = 400\,\mathrm{K}$ (127°C) to the efficiency at 0 K, as we vary the ensemble optical depth, while using the optima derived in Section 6.1.3, for an input photon bandwidth of 100 MHz and ensemble

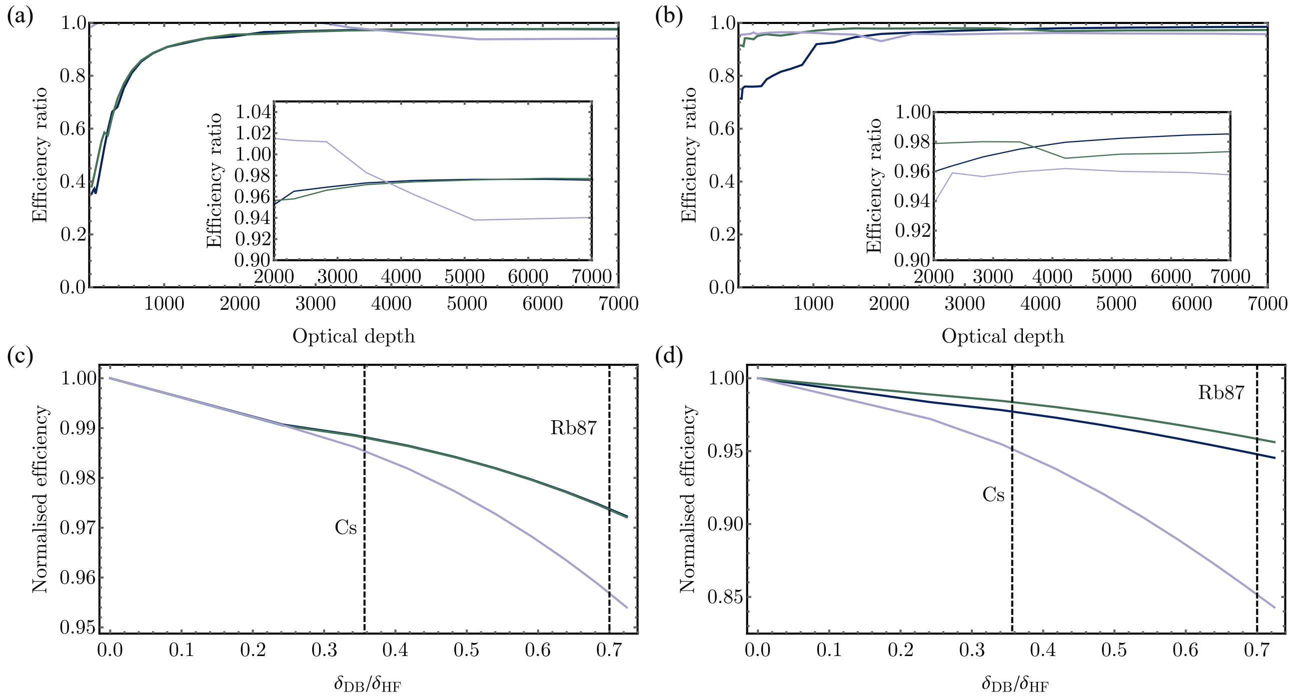

Figure 6.5: Ratio of memory storage efficiency at 400 K to the efficiency at 0 K (using the optima obtained from gradient ascent in Section 6.1.3), plotted against the optical depth of the atomic medium, for ensemble lengths of 3 cm (blue), 7.5 cm (green) and 80 cm (purple), and photon bandwidths of (a) $2\pi \times 100\,\mathrm{MHz}$ (b) and $2\pi \times 1\,\mathrm{GHz}$. Both insets show zoomed in plots of optical depths above 2000 to compare efficiency ratios close to one. In the lower two plots, we show normalised storage efficiency versus the atomic ensemble Doppler width as a linear frequency, δ_{DB}, defined as in Eq.4.6, over the linear frequency splitting between the D1 excited hyperfine states, δ_{HF}. Plotted are photon bandwidths of (c) $2\pi \times 100\,\mathrm{MHz}$ (d) and $2\pi \times 1\,\mathrm{GHz}$, where the efficiencies have been normalised to the $\delta_{\mathrm{DB}} = 0$ values. Additionally for convenience, we have marked the corresponding $\delta_{\mathrm{DB}}/\delta_{\mathrm{HF}}$ ratio for Rb^{87} and Cs at 400 K.

lengths of 3 cm (blue), 7.5 cm (green) and 80 cm (purple). We see that as we approach optical depths of around 2000, the see the storage efficiency tend to the $T = 0\,\text{K}$ case for all lengths. This is in contrast to the case previously in Fig. 5.12, where a 100 MHz input photon failed to reach the $T = 0\,\text{K}$ as we increased the optical depth. Due to the off-resonant Raman nature of the interaction, the intermediate excited state is never populated and so the protocol does not suffer from the same dephasing of atomic polarisation. In the inset, we zoom in on the later optical depths to distinguish the efficiency ratio close to one. For the 80 cm (purple) case, the efficiency ratio above one may again be due to simulation artifacts, originating from too coarse a computation mesh. In Fig. 6.5b, we show the same plot but with an input photon of bandwidth 1 GHz, which shows an efficiency ratio which approaches one at lower optical depths. This may due to the larger single photon detuning used, leading to further resistance to the Doppler broadening of the atoms.

In Fig. 6.5c and Fig. 6.5d, we again plot the results for 100 MHz and 1 GHz respectively, but after including the full hyperfine manifold of the intermediate state (see Appendix B.1) and we vary the ratio $\delta_{\text{DB}}/\delta_{\text{HF}}$, where δ_{DB} denotes the linear Doppler width (see Eq. 4.6) and δ_{HF} is the hyperfine splitting of the two excited D1 hyperfine states. We simulated the configuration where all of the population was prepared in the ground state $|F = 2, m_F = -2\rangle$, the input photon was polarised to be σ_+ and the intermediate manifold was chosen to be $5P_{3/2}$ (D2 transition). While the spacing between the hyperfine states are different on the D2 transition to δ_{HF} (D1 transition), they are related and so δ_{HF} still serves as a reasonable indicator of the hyperfine splitting of the intermediate state manifold. The control field was also set to be σ_+ and at two photon resonance with the storage state $|F = 1, m_F = 0\rangle$ in the manifold $5D_{5/2}$ (the remaining hyperfine states in the storage manifold were not simulated). This is by no means the optimal choice of states and polarisations, but serves to check how well the previously derived optima extrapolate to more complex systems and allows us to compare the ORCA scheme to the near-resonant scheme presented in the previous chapter.

We see a similar story as for the three level model (Fig. 5.13a), in that the efficiency decreases as the $\delta_{\text{DB}}/\delta_{\text{HF}}$ ratio is increased. However, the decrease is much less than the near-resonant scheme presented in the previous chapter, due to the far-detuned nature of the interaction generalising

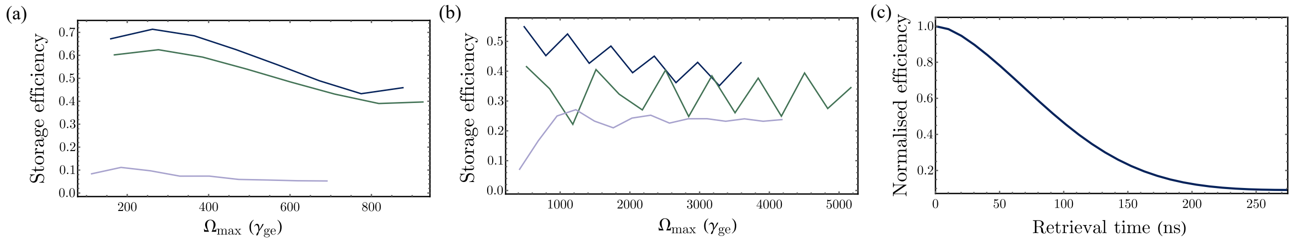

Figure 6.6: Plots of storage efficiency as the control field peak Rabi frequency is increased, using the off resonant cascaded absorption (ORCA) memory protocol with a decaying exponential control field where the characteristic decay time (τ_c) is equal to that of the photon, but with the initial edge ramped on from zero to max height over $\tau_c/10$. The line colours correspond to ensemble lengths of 3 cm (blue), 7.5 cm (green) and 80 cm (purple), and plotted are the cases for an input photon bandwidth of (a) 100 MHz and (b) 1 GHz. (c) Normalised retrieval efficiency for backwards retrieval from a warm vapour, as a function of retrieval time: time between when storage was completed and when the retrieval control pulse entered the cell.

to warm vapours and more complicated hyperfine structures more favourably. Again we have indicated the $\delta_{\mathrm{DB}}/\delta_{\mathrm{HF}}$ ratio for real atoms Rb^{87} and Cs to show how well some of the optima derived here would be expected to perform in warm atomic ensembles found in the lab. The longer cell regimes appear to perform more poorly than the rest, most likely due to the increase in susceptibility to simulation error.

For the near-resonant memories in the previous chapter, we found that for the three level case, while there was some drop in efficiency as the temperature of the ensemble was increased, after increasing the optical depth to typical warm vapour levels and approximating the control field as a decaying exponential of the same bandwidth as the signal photon, with an increased control field amplitude, we could attain greater than 90% efficiency. However, when including the excited manifold, the high optical depth resulted in storage efficiencies of less than < 30%, even after adjusting the control field amplitude. In Fig. 6.6a and b (input photon of 100 MHz and 1 GHz respectively), we have plotted how the storage efficiency varies with maximum control field Rabi frequency, while simulating the full excited hyperfine manifold and approximating the adiabatic control field as a ramped-on exponential decay - that is, rather than a instantaneous step on, the amplitude is ramped up to the maximum value on a timescale of $\tau_c/10$, where τ_c is the characteristic decay time of the input photon. Omitting this ramp reduces the storage efficiency by around 10%. The ensemble was initialised with an optical depth of 150000 and temperature of 400 K. We observe higher efficiencies than the previous chapter, suggesting that the off-resonant scheme offers some protection against the multiple transitions in the intermediate state manifold. However, the efficiency is noticeably lower than that seen for the three level case, though the peak Rabi frequencies required for maximum efficiency are of a similar order to the cold three-level derived optima. The lower efficiencies are likely due to a non-optimal choice of states and polarisations. In the long cell regime, the ramped decaying exponential appears to not generalise as well. The oscillations seen in Fig. 6.6b are likely due to too coarse a mesh in time, space and velocity.

Doppler dephasing

In the previous chapter, we briefly discussed Doppler depahsing, and how differing signal and control field wavelengths can lead to the phase of the stored coherence in different velocity classes to evolve at a different rate. For a $\Lambda-$type memory, Doppler dephasing was negligible over a storage time on the order of microseconds. Yet, for the ORCA protocol, while having signal and control fields separated by nanometers has many benefits, the downside is a much increased Doppler dephasing rate. In Finkelstein et al. [301], ORCA was implemented in a warm Rb vapour where the state $|e\rangle$ was the $5P_{3/2}$ manifold (D2 transition) and the storage state $|s\rangle$ was the $5D_{5/2}$ manifold. The wavelengths for the signal and control fields were therefore 780 nm and 776 nm respectively. Due to such differing wavevectors, the timescale for Doppler dephasing is just 175 ns. In Fig. 6.6c we have plotted the results of simulating the retrieval efficiency as a function of time between storage and retrieval control pulse, showing the characteristic Gaussian decay associated with Doppler dephasing.

How the phase of the spin wave evolves in time is illustrated in Fig. 6.7 where on the left is the spin wave phase just after storage, showing how the phase varies through a short section of the ensemble, for atoms at different velocities. Directly below the real part of the averaged spin wave is plotted . Plotted on the right is the spin wave phase after 175 ns where we can see how different velocities have evolved to have a distinct phase at the same position in the ensemble. The resulting real part of the averaged spin wave is shown below, where we can clearly see a reduced visibility when compared to the plot on the left.

Storage manifold

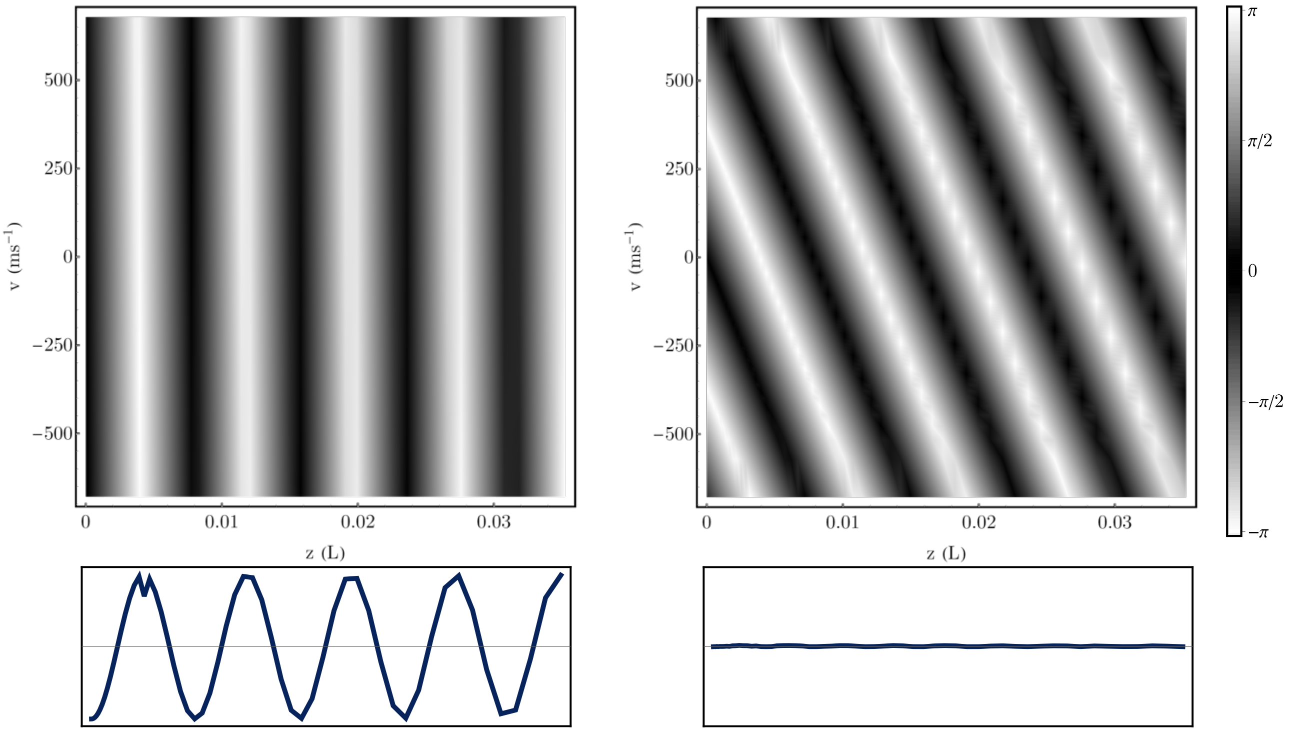

Figure 6.7: Left: Spin wave immediately after storage using the off-resonant cascaded absorption (ORCA) protocol, for a signal wavelength 780 nm and control wavelength 776 nm. Shown below is the real part of that averaged spin wave. Right: Spin wave after 2 ns, with the corresponding real part of the average plotted below.

In the above discussion and simulations, while we have accounted for the intermediate excited state manifold, we have ignored the hyperfine manifold of the storage state. Without any optical preparation of the atoms, transitions to multiple storage states are possible. Since each state has a different energy, the orbital waves stored in each accumulate phase at a different rate, leading to a beating in the retrieval efficiency, as observed in Finkelstein et al. [301]. By first optically preparing the atoms in a particular ground state, the number of storage states involved in the memory can be reduced, thereby removing the retrieval efficiency beating. Even so, the existence of multiple storage states may lead to differing optima then those derived from the three-level case. As for the metric, we could choose to maximise the stored coherence involving specified storage states or coherence stored in the full storage manifold. In Appendix B.1, we outline the necessary modifications to the theory and optimisation including all hyperfine manifolds and Zeeman sublevels.

Alternatively, using a large magnetic field would allow for transitions between individual Zeeman sublevels to be resolved [369].

6.2 Telecom-ORCA

Recently, Thomas et al. [343] used the same ladder configuration as ORCA, but with $4D_{5/2}$ used as the storage state, which has a transition of 1529.3 nm above $5P_{3/2}$, rather than the $5D_{5/2}$ state used as the storage state for ORCA in the previous section [301]. Additionally, the transitions addressed by the signal and control field were swapped, with the control pulse now addressing the ground and intermediate states, and the signal addressing the intermediate to storage states. A schematic of this scheme is pictured on the left of Fig. 6.8a, between the states $|g\rangle$, $|e_1\rangle$ and $|s\rangle$, with optical fields Ω_{c1} (wavelength of 780 nm) and $\mathcal{E}_T$ (1529 nm). This allowed Rb to be used to store telecom light, with a total memory efficiency of 20%, which is competitive with other telecom compatible quantum memories [370], while boasting room temperature operation and no atomic preparation required beforehand (besides the heating of a Rb vapour cell). In contrast, other telecom quantum memories are typically based on solid state crystals and require cryogenic cooling [370, 371, 372, 373]. On top of this, the Rb telecom-ORCA (TORCA) memory benefits from a much higher optical depth of 150000 when compared to other telecom memories, which are typically on the order of 10 [370, 373], but at most 150 [342]. This allowed read in efficiencies of up to 80% for a 1 GHz input signal field at 6 GHz detuning [343]. However, due to the two optical fields being 780 nm and 1529 nm, the large wavevector mismatch results in a Doppler dephasing time of ~ 2 ns.

In Appendix B.2 we derive the equations of motion for TORCA. These are presented below,

$$\partial_z \mathcal{E}_T = -\frac{i\sqrt{\frac{d}{2}}\Omega_c^* S_{gs}}{2(\gamma_s + \gamma_e + i\Delta_t)}\,, \tag{6.21}$$

$$\partial_\tau S_{gs} = -\left(\gamma_s + i(\Delta_c + \Delta_t) + \frac{|\Omega_c|^2}{4(\gamma_s + \gamma_e + i\Delta_t)}\right) S_{gs} - \frac{i\sqrt{\frac{d}{2}}\Omega_c \mathcal{E}_T}{2(\gamma_e + i\Delta_c)} \tag{6.22}$$

where we can see they are almost identical to ORCA equations of the previous section, except for the absence of the absorption/dispersion term in the equation for $\partial_z \mathcal{E}_T$, along with changes to the complex decay term featured in the denominators. The lack of absorption/dispersion is due to the absence of population which can directly interact with the photon, while the modification

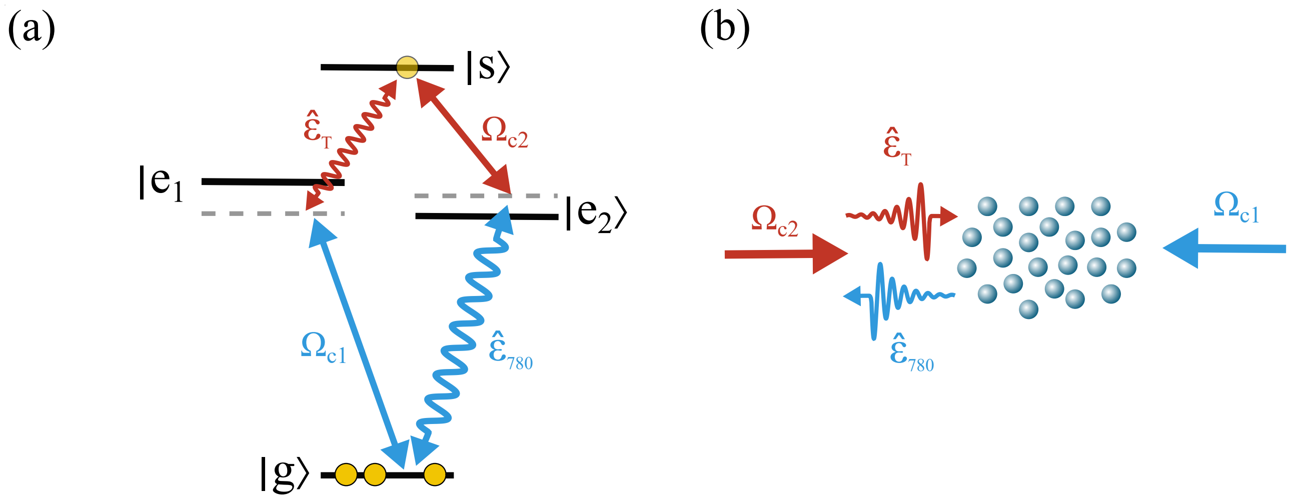

Figure 6.8: (a) Combined schematic of the telecom off resonant cascaded absorption protocol (TORCA) for storage of telecom compatible photons with a 780 nm control field, using the states $|g\rangle$, $|e_1\rangle$ and $|s\rangle$, and the standard off resonant cascaded absorption protocol (ORCA) for storing 780 nm photons with a telecom control field, using the states $|g\rangle$, $|e_2\rangle$ and $|s\rangle$. Using one protocol for storage and the other for retrieval results in a quantum memory with wavelength conversion. (b) Schematic showing the directions of the fields for the storage of telecom compatible single photons with a 780 nm control field, and retrieval of 780 nm photons using a telecom control field.

to the decay results from the dephasing rate of the coherence between levels $|e\rangle\langle s|$.

As with the ORCA protocol, the optical depths needed to realise an efficient TORCA memory require warm vapours. While in the previous section we saw that the optima for ORCA generalised very well to warm vapours, the dramatic increase in Doppler dephasing associated with TORCA means that any optima derived for a cold ensemble will not translate well to warm systems. In this section, rather than optimise storage of telecom light using the TORCA, which ends up being remarkably similar to the results from the previous section (for low optical depths at least), we will instead focus on the storage of 780 nm light using the ORCA protocol, but retrieve using the TORCA protocol, thereby theoretically showing 780 nm to 1529 nm wavelength conversion combined with a memory. This can be viewed as FWM with a controllable delay and the scheme is illustrated in Fig. 6.8. The left side of Fig. 6.8a shows the usual TORCA scheme, while on the right side (using states $|g\rangle$, $|e_2\rangle$ and $|s\rangle$) is the ORCA protocol but with a control field Ω_{c2} of wavelength 1529 nm. States $|e_1\rangle$ and $|e_2\rangle$ in principle need not be different states. In reality, due to the short lifetime of the stored coherence in a warm vapour, the conversion process would have to be completed almost immediately. We will examine telecom conversion

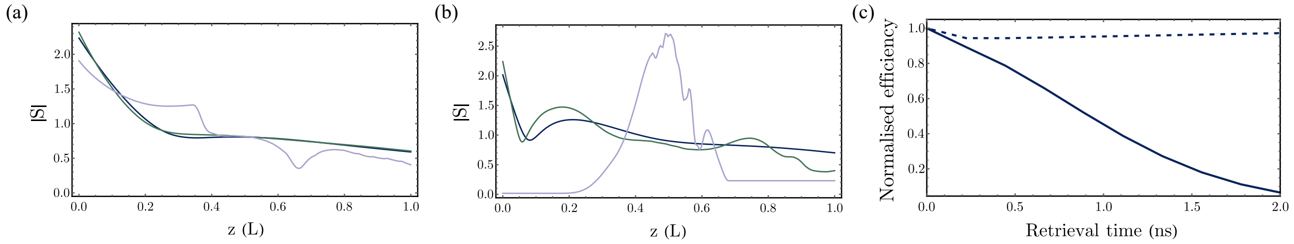

Figure 6.9: Amplitudes of the spin wave for the telecom off-resonant cascaded absorption (TORCA) protocol, when storage was completed using the control fields optimised for the off resonant cascaded absorption (ORCA) protocol, for ensemble lengths of 3 cm (blue), 7.5 cm (green) and 80 cm (purple) with an input photon of bandwidth (a) 100 MHz, and (b) 1 GHz. (c) Normalised retrieval efficiency for backwards retrieval from a warm vapour, as a function of retrieval time: time between when storage was completed and when the retrieval control pulse entered the cell. Plotted in solid blue is the retrieval efficiency for the TORCA protocol, while the dashed blue line is the retrieval efficiency for the ORCA protocol for comparison.

for zero temperature as a proof of principle and later discuss potential approaches to reduce Doppler dephasing and extend the memory lifetime of TORCA (and ORCA). It should also be noted that the reverse process could be used to convert telecom photons to 780 nm.

Wavelength conversion

For optimising backward retrieval of ORCA, as retrieval was the time reverse of storage and therefore both processes had the same optimal orbital wave, it was sufficient to only optimise storage. In Fig. 6.9a and b (input 1529 nm photon of 100 MHz and 1 GHz respectively), we have plotted the resulting orbital wave modes when using the ORCA optimal control fields with the TORCA protocol, for an optical depth of 15000 and a temperature of 0 K. While the orbital waves resemble those found in the ORCA protocol, there is some dissimilarity. For a 100 MHz input photon, the orbital wave is not as localised at the beginning of the ensemble, perhaps because the dispersion cannot be leveraged to slow down the photon. The resulting storage efficiencies for TORCA storage are also slightly lower, though all of the total retrieval efficiencies for the TORCA protocol at this bandwidth are larger than those of the ORCA, as shown in Table 6.1, where retrieval for both ORCA and TORCA were performed $6\tau_c = 10$ ns after storage. While TORCA appears to be more efficient, even without the correct optima, where it falls short is the much reduced spin wave lifetime due to Doppler dephasing. In Fig. 6.9c, the solid blue line shows how the retrieval efficiency for TORCA decreases for an ensemble temperature of 400 K, over 2 ns. Also shown for comparison is the retrieval efficiency

Input photon bandwidth	L (cm)	ORCA storage efficiency (%)	TORCA storage efficiency (%)	ORCA total efficiency (%)	TORCA total efficiency (%)	Telecom conversion efficiency (%)
100 MHz	3	96.1	94.3	90.7	93.3	72.2
	7.5	95.3	93.6	89.4	92.6	78.2
	80	51.5	50	23.1	42.3	9.5
1 GHz	3	74.4	65.2	53.1	62.5	50.4
	7.5	77.8	28.3	53.4	21.1	52.7
	80	18.1	24.4	1.4	8.2	1

Table 6.1: Table showing the efficiencies for the off resonant cascaded absorption (ORCA) and telecom off resonant cascaded absorption (TORCA) protocols, while using the optimal control fields for the ORCA protocol. In the final column are the efficiencies for storage with the ORCA protocol, followed by retrieval with the TORCA protocol, thereby realising delayed wavelength conversion between 780 nm photons and 1529 nm photons.

for ORCA (dashed blue line) for the same parameters.

With a 1 GHz photon (Fig. 6.9b), for lengths 3 cm and 7.5 cm we see a similar story, with the orbital wave distributed more evenly across the ensemble. At a length of 80 cm, while the orbital wave is similarly localised in the middle of the ensemble, it appears smoother than the ORCA case and with the amplitude collected together rather than in two peaks, suggesting that the absence of dispersion allows the photon to be more effectively stored in the long cell limit (or that the simulation had an easier time of solving the equations). This is reflected in Table 6.1 where the storage efficiency for 1 GHz, 80 cm TORCA exceeds that of ORCA. For total efficiency, TORCA again exceeds ORCA at lengths 3 cm and 80 cm, where retrieval was performed 1 ns after storage. Strangely for a 7.5 cm long ensemble, TORCA performs much worse.

For the case of telecom conversion, since the ORCA and TORCA orbital waves differ, it is not the case that the optimisation for the ORCA protocol is sufficient to optimise telecom conversion. A combined optimisation which takes into account the full telecom conversion process is needed, where the telecom field used to read the 780 nm photon into the memory and the 780 nm control field used to read out a telecom photon, in general will not have the same shape, and some compromise would have to be made between the two halves of the conversion process. To do so, the gradient ascent method could be extended to optimise both fields simultaneously, but we leave this to future work. However, motivated by the comparable efficiencies of ORCA and TORCA shown in Table 6.1, here we instead use the previously derived optima for ORCA but change the wavelength of the control field from 1529 nm to 780 nm when retrieving. The efficiencies are shown in the final column of Table 6.1 for an optical depth of 15000 and a temperature of 0 K. We can see how the conversion process lowers the overall efficiency, but that we still achieve an appreciable amount of conversion. Optimisation of the full process may allow for efficiencies approaching those of the individual protocols.

In Fig. 6.10, we show how the output photon temporal shape differs for the case of telecom conversion (solid line), compared with ORCA read out (dashed). For the short cell limit (bandwidth of 100 MHz, and ensemble length of 3 cm and 7.5 cm), plotted in Fig. 6.10a and Fig. 6.10c, there is very little difference between the output photons, apart from a decrease in area for the telecom conversion. This can be attributed to the lack of length for dispersion to significantly alter the result. However, as we move to the longer cell limits, we observe a much larger discrepancy. It is also important to point out how the short cell limit is the only one which faithfully reproduces the exponential decaying input photon (up to time reversal).

Increasing the orbital wave lifetime

Even with the non-optimum control fields, increasing the optical depth by moving to a warm vapour could be used to increase the conversion efficiency to over 90%. Yet any increase in efficiency would be counteracted by the accompanying Doppler dephasing, which would decrease the efficiency to zero over the course of a few nanoseconds, and even fast readout would be subject to significant loss.

In order to realise delayed telecom conversion, or TORCA as a useful quantum memory, we must find a way to extend it lifetime. Firstly, Doppler dephasing is the greatest source of decoherence. For the standard ORCA in Rb, Finkelstein et al. [374] reduced Doppler dephasing to negligible amounts by using an additional classical control field, to induce a light shift which counteracted the different rates of phase evolution of each velocity class. We show this schematically in Fig. 6.11a, where we again store the photon coherence between states $|g\rangle$ and $|s\rangle$, but we add a third field labelled by Ω_1 and dashed, detuned from an auxiliary state $|aux\rangle$. In Fig. 6.11c, we

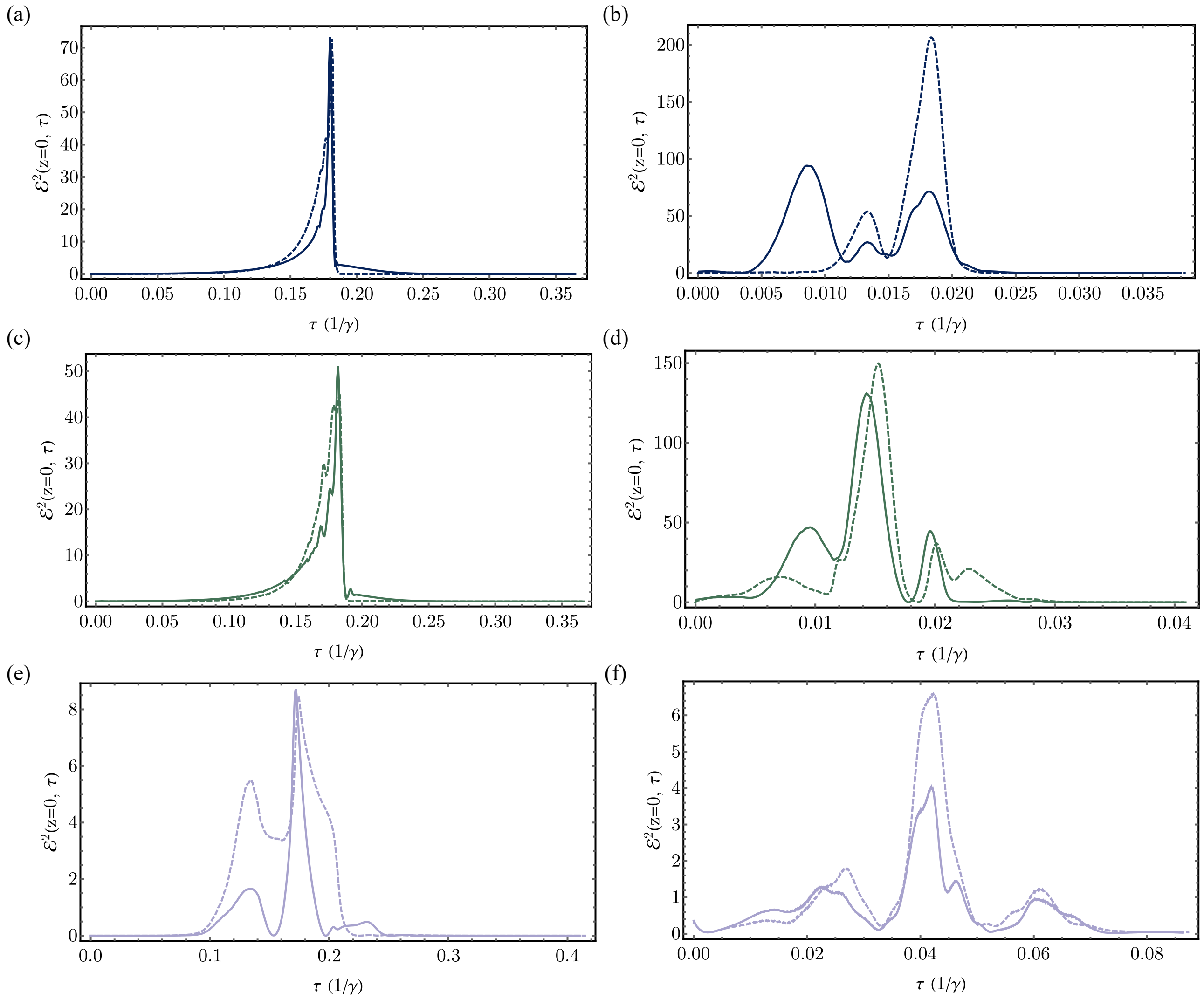

Figure 6.10: Square of the output photon electric field temporal shape after storage with the off resonant cascaded absorption (ORCA) protocol and subsequent backward retrieval using ORCA (dashed line) or telecom off resonant cascaded absorption (TORCA, solid line), for an ensemble length of 3 cm and input photon bandwidth of (a) 100 MHz (b) 1 GHz, length of 7.5 cm, bandwidth of (c) 100 MHz(d) 1 GHz, and length of 80 cm, bandwidth of (e) 100 MHz (f) 1 GHz.

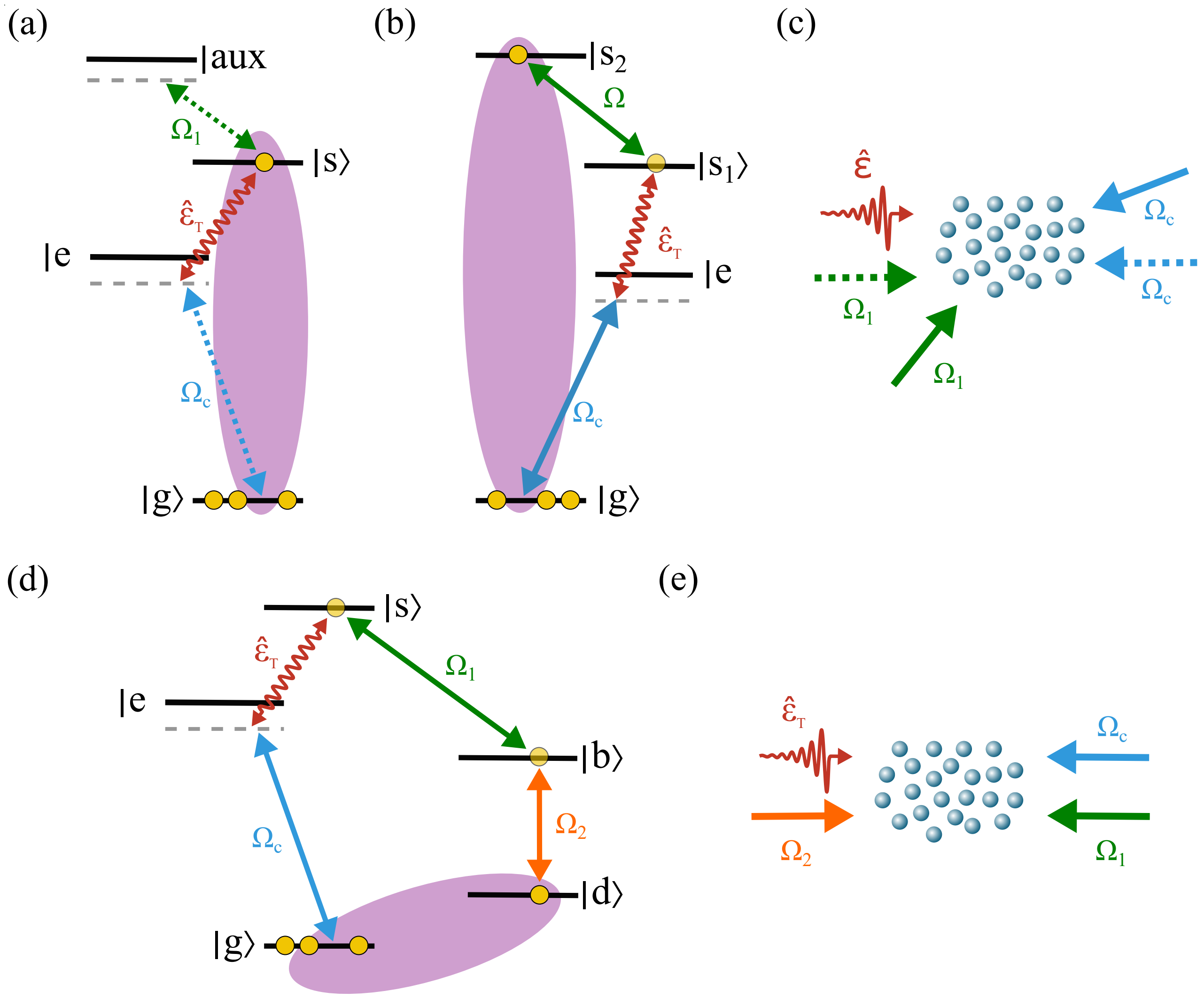

Figure 6.11: Strategies to improve the lifetime of the telecom off resonant cascaded absorption (TORCA) protocol. (a) Adapted from Finkelstein et al. [374] where this setup removed Doppler dephasing from the off resonant cascaded absorption (ORCA) protocol. This scheme stores the coherence between states $|g\rangle$ and $|s\rangle$ as in the usual TORCA protocol, but features an additional classical field Ω_1, detuned from an auxiliary state $|\text{aux}\rangle$, which acts to light shift the individual velocity classes in the opposite way to the Doppler shift. The result is that the phase evolution for each of the velocity classes is more uniform, thereby reducing Doppler dephasing and increasing the memory lifetime up to the electronic state lifetime of $|s\rangle$. (b) An alternative strategy where an additional control field acts to map the stored coherence from the original storage state $|s_1\rangle$, to a different storage state $|s_2\rangle$. The wavelength of the second control field Ω_1 is chosen such that all three optical fields may be placed at an angle to produce an orbital wave with minimal momentum. This scheme also benefits from using a higher lying excited state which typically have longer lifetimes than $4D$ used for $|s_1\rangle$ in the TORCA protocol. (c) Diagram showing the relative direction of the optical fields for the schemes previously described. The angles between the optical fields shown are not exact. (d) Scheme to map the coherence initially stored between states $|g\rangle$ and $|s\rangle$, to between $|g\rangle$ and $|d\rangle$, resembling the spin wave from $\Lambda-$memories discussed in the previous chapter. (e) Diagram showing the relative direction of the four optical fields involved.

show the required direction of dashed Ω_1 field in relation to the optical fields, in order for the light induced phase shift to cancel the Doppler dephasing. While this certainly can extend the memory lifetime by removing Doppler dephasing, the best case scenario is a decay rate equal to the storage state lifetime, which for ORCA is 240 ns and for TORCA is 94 ns.

Another method for removing Doppler dephasing is to use a second classical field to drive another transition and remove momentum from the spin wave. Such a scheme is illustrated in Fig. 6.11b. One potential choice for $|s_2\rangle$ is the $7P$ level, located 1179 nm above the $4D$ state, with corresponding electronic lifetime of 270 ns [375]. With the correct choice of angles, between all the fields, the orbital wave momentum can theoretically be completely cancelled. However, the angles required to fully conjugate the wavevector mismatch would make such a scheme difficult to realise in practice, as well as dramatically reducing the interaction region.

An alternative is to instead map down to the other ground state, illustrated in Fig. 6.11d, as is the case with $\Lambda-$memories. This requires the addition of an extra two classical fields, which would have to be synchronised in time with Ω_c (at least to within a nanosecond). Furthermore, we would need to empty state $|d\rangle$ through optical pumping before performing the storage and there is also the potential to add FWM noise into the system, along with any other problems associated with $\Lambda-$memories which ORCA circumvented. The upside is that such a scheme extends all the *benefits* of $\Lambda-$memories to telecom compatible wavelengths. Overall, this scheme adds significant experimental complexity, but would allow all beams to be co-linear, provided $|e\rangle$ and $|b\rangle$ resided in the same hyperfine manifold (see Fig. 6.11e for the required arrangement of the fields), so may turn out to be the easiest to implement practically and has the potential for the longest memory lifetime.

Chapter 7

Conclusion and Future Work

7.1 Summary

The research laid out in this thesis worked towards integrating dibenzoterrylene (DBT) molecules with rubidium (Rb) ensembles. In Chapter 2, we laid out the theory for characterising DBT molecules, along with the experimental setup used in this thesis. Chapter 3 presented experimental results, investigating the DC Stark tuning of DBT emission as a function of angle relative to the transition dipole moment, together with experiments examining other tuning mechanisms. We went on to realise a method for deterministically placing DBT containing nanocrystals into pre-fabricated photonic structures. Additionally, we presented results from a novel host matrix for DBT, namely *para*-Terphenyl, which showed great promise as a single photon source.

Following this, Chapter 4 moved onto Rb, where we developed a rate equation model to capture the population dynamics, together with an experiment showing the interaction of a single photon level probe with a warm Rb vapour and how the aforementioned model reproduced the measured spectra to a high accuracy. Chapter 5 laid out the theory for $\Lambda-$type quantum memories, and introduced a gradient ascent optimisation method to for determining the control field amplitude (and optionally phase) that maximised single photon storage followed by backwards retrieval. We investigated the dependence of efficiency on the optical depth of the Rb ensemble and the dependence on the bandwidth of the incident photons, for the case of a photon with a decaying exponential shape, as is emitted from DBT. We then extended our model to describe four-wave mixing (FWM) noise, and how the optimsation technique may be adapted to counteract FWM. Next, we included the full excited state manifold of the D1 transition in Rb, compatible with photons emitted from the DBT red insertion site in crystalline anthracene, where we detailed a configuration that removed FWM altogether, and found how efficiency also depended on the detuning within the excited state manifold. We identified optical depth as a key limitation for storing high bandwidth photons in cold Rb memories, and so expanded the model to describe warm vapours where high optical depths are readily available. We found that destructive interference between the multiple transitions to the excited state prevented efficient storage.

In Chapter 6, we investigated a different memory system, using a ladder configuration of levels with the input photon far-detuned from the intermediate state, resulting in no FWM noise and resistance to interference between the intermediate states. The gradient ascent optimisation was adapted to deal with the counter-propagating optical fields required for the ladder configuration and allowed us to derive control fields which achieved high efficiency storage of high bandwidth photons in warm Rb vapour, at the expense of storage time. We then combined these results with a ladder configuration, capable of storing telecom single photons, and showed how delayed FWM could be used to realise wavelength conversion within the memory process. Finally we discussed ways to improve on the storage time of ladder type memories.

In this final chapter, we will describe some of the next steps for the projects described in this thesis, and the current progress in these directions.

7.2 Future work

Dibenzoterrylene

For DBT in Anthracene (Ac), the main research direction is to increase the brightness of the sources by redirecting the emission, such as through bullseye gratings, as well as modifying

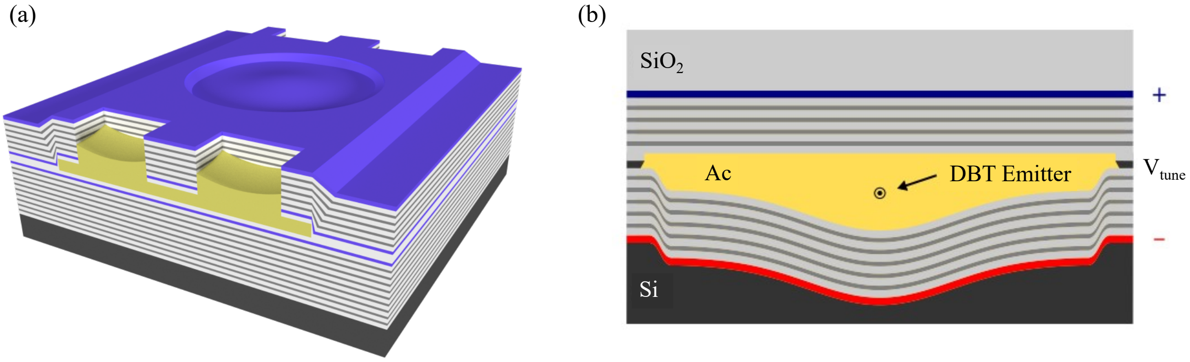

Figure 7.1: (a) 3D illustration of a vertical-emitting defect cavity design, where molten anthracene (Ac) containing dibenzoterrylene (DBT), shown in yellow, can be flown through the side of the structure. The multiple lines either side of the DBT/Ac are alternating layers of niobium pentoxide (Nb_2O_5) and silica (SiO_2) which form distributed Bragg reflectors above and below the DBT molecules, thereby forming a cavity. (b) 2D cut through of the cavity design, showing how a DBT molecule would be situated within the structure. The blue and red bold lines represent the positive and negative sides of an electrode, allowing the DBT molecules to be dynamically tuned.

the DBT emission rate through solid state cavities. One promising research direction is a pillar cavity design, similar to quantum dot pillar cavity desgins [376], where DBT is placed between two distributed Bragg reflectors, effectively redirecting the emission and forming a cavity around the DBT. The design is shown in Fig 7.1. Molten DBT/Ac can be flown through the side of the structure, as was demonstrated in Chapter 2 when capillary channels were filled with DBT/Ac. Additionally, Stark electrodes can be added, as indicated by the bold blue and red lines in Fig 7.1b, to allow tuning of the molecular emission, in order to adjust the coupling of the DBT to the cavity or the coupling to other media such as Rb, as well as improve the spectral overlap between multiple emitters thereby increasing the indistinguishability.

Another future direction will be to use the hole filling method described in Section 1.3 to incorporate PMMA nanocapsules containing DBT into existing photonic structures, such as bullseye gratings or photonic crystal cavities. On the other hand, PMMA balls offer some protection to DBT during the fabrication processes, so patterning structures around deposited nanocapsules is a parallel research direction.

For DBT to be a useful photon source, the issue of laser tuning must be addressed. That is, we require some method by which to prevent or deterministically turn on or off laser induced tuning of the emission frequency. Other host materials, such as n-hexadecane may offer some protection from electron transfer and therefore prevent laser tuning. Aside from new host matrices, the process of laser tuning itself warrants more investigation. If there is a threshold for laser tuning, DBT placed in a cavity would require less laser power to excite, while perhaps inhibiting any multiple photon transition which leads to laser tuning. In this instance, tuning would still be possible with the appropriate light intensity, or by exposing DBT from the side of the cavity, allowing tunable emission without the need to pattern electrodes. Then, laser tuning may turn out to offer a real advantage over other photonic emitters.

As for DBT in para-terphenyl (pT), it still remains to be seen whether more macroscopic crystals produce more repeatable stable emitters, or whether the nanocrystal growth could be refined.

Optical pumping in rubidium

The degree of similarity between simulation and experiment presented in Chapter 4 shows how the theory accurately describes the population dynamics. At the end of Chapter 4, we looked to apply the simulation to calculating the intensity of pumping light needed to prepare population in a particular hyperfine ground states of rubidium (Rb), in both a typical vapour cell, as well as an optical fibre.

The memory optimisations presented in Chapter 5 and 6 assumed all the population began in one ground state (in a single m_F state), such as the case for a magneto optical trap. To obtain this starting condition in a warm vapour however, optical pumping would be required. Expanding the simulation to include all m_F states could aid in pumping vapours optimally, as well as helping confirm experimentally whether the population had been adequately prepared, by predicting the spectrum that would be measured from a weak probe state interacting with the vapour.

Memory simulation

For the memory simulation, the biggest improvement to be made is in speeding up the code. With a faster simulation, it becomes feasible to optimise the warm vapour with a complex control field, which may allow for near-resonant schemes to be utilised in warm vapours.

Further, expanding the four-wave mixing theory to the full hyperfine manifold, would mean we could test the feasibility of using the Rb D2 line for storage of photons emitted by DBT occupying the main insertion site in anthracene. Including all Zeeman sublevels, thereby capturing the effects of the light field polarisation and non-trivial initial population distributions, would allow for a more realistic simulation to inform future experimental improvements.

In the case of the ladder schemes presented in Chapter 6, we saw how the optima derived from the simple three level system generalised well to the more complicated case involving the full intermediate state hyperfine manifold. However, the storage state also features a hyperfine manifold, along with Zeeman sublevels. It will be important to expand the simulation to include the full level structure and the necessary modifications to the theory are outlined in Appendix B.1.

Finally, in order to make the telecom off-resonant cascaded absorption (TORCA) or telecom conversion protocol (and to some extent the off-resonant cascaded absorption (ORCA) protocol) viable in warm vapours, the protocols must be expanded to include extra electronic levels. Including the protocols outlined at the end of Chapter 6 to extend the lifetime would allow the feasibility of the various protocols to be checked, as well as optimised.

7.2.1 Memory experimental work

Magneto-optical trap

Out of the theory and numerical simulations of this thesis, it has become clear that a promising route to efficient memories would be a cold ensemble of atoms with a high optical depth - such as is the case in a magneto-optical trap (MOT). To test the optima derived in Chapter 5, we have begun constructing our own purposely designed MOT.

The design, shown in Fig. 7.2, utilises both a 2D and 3D MOT, where the 2D MOT has a higher background pressure and is connected to the lower pressure 3D MOT chamber by a

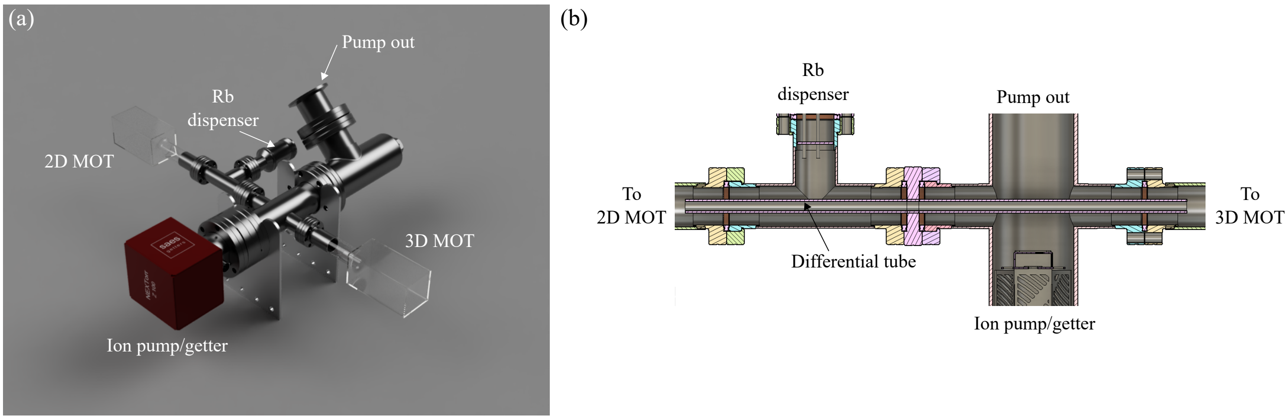

Figure 7.2: (a) 3D CAD render of the design for a magneto-optical trap (MOT), currently under construction. The design features a 2D MOT which is loaded from a rubidium (Rb) dispenser and a 3D MOT, which is loaded from the 2D MOT via a differential pumping tube, not shown. (b) Cross-section of the MOT design, where the differential tube connecting the 2D and 3D MOT is shown.

differential pumping stage. The 2D MOT captures Rb atoms from a thermal vapour, ejected by a Rb dispenser. Such a source of Rb prevents the chamber from achieving high vacuum and limits the achievable optical depth in setups where the 3D MOT is directly loaded from a thermal vapour. The 2D MOT cools atoms in two out of three dimensions, and Rb is allowed to flow through the differential pumping stage, or alternatively it may be assisted through a push beam. This provides an atomic flux to be loaded into the 3D MOT, which has a lower mean temperature and allows the 3D MOT to be held at a higher vacuum. The result is a MOT which can reach peak atomic densities up to $2 \times 10^{11}\,\mathrm{cm}^{-3}$ [377], corresponding to an optical depth of around 4000. Such high optical depths would allow for the efficient storage and retrieval of 100 MHz photons.

However, for storage the presence of both light fields and magnetic fields can lead to increased dephasing and therefore reduce the memory lifetime - this is particularly problematic for magnetically sensitive states. To circumvent this, the trapping light and magnetic field is switched off but time must be allowed for the magnetic field and any induced eddy currents in the surrounding metal to decay. In this time, atoms are lost from the interaction region, reducing the overall optical depth. On top of this, optical pumping may be required to prepare the population in a desired m_F state, adding extra waiting time which can lead to a further reduction in optical depth. To shorten the time between switching the trapping fields off and performing the storage interaction, fast switching and high current electronics can be combined with optimised current waveforms to dynamically correct for eddy currents and stray magnetic fields around the setup, allowing zero magnetic field to be reached in a shorter time.

A further possibility is the misleadingly named 2D MOT [378], which is not the same as the 2D MOT mentioned previously. This configuration utilises trapping beams that are not along the null lines of the magnetic field, but rather at a 45° angle to them, combined with a third pair of beams along the longitudinal direction. In this arrangement, the signal photon maybe directed along the zero field line, potentially removing the need to switch off the magnetic field, or at least reducing the sensitivity to the MOT magnetic field.

Pulse carving

In order to get the most efficiency for a given optical depth, we require a way to shape the control pulses to the optima found in Chapters 5 and 6. For this we intend to use a 20 GHz bandwidth electro-optic modulator (EOM, NIR-MX800-LN-20, iXblue) to carve the pulses from a cw laser, after which the pulses will be amplified using a tapered amplifier (TA, Toptica) to reach the necessary peak powers. The EOM will be controlled via an arbitrary waveform generator (AWG, SDR14TX-PXIE, Teledyne), which will be programmed to produce the theoretical optimal control pulse. Further optimisation to account for experimental imperfections may be required.

When not being used, a DC bias voltage is fed to the EOM to maintain minimum transmission. Overtime the required DC bias can drift and so needs to be corrected. Typically, the DC bias is locked by dithering the bias voltage and performing lock-in amplification on the resulting signal. Instead, we have designed a PCB which performs a gradient ascent using a micro-controller, to maintain minimum output in between runs. The lock will then be muted while running the experiment. The maximum extinction from an EOM is still non-zero (the DC extinction ratio is of order $1000 : 1$) and so there will be a constant leaked control field to the experiment. To prevent this we may need to place an additional acousto-optic modulator (which need not be as fast as the EOM) on the output to remove the control field during storage or during preparation of the atoms.

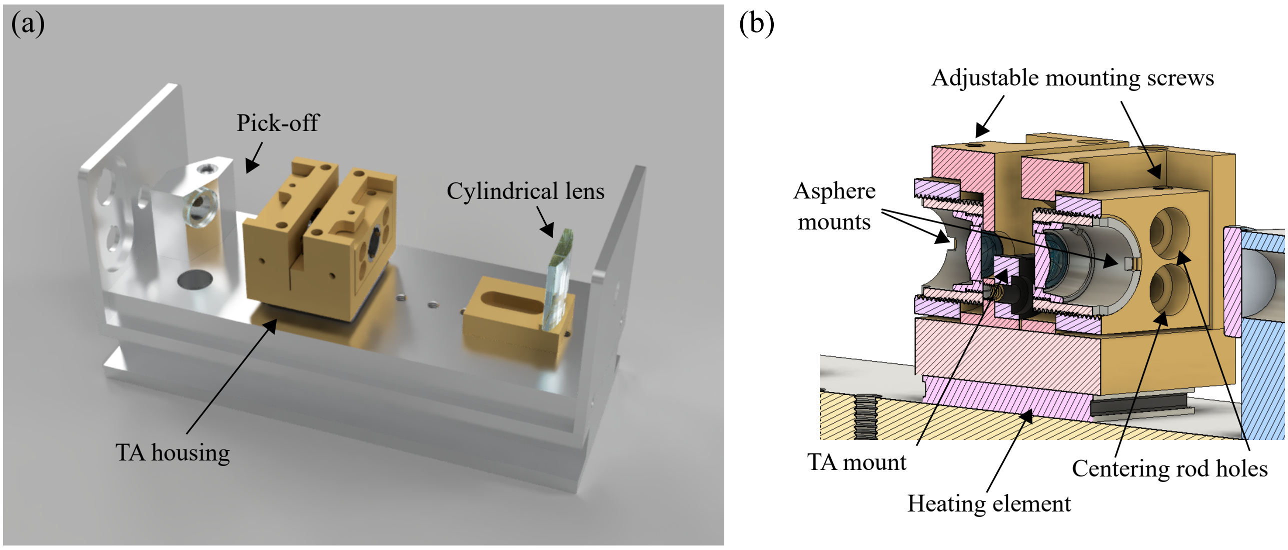

Figure 7.3: (a) 3D CAD render of the tapered amplifier (TA) mount. The seed laser enters from the left, where a pick-off is used to monitor the input power. The TA housing contains two lenses, used to couple the seed laser light to the TA chip, which is located in the centre of the housing. Finally a cylindrical lense is situated just before the output of the device to correct for the asymmetry in the beam output from the TA chip. (b) Cross-section of the TA housing. Shown are the asphere mounts, which will be machined with a fine thread, to allow for fine adjustment of the asphere collimation, needed for coupling in and out of the TA chip. The position of the TA chip is also shown. Each section of the lens mounting assembly features centering rods, along with adjustable mounting screws for both vertical and horizontal (not shown) fine adjustment. Below the TA housing is a heating element, which in combination with a thermistor contained within the TA housing (not shown), will be used to regulate the TA temperature.

The TA chip is housed in a home-built mount, inspired by the design presented in Kangara et al. [379]. Our deisgn is illustrated in Fig. 7.3. The full system is shown in Fig. 7.3a, where the TA chip is located within the TA housing, which will be made up of two brass blocks. The surrounding base and frame will be made of aluminium and will allow the system to be enclosed and secured to the optical table. Dust accumulation on the chip can lead to destruction of the TA, so it important that once aligned, the TA chip is completely covered. A cross-section of the TA housing is provided in Fig. 7.3b.

The seed laser enters from the left of Fig. 7.3a, where a pick-off mirror sends $\approx 1\%$ of the input laser to a photodiode to aid in the TA alignment, as well as allow for the input power to be monitored. Supplying the TA with high intensity input light while it is not powered on can lead to damage of the TA. In addition, supplying the TA with low input laser intensity while the chip *is* powered on, can result in thermal degradation of the chip, as most of the electrical power will be converted into heat, rather than optical power [379]. Therefore, it is necessary to monitor the input power to the device, in order to feedback into the current controller for the TA chip and prevent damage.

The laser then continues to the TA housing, where it is directed through an asphere, located in the left asphere mount in Fig. 7.3b, which couples the seed laser into the TA chip. Both asphere mounts will be machined to have a fine thread, to allow for fine control over the collimation. The TA housing will be held together by centering rods, as well as featuring adjustable screws to fine tune the position of the aspheres relative to the chip, which is mounted in the middle of the assembly. The output light from the TA is then collimated through the second ashpere, located in the right asphere mount of Fig. 7.3b, before passing through a cylindrical lens, shown to the right of Fig. 7.3a. The cylindrical lens is needed to correct for the asymmetric beam output from the TA. Furthermore, the TA will produce broadband amplified spontaneous emission, so additional spectral filtering of the TA may be needed at the output.

The TA housing is situated on a heating element to regulate the temperature of the chip, due to the high electrical currents involved. The temperature is measured by way of a thermistor located in the TA housing assembly. Not shown in Fig. 7.3 are the electrical connections to the

TA chip, thermistor and heating element.

Upon combining the aforementioned devices, we will proceed to demonstrate long-lived atomic storage of on-demand single photons generated by organic molecules. These techniques will then be used in future demonstrations of entanglement swapping and quantum networking.

Appendix A

Modified Radon transform

In Chapter 3, to determine the Stark tuning coefficients, we fit several 2D Lorentzians of the form,

$$L_{2D} = \frac{A}{(\nu - [kV^2 + mV + d])^2 + \left(\frac{\Gamma_2}{2}\right)^2} + B\,, \tag{A.1}$$

to 2D data, an example of which is shown in Fig. A.1a. In Eq. A.1, A denotes the amplitude, ν is the frequency in hertz, V the applied voltage, B is the background and Γ_2 is the frequency full-width-half-maxmimum of the emission peak. In the square brackets, the coefficients k, m and d characterise the curve, gradient and central frequency at $V = 0$, respectively.

In order to obtain good fits to the data, which totalled over 400 Stark tuning molecules, we required a method to provide good initial parameters for m and d. Initialising the coefficient k as zero was sufficient to obtain a good fit. To acquire estimates for m and d, we performed a modified Radon transform.

The Radon transform is an integral transform which takes a function defined on a plane and integrates along a particular line. By performing line integrals and varying the gradient and y-axis offset of the lines, a 2D map can be constructed where coordinates corresponding to m and d represent the totaled intensity along that line. The largest peaks of this transformed function correspond to lines which closely followed the tuning molecular emission in Fig. A.1a.

The final requirement was an estimate on the number of DBT emission lines present in the

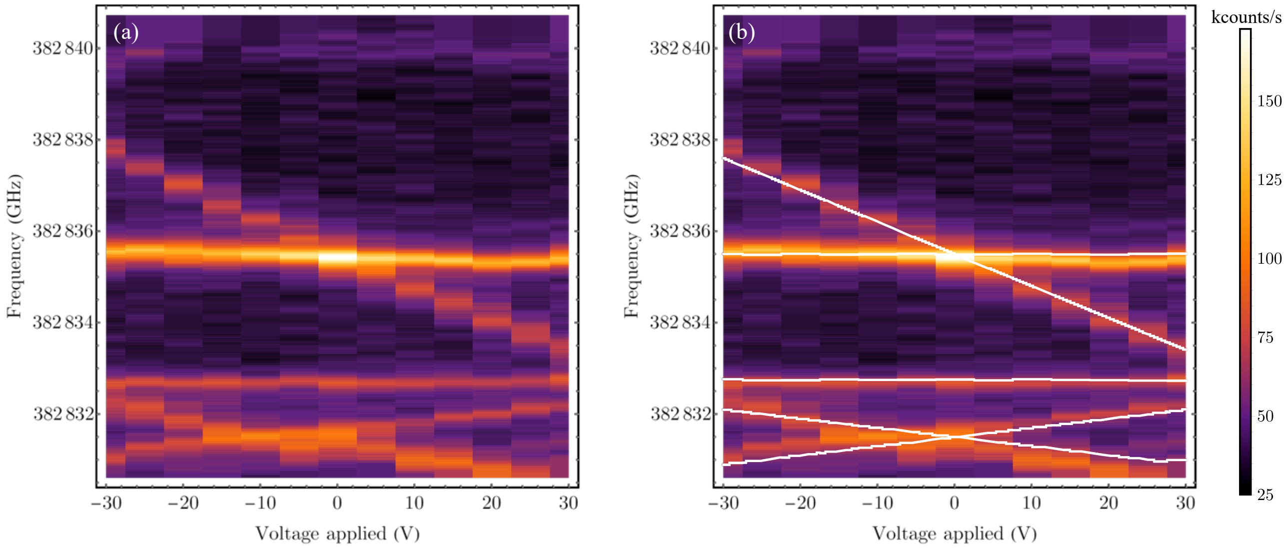

Figure A.1: (a) Density plot showing a collection of bright molecular resonances tuning with applied voltage. (b) After applying the modified Radon transform, the resulting lines, shown in white, are layered over the original density plot. The parameters from these lines can then be used as initial guesses for the fit detailed in Eq. A.1

scan. To obtain this, we counted the number of peaks, defined by a certain threshold above the background, at each voltage and the mode of the resulting list was taken to be the number of (easily discernible) emission lines in a scan. We can then select this number of tallest peaks from the Radon transform to arrive a set of lines which are plotted in white in Fig. A.1b.

Appendix B

Memory simulation sundries

B.1 ORCA derivation

This derivation will largely resemble that in Chapter 5 for the $\Lambda-$type memory for copropagating signal and control fields, and closely follows the derivation in Ref. [264].

Atomic coherences

We have the total system Hamiltonian,

$$H = H_A + H_{ED} + H_L \,, \tag{B.1}$$

with $H_A = \hbar \sum_j \omega_j \sigma_{jj}$ the atomic Hamiltonian where σ_{jj} is the population in state $|j\rangle$ and $H_{ED} = -\hat{\boldsymbol{\mu}} \cdot \boldsymbol{E}$ is the electric dipole Hamiltonian, with $\hat{\boldsymbol{\mu}}$ the atomic transition dipole operator and $\boldsymbol{E}$ is the total electric field. The final term, H_L, is the optical free-field Hamiltonian of the control and photon fields.

We want to find how the atomic coherences evolve in time using the Heisenberg equation,

$$\hbar \partial_t \sigma_{jk} = i[\sigma_{jk}, H_A + H_{ED} + H_L] \,. \tag{B.2}$$

where H_L always commutes with σ_{jk} so we will neglect it going forward.

For the ladder configuration of energy levels, as is the case with off-resonant cascaded absorption (ORCA, see Fig. 6.1a), we can write the dipole operator as $\hat{\boldsymbol{\mu}} = \boldsymbol{\mu}_{ge}\sigma_{ge} + \boldsymbol{\mu}_{se}\sigma_{se} + h.c.$, where μ_{jk} and $\sigma_{jk} = |j\rangle\langle k|$ are the transition dipole strengths and transition operator between states j and k. We have labelled the ground state as $|g\rangle$, the intermediate excited state $|e\rangle$ and the storage state $|s\rangle$. The final term $h.c.$ denotes the hermitian conjugate.

The total electric field $\boldsymbol{E} = \boldsymbol{E}_c + \boldsymbol{E}_s$ is made up of the classical control field $\boldsymbol{E}_c$ and a quantum signal field $\boldsymbol{E}_s$, which we will assume only propagates along the z-axis with negligible divergence such that we can invoke the paraxial approximation [232]. We write our control field with central angular frequency ω_c as,

$$\begin{aligned} \boldsymbol{E}_c &= \boldsymbol{v}_c \frac{\mathcal{E}_c(z,t)}{2} \exp[i\omega_c(t + z/c)] + c.c. \\ &= \boldsymbol{v}_c \frac{\mathcal{E}_c(z,t)}{2} \exp[i\omega_c(t - z/c)] \exp[-2ik_c z] + c.c. \,, \end{aligned} \tag{B.3}$$

with $\boldsymbol{v}_c$ denoting the polarisation vector of the control field and $\mathcal{E}_c$ is the slowly-varying spatio-temporal field amplitude, where we have included a factor of 1/2 so that the amplitude of $\boldsymbol{E}_c$ is $\mathcal{E}_c$ due to the addition of the complex conjugate, $c.c.$.

The signal field requires a quantum mechanical description, which we write in a similar form to the control [232],

$$\boldsymbol{E}_s = i\boldsymbol{v}_s g_s \frac{\mathcal{E}_s(z,t)}{2} \exp[i\omega_s(t - z/c)] + h.c. \,, \tag{B.4}$$

with $g_s = \sqrt{2\pi} g(\omega_s)$, where $g(\omega) = \sqrt{\hbar\omega/4\pi\epsilon_0 c}$ is the photon mode amplitude. In Eq. B.4, the exponent features a minus rather than plus, due to the counter propagating nature of the signal and control fields. We have also defined the slowly varying photon amplitude as,

$$\mathcal{E}_s(z,t) = \frac{\exp[-i\omega_s(t - z/c)]}{\sqrt{2\pi}} \int d\omega \, \hat{a}_s(\omega,t) \exp[-i\omega z/c] \,, \tag{B.5}$$

where $\hat{a}_s(z,t)$ is the slowly varying broadband annihilation operator.

We will make the assumption that most of the population remains in the ground state. which results in the following equations for the atomic coherences,

$$\begin{aligned}
\hbar\partial_t\sigma_{ge} &= i\hbar\omega_{eg}\sigma_{ge} - i\boldsymbol{E}\cdot\left(\boldsymbol{\mu}_{ge}^*(\sigma_{gg}-\sigma_{ee}) + \boldsymbol{\mu}_{es}\sigma_{gs}\right)\\
\hbar\partial_t\sigma_{gs} &= i\hbar\omega_{sg}\sigma_{gs} - i\boldsymbol{E}\cdot\left(\boldsymbol{\mu}_{es}^*\sigma_{gs} - \boldsymbol{\mu}_{ge}^*\sigma_{es}\right)\\
\hbar\partial_t\sigma_{es} &= i\hbar\omega_{se}\sigma_{es} - i\boldsymbol{E}\cdot\left(\boldsymbol{\mu}_{es}^*(\sigma_{ee}-\sigma_{ss}) - \boldsymbol{\mu}_{ge}\sigma_{gs}\right),
\end{aligned} \tag{B.6}$$

where $\omega_{jk} = \omega_j - \omega_k$.

We proceed to transform each of the coherences to a frame rotating at the corresponding resonance frequency, $\widetilde{\sigma}_{jk} = \sigma_{jk}\exp[-i\omega_{kj}\tau]$, where $\tau = t - z/c$ is the retarded time. With this transformation we have,

$$\begin{aligned}
\hbar\partial_\tau\widetilde{\sigma}_{ge} &= -i\boldsymbol{E}\cdot\left(\boldsymbol{\mu}_{ge}^*\exp[-i\omega_{eg}\tau] + \boldsymbol{\mu}_{es}\widetilde{\sigma}_{gs}\exp[-i\omega_{es}\tau]\right)\\
\hbar\partial_\tau\widetilde{\sigma}_{gs} &= -i\boldsymbol{E}\cdot\left(\boldsymbol{\mu}_{es}^*\widetilde{\sigma}_{ge}\exp[+i\omega_{es}\tau] - \boldsymbol{\mu}_{ge}^*\widetilde{\sigma}_{es}\exp[-i\omega_{eg}\tau]\right)\\
\hbar\partial_\tau\widetilde{\sigma}_{es} &= +i\boldsymbol{E}\cdot\left(\boldsymbol{\mu}_{ge}\widetilde{\sigma}_{gs}\exp[+i\omega_{eg}\tau]\right).
\end{aligned} \tag{B.7}$$

Next we insert the full expression for $\boldsymbol{E}$, assuming that the signal field only couples to the $|g\rangle \to |e\rangle$ transition, the control field only couples to $|s\rangle \to |e\rangle$, and only keep terms oscillating at the difference frequencies (the rotating wave approximation),

$$\begin{aligned}
\hbar\partial_\tau\widetilde{\sigma}_{ge} &= -i\boldsymbol{\mu}_{ge}^*\left(i\boldsymbol{v}_s g_s\frac{\mathcal{E}_s}{2}\exp[+i\Delta_s\tau]\right) - i\boldsymbol{\mu}_{es}\widetilde{\sigma}_{gs}\left(\boldsymbol{v}_c\frac{\mathcal{E}_c}{2}\exp[+i\Delta_c\tau]\exp[-2ik_cz]\right)\\
\hbar\partial_\tau\widetilde{\sigma}_{gs} &= -i\boldsymbol{\mu}_{es}^*\widetilde{\sigma}_{ge}\left(\boldsymbol{v}_c^*\frac{\mathcal{E}_c^*}{2}\exp[-i\Delta_c\tau]\exp[+2ik_cz]\right) + i\boldsymbol{\mu}_{ge}^*\widetilde{\sigma}_{es}\left(i\boldsymbol{v}_s g_s\frac{\mathcal{E}_s}{2}\exp[+i\Delta_s\tau]\right)\\
\hbar\partial_\tau\widetilde{\sigma}_{es} &= +i\boldsymbol{\mu}_{ge}\widetilde{\sigma}_{gs}\left(-i\boldsymbol{v}_s^* g_s\frac{\mathcal{E}_s^\dagger}{2}\exp[-i\Delta_s\tau]\right),
\end{aligned} \tag{B.8}$$

where we have defined $\Delta_s = \omega_s - \omega_{eg}$ and $\Delta_c = \omega_c - \omega_{es}$ and $\exp[-2ik_cz]$ accounts for the longitudinal momentum of the counter-propagating control field. We can make a further simplification by only keeping terms that are linear in coherence: any atomic coherence in the system will have originated from the photon coherence, so the multiplication of an atomic coherence by the photon coherence is second order and can be assumed to be small [232]. This leaves us with two equations for the atomic coherences,

$$\begin{aligned}\hbar\partial_\tau\widetilde{\sigma}_{ge} &= \frac{\boldsymbol{\mu}^*_{ge}\cdot\boldsymbol{v}_s g_s\mathcal{E}_s}{2}\exp[+i\Delta_s\tau] - \frac{i\boldsymbol{\mu}_{es}\cdot\boldsymbol{v}_c\mathcal{E}_c\widetilde{\sigma}_{gs}}{2}\exp[+i\Delta_c\tau]\exp[-2ik_cz]\\ \hbar\partial_\tau\widetilde{\sigma}_{gs} &= -\frac{i\boldsymbol{\mu}^*_{es}\cdot\boldsymbol{v}^*_c\mathcal{E}^*_c\widetilde{\sigma}_{ge}}{2}\exp[-i\Delta_c\tau]\exp[+2ik_cz]\,.\end{aligned} \tag{B.9}$$

Photon propagation

Following the same derivation as Chapter 5 we arrive at the propagation equation for the signal field,

$$\Big(\partial_z + \frac{1}{c}\partial_t\Big)\mathcal{E}_s = -\frac{\mu_0\omega_s^2}{g_sk_s}\boldsymbol{v}^*_s\cdot\widetilde{\boldsymbol{P}}_s\,. \tag{B.10}$$

Macroscopic coherences

We relate the macroscopic polarisation $\widetilde{\mathbf{P}}_s$ with the single atomic coherence σ_{ge} by writing,

$$\widetilde{\mathbf{P}}_s = \sqrt{N_v}\mu_{ge}\Big(\frac{1}{\sqrt{N_v}\delta V}\sum_{a(r)}\widetilde{\sigma}^a_{ge}\exp[-i\Delta_s\tau]\Big)\,, \tag{B.11}$$

where N_v is the atomic number density, δV is the volume of an infinitesimal cylindrical voxel and the atoms are labelled by the index a. We can define macroscopic operators as in Chapter 5, such that,

$$P_{ge} = \frac{1}{\sqrt{N_v}\delta V}\sum_{a(r)}\widetilde{\sigma}^a_{ge}\exp[-i\Delta_s\tau]\,, \tag{B.12}$$

but we must change the definition of the orbital wave operator to incorporate the longitudinal momentum,

$$S_{gs} = \frac{1}{\sqrt{N_v}\delta V}\sum_{a(r)}\widetilde{\sigma}^a_{gs}\exp[-i(\Delta_s-\Delta_c)\tau]\exp[-2ik_cz]\,. \tag{B.13}$$

These operators are defined such that they obey the bosonic commutation relation.

We can now write down equations of motion for the macroscopic operators and the photon field, with decoherence included, transforming to the reference frame co-propagating with the photon and control field, and writing our constants in a dimensionless form, we have,

$$\partial_z \mathcal{E}_s = -\sqrt{\frac{d}{2}} P_{ge} \tag{B.14}$$

$$\partial_\tau P_{ge} = -(\gamma_e + i\Delta_s) P_{ge} + \sqrt{\frac{d}{2}} \mathcal{E}_s - \frac{i}{2} \Omega_{es}(\tau + 2z/c) S_{gs} \tag{B.15}$$

$$\partial_\tau S_{gs} = -i(\Delta_s - \Delta_c) - \frac{i}{2} \Omega^*_{es}(\tau + 2z/c) P_{ge} \tag{B.16}$$

Adiabatic elimination

In Chapter 6, we investigated the regime where the single photon detuning was much larger than the bandwidths of the photon and control fields, allowing us to make the adiabatic approximation and set $\partial_\tau P_{ge} \approx 0$, leaving us with,

$$\partial_z \mathcal{E}_s = \frac{+i\sqrt{\frac{d}{2}} \Omega_{es}(\tau + 2z/c) S_{gs} - d\mathcal{E}_s}{2(\gamma_e + i\Delta_s)} \tag{B.17}$$

$$\partial_\tau S_{gs} = -\left(\gamma_s + i(\Delta_s + \Delta_c) + \frac{|\Omega_{es}(\tau + 2z/c)|^2}{4(\gamma_e + i\Delta_s)} \right) S_{gs} - \frac{i\sqrt{d/2}\Omega^*_{es}(\tau + 2z/c)\mathcal{E}_s}{2(\gamma_e + i\Delta_s)} \tag{B.18}$$

Most general set of equations

We can extend our system to describe all hyperfine states, Zeeman sublevels and velocity classes of our system. We redefine $d/2 \to d$, and $\Omega/2 \to \Omega$ to avoid carrying around factors of two. We introduce the index g, j, q to label the electronic ground, intermediate and storage states respectively, along with $m_{g,j,q}$ to label the corresponding Zeeman sublevels. The velocity class is labeled by v, while τ and z index the time and space coordinates. Finally we use Q to index left and right circularly polarised light. The full set of equations can then be written in terms of high dimensional tensors,

$$\begin{aligned} &\partial_z \mathcal{E}^{(\tau,z,Q)} = \\ &+ i \sum_{g,m_g,j,m_j,v} \left(\sqrt{d^{(g,m_g,j,m_j,v,Q)}} \frac{\sum_{q,m_q} \left(\sum_Q \left(\Omega_c^{(j,m_j,q,m_q,Q)} \left[C^{(\tau,z,Q)} \right]^* \right) S_{gs}^{(\tau,z,g,m_g,q,m_q,v)} \right)}{\gamma_e + i\Delta_s^{(g,j,v)}} \right) \\ &- \sum_{g,m_g,j,m_j,v,Q} \frac{d^{(g,m_g,j,m_j,v,Q)} \mathcal{E}^{(\tau,z,Q)}}{\gamma_e + i\Delta_s^{g,j,v}} \end{aligned} \tag{B.19}$$

$$\begin{aligned} &\partial_\tau S_{gs}^{(\tau,z,g,m_g,q,m_q,v)} = -(\gamma_s + i\Delta_{gs}^{(g,q,v)}) S_{gs}^{(\tau,z,g,m_g,q,m_q,v)} \\ &- \sum_{j,m_j} \left(\sum_Q \left(\Omega_c^{(g,m_g,j,m_j,Q)} C^{(\tau,z,Q)} \right) \frac{\sum_{q,m_q} \left(\sum_Q \left(\Omega_c^{(j,m_j,q,m_q,Q)} \left[C^{(\tau,z,Q)} \right]^* \right) S_{gs}^{(\tau,z,g,m_g,q,m_q,v)} \right)}{\gamma_e + i\Delta_s^{(j,q,v)}} \right) \\ &- i \sum_{j,m_j} \left(\frac{\sum_Q \left(\Omega_c^{(g,m_g,j,m_j,Q)} C^{(\tau,z,Q)} \right)}{\gamma_e + i\Delta_c^{(g,j,v)}} \sum_Q \left(\sqrt{d^{(j,m_j,q,m_q,v,Q)}} \mathcal{E}^{(\tau,z,Q)} \right) \right) , \end{aligned} \tag{B.20}$$

where we have incorporated the ground state population distribution into $d^{(g,m_g,j,m_j,v,Q)}$. Additionally, the control field has been split into the transition dipole strengths $\Omega_c^{(g,m_g,j,m_j,Q)}$ and the classical electric field $C^{(\tau,z,Q)}$. While a relatively compact formalism, setting out the equations in this way is also conducive to speeding up the simulation. Python packages such as Numpy use C code which is highly optimised for performing vectorised mathematical operations and so framing the equations this way could result in orders of magnitude speed up.

B.2 TORCA derivation

The derivation for telecom off-resonant cascaded absorption (TORCA) is similar to the previous ORCA derivation. Nevertheless, there are some key differences. We define the detunings,

$$\Delta_{IR} = \omega_{IR} - \omega_{eg} \tag{B.21}$$

$$\Delta_T = \omega_T - \omega_{se} , \tag{B.22}$$

where $\omega_{jk} = \omega_j - \omega_k$, and the subscripts IR and T refer to the infrared and telecom optical fields respectively. In the case of TORCA, the infrared field is the control field and the telecom field is the signal photon.

Atomic coherences

Similarly to the ORCA derivation we have the following equations for the atomic coherences,

$$\hbar\partial_t\widetilde{\sigma}_{ge} = -i\boldsymbol{E}\cdot[\boldsymbol{\mu}^*_{ge}(\sigma_{gg}-\sigma_{ee})\exp[-i\omega_{eg}\tau] + \boldsymbol{\mu}_{es}\widetilde{\sigma}_{gs}\exp[+i\omega_{se}\tau]] \tag{B.23}$$

$$\hbar\partial_t\widetilde{\sigma}_{gs} = -i\boldsymbol{E}\cdot[\boldsymbol{\mu}^*_{es}\widetilde{\sigma}_{ge}\exp[-i\omega_{se}\tau] - \boldsymbol{\mu}^*_{ge}\widetilde{\sigma_{es}}\exp[-i\omega_{eg}\tau]] \tag{B.24}$$

$$\hbar\partial_t\widetilde{\sigma}_{es} = -i\boldsymbol{E}\cdot[\boldsymbol{\mu}^*_{es}\sigma_{ee}\exp[-i\omega_{se}\tau] - \boldsymbol{\mu}_{ge}\widetilde{\sigma}_{gs}\exp[+i\omega_{eg}\tau]]\,. \tag{B.25}$$

Provided the control field detuning (Δ_{IR}) is large enough, we again make the approximation that we do not populate $|e\rangle$ and so set $\sigma_{gg} = 1$ and $\sigma_{ee} = \sigma_{ss} = 0$. The equations for ORCA and TORCA begin to diverge when multiplying out $\boldsymbol{E}$,

$$\hbar\partial_t\widetilde{\sigma}_{ge} = -i\boldsymbol{\mu}^*_{ge}\boldsymbol{v}_{IR}\mathcal{E}_{IR}\exp[+i\Delta_{IR}\tau]\exp[-2ik_{IR}z] - \boldsymbol{\mu}_{es}\boldsymbol{v}_T g_T\mathcal{E}^*_T\widetilde{\sigma}_{gs}\exp[-i\Delta_T\tau] \tag{B.26}$$

$$\hbar\partial_t\widetilde{\sigma}_{gs} = i\boldsymbol{\mu}^*_{es}\boldsymbol{v}_T g_T\mathcal{E}_T\widetilde{\sigma}_{ge}\exp[+i\Delta_T\tau] + i\boldsymbol{\mu}^*_{ge}\boldsymbol{v}_{IR}\mathcal{E}_{IR}\widetilde{\sigma}_{es}\exp[+i\Delta_{IR}\tau]\exp[-2ik_{IR}z] \tag{B.27}$$

$$\hbar\partial_t\widetilde{\sigma}_{es} = +i\boldsymbol{\mu}_{ge}\boldsymbol{v}_{IR}\mathcal{E}_{IR}\widetilde{\sigma}_{gs}\exp[-i\Delta_{IR}\tau]\exp[+2ik_{IR}z]\,, \tag{B.28}$$

where we have absorbed factors of 1/2 into the definitions for $\mathcal{E}_T$ ad $\mathcal{E}_c$. We remove terms pertaining to a photon coherence multiplying an atomic coherence which resulted from a photon coherence - linear approximation. Crucially, this does not remove the equation for $\partial_t\widetilde{\sigma}_{es}$ unlike the other protocols presented in this thesis,

$$\hbar\partial_t\widetilde{\sigma}_{ge} = -i\boldsymbol{\mu}^*_{ge}\boldsymbol{v}_{IR}\mathcal{E}_{IR}\exp[+i\Delta_{IR}\tau]\exp[-2ik_{IR}z] \tag{B.29}$$

$$\hbar\partial_t\widetilde{\sigma}_{gs} = i\boldsymbol{\mu}^*_{es}\boldsymbol{v}_T g_T\mathcal{E}_T\widetilde{\sigma}_{ge}\exp[+i\Delta_T\tau] + i\boldsymbol{\mu}^*_{ge}\boldsymbol{v}_{IR}\mathcal{E}_{IR}\widetilde{\sigma}_{es}\exp[+i\Delta_{IR}\tau]\exp[-2ik_{IR}z] \tag{B.30}$$

$$\hbar\partial_t\widetilde{\sigma}_{es} = +i\boldsymbol{\mu}_{ge}\boldsymbol{v}_{IR}\mathcal{E}_{IR}\widetilde{\sigma}_{gs}\exp[-i\Delta_{IR}\tau]\exp[+2ik_{IR}z] \tag{B.31}$$

Photon propagation

The photon propagation equation for the telecom electric field is,

$$\Big(\partial_z + \frac{1}{c}\partial_t\Big)\mathcal{E}_T = -\frac{\mu_0\omega_T^2}{g_T k_T}\boldsymbol{v}_T^* \cdot \widetilde{\boldsymbol{P}}_T\,. \tag{B.32}$$

Macroscopic coherences

The macroscopic polarisation $\widetilde{\boldsymbol{P}}_T$ is related to the σ_{es} coherence as,

$$\widetilde{\mathbf{P}}_T = \sqrt{N_v}\mu_{es}\Big(\frac{1}{\sqrt{N_v}\delta V}\sum_{a(r)}\widetilde{\sigma}_{es}^a \exp[-i\Delta_T\tau]\Big)\,, \tag{B.33}$$

so we define the macroscopic operators,

$$P_{es} = \frac{1}{\sqrt{n}\delta V}\sum_{a(r)}\widetilde{\sigma}_{es}^a \exp[-i\Delta_T\tau] \tag{B.34}$$

$$S_{gs} = \frac{1}{\sqrt{n}\delta V}\sum_{a(r)}\widetilde{\sigma}_{gs}^a \exp[-i(\Delta_{IR}+\Delta_T)\tau]\exp[+2ik_{IR}z]\,, \tag{B.35}$$

which each obey the bosonic commutation relations.

We also define,

$$P_{ge} = \frac{1}{n\delta V}\sum_{a(r)}\widetilde{\sigma}_{ge}^a \exp[-i\Delta_{IR}\tau]\exp[+2ik_{IR}z]\,, \tag{B.36}$$

which does *not* obey the bosonic commutation relations and therefore does not represent an annihilation operator as $[P_{ge}(r,t), P_{ge}^\dagger(r,t)] = 0$ for all r and t, but just serves the purpose of tidying up the equations. Note that,

$$\int_V P_{es}^\dagger P_{es} dV = N_s \tag{B.37}$$

$$\int_V S_{gs}^\dagger S_{gs} dV = N_s \tag{B.38}$$

where N_s are the number of excitations is the state $|s\rangle$, while,

$$\int_V P_{ge}^\dagger P_{ge} dV \in [0,1]\,. \tag{B.39}$$

Inserting these operators into Eqs. B.29 - B.31, including decay, moving to the frame co-moving with the photon and writing variables in a dimensionless form, we have,

$$\partial_z \mathcal{E}_t = -\sqrt{d} P_{es} \tag{B.40}$$

$$\partial_t P_{ge} = -(\gamma_e + i\Delta_c) P_{ge} - i\Omega_c(\tau + 2z/c) \tag{B.41}$$

$$\partial_t S_{gs} = -(\gamma_s + i(\Delta_c + \Delta_t)) S_{gs} + i\Omega_c(\tau + 2z/c) P_{es} + i\sqrt{d} P_{ge} \mathcal{E}_t \tag{B.42}$$

$$\partial_t P_{es} = -(\gamma_e + \gamma_s + i\Delta_t) P_{es} + i\Omega_c^*(\tau + 2z/c) S_{gs}\,. \tag{B.43}$$

where $d = |\kappa|^2 L/\gamma_e = \boldsymbol{\mu}_{es}^* \boldsymbol{v}_T g_T L/(\hbar\gamma_e)$ and $\Omega = \boldsymbol{\mu}_{ge}^* \boldsymbol{v}_{IR} \mathcal{E}_{IR}/(\hbar\gamma_e)$ are dimensionless.

Adiabatic approximation

For signal and control field detunings much larger than their respective bandwidths, we can set $\partial_\tau P_{ge} = \partial_\tau P_{es} = 0$, leading to,

$$\begin{aligned}
\partial_z \mathcal{E}_t &= \frac{-i\sqrt{d}\Omega(\tau + 2z/c) S}{\gamma_e + i\Delta_c} \\
\partial_\tau S &= -\left(\gamma_s + i(\Delta_t + \Delta_c) + \frac{|\Omega(\tau + 2z/c)|^2}{\gamma_e + \gamma_s + i\Delta_t}\right) S - \frac{i\sqrt{d}\Omega^*(\tau + 2z/c)\mathcal{E}_t}{\gamma_e + i\Delta_c}\,,
\end{aligned} \tag{B.44}$$

Notice the key difference between TORCA and ORCA equations is the absence of the dispersion term from the equation for $\partial_z \mathcal{E}_t$, as well as the modification of the decays on the denominator. For Eqs. 6.21-6.22 we should remember that we absorbed a factor of 1/2 into our definitions for $\mathcal{E}_T$ and $\mathcal{E}_c$. We can recover these equations by redefining $d \to d/2$ and $\Omega_c v \to \Omega_c/2$.

Due to the control field being off resonant from the populated ground state, generalising to include all hyperfine states and Zeeman sublevels is more complicated, and is left to future work.

B.3 Gradient ascent

B.3.1 Wolfe conditions

Throughout the optimisations presented in Chapter 5 and 6, we varied the step size α of the gradient ascent so as to guarantee quick convergence. In Chapter 5, the optimisation was initialised with an amplitude of $1/(10\tau_c)$ (and phase equal to zero for complex optimisation) at all time, where τ_c is the characteristic decay time of the exponentially decaying photon temporal envelope. After each step, the efficiency and gradient for the *next* step were calculated to determine whether the step would meet the Wolfe conditions,

$$\eta\left(\Omega_{i+1}\right) \geq \eta\left(\Omega_i\right) + c_1\alpha_i \left|\frac{\partial J}{\partial \Omega}\right| \tag{B.45}$$

$$\left|\frac{\partial J}{\partial \Omega_{i+1}}\right| \leq c_2 \left|\frac{\partial J}{\partial \Omega_i}\right| , \tag{B.46}$$

with $c_1, c_2 \in (0,1)$. For all the optimisations presented in this thesis, we set $c_1 = 1 \times 10^{-8}$ and $c_2 = 0.9$. The first of the Wolfe conditions (Eq. B.45) sets an upper bound on the step size, requiring that α_i increases η sufficiently. If this condition was violated, the step size was reduced by a factor of two, and the efficiency and gradient for the next step were recalculated. This was repeated until Eq. B.45 was satisfied. The second Wolfe condition (Eq. B.46) sets a lower bound on the step size, requiring that α_i has reduced the gradient sufficiently. If this condition is not met, we increase the step size by a factor of 1.1, until it is satisfied. The optimisation proceeds until the efficiency has converged to within 0.01%, after taking the average of the last three runs.

In Chapter 6 we found that the best performing initial condition was a Gaussian with full-width-half-maximum equal to a 1/4 of the simulation time and an amplitude equal to the input photon bandwidth. The initial step size was set such that the first alteration to the control field was on the order of its amplitude, as the resulting gradient after transforming the coherences ended up being much larger than for the $\Lambda-$type memory optimisation. A dynamic step size was employed as before until the efficiency has converged to within 0.01%.

B.3.2 Extension for four-wave mixing noise

In Section 5.3, we extended the simple three-level $\Lambda-$type memory to include four-wave mixing (FWM) noise. For reference, the modified equations were,

$$\partial_z \mathcal{E}_s = -\sqrt{\frac{d}{2}} P_{ge} \tag{B.47}$$

$$\partial_z \mathcal{E}_F = \sqrt{\frac{d}{2}} \frac{\Omega_{es}}{\Delta_{HF}} S_{gs} \tag{B.48}$$

$$\partial_\tau P_{ge} = -(1 + i\Delta_s - 2i\delta_{ls}) P_{ge} + \sqrt{\frac{d}{2}} \mathcal{E}_s - \frac{i}{2} \Omega_{es} S_{gs} \tag{B.49}$$

$$\partial_\tau S_{gs} = -i(\Delta_s - \Delta_c - \delta_{ls}) S_{gs} - \frac{i}{2} \Omega^* P_{ge} - \frac{i}{2} \sqrt{\frac{d}{2}} \frac{\Omega_{es}}{\Delta_{HF}} \mathcal{E}_F^* \,, \tag{B.50}$$

where Δ_{HF} denotes the hyperfine splitting of the ground states and δ_{ls} refers to the time-dependent light shift $\delta_{ls} = |\Omega_{ge}|^2 / \Delta_{HF}$, with Ω_{ge} referring to control field coupling strength on the $|g\rangle \rightarrow |e\rangle$ transition.

We then adapted the gradient ascent technique to reduce the amount of FWM noise in the system. The cofunctions read,

$$\partial_z \bar{\mathcal{E}}_s = -\sqrt{\frac{d}{2}} \bar{P}_{ge} \tag{B.51}$$

$$\partial_z \bar{\mathcal{E}}_F = \sqrt{\frac{d}{2}} \frac{\Omega_{es}}{\Delta_{HF}} \bar{S}_{gs} \tag{B.52}$$

$$\partial_\tau \bar{P}_{ge} = (1 - i\Delta_s + 2i\delta_{ls}) \bar{P}_{ge} + \sqrt{\frac{d}{2}} \bar{\mathcal{E}}_s - \frac{i}{2} \Omega_{es} \bar{S}_{gs} \tag{B.53}$$

$$\partial_\tau \bar{S}_{gs} = -i(\Delta_s - \Delta_c - \delta_{ls}) \bar{S}_{gs} - \frac{i}{2} \Omega^* \bar{P}_{ge} - \frac{i}{2} \sqrt{\frac{d}{2}} \frac{\Omega_{es}}{\Delta_{HF}} \bar{\mathcal{E}}_F^* \,, \tag{B.54}$$

and the associated boundary conditions,

$$\bar{\mathcal{E}}_s(L, \tau) = 0 \tag{B.55}$$

$$\bar{\mathcal{E}}_F(L, \tau) = -\eta_{storage} \mathcal{E}_F \tag{B.56}$$

$$\bar{P}_{ge}(z, T) = 0 \tag{B.57}$$

$$\bar{S}_{gs}(z, T) = S_{gs}(z, T) \, (1 - \mathcal{F} \, \eta_{FWM}) \tag{B.58}$$

where we have defined,

$$\eta_{storage} = \int_0^1 dz\, S^*(z,T)S(z,T) \tag{B.59}$$

$$\eta_{FWM} = \int_0^1 d\tau\, \mathcal{E}_F^*(L,\tau)\mathcal{E}_F(L,\tau)\,. \tag{B.60}$$

It should be noted that the Eqs B.51 and Eqs B.52 are equivalent to Eqs B.47 and Eqs B.48 after time and space reversal, provided $\bar{\mathcal{E}}_s = -\mathcal{E}_s$ and $\bar{\mathcal{E}}_F = -\mathcal{E}_F$.

The gradient for each iteration for a complex valued control field is then,

$$\frac{\partial J}{\partial \Omega_{es}^*(\tau)} = \frac{i}{2}\int_0^1 dz \left[\bar{P}_{ge}S_{gs}^* - \bar{S}_{gs}^* P_{ge} + \frac{1}{\Delta_{HF}}\sqrt{\frac{d}{2}}\left(\bar{\mathcal{E}}_F S^* - \bar{S}^*\mathcal{E}_F\right)\right], \tag{B.61}$$

and for a real valued control field is,

$$\frac{\partial J}{\partial \Omega_{es}(\tau)} = -\int_0^1 dz\, \mathrm{Im}\left[\bar{P}_{ge}S_{gs}^* - \bar{S}_{gs}^* P_{ge} + \frac{1}{\Delta_{HF}}\sqrt{\frac{d}{2}}\left(\bar{\mathcal{E}}_F S^* - \bar{S}^*\mathcal{E}_F\right)\right]. \tag{B.62}$$

Bibliography

[1] T D Ladd, F Jelezko, R Laflamme, Y Nakamura, C Monroe, and J L O'brien. Quantum computers. *Nature*, 464:45–53, 2010. 1

[2] Peter W. Shor. Polynomial-time algorithms for prime factorization and discrete logarithms on a quantum computer. *SIAM Journal on Computing*, 26:1484–1509, 10 1997. 1, 2

[3] Michael A. Nielsen and Isaac L. Chuang. Quantum computation and quantum information: 10th anniversary edition. *Quantum Computation and Quantum Information*, 12 2010. 1

[4] Charles H Bennett and Gilles Brassard. Quantum cryptography: Public key distribution and coin tossing. *Proceedings of the IEEE International Conference on Computers, Systems and Signal Processing, Bangalore, India*, 175, 1984. 1, 4

[5] L. M. Duan, M. D. Lukin, J. I. Cirac, and P. Zoller. Long-distance quantum communication with atomic ensembles and linear optics. *Nature*, 414:413–418, 2001. 1, 24, 25

[6] Valerio Scarani, Helle Bechmann-Pasquinucci, Nicolas J Cerf, Miloslav Dušek, Norbert Lütkenhaus, and Momtchil Peev. The security of practical quantum key distribution. *Reviews of Modern Physics*, 2009. 1, 4

[7] Vittorio Giovannetti, Seth Lloyd, and Lorenzo Maccone. Quantum-enhanced measurements: Beating the standard quantum limit. *Science*, 306:1330–1336, 11 2004. 1, 4

[8] Elizabeth Gibney. Quantum gold rush: the private funding pouring into quantum start-ups. *Nature*, 574:22–24, 10 2019. 1

[9] Lov K Grover. A fast quantum mechanical algorithm for database search. *arxiv preprint*, 1996. 2

[10] David Deutsch and Jozsa Richard. Rapid solution of problems by quantum computation. *Proceedings of the Royal Society of London. Series A: Mathematical and Physical Sciences*, 439:553–558, 12 1992. 2

[11] Ashley Montanaro. Quantum algorithms: an overview. *npj Quantum Information 2016 2:1*, 2:1–8, 1 2016. 2

[12] Adriano Barenco, Charles H. Bennett, Richard Cleve, David P. Divincenzo, Norman Margolus, Peter Shor, Tycho Sleator, John A. Smolin, and Harald Weinfurter. Elementary gates for quantum computation. *Physical Review A*, 52:3457, 11 1995. 2

[13] David P. DiVincenzo. Two-bit gates are universal for quantum computation. *Physical Review A*, 51:1015, 2 1995. 2

[14] Christof Paar and Jan. Pelzl. *Understanding cryptography : a textbook for students and practitioners*. Springer, 2009. 2

[15] Nathan Wiebe, Daniel Braun, and Seth Lloyd. Quantum algorithm for data fitting. *Physical Review Letters*, 2012. 2

[16] X.-D Cai, C Weedbrook, Z.-E Su, M.-C Chen, Mile Gu, M.-J Zhu, Li Li, Nai-Le Liu, Chao-Yang Lu, and Jian-Wei Pan. Experimental quantum computing to solve systems of linear equations. *Physical Review Letters*, 2013. 2

[17] B. Bell, A. S. Clark, M. S. Tame, M. Halder, J. Fulconis, W. J. Wadsworth, and J. G. Rarity. Experimental characterization of photonic fusion using fiber sources. *New Journal of Physics*, 14:023021, 2 2012. 3

[18] B. A. Bell, M. S. Tame, A. S. Clark, R. W. Nock, W. J. Wadsworth, and J. G. Rarity. Experimental characterization of universal one-way quantum computing. *New Journal of Physics*, 15:053030, 5 2013. 3

[19] R. Raussendorf and H. J. Briegel. A one-way quantum computer. *Physical Review Letters*, 86:5188, 5 2001. 3

[20] K. Kieling, T. Rudolph, and J. Eisert. Percolation, renormalization, and quantum computing with nondeterministic gates. *Physical Review Letters*, 99:130501, 9 2007. 3

[21] Andrew J. Daley, Immanuel Bloch, Christian Kokail, Stuart Flannigan, Natalie Pearson, Matthias Troyer, and Peter Zoller. Practical quantum advantage in quantum simulation. *Nature*, 607:667–676, 7 2022. 3

[22] Dave Wecker. Programming a quantum computer, 2014. 3

[23] Richard P Feynman. Simulating physics with computers. *International Journal of Theoretical Physics*, 21, 1982. 3

[24] Joonsuk Huh, Gian Giacomo Guerreschi, Borja Peropadre, Jarrod R Mcclean, and Alán Aspuru-Guzik. Boson sampling for molecular vibronic spectra. *Nature Photonics*, 2015. 3

[25] Stephen A Cook. An overview of computational complexity. *Communications ofthe ACM*, 26, 1983. 3

[26] Prasanna Date, · Robert Patton, Catherine Schuman, and · Thomas Potok. Efficiently embedding qubo problems on adiabatic quantum computers. *Quantum Information Processing*, 18:117, 2019. 3

[27] Edward Farhi, Jeffrey Goldstone, Sam Gutmann, and Michael Sipser. Quantum computation by adiabatic evolution. *arxiv preprint*, 2000. 3

[28] Steven H Adachi and Maxwell P Henderson. Application of quantum annealing to training of deep neural networks. *arxiv preprint*, 2015. 3

[29] Ryan Babbush, Peter J Love, and Alán Aspuru-Guzik. Adiabatic quantum simulation of quantum chemistry. *Scientific Reports*, 4, 2014. 3

[30] Dorit Aharonov, Wim Van Dam, Julia Kempe, Zeph Landau, Seth Lloyd, and Oded Regev. Adiabatic quantum computation is equivalent to standard quantum computation. *http://dx.doi.org/10.1137/080734479*, 50:755–787, 11 2008. 3

[31] James D Whitfield, Jacob Biamonte, and Al'an Aspuru-Guzik. Simulation of electronic structure hamiltonians using quantum computers. *Molecular Physics*, 109:735–750, 2011. 3

[32] George C. Knee and William J. Munro. Optimal trotterization in universal quantum simulators under faulty control. *Physical Review A - Atomic, Molecular, and Optical Physics*, 91:052327, 5 2015. 3

[33] Ian A. Walmsley and Joshua Nunn. Editorial: Building quantum networks. *Phys. Rev. Appl.*, 6:040001, Oct 2016. 4

[34] Naomi H Nickerson, Joseph F Fitzsimons, and Simon C Benjamin. Freely scalable quantum technologies using cells of 5-to-50 qubits with very lossy and noisy photonic links. *Physical Review X*, 4:41041, 2014. 4

[35] Joseph F. Fitzsimons and Elham Kashefi. Unconditionally verifiable blind computation. *New Journal of Physics*, 17:083040, 3 2012. 4

[36] Artur K. Ekert. Quantum cryptography based on bell's theorem. *Physical Review Letters*, 67:661, 8 1991. 4

[37] Juan Yin, Yuan Cao, Yu Huai Li, Sheng Kai Liao, Liang Zhang, Ji Gang Ren, Wen Qi Cai, Wei Yue Liu, Bo Li, Hui Dai, Guang Bing Li, Qi Ming Lu, Yun Hong Gong, Yu Xu, Shuang Lin Li, Feng Zhi Li, Ya Yun Yin, Zi Qing Jiang, Ming Li, Jian Jun Jia, Ge Ren, Dong He, Yi Lin Zhou, Xiao Xiang Zhang, Na Wang, Xiang Chang, Zhen Cai Zhu, Nai Le Liu, Yu Ao Chen, Chao Yang Lu, Rong Shu, Cheng Zhi Peng, Jian Yu Wang, and Jian Wei Pan. Satellite-based entanglement distribution over 1200 kilometers. *Science*, 356:1140–1144, 6 2017. 4

[38] Alberto Boaron, Gianluca Boso, Davide Rusca, Cédric Vulliez, Claire Autebert, Misael Caloz, Matthieu Perrenoud, Gaëtan Gras, Félix Bussières, Ming Jun Li, Daniel Nolan, Anthony Martin, and Hugo Zbinden. Secure quantum key distribution over 421 km of optical fiber. *Physical Review Letters*, 121:190502, 11 2018. 4

[39] M. Napolitano, M. Koschorreck, B. Dubost, N. Behbood, R. J. Sewell, and M. W. Mitchell. Interaction-based quantum metrology showing scaling beyond the heisenberg limit. *Nature*, 471:486–489, 2011. 4

[40] Sergio Boixo, Steven T. Flammia, Carlton M. Caves, and J. M. Geremia. Generalized limits for single-parameter quantum estimation. *Physical Review Letters*, 98:090401, 2 2007. 4

[41] W. Wasilewski, K. Jensen, H. Krauter, J. J. Renema, M. V. Balabas, and E. S. Polzik. Quantum noise limited and entanglement-assisted magnetometry. *Physical Review Letters*, 104:133601, 3 2010. 4

[42] R. J. Sewell, M. Koschorreck, M. Napolitano, B. Dubost, N. Behbood, and M. W. Mitchell. Magnetic sensitivity beyond the projection noise limit by spin squeezing. *Physical Review Letters*, 109:253605, 12 2012. 4

[43] D. Leibfried, M. D. Barrett, T. Schaetz, J. Britton, J. Chiaverini, W. M. Itano, J. D. Jost, C. Langer, and D. J. Wineland. Toward heisenberg-limited spectroscopy with multiparticle entangled states. *Science*, 304:1476–1478, 6 2004. 4

[44] Dong Sheng Ding, Wei Zhang, Zhi Yuan Zhou, Shuai Shi, Bao Sen Shi, and Guang Can Guo. Raman quantum memory of photonic polarized entanglement. *Nature Photonics*, 9:332–338, 2015. 5, 28, 94

[45] B. Canuel, A. Bertoldi, L. Amand, E. Pozzo di Borgo, T. Chantrait, C. Danquigny, M. Dovale Álvarez, B. Fang, A. Freise, R. Geiger, J. Gillot, S. Henry, J. Hinderer, D. Holleville, J. Junca, G. Lefèvre, M. Merzougui, N. Mielec, T. Monfret, S. Pelisson, M. Prevedelli, S. Reynaud, I. Riou, Y. Rogister, S. Rosat, E. Cormier, A. Landragin,

W. Chaibi, S. Gaffet, and P. Bouyer. Exploring gravity with the MIGA large scale atom interferometer. *Scientific Reports 2018 8:1*, 8:1–23, 9 2018. 5

[46] M. J. Holland and K. Burnett. Interferometric detection of optical phase shifts at the heisenberg limit. *Physical Review Letters*, 71:1355, 8 1993. 5

[47] Luis A. Correa, Mohammad Mehboudi, Gerardo Adesso, and Anna Sanpera. Individual quantum probes for optimal thermometry. *Physical Review Letters*, 114:220405, 6 2015. 5

[48] David P Divincenzo. The physical implementation of quantum computation. *Progress of Physics*, 48, 2000. 5

[49] C. J. Ballance, T. P. Harty, N. M. Linke, M. A. Sepiol, and D. M. Lucas. High-fidelity quantum logic gates using trapped-ion hyperfine qubits. *Physical Review Letters*, 117:060504, 8 2016. 5

[50] Yang Wang, Aishwarya Kumar, Tsung Yao Wu, and David S. Weiss. Single-qubit gates based on targeted phase shifts in a 3d neutral atom array. *Science*, 352:1562–1565, 6 2016. 5

[51] V. M. Schäfer, C. J. Ballance, K. Thirumalai, L. J. Stephenson, T. G. Ballance, A. M. Steane, and D. M. Lucas. Fast quantum logic gates with trapped-ion qubits. *Nature 2018 555:7694*, 555:75–78, 3 2018. 5

[52] Brian C. Sawyer, Joseph W. Britton, Adam C. Keith, C. C.Joseph Wang, James K. Freericks, Hermann Uys, Michael J. Biercuk, and John J. Bollinger. Spectroscopy and thermometry of drumhead modes in a mesoscopic trapped-ion crystal using entanglement. *Physical Review Letters*, 108:213003, 5 2012. 5

[53] Sepehr Ebadi, Tout T. Wang, Harry Levine, Alexander Keesling, Giulia Semeghini, Ahmed Omran, Dolev Bluvstein, Rhine Samajdar, Hannes Pichler, Wen Wei Ho, Soonwon Choi, Subir Sachdev, Markus Greiner, Vladan Vuletić, and Mikhail D. Lukin. Quantum phases of matter on a 256-atom programmable quantum simulator. *Nature*, 595:227–232, 7 2021. 5

[54] Nicolai Friis, Oliver Marty, Christine Maier, Cornelius Hempel, Milan Holzäpfel, Petar Jurcevic, Martin B. Plenio, Marcus Huber, Christian Roos, Rainer Blatt, and Ben Lanyon. Observation of entangled states of a fully controlled 20-qubit system. *Physical Review X*, 8:021012, 4 2018. 5

[55] Y. O. Dudin, L. Li, and A. Kuzmich. Light storage on the time scale of a minute. *Phys. Rev. A*, 87:031801, Mar 2013. 5

[56] Unveiling ionq forte: The first software-configurable quantum computer. `https://ionq.com/posts/may-17-2022-ionq-forte` Accessed: 2022-09-03. 5

[57] Quantinuum — hardware. `https://www.quantinuum.com/hardware` Accessed: 2022-09-03. 5

[58] H. B. Dang, A. C. Maloof, and M. V. Romalis. Ultrahigh sensitivity magnetic field and magnetization measurements with an atomic magnetometer. *Applied Physics Letters*, 97:151110, 10 2010. 6

[59] Xuejian Wu, Zachary Pagel, Bola S. Malek, Timothy H. Nguyen, Fei Zi, Daniel S. Scheirer, and Holger Müller. Gravity surveys using a mobile atom interferometer. *Science Advances*, 5:800–806, 9 2019. 6

[60] G. Wendin. Quantum information processing with superconducting circuits: a review. *Reports on Progress in Physics*, 80:106001, 9 2017. 6

[61] Jay M. Gambetta, Jerry M. Chow, and Matthias Steffen. Building logical qubits in a superconducting quantum computing system. *npj Quantum Information*, 3:1–7, 1 2017. 6

[62] B. E. Kane. A silicon-based nuclear spin quantum computer. *Nature 1998 393:6681*, 393:133–137, 5 1998. 6

[63] L. M. K. Vandersypen, H. Bluhm, J. S. Clarke, A. S. Dzurak, R. Ishihara, A. Morello, D. J. Reilly, L. R. Schreiber, and M. Veldhorst. Interfacing spin qubits in quantum dots and donors—hot, dense, and coherent. *npj Quantum Information*, 3:1–10, 9 2017. 6

[64] Davide Rotta, Fabio Sebastiano, Edoardo Charbon, and Enrico Prati. Quantum information density scaling and qubit operation time constraints of cmos silicon-based quantum computer architectures. *npj Quantum Information*, 3:1–14, 6 2017. 6

[65] Y. He, S. K. Gorman, D. Keith, L. Kranz, J. G. Keizer, and M. Y. Simmons. A two-qubit gate between phosphorus donor electrons in silicon. *Nature*, 571:371–375, 7 2019. 6

[66] J. T. Muhonen, A. Laucht, S. Simmons, J. P. Dehollain, R. Kalra, F. E. Hudson, S. Freer, K. M. Itoh, D. N. Jamieson, J. C. McCallum, A. S. Dzurak, and A. Morello. Quantifying the quantum gate fidelity of single-atom spin qubits in silicon by randomized benchmarking. *Journal of Physics: Condensed Matter*, 27:154205, 3 2015. 6

[67] John J.L. Morton, Alexei M. Tyryshkin, Richard M. Brown, Shyam Shankar, Brendon W. Lovett, Arzhang Ardavan, Thomas Schenkel, Eugene E. Haller, Joel W. Ager, and S. A. Lyon. Solid-state quantum memory using the 31p nuclear spin. *Nature 2008 455:7216*, 455:1085–1088, 10 2008. 6

[68] Kamyar Saeedi, Stephanie Simmons, Jeff Z. Salvail, Phillip Dluhy, Helge Riemann, Nikolai V. Abrosimov, Peter Becker, Hans Joachim Pohl, John J.L. Morton, and Mike L.W. Thewalt. Room-temperature quantum bit storage exceeding 39 minutes using ionized donors in silicon-28. *Science*, 342:830–833, 11 2013. 6

[69] R. Barends, J. Kelly, A. Megrant, A. Veitia, D. Sank, E. Jeffrey, T. C. White, J. Mutus, A. G. Fowler, B. Campbell, Y. Chen, Z. Chen, B. Chiaro, A. Dunsworth, C. Neill, P. O'Malley, P. Roushan, A. Vainsencher, J. Wenner, A. N. Korotkov, A. N. Cleland, and John M. Martinis. Superconducting quantum circuits at the surface code threshold for fault tolerance. *Nature 2014 508:7497*, 508:500–503, 4 2014. 6

[70] Norbert M. Linke, Dmitri Maslov, Martin Roetteler, Shantanu Debnath, Caroline Figgatt, Kevin A. Landsman, Kenneth Wright, and Christopher Monroe. Experimental comparison of two quantum computing architectures. *Proceedings of the National Academy of Sciences of the United States of America*, 114:3305–3310, 3 2017. 6

[71] Yuanhao Wang, Ying Li, Zhang qi Yin, and Bei Zeng. 16-qubit ibm universal quantum computer can be fully entangled. *npj Quantum Information 2018 4:1*, 4:1–6, 9 2018. 6

[72] Frank Arute, Kunal Arya, Ryan Babbush, Dave Bacon, Joseph C. Bardin, Rami Barends, Rupak Biswas, Sergio Boixo, Fernando G.S.L. Brandao, David A. Buell, Brian Burkett, Yu Chen, Zijun Chen, Ben Chiaro, Roberto Collins, William Courtney, Andrew Dunsworth, Edward Farhi, Brooks Foxen, Austin Fowler, Craig Gidney, Marissa Giustina, Rob Graff, Keith Guerin, Steve Habegger, Matthew P. Harrigan, Michael J. Hartmann, Alan Ho, Markus Hoffmann, Trent Huang, Travis S. Humble, Sergei V. Isakov, Evan Jeffrey, Zhang Jiang, Dvir Kafri, Kostyantyn Kechedzhi, Julian Kelly, Paul V. Klimov, Sergey Knysh, Alexander Korotkov, Fedor Kostritsa, David Landhuis, Mike Lindmark, Erik Lucero, Dmitry Lyakh, Salvatore Mandrà, Jarrod R. McClean, Matthew McEwen, Anthony Megrant, Xiao Mi, Kristel Michielsen, Masoud Mohseni, Josh Mutus, Ofer Naaman, Matthew Neeley, Charles Neill, Murphy Yuezhen Niu, Eric Ostby, Andre Petukhov, John C. Platt, Chris Quintana, Eleanor G. Rieffel, Pedram Roushan, Nicholas C. Rubin, Daniel Sank, Kevin J. Satzinger, Vadim Smelyanskiy, Kevin J. Sung, Matthew D. Trevithick, Amit Vainsencher, Benjamin Villalonga, Theodore White, Z. Jamie Yao, Ping Yeh, Adam Zalcman, Hartmut Neven, and John M. Martinis. Quantum supremacy using a programmable superconducting processor. *Nature*, 574:505–510, 10 2019. 6

[73] J. M. Taylor, P. Cappellaro, L. Childress, L. Jiang, D. Budker, P. R. Hemmer, A. Yacoby, R. Walsworth, and M. D. Lukin. High-sensitivity diamond magnetometer with nanoscale resolution. *Nature Physics*, 4:810–816, 9 2008. 6

[74] M. P. Ledbetter, K. Jensen, R. Fischer, A. Jarmola, and D. Budker. Gyroscopes based on nitrogen-vacancy centers in diamond. *Physical Review A - Atomic, Molecular, and Optical Physics*, 86:052116, 11 2012. 6

[75] Hannah Clevenson, Matthew E. Trusheim, Carson Teale, Tim Schröder, Danielle Braje, and Dirk Englund. Broadband magnetometry and temperature sensing with a light-trapping diamond waveguide. *Nature Physics*, 11:393–397, 4 2015. 6

[76] R. C. Jaklevic, J. Lambe, J. E. Mercereau, and A. H. Silver. Macroscopic quantum interference in superconductors. *Physical Review*, 140:A1628, 11 1965. 6

[77] M. B. Simonds, W. A. Fertig, and R. P. Giffard. Performance of a resonant input squid amplifier system. *IEEE Transactions on Magnetics*, 15:478–481, 1979. 6

[78] John Clarke and Frank K. Wilhelm. Superconducting quantum bits. *Nature*, 453:1031–1042, 6 2008. 6

[79] Dimitris Dimitropoulos and Bahram Jalali. Noise and information capacity in silicon nanophotonics. *IEEE Photonics Journal*, 7, 6 2015. 7

[80] Andrea Crespi, Roberta Ramponi, Roberto Osellame, Linda Sansoni, Irene Bongioanni, Fabio Sciarrino, Giuseppe Vallone, and Paolo Mataloni. Integrated photonic quantum gates for polarization qubits. *Nature Communications 2011 2:1*, 2:1–6, 11 2011. 7

[81] J. P. Lee, L. M. Wells, B. Villa, S. Kalliakos, R. M. Stevenson, D. J. P. Ellis, I. Farrer, D. A. Ritchie, A. J. Bennett, and A. J. Shields. Controllable photonic time-bin qubits from a quantum dot. *Phys. Rev. X*, 8:021078, Jun 2018. 7, 141

[82] L. Olislager, J. Cussey, A. T. Nguyen, P. Emplit, S. Massar, J. M. Merolla, and K. Phan Huy. Frequency-bin entangled photons. *Physical Review A - Atomic, Molecular, and Optical Physics*, 82:013804, 7 2010. 7

[83] Benjamin Brecht, Andreas Eckstein, Raimund Ricken, Viktor Quiring, Hubertus Suche, Linda Sansoni, and Christine Silberhorn. Demonstration of coherent time-frequency schmidt mode selection using dispersion-engineered frequency conversion. *Physical Review A - Atomic, Molecular, and Optical Physics*, 90:030302, 9 2014. 7

[84] Zhi Yuan Zhou, Yan Li, Dong Sheng Ding, Wei Zhang, Shuai Shi, Bao Sen Shi, and Guang Can Guo. Orbital angular momentum photonic quantum interface. *Light: Science and Applications*, 5, 1 2016. 7

[85] E. Knill, R. Laflamme, and G. J. Milburn. A scheme for efficient quantum computation with linear optics. *Nature 2001 409:6816*, 409:46–52, 1 2001. 7, 21

[86] Ying Li, Peter C. Humphreys, Gabriel J. Mendoza, and Simon C. Benjamin. Resource costs for fault-tolerant linear optical quantum computing. *Physical Review X*, 5:041007, 10 2015. 7

[87] T. Guerreiro, A. Martin, B. Sanguinetti, J. S. Pelc, C. Langrock, M. M. Fejer, N. Gisin, H. Zbinden, N. Sangouard, and R. T. Thew. Nonlinear interaction between single photons. *Physical Review Letters*, 113:173601, 10 2014. 7

[88] Thibault Peyronel, Ofer Firstenberg, Qi Yu Liang, Sebastian Hofferberth, Alexey V. Gorshkov, Thomas Pohl, Mikhail D. Lukin, and Vladan Vuletić. Quantum nonlinear optics with single photons enabled by strongly interacting atoms. *Nature*, 488:57–60, 2012. 7

[89] A. Javadi, I. Söllner, M. Arcari, S. Lindskov Hansen, L. Midolo, S. Mahmoodian, G. Kiršansk, T. Pregnolato, E. H. Lee, J. D. Song, S. Stobbe, and P. Lodahl. Single-photon non-linear optics with a quantum dot in a waveguide. *Nature Communications 2015 6:1*, 6:1–5, 10 2015. 7

[90] Shuo Sun, Hyochul Kim, Glenn S. Solomon, and Edo Waks. A quantum phase switch between a single solid-state spin and a photon. *Nature Nanotechnology 2016 11:6*, 11:539–544, 2 2016. 7

[91] H. J. Kimble. The quantum internet. *Nature*, 453:1023–1030, 2008. 8

[92] Jeremy L. O'Brien, Akira Furusawa, and Jelena Vučković. Photonic quantum technologies. *Nature Photonics 2009 3:12*, 3:687–695, 12 2009. 8, 11

[93] Kenneth R. Brown, Jungsang Kim, and Christopher Monroe. Co-designing a scalable quantum computer with trapped atomic ions. *npj Quantum Information 2016 2:1*, 2:1–10, 11 2016. 8

[94] R. Hanbury Brown and R. Q. Twiss. Correlation between photons in two coherent beams of light. *Nature*, 177:27–29, 1956. 8, 11

[95] Osip Schwartz, Jonathan M. Levitt, Ron Tenne, Stella Itzhakov, Zvicka Deutsch, and Dan Oron. Superresolution microscopy with quantum emitters. *Nano Letters*, 13:5832–5836, 12 2013. 8

[96] Milena D'Angelo, Maria V. Chekhova, and Yanhua Shih. Two-photon diffraction and quantum lithography. *Physical Review Letters*, 87:013602, 6 2001. 8

[97] The LIGO Scientific Collaboration. A gravitational wave observatory operating beyond the quantum shot-noise limit. *Nature Physics*, 7:962–965, 9 2011. 8

[98] Miles J. Padgett and Robert W. Boyd. An introduction to ghost imaging: quantum and classical. *Philosophical Transactions of the Royal Society A: Mathematical, Physical and Engineering Sciences*, 375, 8 2017. 8

[99] L. Samuel Braunstein and Peter Van Loock. Quantum information with continuous variables. *Reviews of Modern Physics*, 77:513–577, 4 2005. 8

[100] Francesco Lenzini, Jiri Janousek, Oliver Thearle, Matteo Villa, Ben Haylock, Sachin Kasture, Liang Cui, Hoang Phuong Phan, Dzung Viet Dao, Hidehiro Yonezawa, Ping Koy Lam, Elanor H. Huntington, and Mirko Lobino. Integrated photonic platform for quantum information with continuous variables. *Science Advances*, 4, 12 2018. 8

[101] S. Takeda and A. Furusawa. Toward large-scale fault-tolerant universal photonic quantum computing. *APL Photonics*, 4:060902, 6 2019. 8

[102] A. R. McMillan, L. Labonté, A. S. Clark, B. Bell, O. Alibart, A. Martin, W. J. Wadsworth, S. Tanzilli, and J. G. Rarity. Two-photon interference between disparate sources for quantum networking. *Scientific Reports 2013 3:1*, 3:1–5, 6 2013. 8

[103] M. J. Collins, C. Xiong, I. H. Rey, T. D. Vo, J. He, S. Shahnia, C. Reardon, T. F. Krauss, M. J. Steel, A. S. Clark, and B. J. Eggleton. Integrated spatial multiplexing of heralded single-photon sources. *Nature Communications*, 4:1–7, 10 2013. 9

[104] F. Kaneda and P. G. Kwiat. High-efficiency single-photon generation via large-scale active time multiplexing. *Science Advances*, 5, 3 2018. 9

[105] Chaitali Joshi, Alessandro Farsi, Stéphane Clemmen, Sven Ramelow, and Alexander L. Gaeta. Frequency multiplexing for quasi-deterministic heralded single-photon sources. *Nature Communications*, 9:1–8, 2 2018. 9

[106] JunHa Suk, ChanYeop Ahn, S M Mojahidul Ahsan, al, Damien Bonneau, Gabriel J Mendoza, Jeremy L O, Navid Zeraatkar, Kesava S Kalluri, Benjamin Auer, Mercedes Gimeno-Segovia, Hugo Cable, Pete Shadbolt, Joshua W Silverstone, Jacques Carolan, Mark G Thompson, and Terry Rudolph. Relative multiplexing for minimising switching in linear-optical quantum computing. *New Journal of Physics*, 19:063013, 6 2017. 9

[107] Ross C. Schofield, Kyle D. Major, Samuele Grandi, Sebastien Boissier, E. A. Hinds, and Alex S. Clark. Efficient excitation of dye molecules for single photon generation. *Journal of Physics Communications*, 2:115027, 11 2018. 10

[108] Lukas Novotny and Bert Hecht. Principles of nano-optics. *Principles of Nano-Optics*, 9780521832243:1–539, 1 2006. 10, 31

[109] Peter Lodahl, Sahand Mahmoodian, and Soren Stobbe. Interfacing single photons and single quantum dots with photonic nanostructures. *Reviews of Modern Physics*, 87:347–400, 5 2015. 10, 11

[110] Philip Trøst Kristensen, Jakob Egeberg Mortensen, Peter Lodahl, and Søren Stobbe. Shell theorem for spontaneous emission. *Physical Review B - Condensed Matter and Materials Physics*, 88:205308, 11 2013. 10

[111] M. Arcari, I. Söllner, A. Javadi, S. Lindskov Hansen, S. Mahmoodian, J. Liu, H. Thyrrestrup, E. H. Lee, J. D. Song, S. Stobbe, and P. Lodahl. Near-unity coupling efficiency of a quantum emitter to a photonic crystal waveguide. *Physical Review Letters*, 113:093603, 8 2014. 10, 11

[112] N. Somaschi, V. Giesz, L. De Santis, J. C. Loredo, M. P. Almeida, G. Hornecker, S. L. Portalupi, T. Grange, C. Antón, J. Demory, C. Gómez, I. Sagnes, N. D. Lanzillotti-Kimura, A. Lemaítre, A. Auffeves, A. G. White, L. Lanco, and P. Senellart. Near-optimal single-photon sources in the solid state. *Nature Photonics*, 10:340–345, 3 2016. 10, 11, 13

[113] Igor Aharonovich, Dirk Englund, and Milos Toth. Solid-state single-photon emitters. *Nature Photonics*, 10:631–641, 10 2016. 10, 16, 17

[114] Pascale Senellart, Glenn Solomon, and Andrew White. High-performance semiconductor quantum-dot single-photon sources. *Nature Nanotechnology*, 12:1026–1039, 11 2017. 10, 15, 16

[115] M. D. Eisaman, J. Fan, A. Migdall, and S. V. Polyakov. Invited review article: Single-photon sources and detectors. *Review of Scientific Instruments*, 82, 7 2011. 10, 11, 14, 16, 17

[116] D. Stucki, N. Walenta, F. Vannel, R. T. Thew, N. Gisin, H. Zbinden, S. Gray, C. R. Towery, and S. Ten. High rate, long-distance quantum key distribution over 250km of ultra low loss fibres. *New Journal of Physics*, 11:075003, 7 2009. 10

[117] Paul Jouguet, Sébastien Kunz-Jacques, Anthony Leverrier, Philippe Grangier, and Eleni Diamanti. Experimental demonstration of long-distance continuous-variable quantum key distribution. *Nature Photonics*, 7:378–381, 4 2013. 10

[118] Chad A. Husko, Alex S. Clark, Matthew J. Collins, Alfredo De Rossi, Sylvain Combrié, Gaëlle Lehoucq, Isabella H. Rey, Thomas F. Krauss, Chunle Xiong, and Benjamin J. Eggleton. Multi-photon absorption limits to heralded single photon sources. *Scientific Reports 2013 3:1*, 3:1–8, 11 2013. 10

[119] Paul Burdekin, Samuele Grandi, Rielly Newbold, Rowan A. Hoggarth, Kyle D. Major, and Alex S. Clark. Single-photon-level sub-doppler pump-probe spectroscopy of rubidium. *Physical Review Applied*, 14:044046, 10 2020. 11, 95, 102

[120] Tim Kroh, Janik Wolters, Andreas Ahlrichs, Andreas W. Schell, Alexander Thoma, Stephan Reitzenstein, Johannes S. Wildmann, Eugenio Zallo, Rinaldo Trotta, Armando Rastelli, Oliver G. Schmidt, and Oliver Benson. Slow and fast light behavior of single photons from a quantum dot interacting with the excited state hyperfine structure of the cesium d1-line. *arxiv preprint*, pages 1–12, 2019. 11

[121] Wilhelm Kiefer, Mohammad Rezai, Jörg Wrachtrup, and Ilja Gerhardt. An atomic spectrum recorded with a single-molecule light source. *Applied Physics B: Lasers and Optics*, 122:1–12, 2 2016. 11, 18, 46

[122] Axel Kuhn, Markus Hennrich, and Gerhard Rempe. Deterministic single-photon source for distributed quantum networking. *Physical Review Letters*, 89, 2002. 11

[123] J. McKeever, A. Boca, A. D. Boozer, R. Miller, J. R. Buck, A. Kuzmich, and H. J. Kimble. Deterministic generation of single photons from one atom trapped in a cavity. *Science*, 303:1992–1994, 3 2004. 11

[124] Markus Hijlkema, Bernhard Weber, Holger P. Specht, Simon C. Webster, Axel Kuhn, and Gerhard Rempe. A single-photon server with just one atom. *Nature Physics*, 3:253–255, 4 2007. 11

[125] Nicolas Sangouard and Hugo Zbinden. What are single photons good for? *Journal of Modern Optics*, 59:1458–1464, 2012. 12

[126] Mercedes Gimeno-Segovia, Pete Shadbolt, Dan E. Browne, and Terry Rudolph. From three-photon greenberger-horne-zeilinger states to ballistic universal quantum computation. *Physical Review Letters*, 115:020502, 7 2015. 12, 15

[127] C. K. Hong, Z. Y. Ou, and L. Mandel. Measurement of subpicosecond time intervals between two photons by interference. *Physical Review Letters*, 59:2044, 11 1987. 12

[128] Gilbert Grynberg, Alain Aspect, Claude Fabre, and Claude Cohen-Tannoudji. Introduction to quantum optics: From the semi-classical approach to quantized light. *Introduction to Quantum Optics*, 9 2010. 13

[129] Edward B. Flagg, Andreas Muller, Sergey V. Polyakov, Alex Ling, Alan Migdall, and Glenn S. Solomon. Interference of single photons from two separate semiconductor quantum dots. *Physical Review Letters*, 104, 4 2010. 13, 15

[130] Chloe Clear, Ross C. Schofield, Kyle D. Major, Jake Iles-Smith, Alex S. Clark, and Dara P.S. McCutcheon. Phonon-induced optical dephasing in single organic molecules. *Physical Review Letters*, 124:153602, 4 2020. 13, 42, 46, 47

[131] Jake Iles-Smith, Dara P.S. McCutcheon, Ahsan Nazir, and Jesper Mørk. Phonon scattering inhibits simultaneous near-unity efficiency and indistinguishability in semiconductor single-photon sources. *Nature Photonics*, 11:521–+, 8 2017. 13, 42

[132] Kevin G. Schädler, Carlotta Ciancico, Sofia Pazzagli, Pietro Lombardi, Adrian Bachtold, Costanza Toninelli, Antoine Reserbat-Plantey, and Frank H.L. Koppens. Electrical control of lifetime-limited quantum emitters using 2d materials. *Nano Letters*, 19:3789–3795, 2019. 14, 19, 71

[133] Shahriar Aghaeimeibodi, Chang Min Lee, Mustafa Atabey Buyukkaya, Christopher J.K. Richardson, and Edo Waks. Large stark tuning of inas/inp quantum dots. *Applied Physics Letters*, 114:071105, 2 2019. 14

[134] Noel H. Wan, Tsung Ju Lu, Kevin C. Chen, Michael P. Walsh, Matthew E. Trusheim, Lorenzo De Santis, Eric A. Bersin, Isaac B. Harris, Sara L. Mouradian, Ian R. Christen, Edward S. Bielejec, and Dirk Englund. Large-scale integration of artificial atoms in hybrid photonic circuits. *Nature*, 583:226–231, 7 2020. 14

[135] Anastasios Fasoulakis, Kyle D. Major, Rowan A. Hoggarth, Paul Burdekin, Dominika P. Bogusz, Ross C. Schofield, and Alex S. Clark. Uniaxial strain tuning of organic molecule single photon sources. *Nanoscale*, 15:177–184, 12 2022. 14, 19, 77, 78

[136] Yu Ming He, Yu He, Yu Jia Wei, Dian Wu, Mete Atatüre, Christian Schneider, Sven Höfling, Martin Kamp, Chao Yang Lu, and Jian Wei Pan. On-demand semiconductor single-photon source with near-unity indistinguishability. *Nature Nanotechnology*, 8:213–217, 2013. 14, 15, 16

[137] M. Gschrey, A. Thoma, P. Schnauber, M. Seifried, R. Schmidt, B. Wohlfeil, L. Krüger, J. H. Schulze, T. Heindel, S. Burger, F. Schmidt, A. Strittmatter, S. Rodt, and S. Reitzenstein. Highly indistinguishable photons from deterministic quantum-dot microlenses

utilizing three-dimensional in situ electron-beam lithography. *Nature Communications*, 6:1–8, 7 2015. 14

[138] A. Schlehahn, A. Thoma, P. Munnelly, M. Kamp, S. Höfling, T. Heindel, C. Schneider, and S. Reitzenstein. An electrically driven cavity-enhanced source of indistinguishable photons with 61% overall efficiency. *APL Photonics*, 1:011301, 4 2016. 14, 16

[139] A. J. Shields. Semiconductor quantum light sources. *Nature Photonics*, 1:215–223, 2007. 14, 15

[140] S. Stobbe, J. Johansen, P. T. Kristensen, J. M. Hvam, and P. Lodahl. Frequency dependence of the radiative decay rate of excitons in self-assembled quantum dots: Experiment and theory. *Physical Review B - Condensed Matter and Materials Physics*, 80:155307, 10 2009. 14

[141] Deepa Chaturvedi, Ajit Kumar, Akhilesh Kumar Mishra, Wei Shi, Yelong Xu, Hassan Sepehrian, Daniel Huber, Marcus Reindl, Johannes Aberl, Armando Rastelli, and Rinaldo Trotta. Semiconductor quantum dots as an ideal source of polarization-entangled photon pairs on-demand: a review. *Journal of Optics*, 20:073002, 6 2018. 15

[142] Daniel M. Greenberger, Michael A. Horne, and Anton Zeilinger. Going beyond bell's theorem. *Bell's Theorem, Quantum Theory and Conceptions of the Universe*, pages 69–72, 1989. 15

[143] I. Schwartz, D. Cogan, E. R. Schmidgall, Y. Don, L. Gantz, O. Kenneth, N. H. Lindner, and D. Gershoni. Deterministic generation of a cluster state of entangled photons. *Science*, 354:434–437, 10 2016. 15

[144] Glenn S Solomon, Charles Santori, David Fattal, Jelena Vuc, and Yoshihisa Yamamoto. Indistinguishable photons from a single-photon device. *Nature*, 419:594–597, 2002. 15

[145] D. C. Unitt, A. J. Bennett, P. Atkinson, D. A. Ritchie, and A. J. Shields. Polarization control of quantum dot single-photon sources via a dipole-dependent purcell effect. *Physical Review B - Condensed Matter and Materials Physics*, 72:033318, 7 2005. 15

[146] M. B. Ward, T. Farrow, P. See, Z. L. Yuan, O. Z. Karimov, A. J. Bennett, A. J. Shields, P. Atkinson, K. Cooper, and D. A. Ritchie. Electrically driven telecommunication wavelength single-photon source. *Applied Physics Letters*, 90, 2007. 15, 16

[147] A. J. Bennett, R. B. Patel, A. J. Shields, K. Cooper, P. Atkinson, C. A. Nicoll, and D. A. Ritchie. Indistinguishable photons from a diode. *Applied Physics Letters*, 92:1–4, 2008. 15, 16, 141

[148] David Press, Stephan Götzinger, Stephan Reitzenstein, Carolin Hofmann, Andreas Löffler, Martin Kamp, Alfred Forchel, and Yoshihisa Yamamoto. Photon antibunching from a single quantum-dot-microcavity system in the strong coupling regime. *Physical Review Letters*, 98, 3 2007. 15

[149] C. A. Leatherdale, W. K. Woo, F. V. Mikulec, and M. G. Bawendi. On the absorption cross section of cdse nanocrystal quantum dots. *Journal of Physical Chemistry B*, 106:7619–7622, 8 2002. 15

[150] Benoit Mahler, Piernicola Spinicelli, Stéphanie Buil, Xavier Quelin, Jean Pierre Hermier, and Benoit Dubertret. Towards non-blinking colloidal quantum dots. *Nature Materials*, 7:659–664, 6 2008. 15

[151] Lei Qian, Ying Zheng, Jiangeng Xue, and Paul H. Holloway. Stable and efficient quantum-dot light-emitting diodes based on solution-processed multilayer structures. *Nature Photonics*, 5:543–548, 8 2011. 15

[152] Ravitej Uppu, Hans T. Eriksen, Henri Thyrrestrup, Aslı D. Uğurlu, Ying Wang, Sven Scholz, Andreas D. Wieck, Arne Ludwig, Matthias C. Löbl, Richard J. Warburton, Peter Lodahl, and Leonardo Midolo. On-chip deterministic operation of quantum dots in dual-mode waveguides for a plug-and-play single-photon source. *Nature Communications*, 11:1–6, 7 2020. 15

[153] Luca Sapienza, Marcelo Davanço, Antonio Badolato, and Kartik Srinivasan. Nanoscale optical positioning of single quantum dots for bright and pure single-photon emission. *Nature Communications*, 6:1–8, 7 2015. 15, 16, 82

[154] Susanna M. Thon, Matthew T. Rakher, Hyochul Kim, Jan Gudat, William T.M. Irvine, Pierre M. Petroff, and Dirk Bouwmeester. Strong coupling through optical positioning of a quantum dot in a photonic crystal cavity. *Applied Physics Letters*, 94:111115, 3 2009. 15

[155] Xing Lin, Xingliang Dai, Chaodan Pu, Yunzhou Deng, Yuan Niu, Limin Tong, Wei Fang, Yizheng Jin, and Xiaogang Peng. Electrically-driven single-photon sources based on colloidal quantum dots with near-optimal antibunching at room temperature. *Nature Communications*, 8:1–7, 10 2017. 15

[156] Hendrik Utzat, Weiwei Sun, Alexander E.K. Kaplan, Franziska Krieg, Matthias Ginterseder, Boris Spokoyny, Nathan D. Klein, Katherine E. Shulenberger, Collin F. Perkinson, Maksym V. Kovalenko, and Moungi G. Bawendi. Coherent single-photon emission from colloidal lead halide perovskite quantum dots. *Science*, 363, 3 2019. 15

[157] Maxim Rakhlin, Sergey Sorokin, Dmitrii Kazanov, Irina Sedova, Tatiana Shubina, Sergey Ivanov, Vladimir Mikhailovskii, and Alexey Toropov. Bright single-photon emitters with a cdse quantum dot and multimode tapered nanoantenna for the visible spectral range. *Nanomaterials 2021, Vol. 11, Page 916*, 11:916, 4 2021. 15

[158] Yue Ma, Yu Zhang, and William W. Yu. Near infrared emitting quantum dots: synthesis, luminescence properties and applications. *Journal of Materials Chemistry C*, 7:13662–13679, 11 2019. 15

[159] Christopher J. K. Richardson, Edo Waks, Je-Hyung Kim, Richard P. Leavitt, and Tao Cai. Two-photon interference from a bright single-photon source at telecom wavelengths. *Optica, Vol. 3, Issue 6, pp. 577-584*, 3:577–584, 6 2016. 15

[160] T. Müller, J. Skiba-Szymanska, A. B. Krysa, J. Huwer, M. Felle, M. Anderson, R. M. Stevenson, J. Heffernan, D. A. Ritchie, and A. J. Shields. A quantum light-emitting diode for the standard telecom window around 1,550nm. *Nature Communications*, 9:1–6, 2 2018. 15

[161] A. Dousse, L. Lanco, J. Suffczyński, E. Semenova, A. Miard, A. Lemaître, I. Sagnes, C. Roblin, J. Bloch, and P. Senellart. Controlled light-matter coupling for a single quantum dot embedded in a pillar microcavity using far-field optical lithography. *Physical Review Letters*, 101:267404, 12 2008. 15

[162] Kelley Rivoire, Sonia Buckley, Arka Majumdar, Hyochul Kim, Pierre Petroff, and Jelena Vučković. Fast quantum dot single photon source triggered at telecommunications wavelength. *Applied Physics Letters*, 98:083105, 2 2011. 15

[163] P. Michler, A. Kiraz, C. Becher, W. V. Schoenfeld, P. M. Petroff, L. Zhang, E. Hu, and A. Imamoğlu. A quantum dot single-photon turnstile device. *Science*, 290:2282–2285, 12 2000. 15

[164] Charles Santori, Matthew Pelton, Glenn Solomon, Yseulte Dale, and Yoshihisa Yamamoto. Triggered single photons from a quantum dot. *Physical Review Letters*, 86:1502, 2 2001. 15

[165] Arun Mohan, Pascal Gallo, Marco Felici, Benjamin Dwir, Alok Rudra, Jerome Faist, Eli Kapon, P Gallo, M Felici, B Dwir, A Rudra, E Kapon, and J Faist. Record-low inhomogeneous broadening of site-controlled quantum dots for nanophotonics. *Small*, 6:1268–1272, 6 2010. 15

[166] Guang Cun Shan, Zhang Qi Yin, Chan Hung Shek, and Wei Huang. Single photon sources with single semiconductor quantum dots. *Frontiers of Physics 2014 9:2*, 9:170–193, 9 2013. 16

[167] Xing Ding, Yu He, Z Duan, Niels Gregersen, M Chen, S Unsleber, S Maier, Christian Schneider, Martin Kamp, Sven Höfling, Chao yang Lu, and Jian wei Pan. On-demand single photons with high extraction efficiency and near-unity indistinguishability from a resonantly driven quantum dot in a micropillar. *Physical Review Letters*, 020401:1–6, 2016. 16

[168] Liang Zhai, Giang N. Nguyen, Clemens Spinnler, Julian Ritzmann, Matthias C. Löbl, Andreas D. Wieck, Arne Ludwig, Alisa Javadi, and Richard J. Warburton. Quantum

interference of identical photons from remote gaas quantum dots. *Nature Nanotechnology*, 17:829–833, 5 2022. 16

[169] R. M. Stevenson, C. L. Salter, J. Nilsson, A. J. Bennett, M. B. Ward, I. Farrer, D. A. Ritchie, and A. J. Shields. Indistinguishable entangled photons generated by a light-emitting diode. *Physical Review Letters*, 108:040503, 1 2012. 16

[170] Raj B. Patel, Anthony J. Bennett, Ken Cooper, Paola Atkinson, Christine A. Nicoll, David A. Ritchie, and Andrew J. Shields. Quantum interference of electrically generated single photons from a quantum dot. *Nanotechnology*, 21:274011, 6 2010. 16

[171] I. Aharonovich, S. Castelletto, D. A. Simpson, C. H. Su, A. D. Greentree, and S. Prawer. Diamond-based single-photon emitters. *Reports on Progress in Physics*, 74, 7 2011. 16, 17

[172] Marianne Etzelmüller Bathen and Lasse Vines. Manipulating single-photon emission from point defects in diamond and silicon carbide. *Advanced Quantum Technologies*, 4:2100003, 7 2021. 16

[173] Brahim Lounis and Michel Orrit. Single-photon sources. *Reports on Progress in Physics*, 68, 2005. 16

[174] M J Davis, A V Darosa, J P Schaedel, J Klostermeyer, J Roettger, G Breit, and M A Tuve. Charge states of the vacancy in diamond. *Nature*, 269:498–500, 10 1977. 16

[175] Elke Neu, Mario Agio, Christoph Becher, E Gross, F Guldner, C Hepp, D Steinmetz, E Zscherpel, S Ghodbane, H Sternschulte, D Steinmüller-Nethl, Y Liang, A Krueger, and C Becher. Photophysics of single silicon vacancy centers in diamond: implications for single photon emission. *Optics Express, Vol. 20, Issue 18, pp. 19956-19971*, 20:19956–19971, 8 2012. 16, 17

[176] Takayuki Iwasaki, Fumitaka Ishibashi, Yoshiyuki Miyamoto, Yuki Doi, Satoshi Kobayashi, Takehide Miyazaki, Kosuke Tahara, Kay D. Jahnke, Lachlan J. Rogers, Boris Naydenov, Fedor Jelezko, Satoshi Yamasaki, Shinji Nagamachi, Toshiro Inubushi,

Norikazu Mizuochi, and Mutsuko Hatano. Germanium-vacancy single color centers in diamond. *Scientific Reports*, 5, 8 2015. 16, 17

[177] Takayuki Iwasaki, Yoshiyuki Miyamoto, Takashi Taniguchi, Petr Siyushev, Mathias H. Metsch, Fedor Jelezko, and Mutsuko Hatano. Tin-vacancy quantum emitters in diamond. *Physical Review Letters*, 119:253601, 12 2017. 16

[178] Paul E. Barclay, Kai Mei C Fu, Charles Santori, and Raymond G. Beausoleil. Chip-based microcavities coupled to nitrogen-vacancy centers in single crystal diamond. *Applied Physics Letters*, 95, 2009. 16

[179] Christian Kurtsiefer, Sonja Mayer, Patrick Zarda, and Harald Weinfurter. Stable solid-state source of single photons. *Physical Review Letters*, 85:290–293, 7 2000. 16

[180] Ph Tamarat, T. Gaebel, J. R. Rabeau, M. Khan, A. D. Greentree, H. Wilson, L. C.L. Hollenberg, S. Prawer, P. Hemmer, F. Jelezko, and J. Wrachtrup. Stark shift control of single optical centers in diamond. *Physical Review Letters*, 97, 2006. 16

[181] Gang Zhang, Yuan Cheng, Jyh Pin Chou, and Adam Gali. Material platforms for defect qubits and single-photon emitters. *Applied Physics Reviews*, 7:031308, 9 2020. 17

[182] Brendon C. Rose, Ding Huang, Zi Huai Zhang, Paul Stevenson, Alexei M. Tyryshkin, Sorawis Sangtawesin, Srikanth Srinivasan, Lorne Loudin, Matthew L. Markham, Andrew M. Edmonds, Daniel J. Twitchen, Stephen A. Lyon, and Nathalie P. De Leon. Observation of an environmentally insensitive solid-state spin defect in diamond. *Science*, 361:60–63, 7 2018. 17

[183] Audrius Alkauskas, Bob B. Buckley, David D. Awschalom, and Chris G. Van De Walle. First-principles theory of the luminescence lineshape for the triplet transition in diamond nv centres. *New Journal of Physics*, 16:073026, 7 2014. 17

[184] Alexios Beveratos, Rosa Brouri, Thierry Gacoin, André Villing, Jean Philippe Poizat, and Philippe Grangier. Single photon quantum cryptography. *Physical Review Letters*, 89:187901, 2002. 17

[185] Igor Aharonovich and Elke Neu. Diamond nanophotonics. *Advanced Optical Materials*, 2:911–928, 2014. 17

[186] A. Lohrmann, N. Iwamoto, Z. Bodrog, S. Castelletto, T. Ohshima, T. J. Karle, A. Gali, S. Prawer, J. C. McCallum, and B. C. Johnson. Single-photon emitting diode in silicon carbide. *Nature Communications*, 6:1–7, 7 2015. 17

[187] Stefania Castelletto and Alberto Boretti. Silicon carbide color centers for quantum applications. *Journal of Physics: Photonics*, 2:022001, 3 2020. 17

[188] Stefania Castelletto. Silicon carbide single-photon sources: challenges and prospects. *Materials for Quantum Technology*, 1:023001, 3 2021. 17

[189] Naoya Morioka, Charles Babin, Roland Nagy, Izel Gediz, Erik Hesselmeier, Di Liu, Matthew Joliffe, Matthias Niethammer, Durga Dasari, Vadim Vorobyov, Roman Kolesov, Rainer Stöhr, Jawad Ul-Hassan, Nguyen Tien Son, Takeshi Ohshima, Péter Udvarhelyi, Gergő Thiering, Adam Gali, Jörg Wrachtrup, and Florian Kaiser. Spin-controlled generation of indistinguishable and distinguishable photons from silicon vacancy centres in silicon carbide. *Nature Communications*, 11:1–8, 5 2020. 17, 141

[190] Romain Bourrellier, Sophie Meuret, Anna Tararan, Odile Stéphan, Mathieu Kociak, Luiz H.G. Tizei, and Alberto Zobelli. Bright uv single photon emission at point defects in h-bn. *Nano Letters*, 16:4317–4321, 7 2016. 17

[191] L. J. Martínez, T. Pelini, V. Waselowski, J. R. Maze, B. Gil, G. Cassabois, and V. Jacques. Efficient single photon emission from a high-purity hexagonal boron nitride crystal. *Physical Review B*, 94:121405, 9 2016. 17

[192] Toan Trong Tran, Christopher Elbadawi, Daniel Totonjian, Charlene J. Lobo, Gabriele Grosso, Hyowon Moon, Dirk R. Englund, Michael J. Ford, Igor Aharonovich, and Milos Toth. Robust multicolor single photon emission from point defects in hexagonal boron nitride. *2017 Conference on Lasers and Electro-Optics, CLEO 2017 - Proceedings*, 2017-January:7331–7338, 10 2017. 17

[193] Tobias Vogl, Ruvi Lecamwasam, Ben C. Buchler, Yuerui Lu, and Ping Koy Lam. Compact cavity-enhanced single-photon generation with hexagonal boron nitride. *ACS Photonics*, 6:1955–1962, 8 2019. 17

[194] Yoshihiro Yamaguchi, Yoshio Matsubara, Takanori Ochi, Tateaki Wakamiya, and Zen Ichi Yoshida. How the π conjugation length affects the fluorescence emission efficiency. *Journal of the American Chemical Society*, 130:13867–13869, 10 2008. 18

[195] C. Toninelli, I. Gerhardt, A. S. Clark, A. Reserbat-Plantey, S. Götzinger, Z. Ristanović, M. Colautti, P. Lombardi, K. D. Major, I. Deperasińska, W. H. Pernice, F. H.L. Koppens, B. Kozankiewicz, A. Gourdon, V. Sandoghdar, and M. Orrit. Single organic molecules for photonic quantum technologies. *Nature Materials*, 20:1615–1628, 5 2021. 18

[196] B. C. Buchler, T. Kalkbrenner, C. Hettich, and V. Sandoghdar. Measuring the quantum efficiency of the optical emission of single radiating dipoles using a scanning mirror. *Physical Review Letters*, 95:063003, 8 2005. 18

[197] Xiao liu Chu, Stephan Götzinger, and Vahid Sandoghdar. A single molecule as a high-fi delity photon gun for producing intensity-squeezed light. *Nature Photonics*, 11:58–62, 2016. 18

[198] Samuele Grandi. *Single quantum emitters: resonance fluorescence and emission enhancement*. PhD thesis, Imperial College London, 2017. 18, 51

[199] Mohammad Rezai, Jörg Wrachtrup, and Ilja Gerhardt. Coherence properties of molecular single photons for quantum networks. *Physical Review X*, 8, 7 2018. 18

[200] Kyle D Major. *Coupling single molecules to cryogenic optical fiber microcavities*. PhD thesis, Imperial College London, 2016. 18, 65, 66

[201] Pierre Türschmann, Nir Rotenberg, Jan Renger, Irina Harder, Olga Lohse, Tobias Utikal, Stephan Götzinger, and Vahid Sandoghdar. Chip-based all-optical control of single molecules coherently coupled to a nanoguide. *Nano Letters*, 17:4941–4945, 8 2017. 18, 19

[202] Samuele Grandi, Kyle D Major, Claudio Polisseni, Sebastien Boissier, Alex S Clark, and E A Hinds. Quantum dynamics of a driven two-level molecule with variable dephasing. *Physical Review A*, 94, 2016. 18, 52, 74, 141

[203] Chunhuan Zhang, Haiyun Dong, Yong Sheng Zhao, C Zhang, H Dong, and Y S Zhao. Rational design, controlled fabrication, and photonic applications of organic composite nanomaterials. *Advanced Optical Materials*, 6:1701193, 11 2018. 18

[204] Claudio U. Hail, Christian Höller, Korenobu Matsuzaki, Patrik Rohner, Jan Renger, Vahid Sandoghdar, Dimos Poulikakos, and Hadi Eghlidi. Nanoprinting organic molecules at the quantum level. *Nature Communications*, 10:1–8, 4 2019. 18

[205] Daqing Wang, Hrishikesh Kelkar, Diego Martin-Cano, Dominik Rattenbacher, Alexey Shkarin, Tobias Utikal, Stephan Götzinger, and Vahid Sandoghdar. Turning a molecule into a coherent two-level quantum system. *Nature Physics*, 15:483–489, 2 2019. 18, 37, 64, 94

[206] P. Lombardi, A. P. Ovvyan, S. Pazzagli, G. Mazzamuto, G. Kewes, O. Neitzke, N. Gruhler, O. Benson, W. H.P. Pernice, F. S. Cataliotti, and C. Toninelli. Photostable molecules on chip: Integrated sources of nonclassical light. *ACS Photonics*, 5:126–132, 1 2018. 19

[207] Sebastien Boissier, Ross C. Schofield, Lin Jin, Anna Ovvyan, Salahuddin Nur, Frank H.L. Koppens, Costanza Toninelli, Wolfram H.P. Pernice, Kyle D. Major, E. A. Hinds, and Alex S. Clark. Coherent characterisation of a single molecule in a photonic black box. *Nature Communications*, 12:1–8, 1 2021. 19, 66, 82

[208] Dominik Rattenbacher, Alexey Shkarin, Jan Renger, Tobias Utikal, Stephan Götzinger, and Vahid Sandoghdar. Coherent coupling of single molecules to on-chip ring resonators. *New Journal of Physics*, 21:062002, 6 2019. 19

[209] K. G. Lee, X. W. Chen, H. Eghlidi, P. Kukura, R. Lettow, A. Renn, V. Sandoghdar, and S. Götzinger. A planar dielectric antenna for directional single-photon emission and near-unity collection efficiency. *Nature Photonics*, 5:166–169, 1 2011. 19

[210] Michel Orrit, Costanza Toninelli, Maja Colautti, Francesco S. Piccioli, Zoran Ristanović, Pietro Lombardi, Amin Moradi, Subhasis Adhikari, Irena Deperasinska, and Boleslaw Kozankiewicz. Laser-induced frequency tuning of fourier-limited single-molecule emitters. *ACS Nano*, 14:13584–13592, 10 2020. 19

[211] Khabat Heshami, Duncan G England, Peter C Humphreys, Philip J Bustard, Victor M Acosta, Joshua Nunn, Benjamin J Sussman, and Parks Road. Quantum memories: emerging applications and recent advances. *arxiv preprint*, 2016. 20, 36

[212] Alexander I. Lvovsky, Barry C. Sanders, and Wolfgang Tittel. Optical quantum memory. *Nature Photonics*, 3:706–714, 2009. 20, 27, 28, 36

[213] Klemens Hammerer, Anders S. Sørensen, and Eugene S. Polzik. Quantum interface between light and atomic ensembles. *Reviews of Modern Physics*, 82:1041–1093, 2010. 20, 94

[214] J. Nunn, N. K. Langford, W. S. Kolthammer, T. F.M. Champion, M. R. Sprague, P. S. Michelberger, X. M. Jin, D. G. England, and I. A. Walmsley. Enhancing multiphoton rates with quantum memories. *Physical Review Letters*, 110:133601, 3 2013. 20, 29

[215] Dik Bouwmeester, Jian Wei Pan, Klaus Mattle, Manfred Eibl, Harald Weinfurter, and Anton Zeilinger. Experimental quantum teleportation. *Nature*, 390:575–579, 12 1997. 21, 22

[216] S. Gao, O. Lazo-Arjona, B. Brecht, K. T. Kaczmarek, P. M. Ledingham, S. E. Thomas, J. Nunn, D. J. Saunders, and I. A. Walmsley. Optimal coherent filtering for single photons. *Optics InfoBase Conference Papers*, Part F165-:1–6, 2019. 21, 29

[217] Mahdi Hosseini, Ben M. Sparkes, Gabriel Hétet, Jevon J. Longdell, Ping Koy Lam, and Ben C. Buchler. Coherent optical pulse sequencer for quantum applications. *Nature*, 461:241–245, 9 2009. 21

[218] K. F. Reim, J. Nunn, X. M. Jin, P. S. Michelberger, T. F.M. Champion, D. G. England, K. C. Lee, W. S. Kolthammer, N. K. Langford, and I. A. Walmsley. Multipulse addressing

of a raman quantum memory: Configurable beam splitting and efficient readout. *Physical Review Letters*, 108:263602, 6 2012. 21, 162

[219] Peter C. Humphreys, W. Steven Kolthammer, Joshua Nunn, Marco Barbieri, Animesh Datta, and Ian A. Walmsley. Continuous-variable quantum computing in optical time-frequency modes using quantum memories. *Physical Review Letters*, 113:130502, 9 2014. 21

[220] Robert Löw, Hendrik Weimer, Johannes Nipper, Jonathan B. Balewski, Björn Butscher, Hans Peter Büchler, and Tilman Pfau. An experimental and theoretical guide to strongly interacting rydberg gases. *Journal of Physics B: Atomic, Molecular and Optical Physics*, 45:113001, 5 2012. 21

[221] Valentina Parigi, Erwan Bimbard, Jovica Stanojevic, Andrew J. Hilliard, Florence Nogrette, Rosa Tualle-Brouri, Alexei Ourjoumtsev, and Philippe Grangier. Observation and measurement of interaction-induced dispersive optical nonlinearities in an ensemble of cold rydberg atoms. *Physical Review Letters*, 109:233602, 12 2012. 21

[222] Daniel Tiarks, Steffen Schmidt, Gerhard Rempe, and Stephan Dürr. Optical π phase shift created with a single-photon pulse. *Science Advances*, 2, 4 2016. 21

[223] Jeff D. Thompson, Travis L. Nicholson, Qi Yu Liang, Sergio H. Cantu, Aditya V. Venkatramani, Soonwon Choi, Ilya A. Fedorov, Daniel Viscor, Thomas Pohl, Mikhail D. Lukin, and Vladan Vuletia. Symmetry-protected collisions between strongly interacting photons. *Nature*, 542:206–209, 1 2017. 21

[224] W. A. Gambling. The rise and rise of optical fibers. *IEEE Journal on Selected Topics in Quantum Electronics*, 6:1084–1093, 2000. 22

[225] H. J. Briegel, W. Dür, J. I. Cirac, and P. Zoller. Quantum repeaters: The role of imperfect local operations in quantum communication. *Physical Review Letters*, 81:5932–5935, 1998. 22

[226] M. Zukowski, A. Zeilinger, M. A. Horne, and A. K. Ekert. “event-ready-detectors” bell experiment via entanglement swapping. *Physical Review Letters*, 71:4287, 12 1993. 22

[227] B. Hensen, H. Bernien, A. E. Dreaú, A. Reiserer, N. Kalb, M. S. Blok, J. Ruitenberg, R. F.L. Vermeulen, R. N. Schouten, C. Abellán, W. Amaya, V. Pruneri, M. W. Mitchell, M. Markham, D. J. Twitchen, D. Elkouss, S. Wehner, T. H. Taminiau, and R. Hanson. Loophole-free bell inequality violation using electron spins separated by 1.3 kilometres. *Nature*, 526:682–686, 10 2015. 25

[228] Mateusz Mazelanik, Adam Leszczyński, and Michał Parniak. Optical-domain spectral super-resolution via a quantum-memory-based time-frequency processor. *Nature Communications*, 13:1–12, 2 2022. 25, 34, 35, 167

[229] D. L. McAuslan, L. R. Taylor, and J. J. Longdell. Using quantum memory techniques for optical detection of ultrasound. *Applied Physics Letters*, 101:191112, 11 2012. 26

[230] Mateusz Mazelanik, Adam Leszczyński, Michał Lipka, Wojciech Wasilewski, and Michał Parniak. Real-time ghost imaging of bell-nonlocal entanglement between a photon and a quantum memory. *Quantum*, 5:493, 7 2021. 26

[231] Félix Bussières, Nicolas Sangouard, Mikael Afzelius, Hugues De Riedmatten, Christoph Simon, and Wolfgang Tittel. Prospective applications of optical quantum memories. *http://dx.doi.org/10.1080/09500340.2013.856482*, 60:1519–1537, 10 2013. 26

[232] Joshua Nunn. *Quantum Memory in Atomic Ensembles.* PhD thesis, Oxford University, 2008. 27, 121, 122, 123, 125, 126, 127, 130, 131, 168, 202, 203

[233] C. Simon, M. Afzelius, J. Appel, A. Boyer De La Giroday, S. J. Dewhurst, N. Gisin, C. Y. Hu, F. Jelezko, S. Kröll, J. H. Müller, J. Nunn, E. S. Polzik, J. G. Rarity, H. De Riedmatten, W. Rosenfeld, A. J. Shields, N. Sköld, R. M. Stevenson, R. Thew, I. A. Walmsley, M. C. Weber, H. Weinfurter, J. Wrachtrup, and R. J. Young. Quantum memories :a review based on the european integrated project”qubit applications (qap)”. *European Physical Journal D*, 58:1–22, 2010. 27, 28

[234] Nicolas Sangouard, Christoph Simon, Hugues De Riedmatten, and Nicolas Gisin. Quantum repeaters based on atomic ensembles and linear optics. *Reviews of Modern Physics*, 83:33–80, 3 2011. 27, 29

[235] Erhan Saglamyurek, Taras Hrushevskyi, Logan Cooke, Anindya Rastogi, and Lindsay J. LeBlanc. Single-photon-level light storage in cold atoms using the autler-townes splitting protocol. *arxiv preprint*, pages 1–6, 2019. 28, 37, 38, 121

[236] K. T. Kaczmarek, P. M. Ledingham, B. Brecht, S. E. Thomas, G. S. Thekkadath, O. Lazo-Arjona, J. H.D. Munns, E. Poem, A. Feizpour, D. J. Saunders, J. Nunn, and I. A. Walmsley. High-speed noise-free optical quantum memory. *Physical Review A*, 97:1–10, 2018. 28, 38, 39, 162, 163, 165

[237] Jinxian Guo, Xiaotian Feng, Peiyu Yang, Zhifei Yu, L. Q. Chen, Chun Hua Yuan, and Weiping Zhang. High-performance raman quantum memory with optimal control in room temperature atoms. *Nature Communications*, 10:3–8, 2019. 28, 38, 94, 162

[238] Mustafa Gündoğan, Patrick M. Ledingham, Kutlu Kutluer, Margherita Mazzera, and Hugues De Riedmatten. Solid state spin-wave quantum memory for time-bin qubits. *Physical Review Letters*, 114:230501, 6 2015. 28

[239] Robert Raussendorf and Jim Harrington. Fault-tolerant quantum computation with high threshold in two dimensions. *Physical Review Letters*, 98:190504, 5 2007. 28

[240] Melvyn Ho, Jean Daniel Bancal, and Valerio Scarani. Device-independent certification of the teleportation of a qubit. *Physical Review A - Atomic, Molecular, and Optical Physics*, 88:052318, 11 2013. 28

[241] Alexey V. Gorshkov, Tommaso Calarco, Mikhail D. Lukin, and Anders S. Sørensen. Photon storage in λ—-type optically dense atomic media. iv. optimal control using gradient ascent. *Physical Review A - Atomic, Molecular, and Optical Physics*, 77:043806, 4 2008. 29, 36, 136, 140

[242] K F Reim, J Nunn, V O Lorenz, B J Sussman, K C Lee, N K Langford, D Jaksch, and I A Walmsley. Towards high-speed optical quantum memories. *Nature Photonics*, 4:218–221, 2010. 29, 38

[243] K. Surmacz, J. Nunn, K. Reim, K. C. Lee, V. O. Lorenz, B. Sussman, I. A. Walmsley, and D. Jaksch. Efficient spatially resolved multimode quantum memory. *Physical Review A - Atomic, Molecular, and Optical Physics*, 78:1–9, 2008. 29, 33, 152

[244] Denis V. Vasilyev, Ivan V. Sokolov, and Eugene S. Polzik. Quantum memory for images: A quantum hologram. *Physical Review A - Atomic, Molecular, and Optical Physics*, 77:020302, 2 2008. 29, 33

[245] Anna Grodecka-Grad, Emil Zeuthen, and Anders S. Sørensen. High-capacity spatial multimode quantum memories based on atomic ensembles. *Physical Review Letters*, 109:133601, 9 2012. 29, 33

[246] Christoph Simon, Hugues De Riedmatten, Mikael Afzelius, Nicolas Sangouard, Hugo Zbinden, and Nicolas Gisin. Quantum repeaters with photon pair sources and multimode memories. *Physical Review Letters*, 98:190503, 5 2007. 29, 33

[247] Mikael Afzelius, Christoph Simon, Hugues De Riedmatten, and Nicolas Gisin. Multimode quantum memory based on atomic frequency combs. *Physical Review A - Atomic, Molecular, and Optical Physics*, 79:052329, 5 2009. 29, 35, 36

[248] Mustafa Gündoğan, Patrick M. Ledingham, Attaallah Almasi, Matteo Cristiani, and Hugues De Riedmatten. Quantum storage of a photonic polarization qubit in a solid. *Physical Review Letters*, 108:190504, 5 2012. 29, 33

[249] Wolfgang Tittel, Mikael Afzelius, and Thierry Chaneli. Photon-echo quantum memory in solid state systems. *Laser and Photonics Reviews*, 267:244–267, 2010. 29, 33

[250] Neil Sinclair, Erhan Saglamyurek, Hassan Mallahzadeh, Joshua A. Slater, Mathew George, Raimund Ricken, Morgan P. Hedges, Daniel Oblak, Christoph Simon, Wolfgang Sohler, and Wolfgang Tittel. Spectral multiplexing for scalable quantum photonics using an atomic frequency comb quantum memory and feed-forward control. *Physical Review Letters*, 113:053603, 7 2014. 29, 33

[251] Jay E. Sharping, Jun Chen, Paul L. Voss, Prem Kumar, and Xiaoying Li. Storage and long-distance distribution of telecommunications-band polarization entanglement gener-

ated in an optical fiber. *Optics Letters, Vol. 30, Issue 10, pp. 1201-1203*, 30:1201–1203, 5 2005. 30

[252] Kenzo Makino, Yosuke Hashimoto, Jun Ichi Yoshikawa, Hideaki Ohdan, Takeshi Toyama, Peter Van Loock, and Akira Furusawa. Synchronization of optical photons for quantum information processing. *Science Advances*, 2, 5 2016. 30

[253] Feihu Xu, Fumihiro Kaneda, Joseph Chapman, and Paul G. Kwiat. Quantum-memory-assisted multi-photon generation for efficient quantum information processing. *Optica, Vol. 4, Issue 9, pp. 1034-1037*, 4:1034–1037, 9 2017. 30

[254] Peter W. Milonni. The quantum vacuum: An introduction to quantum electrodynamics. *The Quantum Vacuum: An Introduction to Quantum Electrodynamics*, pages 1–522, 10 2013. 31

[255] A. Sipahigil, R. E. Evans, D. D. Sukachev, M. J. Burek, J. Borregaard, M. K. Bhaskar, C. T. Nguyen, J. L. Pacheco, H. A. Atikian, C. Meuwly, R. M. Camacho, F. Jelezko, E. Bielejec, H. Park, M. Lončar, and M. D. Lukin. An integrated diamond nanophotonics platform for quantum-optical networks. *Science*, 354:847–850, 11 2016. 31

[256] Holger P. Specht, Christian Nölleke, Andreas Reiserer, Manuel Uphoff, Eden Figueroa, Stephan Ritter, and Gerhard Rempe. A single-atom quantum memory. *Nature*, 473:190–193, 5 2011. 31, 32

[257] Stephan Ritter, Christian Nölleke, Carolin Hahn, Andreas Reiserer, Andreas Neuzner, Manuel Uphoff, Martin Mücke, Eden Figueroa, Joerg Bochmann, and Gerhard Rempe. An elementary quantum network of single atoms in optical cavities. *Nature*, 484:195–200, 4 2012. 31

[258] A. D. Boozer, A. Boca, R. Miller, T. E. Northup, and H. J. Kimble. Reversible state transfer between light and a single trapped atom. *Optics InfoBase Conference Papers*, 193601:1–4, 2007. 31

[259] D. D. Sukachev, A. Sipahigil, C. T. Nguyen, M. K. Bhaskar, R. E. Evans, F. Jelezko, and M. D. Lukin. Silicon-vacancy spin qubit in diamond: A quantum memory exceeding 10 ms with single-shot state readout. *Physical Review Letters*, 119:223602, 11 2017. 32

[260] Christoph Kurz, Michael Schug, Pascal Eich, Jan Huwer, Philipp Müller, and Jürgen Eschner. Experimental protocol for high-fidelity heralded photon-to-atom quantum state transfer. *Nature Communications*, 5:1–5, 11 2014. 32

[261] E. Togan, Y. Chu, A. S. Trifonov, L. Jiang, J. Maze, L. Childress, M. V.G. Dutt, A. S. Sørensen, P. R. Hemmer, A. S. Zibrov, and M. D. Lukin. Quantum entanglement between an optical photon and a solid-state spin qubit. *Nature*, 466:730–734, 8 2010. 32

[262] G. D. Fuchs, G. Burkard, P. V. Klimov, and D. D. Awschalom. A quantum memory intrinsic to single nitrogen–vacancy centres in diamond. *Nature Physics*, 7:789–793, 6 2011. 32

[263] H. Bernien, B. Hensen, W. Pfaff, G. Koolstra, M. S. Blok, L. Robledo, T. H. Taminiau, M. Markham, D. J. Twitchen, L. Childress, and R. Hanson. Heralded entanglement between solid-state qubits separated by three metres. *Nature*, 497:86–90, 4 2013. 32

[264] Krzysztof Tadeusz Kaczmarek. *ORCA Towards an integrated noise-free Quantum Memory*. PhD thesis, Oxford University, 2017. 32, 121, 122, 145, 168, 201

[265] B. M. Sparkes, J. Bernu, M. Hosseini, J. Geng, Q. Glorieux, P. A. Altin, P. K. Lam, N. P. Robins, and B. C. Buchler. Gradient echo memory in an ultra-high optical depth cold atomic ensemble. *New Journal of Physics*, 15:085027, 8 2013. 33, 34, 35

[266] M Hosseini, B M Sparkes, G Campbell, P K Lam, and B C Buchler. High efficiency coherent optical memory with warm rubidium vapour. *Nature Communications*, 2:174–175, 2011. 33, 34, 35, 94

[267] Christoph Clausen, Imam Usmani, Félix Bussiéres, Nicolas Sangouard, Mikael Afzelius, Hugues De Riedmatten, and Nicolas Gisin. Quantum storage of photonic entanglement in a crystal. *Nature*, 469:508–512, 2011. 33

[268] Christoph Clausen, Félix Bussières, Mikael Afzelius, and Nicolas Gisin. Quantum storage of heralded polarization qubits in birefringent and anisotropically absorbing materials. *Physical Review Letters*, 108:190503, 5 2012. 33

[269] Zong Quan Zhou, Wei Bin Lin, Ming Yang, Chuan Feng Li, and Guang Can Guo. Realization of reliable solid-state quantum memory for photonic polarization qubit. *Physical Review Letters*, 108:190505, 5 2012. 33

[270] D. Main, T. M. Hird, T. M. Hird, S. Gao, I. A. Walmsley, I. A. Walmsley, P. M. Ledingham, and P. M. Ledingham. Room temperature atomic frequency comb storage for light. *Optics Letters, Vol. 46, Issue 12, pp. 2960-2963*, 46:2960–2963, 6 2021. 33, 35, 36

[271] G. Hétet, J. J. Longdell, A. L. Alexander, P. K. Lam, and M. J. Sellars. Electro-optic quantum memory for light using two-level atoms. *Physical Review Letters*, 100:023601, 1 2008. 34, 35, 36

[272] Mahmood Sabooni, Qian Li, Stefan Kröll, and Lars Rippe. Efficient quantum memory using a weakly absorbing sample. *Physical Review Letters*, 110:1–5, 2013. 35, 36

[273] I. D. Abella, N. A. Kurnit, and S. R. Hartmann. Photon echoes. *Physical Review*, 141:391, 1 1966. 34

[274] Mikael Afzelius, Imam Usmani, Atia Amari, Björn Lauritzen, Andreas Walther, Christoph Simon, Nicolas Sangouard, Jiří Minář, Hugues De Riedmatten, Nicolas Gisin, and Stefan Kröll. Demonstration of atomic frequency comb memory for light with spin-wave storage. *Physical Review Letters*, 104:040503, 1 2010. 36

[275] Alessandro Seri, Andreas Lenhard, Daniel Rieländer, Mustafa Gündoğan, Patrick M Ledingham, Margherita Mazzera, and Hugues De Riedmatten. Quantum correlations between single telecom photons and a multimode on-demand solid-state quantum memory. *Physical Review X*, 7, 2017. 36

[276] Jelena V Rakonjac, Dario Lago-Rivera, Alessandro Seri, Margherita Mazzera, Samuele Grandi, and Hugues De Riedmatten. Entanglement between a telecom photon and an

on-demand multimode solid-state quantum memory. *Physical Review Letters*, 127, 2021. 36, 141

[277] P. Jobez, I. Usmani, N. Timoney, C. Laplane, N. Gisin, and M. Afzelius. Cavity-enhanced storage in an optical spin-wave memory. *New Journal of Physics*, 16:083005, 8 2014. 36

[278] Antonio Ortu, Jelena V Rakonjac, Adrian Holzäpfel, Alessandro Seri, Samuele Grandi, Margherita Mazzera, Hugues de Riedmatten, and Mikael Afzelius. Multimode capacity of atomic-frequency comb quantum memories. *Quantum Science and Technology*, 7:035024, 6 2022. 36

[279] Alexey V. Gorshkov, Axel Andre, Mikhail D. Lukin, and Anders S. Sørensen. Photon storage in $\lambda-$type optically dense atomic media. iii. effects of inhomogeneous broadening. *Physical Review A*, pages 1–26, 2006. 36

[280] Alexey V. Gorshkov, Axel André, Michael Fleischhauer, Anders S. Sørensen, and Mikhail D. Lukin. Universal approach to optimal photon storage in atomic media. *Physical Review Letters*, 98:1–4, 2007. 36, 133, 135, 146, 152, 158

[281] Alexey V. Gorshkov, Axel André, Mikhail D. Lukin, and Anders S. Sørensen. Photon storage in $\lambda-$type optically dense atomic media. ii. free-space model. *Physical Review A - Atomic, Molecular, and Optical Physics*, 76:1–25, 2007. 36

[282] Alexey V. Gorshkov, Axel André, Mikhail D. Lukin, and Anders S. Sørensen. Photon storage in $\lambda-$type optically dense atomic media. i. cavity model. *Physical Review A*, 76:033804, 9 2007. 36

[283] K. J. Boller, A. Imamolu, and S. E. Harris. Observation of electromagnetically induced transparency. *Physical Review Letters*, 66:2593, 5 1991. 36

[284] Michael Fleischhauer, Atac Imamoglu, and Jonathan P. Marangos. Electromagnetically induced transparency: Optics in coherent media. *Reviews of Modern Physics*, 77:633–673, 2005. 36, 121

[285] Tony Y. Abi-Salloum. Electromagnetically induced transparency and autler-townes splitting: Two similar but distinct phenomena in two categories of three-level atomic systems. *Physical Review A - Atomic, Molecular, and Optical Physics*, 81, 2010. 36, 121

[286] D. F. Phillips, A. Fleischhauer, A. Mair, R. L. Walsworth, and M. D. Lukin. Storage of light in atomic vapor. *Physical Review Letters*, 86:783, 1 2001. 37, 121, 153

[287] Chien Liu, Zachary Dutton, Cyrus H. Behroozi, and Lene Vestergaard Hau. Observation of coherent optical information storage in an atomic medium using halted light pulses. *Nature*, 409:490–493, 1 2001. 37, 121

[288] Anindya Rastogi, Erhan Saglamyurek, Taras Hrushevskyi, Scott Hubele, and Lindsay J. Leblanc. Discerning quantum memories based on electromagnetically-induced-transparency and autler-townes-splitting protocols. *Physical Review A*, 100:1–15, 2019. 36, 37, 38, 121

[289] A. V. Turukhin, V. S. Sudarshanam, M. S. Shahriar, J. A. Musser, B. S. Ham, and P. R. Hemmer. Observation of ultraslow and stored light pulses in a solid. *Physical Review Letters*, 88:023602, 12 2001. 37

[290] Georg Heinze, Christian Hubrich, and Thomas Halfmann. Stopped light and image storage by electromagnetically induced transparency up to the regime of one minute. *Physical Review Letters*, 033601:1–5, 2013. Long coherence times of EIT in doped crystals, approaching population decay limit, but low efficiency.¡br/¿¡br/¿Method used to prolong coherence time (magnetic fields) complex energy level splitting. Uses optimization technique to find best parameters (based of evolution optimization).¡br/¿¡br/¿Same method to prolong coherence time and technique used to optimize process may be applicable to vapour based systems. 37

[291] Erhan Saglamyurek, Taras Hrushevskyi, Anindya Rastogi, Khabat Heshami, and Lindsay J. LeBlanc. Coherent storage and manipulation of broadband photons via dynamically controlled autler–townes splitting. *Nature Photonics*, 12:774–782, 12 2018. 37, 38

[292] Emanuele Distante, Pau Farrera, Auxiliadora Padrón-Brito, David Paredes-Barato, Georg Heinze, and Hugues De Riedmatten. Storing single photons emitted by a quantum memory on a highly excited rydberg state. *Nature Communications*, 8:1–6, 1 2017. 37

[293] Ya-Nan Qin, Min Li, Kun Liu, al, B Suri, Z K Keane, R Ruskov, Zhao Yan-Ting, Zhao Jian-Ming, Erhan Saglamyurek, Taras Hrushevskyi, Anindya Rastogi, Logan W Cooke, Benjamin D Smith, and Lindsay J LeBlanc. Storing short single-photon-level optical pulses in bose–einstein condensates for high-performance quantum memory. *New Journal of Physics*, 23:043028, 4 2021. 38, 94

[294] A. Kozhekin, K. Mølmer, and E. Polzik. Quantum memory for light. *Physical Review A*, 62:033809, 8 2000. 38

[295] J. Nunn, I. A. Walmsley, M. G. Raymer, K. Surmacz, F. C. Waldermann, Z. Wang, and D. Jaksch. Mapping broadband single-photon wave packets into an atomic memory. *Physical Review A - Atomic, Molecular, and Optical Physics*, 75:1–4, 2007. 38

[296] Benjamin J. Sussman, Connor Kupchak, Duncan G. England, Khabat Heshami, and Philip J. Bustard. Reducing noise in a raman quantum memory. *Optics Letters, Vol. 41, Issue 21, pp. 5055-5058*, 41:5055–5058, 11 2016. 38

[297] Janik Wolters, Gianni Buser, Andrew Horsley, Lucas Béguin, Andreas Jöckel, Jan Philipp Jahn, Richard J. Warburton, and Philipp Treutlein. Simple atomic quantum memory suitable for semiconductor quantum dot single photons. *Physical Review Letters*, 119:060502, 8 2017. 38, 94

[298] Gianni Buser, Roberto Mottola, Björn Cotting, Janik Wolters, and Philipp Treutlein. Single-photon storage in a ground-state vapor cell quantum memory. *PRX Quantum*, 3:020349, 6 2022. 38, 94

[299] Duncan G. England, Kent A.G. Fisher, Jean Philippe W. Maclean, Philip J. Bustard, Rune Lausten, Kevin J. Resch, and Benjamin J. Sussman. Storage and retrieval of thz-bandwidth single photons using a room-temperature diamond quantum memory. *Physical Review Letters*, 114:053602, 2 2015. 38

[300] K. F. Reim, P. Michelberger, K. C. Lee, J. Nunn, N. K. Langford, and I. A. Walmsley. Single-photon-level quantum memory at room temperature. *Physical Review Letters*, 107:053603, 7 2011. 38, 160

[301] Ran Finkelstein, Eilon Poem, Ohad Michel, Ohr Lahad, and Ofer Firstenberg. Fast, noise-free memory for photon synchronization at room temperature. *Science Advances*, 4, 2018. 39, 162, 163, 165, 166, 179, 180, 181

[302] Aurélien A.L. Nicolet, Clemens Hofmann, Mikhail A. Kol'chenko, Boleslaw Kozankiewicz, and Michel Orrit. Single dibenzoterrylene molecules in an anthracene crystal: Spectroscopy and photophysics. *ChemPhysChem*, 8:1215–1220, 2007. 41, 44, 62, 63, 64, 66, 70, 76, 93, 151

[303] Markus Schwoerer and Hans Christoph Wolf. Organic molecular solids. *Organic Molecular Solids*, pages 1–427, 1 2008. 41, 48, 62, 63, 64

[304] Joseph A. Christensen, Jiawang Zhou, Nikolai A. Tcyrulnikov, Matthew D. Krzyaniak, and Michael R. Wasielewski. Spin-polarized molecular triplet states as qubits: Phosphorus hyperfine coupling in the triplet state of benzoisophosphinoline. *Journal of Physical Chemistry Letters*, 11:7569–7574, 9 2020. 41

[305] PW Atkins and RS Friedman. *Molecular quantum mechanics*. Oxford University Press, 5th edition, 2011. 41, 42

[306] Francesco Plastina and Francesco Piperno. Quantum interference in the spontaneous emission spectrum of a driven three-level system in cascade configuration. *Physics Letters A*, 236:16–22, 12 1997. 41, 46

[307] Ross C. Schofield, Paul Burdekin, Anastasios Fasoulakis, Louise Devanz, Dominika P. Bogusz, Rowan A. Hoggarth, Kyle D. Major, and Alex S. Clark. Narrow and stable single photon emission from dibenzoterrylene in para-terphenyl nanocrystals. *ChemPhysChem*, 23, 2 2022. 46, 74, 93

[308] Wim H. Hesselink and Douwe A. Wiersma. Optical dephasing and vibronic relaxation in molecular mixed crystals: A picosecond photon echo and optical study of pentacene in naphthalene and p-terphenyl. *The Journal of Chemical Physics*, 73:648, 7 1980. 47

[309] Thomas Nonn and Taras Plakhotnik. Non-lorentzian single-molecule line shape: Pseudolocal phonons and coherence transfer. *Physical Review Letters*, 85:1556, 8 2000. 47

[310] Rodney. Loudon. *The quantum theory of light.* Oxford University Press, 2000. 47, 48

[311] Ross Charles Schofield. *Dibenzoterrylene as a single photon source.* PhD thesis, Imperial College London, 2021. 51, 69, 82, 83

[312] JB Trebbia, H Ruf, P Tamarat, and B Lounis. Efficient generation of near infra-red single photons from the zero-phonon line of a single molecule. *Optics Express*, 17:23986–23991, 2009. 54, 64

[313] B. Lounis, H. A. Bechtel, D. Gerion, P. Alivisatos, and W. E. Moerner. Photon antibunching in single cdse/zns quantum dot fluorescence. *Chemical Physics Letters*, 329:399–404, 10 2000. 60

[314] Armand Rundquist, Michal Bajcsy, Arka Majumdar, Tomas Sarmiento, Kevin Fischer, Konstantinos G. Lagoudakis, Sonia Buckley, Alexander Y. Piggott, and Jelena Vučković. Nonclassical higher-order photon correlations with a quantum dot strongly coupled to a photonic-crystal nanocavity. *Physical Review A - Atomic, Molecular, and Optical Physics*, 90:3244–3260, 8 2014. 60

[315] Sebastien Boissier. *Coupling of single organic molecules to photonic micro-structures.* PhD thesis, Imperial College London, 2020. 64, 67, 68

[316] Sofia Pazzagli, Pietro Lombardi, Daniele Martella, Maja Colautti, Bruno Tiribilli, Francesco Saverio Cataliotti, and Costanza Toninelli. Self-assembled nanocrystals of polycyclic aromatic hydrocarbons show photostable single-photon emission. *ACS Nano*, 12:4295–4303, 5 2018. 68

[317] Peng Kang, Chunnian Chen, Lingyun Hao, Chunling Zhu, Yuan Hu, and Zuyao Chen. A novel sonication route to prepare anthracene nanoparticles. *Materials Research Bulletin*, 39:545–551, 4 2004. 68

[318] Mauro Croci, Hans Joachim Müschenborn, Frank Güttler, Alois Renn, and Urs P. Wild. Single molecule spectroscopy: pressure effect on pentacene in p-terphenyl. *Chemical Physics Letters*, 212:71–77, 9 1993. 77

[319] Urs P. Wild, Mauro Croci, Frank Güttler, Marco Pirotta, and Alois Renn. Single molecule spectroscopy: Stark-, pressure-, polarization-effects and fluorescence lifetime measurements. *Journal of Luminescence*, 60-61:1003–1007, 4 1994. 77

[320] Yuxi Tian, Pedro Navarro, and Michel Orrit. Single molecule as a local acoustic detector for mechanical oscillators. *Physical Review Letters*, 113:135505, 9 2014. 77

[321] Maja Colautti, Francesco S Piccioli, Zoran Ristanovic, Pietro Lombardi, Amin Moradi, Subhasis Adhikari, Irena Deperasinska, Boleslaw Kozankiewicz, Michel Orrit, and Costanza Toninelli. Laser-induced frequency tuning of fourier-limited single-molecule emitters. *ACS Nano*, 14:39, 2020. 78, 80

[322] M. Davanço, M. T. Rakher, D. Schuh, A. Badolato, and K. Srinivasan. A circular dielectric grating for vertical extraction of single quantum dot emission. *Applied Physics Letters*, 99:041102, 7 2011. 82

[323] S. Kolatschek, S. Hepp, M. Sartison, M. Jetter, P. Michler, and S. L. Portalupi. Deterministic fabrication of circular bragg gratings coupled to single quantum emitters via the combination of in-situ optical lithography and electron-beam lithography. *Journal of Applied Physics*, 125:045701, 1 2019. 82

[324] Ugo Stella, Luca Boarino, Natascia De Leo, Peter Munzert, and Emiliano Descrovi. Enhanced directional light emission assisted by resonant bloch surface waves in circular cavities. *ACS Photonics*, 6:2073–2082, 8 2019. 82

[325] M. M. Hasan, A. S.M.A. Haseeb, R. Saidur, H. H. Masjuki, and M. Hamdi. Influence of substrate and annealing temperatures on optical properties of rf-sputtered tio2 thin films. *Optical Materials*, 32:690–695, 4 2010. 83

[326] Laurent Malaquin, Tobias Kraus, Heinz Schmid, Emmanuel Delamarche, and Heiko Wolf. Controlled particle placement through convective and capillary assembly. *Langmuir*, 23:11513–11521, 11 2007. 84

[327] T. Pinedo Rivera, O. Lecarme, J. Hartmann, E. Rossitto, K. Berton, and D. Peyrade. Assisted convective-capillary force assembly of gold colloids in a microfluidic cell: Plasmonic properties of deterministic nanostructures. *Journal of Vacuum Science & Technology B: Microelectronics and Nanometer Structures Processing, Measurement, and Phenomena*, 26:2513, 12 2008. 84

[328] J. Cordeiro, M. Zelsmann, T. Honegger, E. Picard, E. Hadji, and D. Peyrade. Table-top deterministic and collective colloidal assembly using videoprojector lithography. *Applied Surface Science*, 349:452–458, 9 2015. 84

[329] D. R. Lide. *CRC Handbook of Chemistry and Physics*. CRC Press Inc, 75 edition, 1995. 86

[330] H. C. Fleischhauer, Carola Kryschi, Birgit Wagner, and Hans Kupka. Pseudolocal phonons in p-terphenyl: pentacene single crystals. *The Journal of Chemical Physics*, 97:1742, 8 1998. 86, 89

[331] S. Kummer, Th Basché, and C. Bräuchle. Terrylene in p-terphenyl: a novel single crystalline system for single molecule spectroscopy at low temperatures. *Chemical Physics Letters*, 229:309–316, 10 1994. 86, 89

[332] T. G. Tiecke. Properties of potassium. `https://www.tobiastiecke.nl/archive/PotassiumProperties.pdf`. version 1.03, June 2019. Accessed: 2022-10-12. 87

[333] Zhengyi Xu, Xinxin Peng, Lianhua Li, al, Baodong Yang, Jiangyan Zhao, Tiancai Zhang, Grzegorz Dudzik, Karol Krzempek, and Krzysztof M Abramski. Laser frequency sta-

bilization on 5p→5d transition by double resonance optical pumping and two-photon transition spectroscopy in rubidium. *Laser Physics*, 30:025201, 12 2019. 87

[334] Paul Siddons, Charles S. Adams, Chang Ge, and Ifan G. Hughes. Absolute absorption on rubidium d lines: Comparison between theory and experiment. *Journal of Physics B: Atomic, Molecular and Optical Physics*, 41, 2008. 94

[335] Daniel J. McCarron, Ifan G. Hughes, Patrick Tierney, and Simon L. Cornish. A heated vapor cell unit for dichroic atomic vapor laser lock in atomic rubidium. *Review of Scientific Instruments*, 78:093106, 9 2007. 94, 95

[336] C. Wieman and T. W. Hänsch. Doppler-free laser polarization spectroscopy. *Physical Review Letters*, 36:1170, 5 1976. 94

[337] G. C. Bjorklund, M. D. Levenson, W. Lenth, and C. Ortiz. Frequency modulation (fm) spectroscopy. *Applied Physics B 1983 32:3*, 32:145–152, 11 1983. 94

[338] T. Petelski, M. Fattori, G. Lamporesi, J. Stuhler, and G. M. Tino. Doppler-free spectroscopy using magnetically induced dichroism of atomic vapor: a new scheme for laser frequency locking. *The European Physical Journal D - Atomic, Molecular, Optical and Plasma Physics 2003 22:2*, 22:279–283, 2003. 94

[339] Federica A. Beduini, Joanna A. Zielińska, Morgan W. Mitchell, and Nicolas Godbout. Ultranarrow faraday rotation filter at the rb d¡sub¿1¡/sub¿ line. *Optics Letters, Vol. 37, Issue 4, pp. 524-526*, 37:524–526, 2 2012. 94

[340] Mark Kasevich and Steven Chu. Atomic interferometry using stimulated raman transitions. *Physical Review Letters*, 67:181, 7 1991. 94

[341] Peter D.D. Schwindt, Svenja Knappe, Vishal Shah, Leo Hollberg, John Kitching, Li Anne Liew, and John Moreland. Chip-scale atomic magnetometer. *Applied Physics Letters*, 85:6409, 12 2004. 94

[342] A. G. Radnaev, Y. O. Dudin, R. Zhao, H. H. Jen, S. D. Jenkins, A. Kuzmich, and T. A.B. Kennedy. A quantum memory with telecom-wavelength conversion. *Nature Physics*, 6:894–899, 2010. 94, 181

[343] S. E. Thomas, S. Sagona-Stophel, Z. Schofield, I. A. Walmsley, and P. M. Ledingham. A single-photon-compatible telecom-c-band quantum memory in a hot atomic gas. *arxiv preprint*, 11 2022. 94, 100, 164, 181

[344] C. P. Pearman, C. S. Adams, S. G. Cox, P. F. Griffin, D. A. Smith, and I. G. Hughes. Polarization spectroscopy of a closed atomic transition: applications to laser frequency locking. *Journal of Physics B: Atomic, Molecular and Optical Physics*, 35:5141, 12 2002. 95

[345] John Kitching, Leo Hollberg, Peter D. D. Schwindt, Svenja Knappe, Vishal Shah, and Vladislav Gerginov. Long-term frequency instability of atomic frequency references based on coherent population trapping and microfabricated vapor cells. *JOSA B, Vol. 23, Issue 4, pp. 593-597*, 23:593–597, 4 2006. 95

[346] M. Himsworth and T. Freegarde. Rubidium pump-probe spectroscopy: Comparison between ab initio theory and experiment. *Physical Review A - Atomic, Molecular, and Optical Physics*, 81:1–8, 2010. 95, 109

[347] Alok K. Singh, Sapam Ranjita Chanu, Dipankar Kaundilya, and Vasant Natarajan. Hyperfine spectroscopy using co-propagating pump-probe beams. *arXiv preprint*, page 9, 2010. 95

[348] A K Mohapatra, T R Jackson, and C S Adams. Coherent optical detection of highly excited rydberg states using electromagnetically induced transparency. *Physical Review Letters*, 113003:1–4, 2007. 95

[349] Christopher J. Foot. *Atomic Physics*. Oxford University Press, 2007. 96, 103

[350] Daniel A. Steck. Rubidium 87 d line data. `https://steck.us/alkalidata/rubidium87numbers.1.6.pdf`. revision 1.6, 14 October 203. Accessed: 2023-03-03. 96, 98, 101, 113, 144

[351] Daniel A. Steck. Rubidium 85 d line data. `http://steck.us/alkalidata/rubidium85numbers.pdf`. revision 2.2.3, 9 July 2021. Accessed: 2023-03-03. 96, 98, 113

[352] Von A. N. Nesmeyanov and R. Gary. *Vapor Pressure of the Chemical Elements*, volume 76. Elsevier Publishing Co., 1963. 97

[353] M.P.R. Thomsen, L.J. Stief, and R.J. Fallon. Study of the phenomena affecting the composition of rubidium vapor cells. *22nd Annual Symposium on Frequency Control*, pages 559–572, 7 1968. 97

[354] J Ma, A Kishinevski, Y.-Y Jau, C Reuter, and W Happer. Modification of glass cell walls by rubidium vapor. *Physical Review A*, 79, 2009. 97

[355] Vapor reference cells. `https://www.thorlabs.com/newgrouppage9.cfm?objectgroup_id=1470`. Accessed: 2023-07-16. 97

[356] Kyle N Jarvis. *The Blue-Detuned Magneto-Optical Trap*. PhD thesis, Imperial College London, 2018. 97, 98

[357] Paul Siddons, Charles S Adams, Chang Ge, and Ifan G Hughes. Absolute absorption on rubidium d lines : comparison between theory and experiment. *Journal of Physics B: Atomic, Molecular and Optical Physics*, 41:1–10, 2008. 101

[358] Metcalf H. and van der Straten P. *Laser Cooling and Trapping*. Springer, New York, 1999. 102

[359] Mark S. Fox. *Quantum Optics: An Introduction*. Oxford University Press, 2006. 103

[360] David A. Smith and Ifan G. Hughes. The role of hyperfine pumping in multilevel systems exhibiting saturated absorption. *American Journal of Physics*, 72:631–637, 2004. 109

[361] Sarah Ellyn Thomas. *Efficient, Low Noise, Mode-Selective Quantum Memory*. PhD thesis, Imperial College London, 2019. 121, 168

[362] Joseph H D Munns. *Optimisation and Applications of a Raman Quantum Memory for Temporal Modes of Light*. PhD thesis, Imperial College London, 2018. 121, 168

[363] Matthew T. Rakher, Richard J. Warburton, and Philipp Treutlein. Prospects for storage and retrieval of a quantum-dot single photon in an ultracold 87rb ensemble. *Physical Review A - Atomic, Molecular, and Optical Physics*, 88:053834, 11 2013. 136

[364] Daniel M. Reich, Mamadou Ndong, and Christiane P. Koch. Monotonically convergent optimization in quantum control using krotov's method. *The Journal of Chemical Physics*, 136:104103, 3 2012. 140

[365] Pin Ju Tsai and Ying Cheng Chen. Ultrabright, narrow-band photon-pair source for atomic quantum memories. *Quantum Science and Technology*, 3:034005, 5 2018. 141

[366] A. D. Tranter, H. J. Slatyer, M. R. Hush, A. C. Leung, J. L. Everett, K. V. Paul, P. Vernaz-Gris, P. K. Lam, B. C. Buchler, and G. T. Campbell. Multiparameter optimisation of a magneto-optical trap using deep learning. *Nature Communications*, 9:1–8, 10 2018. 141

[367] D. J. Saunders, J. H.D. Munns, T. F.M. Champion, C. Qiu, K. T. Kaczmarek, E. Poem, P. M. Ledingham, I. A. Walmsley, and J. Nunn. Cavity-enhanced room-temperature broadband raman memory. *Physical Review Letters*, 116:090501, 3 2016. 145, 162

[368] Nathaniel B. Phillips, Alexey V. Gorshkov, and Irina Novikova. Light storage in an optically thick atomic ensemble under conditions of electromagnetically induced transparency and four-wave mixing. *Physical Review A - Atomic, Molecular, and Optical Physics*, 83:063823, 6 2011. 147

[369] Roberto Mottola, Gianni Buser, and Philipp Treutlein. Electromagnetically induced transparency and optical pumping in the hyperfine paschen-back regime. 7 2023. 180

[370] Anne Louchet-Chauvet, Julián Dajczgewand, Thierry Chanelière, and Jean-Louis Le Gouët. Large efficiency at telecom wavelength for optical quantum memories. *Optics Letters, Vol. 39, Issue 9, pp. 2711-2714*, 39:2711–2714, 5 2014. 181

[371] Andreas Wallucks, Igor Marinković, Bas Hensen, Robert Stockill, and Simon Gröblacher. A quantum memory at telecom wavelengths. *Nature Physics*, 16:772–777, 5 2020. 181

[372] Ioana Craiciu, Mi Lei, Jake Rochman, Jonathan M. Kindem, John G. Bartholomew, Evan Miyazono, Tian Zhong, Neil Sinclair, and Andrei Faraon. Nanophotonic quantum storage at telecommunication wavelength. *Physical Review Applied*, 12:024062, 8 2019. 181

[373] Miloš Rancic, Morgan P. Hedges, Rose L. Ahlefeldt, and Matthew J. Sellars. Coherence time of over a second in a telecom-compatible quantum memory storage material. *Nature Physics*, 14:50–54, 9 2017. 181

[374] R. Finkelstein, O. Lahad, I. Cohen, O. Davidson, S. Kiriati, E. Poem, and O. Firstenberg. Continuous protection of a collective state from inhomogeneous dephasing. *Physical Review X*, 11:011008, 1 2021. 185, 187

[375] Constantine E. Theodosiou. Lifetimes of alkali-metal—atom rydberg states. *Physical Review A*, 30:2881, 12 1984. 188

[376] O. Gazzano, S. Michaelis De Vasconcellos, C. Arnold, A. Nowak, E. Galopin, I. Sagnes, L. Lanco, A. Lemaître, and P. Senellart. Bright solid-state sources of indistinguishable single photons. *Nature Communications*, 4, 2013. 191

[377] Simone Götz, Bastian Höltkemeier, Christoph S. Hofmann, Dominic Litsch, Brett D. DePaola, and Matthias Weidemüller. Versatile cold atom target apparatus. *Review of Scientific Instruments*, 83:073112, 7 2012. 194

[378] Shanchao Zhang, J. F. Chen, Chang Liu, Shuyu Zhou, M. M.T. Loy, G. K.L. Wong, and Shengwang Du. A dark-line two-dimensional magneto-optical trap of 85rb atoms with high optical depth. *Review of Scientific Instruments*, 83:073102, 7 2012. 195

[379] Jayampathi C. B. Kangara, Andrew J. Hachtel, Matthew C. Gillette, Jason T. Barkeloo, Ethan R. Clements, Samir Bali, Brett E. Unks, Nicholas A. Proite, Deniz D. Yavuz, Paul J. Martin, Jeremy J. Thorn, and Daniel A. Steck. Design and construction of cost-effective tapered amplifier systems for laser cooling and trapping experiments. *American Journal of Physics*, 82:805, 7 2014. 197